DEVELOPMENT AND CHARACTERISATION OF NOVEL LOW-FRICTION WEAR-RESISTANT MULTILAYER NANOCOMPOSITE CrAlTiCN COATINGS

by

WENWEN WU

A thesis submitted to

The University of Birmingham

for the degree of

DOCTOR OF PHILOSOPHY

School of Metallurgy and Materials

College of Engineering and Physical Sciences

The University of Birmingham

September 2010

Synopsis

The present investigation has been focused on the design, deposition and characterisation of novel low-friction, wear-resistant multilayer nanocomposite CrAlTiCN coatings. Systematic materials characterisation and property evaluation were conducted on the as-deposited and oxidation-tested CrAlTiCN coatings, and the results are presented and discussed.

It is possible to generate novel CrAlTiCN coatings with the carbon content up to 24.34 at% by closed-field unbalanced magnetron sputtering of graphite target. The microstructure of the CrAlTiCN coatings mainly depends on their carbon content. When the carbon content is low, carbon atoms are mainly dissolved in the fcc metastable phase (Cr, Al, Ti) (C, N); when the carbon content is high, the major carbon atoms will form amorphous carbon with a C-C bond state and in a sp^2 dominated graphitic environment.

Both the hardness and brittleness of CrAlTiCN coatings reduce with increasing the carbon content. When tested at room temperature under unidirectional sliding conditions, the friction coefficient and wear of the CrAlTiCN coatings decrease with the carbon content, and the thermal stability of CrAlTiCN coatings is similar to the CrAlTiN coating but better than graphite-like carbon coatings.

The good performance of the new CrAlTiCN coatings can be attributed to the optimised design of the coating system: the Cr/Al for oxidation resistance, the amorphous C for low-friction and the multi-layered nano-composite microstructure for high toughness.

Publications

[1] Wenwen Wu, Xiaoying Li, Jian Chen, Hanshan Dong, Design and characterisation of an advanced duplex system based on carbon S-phase case and GiC coatings for 316 LVM austenitic stales steel, Surface and Coatings Technology, 203 (2009) 1273-1280

[2] Wenwen Wu, Hanshan Dong, Bailing Jiang, 11th International Conference on Plasma Engineering, 2008, Garmisch-Partenkirchen, Germany

[3] Wenwen Wu, Xiaoying Li, Hanshan Dong, Microstructural characterisation of new carbon doped CrAlTiCN nanoscale multilayer coatings, Surface and Coatings Technology, submitted

List of abbreviations and acronyms

AFM   Atomic Force Microscopy

BS   British Standards

BSE   Back Scattered Electron (imaging)

COF   Coefficient of Friction

CVD   Chemical Vapour Deposition

EDX   Energy Dispersive X-Ray spectroscopy

EELS   Electron Energy Loss Spectroscopy

fcc   face centred cubic

GAXRD   Glancing-angle X-ray Diffraction

GDOES   Glow Discharge Optical Emission Spectroscopy

HSS   High Speed Steel

LBC   Load Bearing Capacity

OES   Optical Emission Spectroscopy

OM   Optical Microscopy

PVD   Physical Vapour Deposition

SAD   Selected Area Diffraction

SEM   Secondary Electron Microscopy

STEM   Scanning Transmission Electron Microscopy

TEM   Transmission Electron Microscopy

XPS   X-ray Photoelectron Spectroscopy

XRD   X-Ray Diffraction

Table of contents

III

Chapter 1: Introduction and Objectives

1.1 Introduction

Thin wear-resistant hard coatings are widely applied on cutting and forming tools to improve their lifetime and performance, increase productivity, and enable some new engineering applications as well. Hard coating deposition has now become a routine processing step in the tools industry [1]. Currently, a wide range of PVD hard coatings are available for a variety of applications. TiN is the first generation of PVD hard coating and is still being used as protective hard coatings for bearings, gears, and cutting and forming tools [2,3,4]. However, the fracture toughness and oxidation resistance ($<$ 550 ℃) of the TiN coatings are not satisfactory for many advanced engineering applications [5,6]. As one of the major milestones in the advances of hard coating development, TiAlN has been successfully commercialised particularly for high-speed cutting because of its significantly improved oxidation resistance (around 700～900℃) and hardness over TiN [7,8,9,10,11].

However, the oxidation resistance at elevated temperatures of the Ti-based coatings is limited although it has been improved with aluminium incorporation. These drawbacks of the Ti-based coatings have strongly limited their practical applications [12], which has resulted in a critical challenge for the Ti-based hard coatings. Recently, the new formula of wear resistance coatings has been explored by various research groups worldwide [13,14,15,16,17]. CrN-based multi-component nitride is a typical example. Similar to TiN, chromium nitride (CrN) has been successfully applied to the metal forming and plastic moulding dies and wear components, which is known to be superior to TiN in wear

resistance, friction behaviour, and toughness [18,19,20]. Similar to the TiAlN coating system, the incorporation of Al into the cubic CrN crystalline structure greatly enhances the hardness (around 20 GPa) and oxidation resistance up to around 900 ℃ [21] of the CrAlN coating system. A better abrasive wear resistance, which is believed to be the major wear mechanism in machining and forming applications, of the CrAlN coatings (particularly with higher Al-content) was also reported. It has been showed that the tribological properties of CrAlN coatings are much better (with both lower wear rate and friction coefficient) than those of the TiAlN coatings under sliding wear conditions. Most recently, a CrN-based Cr-Ti-Al-N coating system has been developed by Teer Coatings Ltd to improve the performance of twist drills and extrusion dies [22,23]. It has been revealed that quaternary Cr-Ti-Al-N coatings demonstrate an even higher hardness (25-30 GPa), higher wear resistance, and outstanding oxidation resistance (around 1000 ℃) as compared to that of the ternary CrAlN coatings [19,24,25]. However, the coefficient of friction of these so-called super-hard coatings is relatively high (around 0.7~0.9) [26,27] at room temperature and extra lubrication is needed in many applications, which present health and/or environmental concerns [28].

On the other hand, the design and development of low-friction coatings are of continuously increasing importance. The first design concept utilises a matrix of amorphous diamond-like carbon (DLC) with low friction is obtained by the carbon sp^3 to sp^2 structural transformation, i.e. graphitisation [29,30]. Furthermore, graphite-like carbon (GLC) coatings were reported to have excellent tribological properties, very low friction and low wear rate at room temperature in dry and ambient environments. The low friction properties are attributed to the formation of easily sheared graphitic carbon [31,32,33]. However, all

these carbon-based coatings degraded under high-temperatures, and were found to be non-functional beyond approximately 400 ℃ in air [34], which eliminates their use for dry and high-speed cutting tools.

A complex interactive effect often determines the point at which a new synthetical coating is expected to fulfil the manufacture purpose. Adding solid carbon into quaternary Cr-Al-Ti-N coatings with a nanocomposite structure may present more desirable combined properties. However, research work on the design, synthesis, and characterisation of carbon-doped CrAlTiN coating (i.e. CrAlTiCN) which possess both low frictional coefficients (high wear resistance and self-lubrication) and oxidation resistance has been relatively sparse and there is limited work reported on the influence of carbon concentrations on the structure, tribological and thermal properties.

1.2 Aims of the project

The overall aim of this PhD project was to explore the feasibility of doping CrAlTiN coatings with carbon to form a novel nano-composite coating with a good combination of a high hardness, good wear resistance and a low friction coefficient, and to detailed investigate the effect of carbon content onto the morphology, microstructure, mechanical properties, tribological behaviour and oxidation resistance. Hence, the scientific and technological objectives of the present project are the following:

- To design/develop and synthesise of novel nano-composite coatings by doping CrAlTiN coatings with different amount of carbon;

- To fully characterise the microstructures of the novel CrAlTiCN coatings to understand the role of carbon in the novel CrAlTiCN nanostructure coatings; and

- To assess the mechanical and tribological properties and the oxidation behaviour of the new CrAlTiCN coating materials.

1.3 The structure of the thesis

In this thesis, the fundamentals of friction and wear of coatings materials, the current status of design and development of tribological coatings, the development of coating technologies, and the characterisation and evaluation of coatings materials are first reviewed (*Chapter 2*), which is followed by the experimental procedure and techniques employed (*Chapter 3*). The experimental results obtained from the project are reported in *Chapter 4* according to the research subtopics, which are interpreted and discussed in *Chapter 5* to understand the mechanisms involved. Finally, conclusions from the research and suggestions for future work are given in *Chapter 6* and *Chapter 7*, respectively.

Chapter 2: Literature Review

2.1 Introduction to tribology

Tribology, derived from the Greek tribos—rubbing and first enunciated in the famous Jost Report [35], has been defined as 'the science and technology of interacting surfaces in relative motion and of the practices related thereto [36]. Normally, the basic mechanisms are combined in a very complex way due to more complicated contact geometry, involving roughness and debris, due to inhomogeneous surface materials with changing properties and due to variations in loading and sliding conditions. Certainly, tribology is multidisciplined, drawing on mechanical engineering, physics, chemistry and metallurgy. The main parameters influencing the tribological process are illustrated in Figure 2.1-1. During the sliding contact some of the parameters will change, surface layers are formal, strain hardening takes place, local temperature rises causing softening, etc. and after one sliding event it may have a new set of parameters controlling the friction and wear [37].

Now, tribology is recognized as a vital ingredient of our technological age and is among the most rapidly developing disciplines, largely because of its highly practical and economic importance. In view of the scope of the study, this section is mainly an overview of the mechanisms and affecting factors of friction and wear. There are a number of classifications of friction and wear mechanisms published [38,39,40], the classification of basic friction and wear mechanisms can be developed even further and suggest the classification shown in Figure 2.1-2.

2.1.1 Friction

Friction is the resisting force tangential to the common boundary between two bodies when, under the action of an external force, one body moves or tends to move relative to the surface of the other [36]. Accordingly, there are two types of friction, static and dynamic. The static frictional force f_s is defined as a minimal force needed to initiate sliding. The kinetic frictional force f_k has to be considered as the mechanism to convert the energy of translational motion into heat. Essentially, both energy and material loss result from the interaction of surfaces due to relative motion. In order to minimize friction and wear, it is necessary to understand how surfaces interact when they are in contact.

2.1.1.1 The laws of friction

The main friction laws, which is the famous Amontons' laws (see below section), belong to the oldest physical laws and have been known for more than three hundred years. However, a physical explanation of the empirical Amontons' laws was given by Bowder and Tabor [41]. A new era in tribology began later on, when this science approached a microsopic and even atomic level in the study of the contacts themselves.

First of all, the two famous Amontons' tribological laws date back to 1699 [42]:

The first Amontons law: The frictional force is directly proportional to the load.

The second Amontons law: The frictional force is independent of the apparent area of contact.

It must be emphasised that these two laws of friction are based on empirical observations. While they are applicable in most cases, there are also many exceptions. What is more, these laws do not give any information about the origin of friction, i.e. friction mechanisms, which are essential to the control of friction.

Friction is commonly represented by the friction coefficient, which is usually denoted by the symbol µ:

$$\mu = \frac{F}{N} \qquad\qquad (2.1\text{-}1)$$

where F is the friction force, and N the normal load. It should be pointed out that the friction coefficient is a function of the system, governed by some factors such as material properties, surface roughness of each solid, nature of the environment, load, speed, nature of contact, nature of relative motion (rolling or sliding) [43]. So there is no simple model to predict or to calculate friction for a given pair of materials. A qualitative explanation of these laws was given by Bowden and Tabor (see below section).

2.1.1.2 Friction mechanisms

Historically, there are two basic mechanisms: the molecular force model and the mechanical interaction model [37, 44]. However, most current theories of sliding stem from the important work of Bowden and Tabor between the 1930s and 1970s and much of our present understanding is due to their dedicated efforts.

An explanation of the second Amontons law (that µ is a constant ≤1), was first given by Bowden and Tablor [3]. It is based on the assumption that the surfaces in contact are rough,

therefore the real (actual) contact area, A_{real}, is much smaller than the normal contact area, A, and proportional to the load, $A_{real} \propto N$. The area A_{real} should grow until the external loading force will be balanced by the counteracting contact pressure integrated over A_{real}. Namely, let $\sigma_{real} = (\sigma_s \cdot A)/A_{real}$ be the real pressure at the contact. Then at low loading pressure, $\sigma_{real} < \sigma_s$ when the substrates are in the elastic regime, the area of each contact is approximately constant, while the number of contacts increases with the load. At a high load, $\sigma_{real} > \sigma_s$ (i.e., in the plastic regime), the area of real contact should increase with the load until $\sigma_{real} = \sigma_s$, because of its plastic deformation.

Therefore $N = \sigma_{real} \cdot A_{real} = \sigma_s \cdot A_{real}$ $\quad\quad \sigma_s$ --normal yield stress

While $F = \tau_s \cdot A_{real}$ $\quad\quad \tau_s$ --shear yield stress

According to Equation 2-1,

$$\mu = \frac{F}{N} = \frac{\tau_s \cdot A_{real}}{\sigma_s \cdot A_{real}} = \frac{\tau_s}{\sigma_s} \quad\quad\quad\quad (2.1\text{-}2)$$

2.1.1.3 The temperature of sliding surface

When two surfaces slide together, most of the work done against friction is turned into frictional heat [45]. Since the frictional heat generated is at the tiny contact area, the resulting rise in temperature can be appreciable.

There are two types of temperature describing the frictional heat during sliding. One is the average or bulk temperature on the friction surface; the other occurs at the tiny contact areas at which the energy is dissipated immediately, therefore this temperature is instantaneous

with short duration and are called local or flash temperature. Although the duration of the flash temperatures is only in the order of a few microseconds [45] and they occur only over small regions, the flash temperature can cause appreciable changes in the surface zone, such as metallurgical transformations [46], mechanical property degradation and surface oxidation [47], which can in turn greatly influence friction and wear. The direct observation of surface hot spot temperature was made by Quinn and Winer [48], who slide a 6 mm diameter tool steel pin on a sapphire disk with a load of 26 N and at a speed of about 2 m/s. Most of the hot spots, they found, were at 950 ˚C while maximum flash temperature was as high as 1200˚C.

Based on theoretical analysis, some models [49, 50, 51] for the calculations of the sliding surface temperature have been put forward. According to the theory of Lim and Ashby [51], the theoretical average temperature T_b and flash temperature T_f on the friction surface can be calculated by Eqs.

$$T_b = T_0 + \frac{\mu T^* \beta}{2 + \beta(\pi v/8)^{1/2}} Fv \qquad (2.1\text{-}3)$$

$$T_f = T_b + \frac{\mu T^* \beta}{2}\left(\frac{F}{N}\right)^{1/2} v \qquad (2.1\text{-}4)$$

T_b-average temperature; T_f -flash temperature; T_0-room temperature; T^*-equivalent temperature, $T^* = aH/K_m$, a represents the thermal diffusion coefficient. H is surface hardness. K_m represents the coefficient of thermal conductivity; β-equivalent distance, $\beta = l_b/r_0$, l_b is the thermal diffusion distance, r_0 means the radius of the contact units; F-normal force; N-total number of asperity; v- sliding velocity; The two equations show that average temperature and flash temperature depend strongly on both the load and the velocity.

2.1.2 Wear

When considering the efficiency and/or operating lifetime of a product or component [52]--friction within bearings will result in wasted power and generate heat, whereas any ensuing wear will lead to poor working tolerances, loss of efficiency and may ultimately lead to premature failure [53, 54, 55]. The wear process has been defined as "the progressive loss of substance from the operating surface of a body occurring as a result of relative motion at that surface [56]. Like friction, wear is not an intrinsic material property but rather a characteristic of the tribosystem, consisting generally of three elements: material properties, mechanical interaction and environmental atmosphere.

2.1.2.1 Wear mechanisms

Although wear has for long been a subject of practical interest, fundamental knowledge of wear is still being developed. The subject of wear is, to a large extent, complicated by inconsistent terminology and a persistent confusion of wear processes and wear mechanisms [57, 58]. To understand the mechanisms termed "wear" there is an implicit need to understand the nature of contact between surfaces as they are brought together and then slide over one another. The nature of this contact involves five factors [59]:

   (1) The surface texture (finish);

   (2) The yield properties of the metal at or near the contact surface;

   (3) The strength of bonds formed at the regions of real contact;

   (4) The way in which these bonds are broken during sliding;

   (5) The nature of surface films that may be present, e.g. natural oxides, tailored finishes, grease etc.

Generally there are two broad approaches to the classification of wear: the first being descriptive of the results of wear, with the second being based upon the physical nature of the underlying process [55]. Whilst the issue of wear mechanisms in terms of types and relative importance remains a subject of debate, it is now widely accepted that major wear mechanisms can be categorized into four groups: abrasive, adhesive, tribochemical, and fatigue [60,61,62]. The relationship among the wear mechanisms, tribological interactions and types of surface damage has been summarized by Czichos et al. [63], as shown in Figure 2.1-3. It is generally recognized that there are three primary types of wear [64,65,66]: adhesive wear, abrasive wear and oxidation wear.

2.1.2.2 Adhesive wear

Adhesive wear—is the transfer of material from one surface to another during relative motion, which may be distinguished as the most fundamental of the several types of wear. So adhesive wear is most widely encountered over the full spectrum of engineering situations and represents the most persistent mode of wear [55].

Two important points from a forensic perspective:

(1) When two identical (or similar) materials slide over each other, both surfaces will become roughened. The asperities on each surface gouge and score the other surface, so that both deteriorate—rapid wear will then occur.

(2) If two different metals slide over each other, junctions at asperities will have a strength intermediate between the two. Consequently, when sliding occurs, shear will tend to dominate, leaving small fragments of the softer material attached to the harder one. In this instant, damage will be largely confined to the softer surface, as

shown in Figure 2.1-4.

An important conclusion derived from the above is that if adhesion is dominant in the friction process it is not recommended to slide identical metals together particularly if they are ductile—lumps will be torn out of both surfaces and wear will be rapid.

2.1.2.3 Abrasive wear

Abrasive wear—is the removal or displacement of material from a surface by the sliding of hard particles along the surface [67], which can be divided into two types: two-body and three-body abrasive wear.

If one surface is harder than the other (and adhesion is not dominant) the asperities on the hard surface may remove material from the other in one or two ways:

(1) If the asperities have an appropriate geometry they can act as minute cutting tools, removing material in the form of fine chips;

(2) Hard sharp particles (such as dust or hard particles from another part of the machinery) get embedded in a softer of the sliding pair and thus abrade the harder counterface.

A much slower form of abrasion will occur when 'cutting' does not happen. Instead, hard asperities may plastically deform grooves in the softer surface. Edges of the generated grooves will be raised above the general level, therefore easily subjected to further deformation. Continued sliding across the grooves will result in edges being swept away by plastic deformation or by a fatigue process.

2.1.2.4 Oxidational wear

Oxidational wear—is a mechanism of mild wear in which protective oxide films are formed at the real areas of contact (during the time of a contact) at the contact temperature, T_c.

When the oxide reaches a critical thickness, the oxide breaks up and eventually appears as wear particles. These oxides are preferentially formed on plateau, which alternately carry the load—as they reach their critical thickness—and are removed. Temperature is important in determining the structure of the oxide film present, which in turn affects the wear properties of the sliding interfaces [68]. Production of oxidized debris is one of the characteristics of mild wear. Leaving aside the often-posed question about whether the oxidation occurs after removal (in which case there would not have an oxidation wear mechanism). It is possible to make three alternative assumptions about the temperatures at which the surfaces oxides before removal as wear debris. These are: the oxides produced at the hot-spot temperature (θ_m) at the real areas of contact, the oxides are formed at the general surface temperature (T_s), or the oxides formed at some intermediate temperatures.

Two possible mechanisms of wear particle formation were proposed:

(1) The bulk of the oxidation occurs at the instant the virgin metal is exposed, followed by further contacts which merely cause the oxide to shear at the oxide metal interface;

(2) Or an equal amount of oxidation reached, beyond which shearing occurs at the oxide-metal interface. The second alternative is currently favored.

2.1.2.5 Other wear mechanism [21]

Delamination—a different fatigue failure occurs if lubrication of a sliding surface is poor. Even though the adhesion may not be strong enough to tear out wear fragments it may produce very large surface forces. The surface layers become extremely heavily work hardened and generate subsurface cracks parallel to the surface and at some point these will emerge at the surface releasing a typical flake of metal.

Chemical or corrosive wear—the process of wear associated with chemical effects. The most common example with most metals is the repeating cycle of formation, removal and reformation of oxides. The fragments are usually small and may appear as compacted flakes consisting of a mixture of fine oxide and metal particles.

Erosive wear—is the loss of material due to relative motion between the material and solid particles in suspension in a fluid medium. When the relative motion is nearly parallel, the mechanism is termed erosion, whereas impingement describes the mechanism where the relative motion is nearly normal to the material. Erosive wear can have a detrimental effect on pipe joints and bends, valve components, centrifugal pumps, compressors and turbines.

2.1.3 Factors affecting friction and wear

Friction and wear share one common feature, that is, complexity. It is now widely accepted that the results from complex interactions between contacting bodies which include the effects of surface asperity deformation, plastic gross deformation of a weaker material by hard surface asperities or wear particles and molecular interaction leading to adhesion at the points of intimate contact. In almost every situation it is possible to identify the main factors,

which are usually determined by the mechanical properties and physical-chemical stability of the material, temperature within the contact zone, micro/nano contact geometry, and operating conditions [69].

2.1.3.1 Material properties

<u>Metallurgical compatibility</u>

Metallurgical compatibility is a measurement of the extent to which materials are mutually soluble in the solid state. Based on systematic work, Rabinowicz [70,71] produced a famous metallurgical compatibility chart and correlated the compatibility with adhesion, friction and wear. Higher mutual solubility or ability to form intermetallic compounds may result in more material transfer and higher adhesive wear rate, however this is not a universal law [72]. According to the theory of Rabinowicz [70,71], surfaces of identical metals in sliding contact should be avoided and low mutual solubility is desirable in a dissimilar metallic counterface situation. It can be assumed that oxides and thin ceramic coatings on the sliding surfaces can effectively reduce the metallurgical compatibility and hence the adhesive wear.

<u>Nature of deformation</u>

The nature of deformation of contacting surfaces plays a very important role in adhesive wear. It has been pointed out that if the tribological contact between surfaces is, in the engineering sense, totally elastic, a significant reduction in wear rate can be anticipated [73,74]. The plasticity index φ introduced by Greenwood and Williamson [75] is a useful parameter and can be used to predict the extent of plastic deformation.

$$\varphi = \frac{E^*}{H}\sqrt{\frac{\sigma}{\beta}} \qquad (2.1\text{-}5)$$

H is the hardness; E^* is the composite elastic modulus of the two contacting surfaces; β is the typical radius for an asperity and σ is the standard deviation of the asperity height distribution. Therefore, the value of E^*/H is a key factor in determining the nature of deformation of the surface with a given surface topography.

Ductility of sliding surfaces

Ductility is a mechanical property that describes the extent in which solid materials can be plastically deformed without fracture [76]. Ductility of sliding surfaces is one of the important properties determining the transition layer or interface between two different material surfaces, namely adhesion junctions. Ductility materials might exhibit the diffusions at certain junctions, resulting stronger adhesion. According to the strength-failure theory [77], failure can be classified into brittle/fracture failure and ductility/yield failure. Failure of brittle materials is caused by the normal stresses (perpendicular to the contact surface), while failure of ductile materials is determined by its shear strength (parallel to the contact surface). It has been reported that the maximum normal stresses are located at the surface in contact, whereas the maximum shear strength is at certain distance below the contacting surface [77]. Consequently adhesion junctions of ductile materials will rupture at a certain depth, forming coarse wear debris. Budiski concluded that galling tendencies, which were defined as the early stages of surface deformation and adhesive interaction in the wear, were the lowest with materials that have limited plasticity [77]. It could be concluded that the higher the ductility, the more severe the adhesive wear.

Hardness

For hard coatings, due to the abrasive wear probably being more relevant than adhesive wear, high hardness is often beneficial. Because abrasive wear arises when two interacting surfaces are in direct physical contact and one of them is significantly harder than the other. Under the action of a normal load, the asperities on the harder surface penetrate the softer surface thus producing plastic deformation. When a tangential motion is introduced, the material is removed from the softer surface by the combined action of micro-ploughing and micro-cutting.

In the situation of abrasive-wear, a hard conical asperity with slope, θ, under the action of a normal load, W, is traversing a softer surface. The amount of material removed in this process can be estimated from the expression [78]

Simplified
$$V_{abr} = \frac{2}{\pi} \frac{\tan \theta}{H} WL \qquad (2.1\text{-}3)$$

Refined
$$V_{abr} = n^2 \frac{P_\gamma E W^{3/2}}{k_{1c}^2 H^{3/2}} L \qquad (2.1\text{-}4)$$

Where E is the elastic modulus, H is the hardness of softer material, L is the removed length, K_{1c} is the fracture toughness, and n is the work-hardening factor and P_γ is the yield strength. The simplified model takes only hardness into account as a material property. Its more advanced version includes toughness as recognition of the fact that fracture mechanics principles play an important role in the abrasion process.

In summary the amount of adhesive wear depends on the strength of the adhesion, the area of the junctions and the position at which junctions are sheared. Therefore, high hardness, low metallurgical compatibility, low ductility and low E/H value are desirable mechanical properties for eliminating adhesive wear. The ability of the material to resist abrasive wear is influenced by the extent of work-hardening it can undergo, its ductility, strain distribution, crystal anisotropy and mechanical stability.

2.1.3.2 Lubrication

Lubrication is an essential feature of all modern machinery and has been so throughout the ages. A wide variety of materials, gases, liquids or solids, may be used as lubricants. It is convenient in discussing the subject to distinguish between various types of lubrication. In hydrodynamic lubrication the surfaces are separated by a fluid film, whose thickness is much larger than the asperity heights on the bearing surfaces. The hydrostatic pressure in the film causes only small elastic distortion of the surfaces which, to a first approximation, can be treated as rigid. The resistance to motion of a hydrodynamically lubricated system is determined by the shear forces which exist in a moving fluid. Elastonhydrodynamics describe the case where the local pressure are so high and the lubricant film so thin that elastic deformation of the surfaces must be taken into account. The friction resistance of an elastohydronamic system is due partly to the shearing of the lubricant film and partly to the asperity interactions. In boundary lubrication, the surfaces are separated by adsorbed molecular films, usually laid down from an oil or grease containing a suitable boundary lubricant; appreciable asperity contact and junction formation may nevertheless occur. The tribological properties are determined by surface interaction between thin layers of boundary lubricants and the solid surfaces [79,80,81,82].

It is possible to separate completely the moving surfaces of a tribo-engineering system by solid lubricant films, whose shear strength then determines the friction. A comparison of the advantages and limitations between solid and liquid lubricants has been provided [83].

2.1.3.3 Surface engineering—its impact on tribology

Unlike developments in bulk materials, many of the advances in surface engineering have been motivated by tribological goals, and it seems probable that developments in this area will continue to play a major role in the future. Surface modification and surface coating not only allow surfaces with good tribological properties to be produced, but also contribute to the conservation of scarce high-performance materials by localizing them where they are required.

Surface engineering is a wide-ranging technology, covering traditional electroplating, weld surfacing, thermal spraying and thermochemical treatments, through to the modern techniques including physical vapor deposition (PVD), chemical vapor deposition (CVD), ion-implantation, energy beam surface modification and plasma thermochemical treatments, to recently developed hybrid technologies and duplex treatments [84,85]. The thickness and hardness of a surface engineered layer span wide ranges, as are summarized in Figure 2.1-5, respectively.

In selecting a technique for a given application, not only must the resulting properties of the surface be considered, but also the thickness of modified layer in relation to the depth of penetration of the surface stress field, and in relation to the wear rate, design life and

tolerate change in dimensions of the part. Other factors must also be taken into account, such as the temperature to which the component is subjected during the procedure.

The design sequence and fundamental principles of surface engineering and its impact on tribology has been reviewed by Bell [48]. Erdemir presented an up-to-date review on solid lubricants and self-lubricating films [86], including a classification of traditional and engineering solid lubricants.

One of the most exciting developments in surface engineering solid lubricants in the past decade has been in the area of diamond coatings. Diamond possesses very attractive properties for tribological applications: low friction in air against many counterfaces, high thermal conductivity, chemical, inertness and of course extremely high hardness [87].

2.2 Tribological coatings

2.2.1 Introduction

In this section, major emphasis is placed on the various approaches that have been used to optimise tribological coatings. This historical description, though not exhaustive, will include the research of specific material compositions, the development of deposition processes and the structure and properties of tribological coatings. Figure 2.2-1[88] shows a portfolio of the tribological hard coatings developed over the past 25 years. The objective is to propose a guideline to identify the major milestones in the development of tribological coatings.

2.2.2 Compositions of tribological coatings

2.2.2.1 Classification of tribological coatings

Historically, the important developments in the formulation and use of tribological materials were first due to the natural ability of various materials to exhibit rather low friction and low wear under specific conditions. Tribological coatings are generally classified in two categories, (1) soft low-friction coatings and (2) hard wear-resistant coatings, depending on whether the hardness value is lower or higher than ≈10 GPa [89,90]. Hard wear-resistant coatings include oxides, carbides, nitrides, borides, and some carbon-based materials (diamond and sp^3 dominated diamond-like carbon). Most of these coating materials have been extensively studied and some of them present properties that are attractive when the materials are used under specific conditions [91,92,93,94]. Soft low-friction coatings include PTEF [95], MoS_2 and some carbon-based materials [96] (Graphite and sp^2 dominated graphite-like carbon).

2.2.2.2 Coating compositions

The combination of basic tribological materials to build various film structures (nanocomposites, superlattice, gradient, etc.) has been the subject of intense research for the past decade. However, these developments did not prevent the emergence of new structures or original concepts in tribological coatings.

One direction is to develop low friction coatings; some recent reports [97,98] have shown that the sputtered carbon-based coatings have attractive tribological properties, low wear rates and low coefficients of friction. DLC materials are thin films of amorphous metastable carbon based solids, pure or alloyed with hydrogen having properties similar to that of

crystalline diamond [99]. DLC coatings have high hardness (from 20 to 40 GPa) [100,101,102], low friction coefficient (0.01-0.02 in vacuum and 0.15 in atmosphere) [103,104], low wear rate (10^{-16} m^3mN^{-1}), and chemical inertness and, therefore, are accepted as outstanding wear-resistant coatings. This resemblance to diamond is due to the DLC structure, which is characterized by a high fraction of highly cross-linked sp^3-hybridised carbon atoms, as shown in Figure 2.2-2 [105].

Fairly detailed observations of tribological properties of DLC coatings at room and elevated temperatures have been made [106,107,108,109]. The values of the friction coefficients of DLC coatings and their wear resistance are known to depend substantially on the type of valence electron hybridization (sp^3 or sp^2), and the sp^2:sp^3 ratio in turn depends on the technique of synthesising these coatings and affects to a great extent the initial physical and mechanical properties of DLC coatings [110]. Figure 2.2-3 shows the typical Raman spectra of DLC films at different temperatures indicating sp^2:sp^3 ratio changes with temperature [107].

In order to improve the properties of DLC films, addition of impurities such as silicon, nitrogen, boron, phosphorus, fluorine and some metals has been deployed by several researchers. In brief, the addition of such impurities reduces the internal stress, electrical resistance and friction coefficient of DLC thin films [111]. Arora et al. [112] reported that nitrogen (N) incorporation into DLC films could lower the compressive stress. According to the results of some other studies [113,114,115,116] good tribological properties are noted for hydrogenated amorphous metal-containing carbon coatings (α-C: H). These coatings have a low friction coefficient (f=0.12-0.18) and high wear resistance under friction in

ambient air [117]. Ultralow friction coefficients (f<0.01) have been reported under vacuum conditions for DLC coatings if the hydrogen content was high enough (about 40 at %).

Graphit-iC coatings, developed by Teer Coatings, are a new type of hard carbon coatings [31,32] and were shown to have excellent tribological properties, low friction (<0.1), low wear rate (10^{-17} m^3 mN^{-1}), and high load-bearing capacity (>2.1 GPa) [118,119]. As shown in Figure 2.2-4 [120], these were normally better than those conventional diamond-like carbon (DLC) or Me:C DLC coating, especially in humid air and in water. In this case, though, there are three targets and one chromium target. A thin chromium bond layer is deposited, followed by a pure carbon coating. Analysis by Raman spectroscopy has shown that Graphit-iC coatings exhibit predominantly sp^2-type bonding, unlike DLC coatings, where the bonding is mainly sp^3-type. Despite this, coating hardness values of between 15 and 40 GPa have been recorded, depending on deposition conditions.

Another direction is to improve wear resistance under severe conditions, rather than to decrease friction. Knotek et al. [121] focused on the optimisation of the composition of (Ti, Al, V) (C, N), which allowed significant improvements in the wear life of tools. This was probably the beginning of numerous attempts to deposit complex multicomponent coatings, as recently reviewed by Jehn [122]. From the initial binary hard materials, multi-component coatings based on TiN and CrN have been developed by alloying these binary structures with metal and/or metalloid components. The nature and amount of alloying elements strongly influence their friction and wear behavior. Such investigations were extended to a large number of elements, including Zr, Hf, V, Nb, Cr, Mo, W, Al and Si, with various chemical combinations.

2.2.3 Coating structure

2.2.3.1 Single-component coatings

Most commercial PVD and CVD coatings consist of a one single layer, often containing one single phase. Probably, in many cases, cost-effectiveness explains the persistence of this first generation of tribological coatings in many industrial operations. The commercially successful single layer coatings include TiC, TiN, CrN, CrC, Al_2O_3, DLC, W_2C, WC/C, MoS_2, diamond, soft metals and some polymers. To fulfill the functional demands, an adhesion interlayer may be necessary.

Considerable works have been devoted to carbonaceous materials, including DLC films. These amorphous structures which contain both sp^2 and sp^3 hybridizations, have hydrogen content that ranges between <1 and ≈50 at%, from which most of the structure's properties are derived [123]. Among solid lubricants, they probably exhibit the widest range of friction and wear behavior.

Diamond films are extremely hard and offer several outstanding properties, such as high mechanical strength, chemical inertness and very attractive friction properties. At present, several CVD techniques are available to produce high-quality diamond films with micro- and nancrystalline structures on various substrates. The high-quality diamond coatings produced by CVD exhibit most of the desired mechanical and tribological properties of natural diamond [94]. However, the surfaces of diamond coatings are generally rough with sharp facets, which need to be polished using expensive methods.

2.2.3.2 Multi-component coatings

Multi-component coatings are made up of two or more constituents in the form of grains, particles or fibers. Depending upon the size and distribution of secondary phases in the primary matrix, a coating can either be called multiphase or composite. The term "composite" is used when one phase is dispersed in a matrix which is continuous; the term "multiphase" is used when both are equally present and none of them is continuous [124].

Initially mononitride and monocarbide were produced as coating materials on various substrates to improve tribological and corrosion behavior. Table 2.2-1 lists various borides, carbides, nitrides and oxides which can be employed in mitigating corrosion and wear [125]. Table 2.2-2 shows various compounds used as coatings. They are mainly based on transitional metals and elements. Like metals forming alloys, these mononitrides and monocarbides can form binary nitrides and binary carbides (ternary phase systems) by adding another suitable metallic element to them. For example, titanium aluminium nitride films deposited on various metallic and PM materials have been proved to be effective in many applications including machining [126, 127, 128], dry metal forming [129] and molding [130], oxidation, wear and corrosion resistant materials at high temperature [131], biocompatible surgical implants [132] and prosthesis and dental alloys [133]. The lattice of Ti can be partly or fully substituted by other suitable elements. It has been proven by many academic and industry research groups that the thermo-mechanical properties and machining performance of $Ti_{1-x}Al_xN$ coated tools depend on many factors including mainly the stoichiometry (Al/Ti ratio) [134, 135], process conditions like bias variation in the cathodic arc evaporation to control microhardness, residual stresses and texture [136,137],

incorporation of the third metal to fabricate quaternary TiAlMeN coatings (Me=metal, e.g. Si, Cr, V, Hf, Nb and B) [138,139].

However, it is clear from Tables 2.2-2 and 2.2-3 that not all the compounds listed in Table 2.2-1 are used as coatings. These hard compounds can be classified based on the bonding type-metallic, covalent or ionic (Table 2.2-4). The properties of each group of materials are qualitatively compared in Table 2.2-5; it is obvious that no one group has all the properties to the highest level.

One of the ways to improve/optimize properties of a hard material is to substitute the metal lattice of the compound phase with another compatible metal, e.g. the lattice of TiN is partly substituted by Al. Another method is to vary the relative concentrations of the non-metallic elements. As an example, Figure 2.2-5 shows microhardness values of certain carbides, mixed carbides and carbonitrides [140].

Even in a simple nitride, depending on the concentration ratios of Ti/Al, friction and wear properties of TiAlN films vary. For instance, in ref [141], the Al content in $Ti_{1-x}Al_xN$ has been varied as $0.16<x<0.84$ by varying the sputter pulse times and the N_2 pressure, and these variations revealed that the coating with low Al content are columnar, whereas the coatings with the highest Al contents ($x>0.85$) are XPS amorphous with a glass morphology. The higher the aluminium content, the better the resistance to oxidation and high-temperature wear. The aluminium in the coating material reacts with the oxygen in the air and forms a passive Al_2O_3 layer, which prevents the film from further intensive oxidation. Moreover, many properties can be achieved in binary and ternary coatings by alloying with

Cr which has very high potential for developing multifunctional protective coatings. It is known that Cr has a positive effect on the oxidation resistance of titanium carbides, borides, and nitrides and improves their wear resistance, especially at elevated temperatures [142]. A CrN-based CrTiAlN coating system has been recently developed by Teer Coatings to improve the performance of twist drills and extrusion dies [22,23]. It has been revealed that CrTiAlN coatings demonstrate a wear resistance significantly higher than TiAlN coatings [143]. Furthermore, CrTiAlN coatings exhibit a high oxidation resistance and good thermal stability, which are important factors for their excellent dry cutting performance [25,144].

2.2.3.3 Multi-layer coatings

Multilayered coatings are composed of a periodically repeated structure of lamellae of two or more materials, with thickness up to a few tens of a micrometer (if the thickness of each lamellae is in the nanometer range, these films may become a superlattice). According to Yashar and Sproul [145], multilayer coatings can be classified in two categories: iso-structural (individual layers have the same structure) and non-isostructural (individual layers have different structure).

As a first example of hard coating multilayers, the magnetron-sputtered system TiB_2/TiC shall be mentioned. The TiC films first grow epitactic layer structures in (111)-orientation on (001)-TiB_2 and form their 'own' (200)-TiC only after a certain transition zone. In contrast, TiB_2 first grows untextured on (200)-TiC and only later is the (001)-texture formed. This allows the composition of a multilayer-structure with a sequence of (001)-TiB_2/(111)-TiC. Very thin individual layers show only untextured TiC/TiB_2 multilayers [146]. Also in the system TiB(N)/TiN variations in the texture sequence are found for peridicties between

2.8 and 17 nm depending on the deposition conditions. A maximum in hardness is found for a periodicity of 10 nm and less [147]. Another type of multilayer coating consists of transition metal compounds alternating with carbon-based films, e.g. TiC/DLC (on a Ti/TiC interlayer) [148] or TiN/CN$_x$ (Figure 2.2-6) [149].

In addition, nano-multilayer corresponds to the multilayer concept extrapolated to a thickness of individual layers $\cong$ 100 nm range. The major function of these structures is to significantly enhance hardness, fracture toughness and adhesion of the coatings, and thus to improve their wear resistance. When the thickness of one layer is several nanometers, a periodic structure of layers of two (or more) materials is a so called superlattice. Superlattice reflections are those present because the material is ordered such that the actual realspace unit cell is layer and thus the reciprocalspace cell is smaller. Some superlattices are listed here with regard to their significant improvement of tribological properties, TiAlN/TiAlCrN [150], TiCN/ZrCN [151], CrAlYN/CrN [152], and TiHfN/CrN [153].

The properties of multi-layer coatings depend on the material selection, the deposition processes and kinetics of growth, and on the special nanoscale thin film architecture. The advantage of combining several structures and compositions within one coating include achievement of various individual physical properties (i.e. diffusion barrier + low friction), reduction of the mismatch in mechanical and chemical properties between the substrate and the coating (mainly to enhance adhesion), control of the residual strain and therefore the stress within the coatings, the ability to stop cracks during operation under severe conditions, and enhancement of hardness and/or toughness by allowing layers or phases to slide over each other when they deflect under load. Mechanisms for toughening layered ceramic

coatings [154] are schematically represented in Figure 2.2-7. These mechanisms include: (1) crack splitting at the boundaries of small sized grains; (2) crack deflection at the interface between layers; (3) reduction or stress concentration by interface opening, and (4) plastic deformation at the interface for energy dissipation and stress relaxation, "nanoplasticity". The versatility of vacuum technology and emergence of multiplex/hybrid processes has led to considerable developments of this generation of coatings, which has recently found as major industrial applications [124].

2.2.3.4 Gradient and nanostructured coatings

In recent years, the literature and the theoretical understanding of this new generation of films have been grown, in particular with regard to nanocrystallized and nanocomposite [155] coatings. On the macroscopic scale, the concept associated with this generation of coatings is maximization of hardness (H) while ensuring an adequately low elastic modulus (E), to provide an appropriate 'elastic stain to failure,' as determined by the H/E ratio [156]. On the nanometer scale, the mechanism corresponds to higher resistance to dislocation movement by precluding the formation of stable ones. This is achieved by decreasing the grain size, in accordance with the well-known Hall-Petch relationship, or by controlling the presence of interfaces between nanocrystallized (nc) metal nitride/metal [157], or between amorphous and nanocrystallized phases as with nc-MnN/α-Si$_3$N$_4$ (where M is Ti, W, V or other transition metal) [129]. The most recent developments to extend the use of nanometer-scale coatings are probably devoted to their stability at high temperature, to avoid phase transformation, grain growth and diffusion processes. This seems to be possible if the layer materials are thermodynamically stable with respect to each other and are stable to form low-energy coherent interfaces [158].

Control of the structure and composition of coatings at nanoscale is an exciting scientific subject combined with an industrial challenge. This control can be achieved mainly through three structural configurations. The first configuration is the functionally graded coatings, which are regarded as the logical progression from multilayered coatings. Grading the composition by a drastic control of the deposition process has been achieved to combine a relatively hard TiAlN phase with a softer MoS_2 phase with an increase in the latter phase towards the top surface [159]. One other benefit of grading the composition is that it improves adhesion of DLC-based coatings that contain metal additions. Such improvements have been obtained by Ti and TiC(H) graded underlayers to increase the wear resistance of DLC films [160,161]. Second, nanostructured coatings include nanocrystallized films (with grain sizes in the nanometer range) and nanocomposite films. Nanocomposites include structures that combine amorphous phases with crystallized ones, as widely emphasized by Veprek [162].

In summary, as shown in Figure 2.2-8 [163] on the basis of the 'simple' hard coatings, the following concepts were used for an improvement of coating properties and performances:

(1) Multi-component coatings and graded coatings;

(2) Multiple-film coatings and multi-layers on the base of hard /hard, hard/soft, and hard lubricating components; and

(3) Nano-structured coatings;

A rating of the properties of different coating systems is extremely difficult, because they depend not only on the materials and their chemical distribution but most often even more

on the deposition processes and parameters. The same holds for the tribological performance as the counter body material, the load and probably lubrication govern to a large part the wear and friction behaviour.

2.2.4 Technology for the deposition of tribological coatings

2.2.4.1 Traditional methods

Surface coating of tribological applications is associated with deposition temperatures ranging from room temperature to over $1000℃$. It can be seen from Figure 2.2-9 [164], the coating thickness range from microns to severval millimeters by different means. The oldest and simplest method is to sprinkle, rub, or burnish the fine powders of solid lubricant on surfaces to be lubricated. Fine powders of certain solid lubricants (such as graphite and MoS_2) were also used to lubricate sliding bearing surfaces with great success [165]. Such solid lubricants have been blended in an aerosol carrier and sprayed directly onto the surface to be lubricated. Powders of solid lubricants can be strongly bonded to a surface by appropriate adhesives and epoxy resins to provide a large wear life [166]. However, in most modern applications, thin films of solid lubricants are preferred over powders or bonded forms. They are typically deposited on surfaces by advanced vacuum deposition processes. (see 2.2.4.2 and 2.2.4.3)

2.2.4.2 PVD & CVD

Surface engineering, where the surface properties of components and tools are changed in a favourable way by deposition of surface coatings, offers an efficient way of controlling

friction and wear. The development of vacuum deposition techniques, chemical vapour deposition (CVD) and physical vapour deposition (PVD), has been of major impact, since they make it possible to deposit a thin layer of only a few micrometers on the surfaces of most engineering materials. The geometrical change is minimal and the surface layer may have properties covering an extremely wide range, from hard diamond and ceramic coatings to very soft polymeric or lamella-structured films [167].

The deposition of tribological coatings and solid lubricants may require deposition temperatures ranging from room temperature to more than 1000 ℃. The heat resistance of the substrate materials may strongly limit the number of possible coating/substrate combinations. For some methods, including CVD, high deposition temperatures can cause undesired phase transitions, softening and distortion of the substrate. For Al, Cu and Mg alloys the deposition temperatures should be below 100 ℃, for most steels, the deposition temperatures range from 100 to 500 ℃, whereas for ceramic materials the deposition temperatures can reach typically up to 1000 ℃. Normally, CVD processes induce significant temperature increase during deposition, ranging from 600 to 1000℃ (CVD). Thus, CVD coatings can only be applied to ceramic materials and cemented carbides. Some heat-resistance steels, such as high-speed steel (HSS), can be treated by all types of PVD and some low-temperature CVD processes.

2.2.4.3 Magnetron sputtering

In physical vapor deposition (PVD) processes, the coating is deposited in vacuum by condensation from a flux of neutral or ionized atoms of metals. Several PVD techniques are

available for deposition of hard coatings. Among them, cathodic arc vapor (plasma or arc ion plating) deposition, magnetron sputtering, and combined magnetron and arc processes are the most widely used techniques (Figure 2.2-10) [168,169,170,171].

Magnetron sputtering is a powerful process which is currently used in industry for the production of thin films and coatings, mainly because (1) magnetron technology is relatively simple and reliable; (2) the deposition rate of coatings is sufficient to meet economic and functional requirements in industrial production and is fully comparable to that achieved in evaporation of coatings; (3) the sputter deposition process operates under different physical conditions compared to the evaporation which makes it possible to form films with new physical and functional properties and even films not obtainable by evaporation, e.g. alloy films; and (4) the sputtering sources can be scaled up into large industrial coaters.

The basic sputtering process has been known and, despite its limitations, used for many years. The introduction of what are now termed 'conventional', or 'balanced' magnetron in the early 1970s [172,173] was an important step forward in overcoming these limitations. However, it was the development of the unbalanced magnetron in the late 1980s [174,175,176] and its incorporation into multi-source 'closed-field' systems in the early 1990s [177,178] that transformed the capabilities of this technique, and has subsequently been responsible for its rise in importance. Closed-field unbalanced magnetron sputtering (CFUBMS) is an exceptionally versatile technique, suitable for the deposition of high-quality, well-adhered films of a wide range of materials at commercially useful rates.

In an unbalanced magnetron the outer ring of magnets is strengthened relative to the central pole. A comparison between the plasma confinements obtained in different magnetron modes is shown schematically in Figure 2.2-11 [178]. In this case, not all the field lines are closed between the central and outer poles in the magnetron, but some are directed towards the substrate, and some secondary electrons are able to follow these field lines. Consequently, the plasma is no longer strongly confined to the target region, but is able to flow out towards the substrate. Thus, high ion currents can be extracted from the plasma without the need to externally bias the substrate [179,180,181].

Despite the benefits offered by unbalanced magnetrons, it is still difficult to uniformly coat complex components at acceptable rates from a single source. Therefore, in order to commercially exploit this technology, multiple magnetron systems have been introduced.

In a multiple magnetron system, the magnetic arrays in adjacent magnetrons can be configured with either identical, or opposite magnetic polarities. In the former case the configuration is described as 'mirrored' and in the latter case 'closed field', and both configurations [182] are shown in Figure 2.2-12. In the closed field configuration, the field lines are linked between the magnetrons. Losses to the chamber walls are low and the substrate lies in a high density plasma region [182,183].

In addition, sputtering technology is continuously being improved not only through the improvement of existing sputtering systems, but also mainly through the development of a new system. This makes it possible to form films with new properties and to develop new technological processes for their production, such as low-pressure sputtering, pulsed

sputtering, coating material ions-assisted sputtering, high-rate sputtering and self-sputtering [184,185,186,187].

2.3 Properties and characterisation of nano-structured coatings

2.3.1 Introduction

Deposition of thin films with a few microns in thickness is a common technology to improve the performance of tools, dies, and moulds for many different applications [188]. An important requirement for these coatings is to blend together hardness, low friction, and toughness in a coating such that low wear is realized in diverse environments (e.g., hot, cold, wet, and vacuum). Thin film deposition has undergone tremendous advances and it is now possible to grow multilayered, functionally gradient, and nanocomposite coatings that have impressive properties, such as high hardness and good resistance to wear, corrosion and oxidation.

As discussed in Section 2.2.4.1, adding different elements to an existing coating is one possibility to adapt some of its properties to a value desired for specific applications. This allows modification of the basic physical properties such as lattice constant, thermal expansion coefficient, optical properties, electrical properties, chemical reactivity, diffusion coefficient, elasticity, oxidation behavior, internal stress, grain size, texture, defects, and impurities, etc. altering the final performance. Some basic correlations between the basic parameters and final performance of the coating are known [189]. In this section, the desired properties of coatings for tools and their characterization methods are discussed.

2.3.2 Desired characteristic of nano-structured coatings

2.3.2.1 Hardness

As discussed in 2.1.2.1, the hardness of a material is one of the most important mechanical properties in wear and has been widely employed as a criterion to determine the abrasive wear resistance [190,191].

The dependence of the abrasive wear resistance of metals on hardness is illustrated schematically in Figure 2.3-1 [192]. Generally, the abrasion resistance is proportional to the specimen hardness. The resistance against three-body abrasion is normally much higher than against two-body abrasion.

However it should be mentioned that wear models are also often presented [193] in which both the Young's modulus E and fracture toughness K_{1c} play an important role (both are inversely related to the wear rate). Although hard materials are usually, because of their low ductility, susceptible to brittle fracture, pressures in magnetic storage devices are relatively low [194], despite the fact that some localized areas of high pressures may exist. Hence, one should try to optimize the hardness. Sundgren and Hentzell [195] have described a number of relations between microstructure and hardness in hard coatings.

Alloy strengthening can be obtained in two ways. First, the chemical bonding between the involved atoms can be changed by the element added. Second, the hardness of a material would also be increased by hindering the dislocation movement by the introduced defects (precipitations, grain boundaries, diffusions, dislocations). For instance, adding aluminum to TiN can effectively increase its hardness because of the incorporation of smaller

aluminum atoms into the lattice of TiN leading and enhancing a local tensile stress (lattice distortion) [196,197]. Additionally, the internal stress in the films also contributes to the hardness of the film, but on the other hand large internal stress causes or favours the delamination of the film. Further approaches towards the development of innovative high performance coatings address the design of ternary and quarternary (or even multi-elemental) multilayer and superlattice structures. Superlattice structures with more or less pronounced hardness modification were reported for material combinations like TiAlN/ZrN [198], and TiAlN/CrN [199]. A systematic approach to improve the performance of PVD coatings for tool applications is described by Loffler [200].

2.3.2.2 High temperature oxidation

Surface oxidation at high temperatures is a concern not only for applications in hot environments, but also in cutting and drilling operations, where locally temperatures of up to 800℃ can be reached at cutting edges, because of server friction. Efforts have therefore been made to improve the high temperature oxidation behaviour of coatings. TiN, for example, oxidises severely at temperatures above 500℃. The concept of adding oxidation-resistant elements such as Al, Zr and Cr during the deposition process of TiN has led to the development of several new single-phased materials derived from TiN such as TiAlN [160], and CrZrN [201]. In TiAlN, which is commercially available since the first half of the 90s, the introduction of aluminum in TiN increased the oxidation resistance from approximately 550℃ to 800℃ and additionally an increased hardness is observed [160]. The enhanced oxidation resistance is a consequence of the formation of an aluminum-rich protective Al_2O_3 passive layer at the surface [202,203].

2.3.2.3 Friction and wear

The tribological behaviour of a coating can be influenced by adding different elements to the coating; however, a prediction of the influence of the elements added is usually not possible. The real response of a coating in a specific application has to be determined by conducting field tests [204,205]. In a tribological system many properties and parameters (the different material properties of the friction counterparts, environments, test conditions) interact with each other in a nonlinear and locally different way which prevents a reliable theoretical prediction of the real triboligical behavior of a coating from its composition. However, as discussed in Section 2.1.3, the tribological behaviour of coating could be predicted to some extent by its hardness for abrasive wear and by E/H for adhesive wear.

While the classical hard coatings such as TiN, TiAlN, TiC, TiCN have friction coefficients of 0.5-0.8 against steel [206,207], amorphous DLC exhibits low friction coefficients between 0.05 and 0.2 against most materials except some polymers. These properties are the main reasons for its application as a low friction coating. Amorphous DLC, modified by alloying with different elements has, due to its outstanding properties, been studied extensively as a tribological coating as described in the review articles by Grill, Donnet, and Gangopadhyay [208,209,210,211] and is also used in several industrial applications [212,213,214].

2.3.3 Mechanical property characterisation

Mechanical property characterization is one of the essential parts in the research, development and successful application of a surface-engineering system.

Indentation tests have been widely used as an economical and routine method for measuring the strength and stiffness of engineering materials [215]. Moreover, micro and nano-indentation techniques have become major tools for investigating the micromechanical properties of small scale volumes (e.g. thin films, nano-wires, nano-tubes, fibers, small particles, electronics) due to difficulty in conducting the conventional techniques and because of their fast, precise, and non-destructive merit.

2.3.3.1 Microindentation technology

Hardness measurements using microindentation is simple: a load P is applied to a flat surface with a rigid pyramidal tip, and the resulting imprint area A measured. Early researchers proposed that the hardness H=P/A has been widely used in the materials community for more than half a century [216,217]. It is inspiring and slightly humbling to mention that these and other contact mechanics analyses prior to the 1970s were performed without the aid of computers. However, one factor that has limited the applicability of hardness tests on a smaller scale is the need to accurately measure imprint dimensions (contact area) after unloading.

In addition, to obtain an intrinsic hardness value of a surface layer, the indentation depth should be at least less than one tenth the thickness of the surface layer concerned. And for tests on the cross section of a layered structure, the layer thickness must be at least twice as

large as the diagonal of the indentation. However, the thickness of surface engineered layers is only, in many cases, a few microns, and therefore this has limited the application of the micro indentation test for thin coatings.

2.3.3.2 Nanoindentation

Recently, technological advances in instrumentation, and especially computational power, have led to significant expansion in indentation interpretation. Depth-sensing indentation can now be used to accurately extract not only hardness, but the entire compressive stress-strain curve of bulk metals, including elastic modulus, plastic stress-strain behaviour and creep directly from the load (P) vs. penetration depth (h) curve, without the need of measuring residual contact impression [218,219,220].

Nanoindentation testing is a fairly mature technique which was developed in the late 1970s and uses the recorded depth of penetration of an indenter into the specimen along with the measured applied load to determine the area of contact and hence the hardness of the test specimen. Many other mechanical properties can also be obtained from the experimental load-displacement curve, the most straight-forward being the elastic modulus. Other properties such as the strain-hardening index, fracture toughness, yield strength and residual stress can also be measured.

The nanoindentation technique provides a means for the determination of the mechanical properties, such as hardness, elastic modulus, stress of surface layers and bulk materials, etc.

<u>Basic principles</u>

The method was developed to measure the hardness and elastic modulus of a material from indentation load-displacement data obtained during one cycle of loading and unloading. A schematic representation of a typical data set obtained with a Berkovich indenter is presented in Figure 2.3-2 [222], where the parameter P designates the load and h the displacement relative to the initial underformed surface. For modelling purposes, deformation during loading is assumed to be both elastic and plastic in nature as the permanent hardness impression forms. During unloading, it is assumed that only the elastic displacements are recovered; it is the elastic nature of the unloading curve that facilitates the analysis. The exact procedure used to measure H and E is based on the unloading processes shown schematically in Figure 2.3-3 [221].

There are three important quantities that must be measured from the P-h curves: the maximum load, P_{max}, the maximum displacement, h_{max}, and the elastic unloading stiffness, $S = dP/dh$, defined as the slope of the upper portion of the unloading curve during the initial stages of unloading (also called the contact stiffness). Another important quantity is the final depth, h_f, the permanent depth of penetration after the indenter is fully unloaded.

Oliver-Pharr model

Oliver and Pharr proposed "an improved technique for determining hardness and elastic modulus using load and displacement sensing indentation experiments" [226] Accounting for the curvature in the unloading curve, a physically justifiable data-processing procedure was established to determine the contact depth which should be used in conjunction with the indenter shape function in order to obtain the contact area at peak load. The Oliver-Pharr method is outlined as follows.

In a schematic indentation load-displacement curve (Figure 2.3-2), the three key experimental parameters needed to calculate hardness (H) and modulus (E) is the peak load (P_{max}) the contact depth at the peak load (h_c) and the initial unloading contact stiffness (S). Using the equation

$$E_r = \frac{\sqrt{\pi}}{2} \frac{S}{\sqrt{A}} \qquad (2.3\text{-}1)$$

which relates the reduced modulus, E_r, to the indent contact area, A, and the unloading stiffness, S, and the equation

$$H = \frac{P_{max}}{A} \qquad (2.3\text{-}2)$$

hardness H and elastic modulus E_r can thus be calculated.

Measurement of Indent Size

In the traditional microindentation hardness (i.e., "microhardness") tests, the residual indented impression size needs to be measured in order to calculate the required hardness number.

In the nanoindentation test, the accurate determination of indent sizes is important for the calculation of hardness **(H)** and elastic modulus **(E)** values. In addition to the indirect determination of indent sizes using the models and methods discussed previously, indent sizes can be directly determined in the following two ways: direct imaging of the indent left on the specimen surface, and three dimensional (3-D) imaging of the diamond indenter tip.

2.3.3.3 Microscratch

The scratch test has been used for many years to provide a measure of coating/substrate adhesion [222,223,224]. In the normal configuration of the test a diamond stylus is drawn across the coated surface under an increasing load until some well-defined failure occurs at a load which is often termed the critical load, L_c. Many different failures are observed which include deformation or cracking in the coating or substrate [225,226,227]. In fact, the critical load may or may not be related to coating adhesion, depending on the actual failure mechanism, but can be used to rank the practical 'scratch-resistance' or 'durability' of the coating. If the failure does depend on adhesion then the critical load can be used as a semi-quantitative measure of experimental adhesion [228,229].

2.3.3.4 Nanotribology

Nanotribology or microtribology is of increasing interest in recent years for tribologists. It is necessary not only for the fundamental understanding of the friction and wear mechanism, but also for the understanding of the interfacial phenomena and wear process in some real applications. For example, many surface engineered systems consist of very thin films on bulk material. In such cases, it is very difficult to use traditional tribological methods and theories to study and explain the tribological behaviour of these thin films for special applications. As a result, nanotribology has emerged as an essential research area for modern science and technology.

Many publications can be found in literature and several papers have reviewed the progress in nanotribology [230,231,232,233]. For most of the researchers, an atomic force microscope (AFM) was used, where the AFM tip simulates a sharp single asperity travelling

over a surface at a small contact load. Microscratching, microwear and nanowear of solid surfaces and thin films have been studied with this technique.

More recently, nanoindentation testers have also been used to study microscratching, microwear and nanowear by a few investigators [234,235,236]. The principle involved is similar to that in AFM, before and after scratching, the surface was scanned to record surface and residual wear depth profiles, respectively. Scratch depth, wear depth and critical sliding number for debonding events were obtained. Compared with an AFM, a nanoindentation tester has the ability to accurately control the load and record the surface profiles for each scan, leading to a clear image of the evolution of coatings failure.

2.3.3.5 Micro mar resistance

Mar/scratch resistance is crucial for coatings/materials in many applications [237,238,239,240], which refer to the light surface damages encountered in the real field that are usually shallow and narrow while scratches/scratching refer to the medium to severe damages. The scraping tip made a fairly neat trough in the surface, which consisted of a ditch with a smooth bottom and two well-shaped shoulders on both sides of the ditch, i.e. Figure 2.3-4 [241]. Cross-sections of the ditches and of the shoulders (if any) of the mars can be closely approximated by triangles. Figure 2.3-5 is an illustration of how to calculate the micro mar resistance (MMR) and three different responses of coatings to marring stress, based on the dimensions of the mar [244]. The largest inverted triangle represents the cross-section area of the tip that penetrated the surface during the marring, which was calculated based on the real-time penetration depth during the marring and the shape of the tip. The difference between it and the cross-section area of the residual ditch reflects the immediate

elastic recovery. To make the MMR more consistent with the visual, judgment and other optical evaluations, the cross-section area of the trough was used to replace the cross-sectional area of the ditch in the calculation of MMR [242,243,244]:

$$MMR = F_N / A_{trough} \qquad\qquad (2.3\text{-}3)$$

2.4 Summary

The application of hard coatings on cutting tools and mechanical components has become a common practice in the manufacturing industry in the last two decades [245,246,247,248].

TiN and CrN are common PVD hard coatings, but the fracture toughness and oxidation resistance are far from satisfactory [12,18]. Later on, the ternary Cr-X-N coatings were increasingly adopted due to the improved properties. The "X" can be pointed as Ti [5,249], Al [250], Si [251], B [252], C [253], and Ni [254], etc. Cr-Al-N coatings were remarkable because of the higher hardness (25-32 GPa) and the enhanced oxidation resistance up to 900℃ [255]. Recently, the quaternary Cr-Ti-Al-N coatings are desirable for the higher hardness and wear resistance [25,206,256,257]. However, these hard coatings have relative high coefficient of friction (0.7-0.9) [26,27] at room temperature requiring extra lubrication, which was the main limitation for the use of CrAlTiN coating. Self-lubricated Graphite-like carbon (GLC) coatings were reported to be effective in reducing friction coefficient due to the sheared graphitic carbon [31,32]. However, GLC was reported to be functional only under 400 ℃ in air [34], the oxidised process was explained in terms of the generation of a porous structure in the coating due to the vaporization of carbon oxide. With the porous structure and micro-cracks inside the oxide layer, the oxidation diffusion mechanism for oxygen transport changed from atomic diffusion to mass transfer, namely it cannot be used for the dry and high-speed cutting tools. Adding solid graphitic carbon into hard coatings may present the desirable combination of properties in terms of high hardness, good oxidation resistance and low friction. It has already been indicated that $TiC_{1-x}N_x$ coating can present low-friction behaviour and relative good thermal properties [258]. The improved tribological properties are attributed to the formed amorphous carbon phase, and the oxidation resistance is achieved by the thin titanium oxide film, which was formed on the coating surface and can act as an oxygen diffusion barrier to protect the coatings underneath from oxidation. However, it has not been examined that the microstructure evolution,

mechanical and tribological properties, and oxidation behaviour of novel CrAlTiCN coating with solid graphite carbon doped.

Chapter 3: Materials and Experiments

3.1 Sample preparation

3.1.1 Substrate materials

The material used in this study was M2 high speed steel (HSS) with a hardness $HRC \cong 62$ and Si wafer. The final dimensions of HSS samples were 27.2 mm in diameter and 3 mm in thickness with the composition given in Table.3.1-1. The thickness of the Si wafer is 500 μm. One flat surface of the disc was wet ground using silicon carbide papers from 120 grit down to 2400 grit. Some samples were mirror polished with 6 μm and 1 μm diamond pastes and finally polished with 0.25 μm colloidal silica, on a Struers DAP-7 automatic polisher. Samples were then washed with soapy water and cotton, degreased with acetone in an ultrasonic bath for 10 minutes, and dried with hot air.

3.1.2 Preparation of cross-sectional samples

Cross sections were cut from the samples with diamond cutting discs on a Struers Accutoom-5 cutting machine, nickel plated when necessary, and mounted in conductive Bakelite using MetPrep PA30 or Opal 400 mounting presses. The grinding, polishing and cleaning procedures were equivalent to the ones described before.

3.1.3 Preparation of TEM samples

Figure 3.1-1 shows a schematic of XTEM sample preparation and the steps (1) to (5) will be explained as follows [259]. (1) Two slabs were glued using G-1 epoxy with the treated surface facing each other; (2) The assembly was cut to a thickness of less than 1 mm with the interface of the two glued treated layers in the centre followed by fine grinding and polishing to 50 μm in thickness; (3) This thin assembly was then glued to a 3 mm (o.d) and 0.5 mm (i.d) brass reinforcing disc and the exposed side was further polished to a thickness of approximately less than 20 μm; (4) The sample is then placed in an ion beam miller (Gatan 691 Precision Ion Polisher System, PIPS™), making sure that the milling is done in interface of the glued surface; The two Ar guns were set at angles between 6° and 10° to ion mill the sample. The ion current was between 8 μA and 14 μA at 4 KeV, and the sample was constantly rotated. (5) The milling is terminated once a desired thin area around the interface of the glued surfaces is created.

FEI Quanta-3D FEG Dual Beam System was also used to prepare the cross-sectional TEM samples of oxidised 0#, 3# and pin-on-disc wear track of 5# coating. Cross sections of each sample were cut using a diamond plate, and manually pre-thinned to ～20 μm in thickness; the same process was explained in 3.1.3 from step (1) to (2). Sections of the coating approximately 1×2 mm^2 were attached to a sectioned copper grid using G-1 epoxy. The samples were then transferred to FIB miller for final thinning. Prior to milling, tungsten coating was deposited along the edge of the region from which the sample was to be prepared in order to promote uniform milling and preserve the edge structure, as shown in Figure 3.1-2. Rough mills were performed with beam currents from 50 nA to 5 nA at 30 KV and final polish mills at 5 KV 48 PA after final thinning at 1 nA～0.1 nA, 30 KV.

3.2 Surface coating and oxidation

3.2.1 Coating deposition process

Cr-Al-Ti-C-N coatings with different compositions were prepared with a Teer Coatings UDP 450 closed-field unbalanced magnetron sputtering ion plating (CFUBMSIP) system, as shown in Figure 3.2-1. The equipment was equipped with four unbalanced magnetrons uniformly arranged at 90° intervals around the vertical stainless steel vacuum chamber, which was approximately 425 mm internal diameter. Figure 3.2-2 shows a cross-section schematic drawing of arrangement plan of magnetron and substrate holder. Each magnetron was fitted with a target, which was approximately 10 mm thick, and 134×330 mm in size. One target each of chromium, titanium, aluminium and graphite were employed. The magnetrons were configured in a closed-field arrangement and were magnetically unbalanced, their outer poles being stronger than their centre poles. The substrate fixture comprised a central, rotating, vertical rod, supporting a pair of horizontal spoked rings between which the substrates were clamped. After cleaning, the samples were fixed on vertical rod of sample holder and the system was pumped down into a high vacuum condition with a background pressure less than $3.0×10^{-3}$ Pa, as shown in Figure 3.2-3.

Firstly argon and then a mixture of argon and nitrogen gases was introduced into the chamber during the process, and the nitrogen content was controlled by plasma optical emission monitor (OEM) with a feedback control. The deposition started with a 20 min of argon plasma cleaning, followed by deposition of a Cr adhesion layer. A Cr-N monolithic nitride layer was then deposited reactively, and then the Cr content gradually reduced and the fractions of Ti and Al increased to produce a constant CrAlTiN multilayer. Finally the

carbon content was gradually induced and a composited CrAlTiCN multilayer was formed. Figure 3.2-4 schematically illustrates the layer structure of CrAlTi(C)N coating systems. The period constant of the resulting multilayer was adjusted by controlling the sputtering power of the targets and the rotation speed of the substrate turnable. The relative concentration of the elements in the coating was controlled by the relative sputtering power on each target during the deposition. The treatment parameters-bias, target current, gas composition and pressure-were selected after a literature survey on similar work [271]. The study was concerned with the effects of carbon content, which were controlled by the carbon target current from 0 A～5 A. Typical deposition conditions for the carbon doped CrAlTiCN coatings by the CFUBMSIP system are summarised in Table 3.2-1.

3.2.2 Thermal oxidation treatment

In order to evaluate the thermal stability of the designed carbon doped CrAlTiCN coatings for cutting tools, oxidation tests were performed in an air circulating BSF 12/10-2416-2116 Elite thermal furnace with a maximum temperature of 1150℃. All the specimens were carefully degreased using suitable solvents and were heated up to 300℃, 400℃, 500℃, 600 ℃, 700℃, 800℃, 900℃, and 1000℃, held for 2 h at the temperatures, and were cooled down in the furnace.

3.3 Characterisation and evaluation

3.3.1 Phase and microstructure identification

3.3.1.1 X-ray diffraction (XRD)

The phase constituents in the coated and oxidised surfaces were analysed with an X'Pert Philips X-Radiation diffractometer using Cu-Kα radiation (Table 3.3-1). The diffraction patterns obtained were analysed and indexed using X'Pert High Score analytical software for automated powder diffraction. A computer analysed the intensity of the diffracted beam, recorded any change in beam intensity and automatically calculated the d-spacing corresponding to the peak. Interpretation of the X-ray results was undertaken using the PCPD cards.

3.3.1.2 Glancing-angle X-ray diffraction (GAXRD)

GAXRD measurements were performed on a D8 advance diffractometer (from Bruker AXS) equipped with a sealed X-ray tube with copper anode (λ=0.15418 nm) and with a Goebel mirror in the primary beam. A soller collimator with a divergence of 0.4° and a flat LiF monochromator were inserted into the diffracted beam. The LiF monochromator changes the intensity ratio between the spectral line Cu $K_{\alpha 2}$ and Cu $K_{\alpha 1}$ to $I(CuK_{\alpha 2})/I(CuK_{\alpha 1}) = 0.07$. For detailed phase identification, the GAXRD line profile analysis was applied. In this method, the individual diffraction lines are approximated by analytical functions, in our case, the Pearson VII function was used.

Crystallite size was calculated from the dependence of the integral broadening of the XRD lines measured in the GAXRD geometry on the sine of the diffraction angle by taking the partial coherent of crystallites for X-rays into account [260]. For partially coherent nanocrystallites, i.e. for nano-sized crystallites with a very small mutual disorientation, XRD recognizes not only their size but also their mutual disorientation and the size of clusters that are composed of these partially coherent nanocrystallites [261].

3.3.1.3 Glow discharge optical spectroscopy (GDOES)

A Leco GDS-750 unit was used to obtain the composition-depth profiles of coated samples. The method and measurement programme were calibrated using standard blocks of known composition, according to the instructions of the manufacturer.

3.3.1.4 X-ray photoelectron spectroscopy (XPS)

To understand the chemical composition of carbon doped CrAlTiCN coatings, X-ray Photoelectron Spectroscopy (XPS) with AXISULTRAX unit was conducted. The spectrometer was equipped with a hemispherical energy analyzer. An X-ray tube with monochromatic Al K_α radiation (h_v =1486.6 ev) was used as signal excitation source. The investigation was carried out under vacuum of the order of 10^{-8} Pa. Samples were subjected to etching by argon ions with Ar^+ ion bombardment of energy 4 KeV and ion current of 1.0 μA to remove the top contamination layer, which can reduce the occurrence of preferential sputtering in the etching process.

3.3.1.5 Scanning electron microscopy (SEM)

As-deposited, wear tracks, and oxidised samples were examined using a field emission JEOL7000 scanning electron microscope (SEM) with EDX and WDX capability. The depth profile of chemical compositions of selected oxidised samples was analysed using Oxford Instruments Inca EDX line scanning on the cross sections. The analysis was carried out both qualitatively to determine the existence of certain elements and quantitatively to determine the amount of each element present.

3.3.1.6 Atomic force microscopy (AFM)

Digital Instruments Dimension 3100 nanoscope, using Veeco NanoScope V.5.12r3 software and Veeco NP gold coated silicon nitride probes (Table 3.3-2) was used to examine the morphology of the coated surfaces. The AFM worked in a contact mode by scanning a sharp probe attached to the end of a cantilever across the sample surface while monitoring the change in cantilever deflection with a split photodiode detector. The distance the scanner moved vertically at each (x,y) data point was stored by the computer to form the topgraphic image of the sample surface.

3.3.1.7 Transmission electron microscopy (TEM)

TEM observations of the microstructural variation through the depth of surface modified layers and the interface structure was carried out by FEI Tecnai F20-FEG (EDX). The micrographs and electron diffraction pattern (EDP) were obtained on Kadak SO-163 eletron image film ($3^{1/4}$ in ×4 in) developed. CrAlTiCN-1#, 3#, and 5# coated samples, 0# and 3#

oxidised samples, and pin-on-disc wear tracks of 5# sample were selected for the TEM analysis.

The electron energy loss spectroscopy (EELS) measurement was performed with a Gatan Parellel Electron Energy-loss Spectrometer attached to an FEI Tecnai F20. The energy resolution at the zero loss peak was 0.75～0.8 eV with a beam voltage of 200 KeV. The spectra were analysed with Gatan ELP 3.0 PEELS software.

3.3.2 Surface topography measurement

A stylus profilometer, KozakaLab Surfcorder SE 1700, was used to profile the wear tracks and to measure the surface roughness of the testing samples. Standards BS EN ISO 4287 and 1134-1 were taken as reference for these measurements. Different pick up settings were selected depending on the objective of the measurement (Table 3.3-3). To obtain the wear volume, the area of the wear scar was calculated and then multiplying by the circumferential length of the wear track.

3.4 Mechanical property measurement

3.4.1 Nano-indentation

A mechanical properties microprobe (MPM), Nano-Test 600 machine (Micromaterials, UK) as shown in Figure 3.4-1 was employed to evaluate the surface hardness (H) and elastic modulus (E) of the coated and oxidised samples. The indentation tests were carried out normal to the surface and 10 points with 50 mN load were selected in order to determine the values of H and E. As discussed in Section 2.3.3.2, a standard procedure developed by Oliver and Pharr [262] was used to process the load-depth data. Accounting for the curvature in the unloading curve, a physically justifiable data-processing procedure was established to determine the contact depth which should be used in conjunction with the indenter shape function in order to obtain the contact area at peak load. The detailed method is outlined as follows.

Elastic modulus

When the indenter penetrates a surface layer, both elastic and plastic deformation will take place. On withdrawal of the indenter, elastic recovery will occur. The slope of the unloading curve can be used to measure the elastic properties of the material. Accordingly, the reduced modulus (E_r) is obtained from the equation

$$E_r = \frac{\sqrt{\pi}}{2} \times \frac{S}{\sqrt{A}} \qquad (3.4\text{-}1)$$

where S (S=dp/dh) is the stiffness of the upper portion of the unloading curve, E_r is the reduced modulus of both the sample and the indenter

$$\frac{1}{E_r} = \frac{1-v^2}{E} + \frac{1-v_i^2}{E_i} \qquad (3.4\text{-}2)$$

E and v are Young's modulus and Poisson's ratio for the sample and E_i (1141 GPa) and

v_i (0.07) are the same parameters for the indenter.

The contact area A is determined by the geometry of the indenter and plastic depth h_c,

which is defined as the plastic displacement of the indenter in contact with the sample under

load and is obtained from linear fitting 20% of the unloading curve at maximum load and

extrapolating to zero load, the intercept is then the plastic depth (h_c).

$$h_c = h_{max} - \varepsilon \times \frac{P_{max}}{dp/dh} \qquad (3.4\text{-}3)$$

The value of ε depends on the geometry of the indenter.

Once h_c is determined from above Equation 3.4-3, the contact area can be calculated from

the area function

$$A = A(h_c) \qquad (3.4\text{-}4)$$

The function $A(h_c)$ can be calculated as a deviation from the ideal $A(h_c) = 24.5h_c^2$

Hardness

Hardness is a measure of resistance to local plastic deformation and can be expressed by the

ratio:

$$H = \frac{P_{max}}{A} \qquad (3.4\text{-}5)$$

where P_{max} is the peak load applied to a given type of indenter and A is the projected area of contact at peak load evaluated from Equation 3.4-4.

3.4.2 Micro mar resistance (MMR) tests

To measure the ability of the samples against light damages, MMR was selected, using a conical shaped diamond tip with a radius of 1µ at the apex to scrape the surface of the samples under a constant force of 50 mN. A modified scanning probe microscope (SPM) was used to measure mar resistance. The tip of the high modulus probe is pressed into the coating surface, and the feedback loop of the instrument is set to hold the normal force constant. Depth of penetration is measured. The damages of all the samples made with 50 mN belong to the mar category. The data for calculating the three responses are obtained by measuring the depth of penetration and the dimensions of each mar made by a single scrape as described in Section 2.2.3.4. Then, the cross sectional area of the trough was measured and MMR of each sample was calculated, using the formula,

$$MMR= F_N/A_{trough} \qquad (3.4-6)$$

Mar resistance is a complicated issue, and it cannot be characterized with a single quantity. In performing the scratching, the tip first makes a pre-scan under a light load to measure the surface profile along the line to be tested. The surface profile is stored and used to automatically correct subsequent data. During the scratching procedure, lateral motion, applied load, real-time penetration depth, and the frictional force encountered by the tip are recorded. Following the scratching, the tip will make a post-scan to measure the residual depth of the scratch. Curves of applied load, real-time penetration depth, residual depth, and

frictional force versus the lateral movement of the tip can be plotted. The plot of the profiles which was made by the software allows to measure the dimensions of the mars with great accuracy, thus calculating the micro mar resistance, MMR, quantitatively [263].

3.4.3 Pin-on-disc unidirectional sliding wear tests

Figure 3.4-2 shows a schematic view of the pin-on-disc tribometer. Disc samples were made to rotate against a stationary WC-Co ball of 5 mm in diameter at a speed of 420 r/min for 1 h under non-lubricated conditions at room temperature. The normal contact load acting on the ball was 20 N and a wear track of 11 mm in diameter was produced. The friction was recorded during the wear tests. WC-Co balls were used during this test because of their high hardness and high wear resistance.

The profile of all wear tracks left on the tested samples was measured at not less than 20 different positions, by means of a KozakaLab Surfcorder SE1700 stylus profilometer. The obtained profile was integrated for the whole wear track and the total worn area could be thus calculated.

3.4.4 Reciprocating sliding wear tests

Figure 3.4-3 shows a schematic view of the reciprocating wear tester. During tests, the sample was glued to blocks and made to move linearly against a stationary WC-Co ball (surface finish as supplied) of 8 mm in diameter at an average speed of $10 mms^{-1}$ for 100 m. The normal contact load acting on the ball was of 50 N and a wear scar of 10 mm in length was produced. The test was repeated twice. WC-Co balls were used.

3.4.5 Fretting wear tests

Fretting wear tests were carried out on a horizontal servo-hydraulic fretting test machine (DS20 PLINT, France). The coated coupons were cut into blocks 10 mm by 10 mm by 7 mm, and then clamped to another block. During the test, a hardened SAE 52100 steel ball of 40 mm in diameter fretting against the specimen surfaces at an average speed of 3 Hz with 100 μm displacement amplitude for repeated 5000 times at room temperature and 350℃. The normal contact load acting on the ball was 100 N. The test was repeated 4～5 times per condition.

3.5 Load bearing capacity evaluation

3.5.1 Indentation tests

The indentation technique has been used to characterise the material properties and of coating materials because it is simple and can be performed on small specimens. The load bearing capacity of the surface coated HSS samples was assessed by static micro-indentation using a Mitutoyo MVK-H1 micro-hardness tester with a Vickers indenter under 1 Kgf. An Olympus LEXT ols 3100 confocal microscope was used to investigate the 3D damage by the Vickers indenter after LBC tests.

3.5.2 Micro-scratch tests

Microscratch tests were carried out on the treated surface using a Teer ST 3001 friction-monitored scratch tester. During the test, a linear-increased load was applied to the static indenter at a loading rate of 100 N/min, while the sample moved with a table at a speed of 10 mm/min. The tip slid at the surface of samples under a linearly increasing normal force from $0 \sim 60$ N. At the same time, the friction force was recorded and displayed as a function of load. The critical load, L_c, was defined as the load at which the friction force suddenly increased and surface layer failure occurred.

Chapter 4: Experimental Results

4.1 Introduction

The present investigation has been focused on the design, deposition and characterisation of novel carbon-doped low-friction nano-scale multilayer CrAlTiCN coatings. Systematic materials characterisation and property evaluation have been conducted for the as-deposited and oxidation tested novel carbon-doped CrAlTiCN coatings.

Of the following sections, Section 4.2 concerns the effect of addition of carbon on the microstructure of the as-deposited carbon-doped CrAlTiCN coatings. Sections 4.3 and 4.4 focus on the tribological behavior and surface damage resistance of the as-deposited novel carbon-doped CrAlTiCN coatings. Finally, Section 4.5 details the effect of high-temperature oxidation on the microstructural and properties of the carbon-doped CrAlTiCN coatings.

4.2 Microstructure of as-deposited coating materials

4.2.1 Surface morphology and fractography

Figure 4.2-1 illustrates the typical SEM surface morphologies of the as-deposited coatings. The referenced numbers of coatings are designated in terms of the carbon target current. As can be seen, all the coatings are dense and there is no observable porosity or cracks on the surface. The results for each coating were reproducible. The surface morphologies of the carbon-doped CrAlTiCN coatings (Figs. 4.2-1 b-f) are similar to that of carbon-free CrAlTiN coating (Fig. 4.2-1a). The coating surfaces reveal particle boundaries with an average diameter around 100~300 nm. This was further confirmed by three dimensional AFM studies, as illustrated in Figure 4.2-2, and the quantitative surface roughness values are summarised in Table 4.2-1. It can be seen that although the surface roughness of the carbon-doped CrAlTiCN coatings is in general higher than that of the carbon-free CrAlTiN coating, the difference is not significant if the experimental errors are taken into account.

SEM micrographs presented in Figure 4.2-1 also show the fractural cross sections of the carbon-doped CrAlTiCN coatings deposited as well as carbon-free CrAlTiN coating for comparison. As can be seen, the total layer thickness for all the samples is about 4.5 μm, thus eliminating the potential influences of the layer thickness. All the coatings are densely packed and there is no sign of cracking at the coating-substrate interfaces or within the coatings, indicating that relatively good compactness has been achieved in general. The coatings deposited by the magnetron sputtering ion plating (MSIP) method were well adherent to the metal substrates.

However, as compared with carbon-free CrAlTiN-0# sample, the carbon-doped coatings presented two sub-layers with different contrasts, especially for CrAlTiCN-4# and 5# samples doped with a relatively higher carbon content (Figure 4.2-1e & f). This was most probably caused by introducing the carbon atoms into the coatings, which changed their chemical composition and microstructure. More detailed investigations on the microstructure of these coatings will be carried out in the next section.

4.2.2 Composition, structure and bonding

Chemical composition

Table 4.2-2 summarises the composition of the coatings which was analysed by WDX for the light elements of carbon and nitrogen and EDX for other Cr, Ti, and Al elements.

It can be seen that the carbon content (Table 4.2-2) in the coatings increased with the current of the carbon target (Table 3.2-1) used during the deposition of these carbon-doped coatings. When increasing the carbon target current from 0 to 5A, the carbon content of the CrAlTiCN coatings was found to be increased to 24.34 at% for CrAlTiCN-5# coating. Except for CrAlTiCN-5# coating, the nitrogen content of all other deposited samples is similar in view of the experimental errors (3-5%) of WDX for light elements.

In general, the absolute content of the metallic elements Cr, Al, and Ti decreased with increasing the carbon content in the carbon-doped CrAlTiCN coatings; however, the ratios of the metallic element contents did not change obviously in the doped coatings. This is in line with the fact that the current of Cr, Al, and Ti targets was constant during the deposition of all the coatings (Section 3.2.1).

Composition depth

Figure 4.2-3 shows the composition depth profiles of carbon-doped CrAlTiCN-3# (Fig. 4.2-3a) and 5# (Fig. 4.2-3b) coatings on HSS substrate. All the composition profiles fluctuated within the first ~ 0.20 μm (200 nm), which is most likely related to the surface roughness of these coatings [264]. The composition changed greatly at the coating-substrate interface, where the signals of iron and carbon (dissolved in steel) appeared while the signals belonging to the coating elements disappeared. However, the change of composition at the interface was not abrupt but gradual. This is because the bottom of the GDS craters was not ideally flat but rough and sputtering occurred at slightly different depths [265].

According to the composition-depth profiles of species (Cr, Al, Ti, N, and C), the whole coating layer could be divided into several sublayers as indicated by dotted lines. A thin Cr adhesion sublayer (Sublayer I Cr) was observed above the substrate as indicated by the very high Cr peak. Then, the amount of Cr reduced while Ti, Al and N increase gradually until a short plateau was reached. This sublayer (Sublayer II Cr-N) seems to be dominated by Cr and N together with a small amount of Ti and Al. The relative amounts of Ti and Al in Sublayer III (CrAlTiN), corresponding to the plateau, increased and the ratio between the alloying elements of Cr, Ti, Al and N is fairly constant. Finally, a long composition plateau was formed when carbon was doped into the sublayer (Sublayer IV CrAlTiCN).

The main difference between Figs. 4.2-3a and b is the level of carbon in the carbon-doped surface layer, which is in line with the different carbon target current used to deposit these two coatings. More detailed layer structure investigation by TEM will be presented in the next section.

Crystal structure

Figure 4.2-4 shows the XRD patterns obtained from the carbon-free and carbon-doped coatings. Due to the substrate contribution, it is difficult to distinguish the peaks accurately. A tentative indexing shown in Fig. 4.2-4 displayed fcc (111), (200), (220), and (311) reflections of all the coatings, and the (110), (200), (211), and (220) reflections of the bcc α-Fe substrate. The intensity of the peaks is relatively weak except the peak around $2\theta=45^0$, which was superimposed with α-Fe (110) from the substrate.

In order to avoid substrate interference effects, glancing angle XRD was employed and the typical GAXRD charts are given in Figure 4.2-5. As shown in Fig. 4.2-5a, a set of fcc (111), (200), (220), (311), (222), and (400) reflections were obtained from the coatings, which confirmed the indexes in Figure 4.2-4. The results of the XRD line fitting are shown in Figs. 4.2-5b, c, and d on the examples of the low-angle diffraction lines. A slight increase of the peak broadening with increasing the carbon contents in the coatings is observed, which might indicate an increase in stress and a decrease in grain size [266]. Table 4.2-3 summarises the lattice parameters and average crystallite size of the fcc phase in the respective samples, which were calculated using the $\sin^2\Psi$ method [267,268]. The lattice parameter for stoichiometric TiN (0.424 nm), CrN (0.417 nm) [269,270], TiC (0.431 nm) [271], AlN (0.412 nm) [272] and TiCN (0.426 nm) [273], the calculated lattice parameters of this fcc structure does not exactly match any known phases, but is close to CrN.

It could be concluded that the most likely phase existing in the carbon-doped CrAlTiCN coatings is the fcc structured intermixed (Cr, Al, Ti)(C, N) phases in general. Further elucidation has been achieved through the following XPS and TEM studies.

Bonding status

Figure 4.2-6 illustrates a typical XPS survey spectrum of carbon-doped CrAlTiCN-5# coating, which shows Cr2p, O1s, Ti2p, N1s, C1s, Al2s, Cr2s, Cr3s and Cr3p peaks. Although cleaning was conducted at the beginning using Ar^+ to remove the top contamination layer, the oxygen peak was still observable in all the coatings. This might be caused by the residual air present in the chamber during deposition period. The Ti2p and Al2s XPS spectra were very week.

Figure 4.2-7 shows the spectra of Cr2p, C1s, N1s and O1s from CrAlTiCN-5# coating. In the fitting spectrum of Cr2p, four group peaks are observed, as shown in Figure 4.2-7a. The Cr2p levels at 574.6 eV is typical for the metallic Cr^0 binding state [274]. The Cr2p peak centers at 575.6eV could be assigned to CrN [275], while the tail of the peak could be assigned to Cr-O [276]. In addition, the shoulder at a higher binding energy of 583.5 eV is allocated to Cr-C and/or Cr-N bonds [277,278].

The C1s spectrum (Figure 4.2-7b) shows an asymmetrical peak, which can be fitted into two components located at 282.3 and 284.6 eV. The 282.3 eV peak could be attributed to Cr-C binding and the peak at 284.6 eV is typical for amorphous free carbon sitting in a graphic environment [279].

Figure 4.2-7c shows the spectrum of N1s which were ideally fitted by two peaks. The peak at 396.9 eV and Cr2p 575.6 eV peak positions are in agreement with the literature data for the CrN phase [280,281,282,283]. Moreover, the Cr_2N (397.2±0.2 eV) [284,285] could also be detected.

The peaks of O1s are decomposed to two peaks, as shown in Figure 4.2-7d. The maximum

peak at 531.4±0.2 eV is Cr-O [286,287], which is consistent with the Cr2p peak at 576.9 eV.

The secondary peak could be allocated to the presence of Al_2O_3 (531.8 eV) [288].

4.2.3 Multilayer microstructure

Figure 4.2-8 shows a typical bright field cross-sectional TEM observation and EDX

compositional analysis of carbon-doped CrAlTiCN-5# coating. It can be seen that the

coating contained four sublayers starting from the substrate: a pure chromium interface

layer (Sublayers I); a chromium nitrides layer (Sublayers II); a CrAlTiN alternative layer

(Sublayers III); and a carbon-doped composited CrAlTiCN sublayer (Sublayer IV).

Sublayers I, II and III

Figure 4.2-9 shows a higher magnification bright field TEM taken from Sublayers I & II. As

shown in Figures 4.2-8 and 4.2-9a, Sublayer I is a pure chromium interface layer and

presents a dense columnar structure with the column diameter on the order of $150\sim170$ nm.

The average thickness of Sublayer I is about 0.5 μm.

When N_2 was introduced with Cr deposition, a chromium nitride layer (Sublayer II) was

formed. The TEM microstructure shown in Figure 4.2-9a indicates that, similar to Sublayer

I, the chromium nitride Sublayer II is also columnar structured but the diameter of the

columns is smaller ($30\sim50$ nm) than the columns in Sublayer I. Figure 4.2-9b shows a

selected area diffraction (SAD) pattern taken form the region "A" in the interface between

sublayers I and II, and confirms that the sublayers are mainly composed of Cr, CrN and Cr$_2$N.

Figure 4.2-10 exhibits an image of adjacent to the interface between Sublayer III and Sublayer IV. It can be seen the multilayer structure with interval thickness of 5～10 nm (Figures 4.2-10a & d) was formed in Sublayer III and Sublayer IV, which could be produced when samples were rotating against the different targets: chromium, aluminum, and titanium during the deposition process. The thickness of a single interval is based on the target power and substrate rotation (rev./min) [289]. In addition, as shown in Fig. 4.2-10d, there existed many finer columnar microstructures with the columnar diameter around 20～25 nm. These columns do not extend through the entire Sublayer III but they nucleated and grew following the growth direction of the whole coating. Figure 4.2-10c shows an SAD pattern taken from the region of Sublayer III, which confirmed a typical fcc structure with the crystal constant a=0.414 nm. It can be noticed that (111) and (200) rings are not homogenous. The discontinuous bright arcs may indicate preferential orientation of the crystal.

Sublayer IV

The effect of carbon content on the microstructure of Sublayer IV was studied. Figure 4.2-11 shows the bright field TEM micrographs taken from the Sublayer IV of carbon-doped CrAlTiCN-1# sample. As shown in Figure 4.2-11a, it consists of an obvious multilayer structure. The thickness of each interval is around 5～10 nm. The columnar structure with the diameter in the range of 100～200 nm is also observed. Figure 4.2-11b shows a high resolution TEM observation of the marked region in Fig. 4.2-11a. The lattice fringes which

showed apparent crystalline structure continuously cross the multilayer boundaries (Figure 4.2-11b). The origin of the contrast between intervals in this case in the TEM bright field mode might be due to the slightly changed compositions during the deposition. The brighter regions might be dominated by the lighter element - carbon. Figure 4.2-11c is a selected area diffraction (SAD) pattern, which corresponds to a typical single cubic B1 NaCl-type structure.

Figure 4.2-12 shows the bright field TEM micrographs taken from the Sublayer IV of the carbon-doped CrAlTiCN-3# sample. As shown in Figure 4.2-12a, the columnar structure with the diameter in the range of 200-300 nm can be observed. High resolution TEM which taken from the marked region proved that the lattice fringes discontinued across the multilayer boundaries (Fig. 4.2-12b). Within the area defined as amorphous phase small ordered domains are found (circled in Fig.4.2-12b), suggesting that its structure is indeed a dispersion of nanocrystals in an amorphous matrix. The inset SAD pattern shown in Figure 4.2-12c is slightly diffused compared to the CrAlTiCN-1# sample (Figure 4.2-11c).

Figure 4.2-13 shows the bright field TEM micrographs taken from the Sublayer IV of carbon-doped CrAlTiCN-5# sample. The HRTEM image (Fig. 4.2-13b) taken from the marked region indicated a larger ratio of the bright region to the dark region, which could be also composed of amorphous carbon cluster and nanocrystalline structures (circled in Fig. 4.2-13b), respectively. As shown in Figure 4.2-13c, the inset electron diffraction pattern presents continuous rings superimposed with diffused rings, indicating a random orientation and no texture are presented in this sublayer.

In summary, comparisons of TEM observations in the carbon-doped CrAlTiCN layer or Sublayer IV revealed some common microstructure features. Firstly, Sublayer IV is characterised by columnar and multilayer structures as shown in Figures 4.2-10～13. Secondly, Sublayer IV possesses a single cubic B1 NaCl-type structure as evidenced by the SAD patterns shown in Figures 4.2-11c, 4.2-12c and 4.2-13c. However, by comparing the SAD patterns from these three samples, it can be seen that the diffraction rings changed from sharp/inhomogenous to diffuse/homogenous with the increasing of carbon contents, which indicates a reduction of crystallization and loss of preferred orientation as also clearly indicated in the high resolution TEM microstructures (Figures 4.2-11b, 4.2-12b, and 4.2-13b).

Figure 4.2-14 shows that the crystallinity and the size of the crystals changed along the distance from the interface between Sublayer III and Sublayer IV for carbon-doped CrAlTiCN-5# coating, which has the highest carbon content (23.34 at%). It can be seen from Figure 4.2-14a that when carbon was first introduced into the coating, the nano-scale multi-layer shows relatively sharp interfaces between the dark region and the bright region. Clear lattice fringes can be observed in the dark crystalline region while the bright carbon-rich regions are mainly amorphous embedded with few fine crystals. In the middle areas of the (Cr, Al, Ti)(C, N) sublayer (Figure 4.2-14b), the amorphous carbon layer is thicker and the crystals are smaller than those showed in Figure 4.2-14a. At the outermost area, only extremely fine crystal clusters are embedded in the amorphous structure in both dark and bright regions (Figure 4.2-14c).

4.3 Mechanical properties

4.3.1 Nano-hardness and Young's modulus

The hardness (H) and Young's modulus (E) of CrAlTiN and CrAlTiCN coatings were probed using the nano-indentation technique [290]. A typical load/unload against displacement curve is plotted in Figure 4.3-1.

Figure 4.3-2 summarises the surface nano-mechanical properties in terms of hardness and Young's modulus of CrAlTiN and carbon-doped CrAlTiCN nano-scale multilayer coatings. It can be seen that both the hardness and Young's modulus decreased gradually with increasing the carbon content from 1# (2.34 at% C) to 3# (9.65 at% C) and then flattened out once the carbon content exceeded about 10% for 4# (12.53 at% C) and 5# (24.34 at% C) samples (Table 4.2-2).

4.3.2 Cracking and toughness characteristics

The toughness characteristics of carbon-free CrAlTiN coating and carbon-doped CrAlTiCN coatings were investigated using a Vickers micro-indenter under a load of 1000g. Figure 4.3-3 shows laser confocal images of indentation crack patterns formed in the CrAlTiN-0# and carbon-doped CrAlTiCN (1#-5#) coatings during micro-indentation.

It can be seen from Figure 4.3-3 that none of the coatings exhibit obvious delamination at the indentation corners, indicative of relatively good bonding between the surface coating and hardened high-speed steel substrate. Although cracks were observed for all the coatings, the crack patterns varied with the carbon content of the coatings.

As shown in 4.3-3a, in addition to circular or ring cracks, the corner area of the indented surface of CrAlTiN (0# without carbon) coating revealed damage in the form of radial cracks (as circled), which is a typical feature of a brittle material [291]. When the CrAlTiN coating was doped with carbon, the length of the radial cracks formed in the carbon-doped CrAlTiCN coatings which reduced gradually with the increase in carbon content (especially for 3#-5# CrAlTiCN coatings). Indeed, almost no appreciable radial cracks could be observed for the CrAlTiCN-5# coating containing the highest carbon content (24.34 at%). Clearly, addition of carbon can effectively improve the toughness of the hard CrAlTiN coating.

In order to acquire supplementary (especially 3-D) damage feature information, depth profile across the Vickers indentation impressions were generated based on laser confocal microscopy and the results are given in Figure 4.3-4. The V-shaped lines (i.e. cross section of the indentation surfaces) of the CrAlTiN-0# (without carbon) coating was evidently zigzagged, indicative of severe cracking of the surface coatings; on the other hand, the V-shaped lines of the carbon-doped CrAlTiCN-1# and 5# became much smoother.

It is also noted from Figure 4.3-4 that the final displacement of the indentations after complete unloading decreased from 1# to 5# samples as the carbon content was increased in the coatings, which is evidence of increased elastic recovery of the carbon-doped coatings.

4.3.3 Scratch resistance

As discussed in Chapter 3, two scratching techniques, micro-mar and micro-scratch, were used to investigate the effect of carbon addition on the scratch resistance of carbon-doped CrAlTiCN coatings.

Micro-mar resistance (MMR)

Mar resistance is a measure of a material's ability to resist surface damage under a light load. Figure 4.3-5 shows typical surface morphologies and the cross-sectional profiles of the mars formed in bench-mark CrAlTiN coating (0# without carbon) and carbon-doped CrAlTiCN coating (5# with highest carbon content). It is evidenced in Figure 4.3-5 that plastic deformation dominated in the mars of these coatings; two small shoulders sit on both sides of the ditch, indicating that the material was displaced from the ditch to build these two shoulders during the marring.

Depths vs. the scratching distance plots measured in micro-mar resistance tests are shown in Figure 4.3-6. In all the plots, the lower curve is the real-time scratching depth, and the upper curve is the residual depth of the ditch. It can be seen that the real time depth increased from about 280 nm for 0# sample (Figure 4.3-6a) to about 290 nm for 1# sample (Figure 4.3-6b) and to around 350 nm for 5# sample (Figure 4.3-6c). This is largely in line with the hardness trend (Figure 4.3-2), the real time depth (i.e. total depth) of the mars formed increased with the decrease in hardness.

Be aware of that the real-time scratching depth is normally different from the residual depth because the elastic deformation of the scratched surface might make a large contribution to

the real-time scratching depth. The distance between the real-time depth and the residual depth indicated the elastic recovery of the coatings when the force was removed. With the higher carbon content involved in the coating, it can be seen that this difference increased from about 200 nm for CrAlTiCN 1# sample (Fig. 4.3-6b) to around 250 nm for 5# sample (Fig. 4.3-6c), which indicated the improved elastic deformation capacity.

Table 4.3-1 lists the values of MMR of the deposited samples measured under a constant force of 50 mN. Comparing these values, measurable before the cracking or delamination occurred, the bench-mark CrAlTiN coating (0# without carbon) had a higher MMR than the CrAlTiCN coatings (1#-5#). This is consistent with their nano-hardness values (Figure 4.3-2).

<u>Scratch resistance</u>

Scratch tests were carried out on 0#, 3#, and 5# samples under both normal and tangential forces. Figure 4.3-7 shows the load-friction force curves for these three representative samples. The 1st derivative curve shows the instantaneous rate of change of the friction. It can be seen that the friction force increased smoothly with the increase in the applied load before it fluctuated greatly when the applied load reached a critical value – the so-called the first critical load L_c. As summarised in Table 4.3-2, the critical load decreased from around 42 N for 0# sample to around 36 N for 3# sample and around 33 N for 5# sample.

Figure 4.3-8 shows the typical surface scratched damage morphologies of CrAlTiCN-3# sample. At the beginning of the scratch test, the scratch track looked smooth without any cracks (Figure 4.3-8a). Elastic and plastic deformation might have occurred. Then, as shown

in Figure 4.3-8b, buckling cracks on both sides further occurred and fish bone like cracks can be seen inside the track. Further increase in load led to the buckle spallation inside the track (Figure 4.3-8c), which is corresponding to the critical load L_c.

Figures 4.3-9～4.3-11 show the EDX analysis of the scratched end region of the track for CrAlTiN-0#, CrAlTiCN-3# and 5# samples, respectively. It can be seen for these three coatings, Fe element can only be detected at the very end of the scratch track, which means delamination appeared between coatings and substrate. In general, relatively good adhesion ability can be attained.

4.4 Tribological behaviour

4.4.1 Unidirectional sliding wear

Pin-on-Disc unidirectional sliding wear tests were carried out to evaluate the tribological properties of carbon-doped CrAlTiCN coatings as well as the benchmark carbon-free CrAlTiN coating for comparison. The evolutions of the carbon content vs. frictional coefficient of the coatings are shown in Table 4.4-1. It can be seen that the coefficient of friction (CoF) of the benchmark carbon-free CrAlTiN-0# coating is about 0.655, typical value for hard ceramic coatings [292,293]. When a small amount (2.34 at%) of carbon was added (i.e. 1# sample), the CoF of CrAlTiCN-1# coating was effectively reduced from 0.655 to 0.420 representing a reduction of 36%. Further increase in carbon content did not lead to significant reduction in CoF until a larger amount of carbon (24.34 at% for 5# sample) was added, which led to a CoF of 0.350. Clearly, doping of carbon can effectively reduce the frictional coefficients of hard ceramic CrAlTiN coatings—one of the objectives of this PhD studies.

The wear of the tested coatings in terms of wear volume lost was quantitatively measured and the results are compared in Figure 4.4-1a. In general, the wear volume lost of the carbon-doped CrAlTiCN coatings reduced with increasing carbon content under the current test conditions. In particular, the high-carbon CrAlTiCN 3#, 4# and 5# samples exhibited obviously reduced worn volumes in relative to the carbon-free CrAlTiN coating.

Observations of the wear tracks under SEM revealed differences in morphology (Figures 4.4-2～5), and the EDX compositional analysis of the wear surfaces also showed the difference in their compositions.

Figure 4.4-2 shows the typical wear morphologies of carbon-free CrAlTiN-0# coating after unidirectional sliding against a WC-Co ball under unlubricated conditions at room temperature. It can be seen that the surface of undoped CrAlTiN-0# coating was severely damaged as evidenced by many coarse scratches. Chipping or cracking can be clearly found from the higher magnification image (Figure 4.4-2b). This suggests that under the present test conditions severe abrasive wear occurred and a micro-cutting effect may constitute the main wear mechanism [294]. In this case, the protruding parts of the counterpart exert plowing and cutting effects on the coatings surface. In addition, EDX compositional analysis has probed a relatively high amount of W in the wear surface after sliding against a WC-Co ball, indicative of the transfer of W from the counterpart to coating surface (i.e. adhesive wear). Furthermore, a large amount of oxygen was detected from the wear surface, indicating that oxidational wear also played a role in the wear of the undoped CrAlTiN-0# coatings.

Figure 4.4-3 shows the wear morphologies of carbon-doped CrAlTiCN-1# sample, which looks similar to that of the undoped CrAlTiN-0# coating. However, comparison indicated that although both surfaces were dominated by abrasive wear, the scratches formed in carbon-doped CrAlTiCN-1# sample were finer and more even than those formed in the undoped CrAlTiN-0# sample. In addition, the W content is relatively lower in the wear

surface of 1# sample (1.05 at%) than in 0# sample (3.35 at%). This implies that the addition of a small amount of carbon can reduce the transfer of W from the WC-Co ball counterpart.

Figures 4.4-4 and 4.4-5 show the wear morphologies of high-carbon doped CrAlTiCN samples (3# and 5#) respectively, which indicate great difference from those for undoped (0#, Fig. 4.4-2) or low-carbon doped (1#, Fig. 4.4-3) samples. It can be seen that the coatings were lightly scratched with fine and evenly distributed wear grooves. Higher magnification images (Figs. 4.4-4b & 4.4-5b) further revealed that most of the wear surface was of regular pattern with fine rumple features, which is most probably consisted of compacted wear debris. Small patches (B in Figs. 4.4-4b and 4.4-5b) with different surface morphologies were also observed, which contained a relatively lower amount of W as compared with the rest of the surfaces.

In general, no iron was identified by EDX examination from the wear surfaces with different morphologies. This indicates that although the surface coating was worn by the sliding of WC-Co balls, the substrate was still covered by the surface coating.

4.4.2 Reciprocating sliding wear

Reciprocating sliding wear tests against a WC-Co ball without lubrication at room temperature was also carried out. The results of wear volume lost are summarised in Figure 4.4-1b, and it is clear that no obvious difference in wear volume lost can be found among all the tested coatings.

Figures 4.4-6～8 show the SEM micrographs and EDX compositional analysis of the wear tracks formed in CrAlTiN-0#, CrAlTiCN-3# and 5# samples by the sliding of a counterpart WC-Co ball. In general, the wear tracks formed in these coatings appeared similar around 300 μm wide with dark wear debris piled up at both ends of the wear track. Observations under higher magnifications revealed fine scratches along the sliding direction inside the wear track and small black spots. Parallel cracks perpendicular to the sliding direction were observed near both the ends of the wear track under a higher magnification.

EDX compositional analysis indicated that the composition inside the wear track was similar to that of the original surface and Fe was not detected. This demonstrated that wear occurred within the thickness of the coating. The dark areas near the ends of the wear track contained 40-50 at% oxygen with almost no nitrogen. This implied that oxidation wear occurred during the reciprocating sliding and the generated oxide debris was pushed to the both ends of the wear track, compacted by repeated rubbing of WC-Co ball and eventually cracks under repeated compression and tension stressing. A certain amount of W was also detected from the wear debris piled up near the both ends of the wear track, which was thought to be transferred from the counterpart WC-Co ball.

Therefore, rubbing of WC-Co ball caused abrasive and oxidative wear of the CrAlTiN and CrAlTiCN coatings. The similar wear morphologies and wear mechanisms can explain the almost the same wear resistance of these coatings under reciprocating sliding conditions against a WC-Co ball under unlubricated conditions at room temperature.

4.4.3 Fretting wear

The fretting wear behaviour of CrAlTiN and CrAlTiCN coatings were investigated by fretting against a hardened SAE 52100 steel ball at a speed of 3HZ with an 100 micron displacement amplitude repeated 5000 times at both room temperature and 350℃.

Figure 4.4-9 shows the effect of carbon content on the fretting wear of undoped CrAlTiN (0#) and carbon-doped CrAlTiCN coatings (1#-5#) at room temperature and 350℃. In general, the doping of carbon possesses a moderate effect on the fretting wear of these coatings at room temperature and 350℃ under the current fretting wear test conditions. However, some differences have also been observed in terms of the effect of the carbon content and the test temperatures.

It can be seen from Figure 4.4-9a that the high-carbon doped 4# and 5# CrAlTiCN coatings show a marginally lower fretting wear volume lost compared with the undoped 0# and low-carbon doped CrAlTiCN 1#, 2# and 3# samples. This is probably attributed to the friction-reduction of the high carbon content in 4# and 5# CrAlTiCN coatings. On the other hand, for 350℃ testing, as shown in Figure 4.4-9b, the fretting wear increased of these coatings with increasing the carbon doped in the coatings, which will be discussed in the next chapter. It is of interest to note that except for sample 5#, the fretting wear for all other samples was lower when tested at 350℃ than at room temperature.

The fretting scars formed were examined using microscopy and the typical optical images and SEM/EDX results are given in Figures 4.4-10～13. Figure 4.4-10 shows optical micrographs of the wear scar after testing at room temperature. The wear carters can be

divided into two regions: (1) middle regions, which correspond to the main scar and (2) end regions corresponding to the edges of the scar. The micrographs show wear scratches parallel to the sliding directions, indicative of the abrasion action during the fretting wear processes.

Figures 4.4-11～13 are the SEM micrographs showing the wear scars formed in room temperature tested 0#, 1# and 4# samples. Fine scratches were observed within the middle region of wear scars. Note that shear stress pushed the wear debris out of the scar which was piled up at the end region of the wear scar with a number of cracks and loose particles. EDX compositional analysis (Fig. 4.4-12) proved that the wear debris formed in all the coatings is rich in oxygen and therefore oxidation should have played an important role in the fretting of these coatings.

The EDX compositional analyses also reveal a very high amount of Fe especially in the wear debris piled up at the ends of wear scars. Judging by the fact that the wear depth (around 1μm) is much smaller than the coating thickness (around 4.5μm), the Fe detected by EDX should be contributed by the SAE 52100 counterpart ball. Hence, damage of the counterpart balls and transfer of steel from the ball to the coating surface occurred.

Figures 4.4-14～17 show the optical and SEM micrographs of the wear scars formed at 350 ℃ tested 0#, 1# and 4# samples. In general, the wear scar morphologies of the 350℃ fretting wear tested coatings are similar to that for the room temperature tested coatings (Figs. 4.4-10～13). As shown in Figure 4.4-14, the wear scar formed in carbon-doped CrAlTiCN-5# sample is larger than that formed in carbon-free CrAlTiN-0# sample, which

is consistent with the fretting wear results shown in Figure 4.4-9b. It is also noted that while the wear scar formed in CrAlTiN-0# sample showed only one oval-shaped edge crater, the wear scar formed in CrAlTiCN-5# sample showed a white oval-shaped band outside the grey middle region. As shown in Figure 4.4-14, the fretting scar have not penetrated the top layer (i.e. Sublayer IV in Fig. 4.2-10)

Qualitatively, EDX compositional analyses (Fig. 4.4-16) of the wear debris formed from the 350℃ fretting wear tested coatings demonstrate similar elements to that formed from room-temperature testing. However, the quantitative measurement indicated that more oxygen was detected from the debris which formed from the 350℃ fretting wear tested coatings.

4.5 Effect of high-temperature

4.5.1 Microstructure and composition of the oxidised layers

SEM observations on the surfaces of as-deposited and oxidised coatings at different temperatures were conducted and some representative SEM images are shown in Figure 4.5-1. Below 700 ℃, all the oxidised coating surfaces looked similar, which were characterised by fine homogenous particles (100～300 nm) on dense coating surfaces without visible cracks. In general, the size of these surface particles increased with increasing the oxidation temperature. However, when oxidised at 800 ℃ or above, some surface particles grown faster than the others as evidenced by some large particles (Fig. 4.5-1).

Obvious difference in surface morphologies between the benchmark carbon-free CrAlTiCN-0# and carbon-doped CrAlTiCN coatings were observed when they were oxidised at 1000 ℃. While most of the particles on the 1000 ℃ oxidised CrAlTiN-0# sample were still round-shaped with a diameter in the range of 500 to 700 nm (Fig. 4.5-1a), the 1000 ℃ oxidised CrAlTiCN-4# and CrAlTiCN-5# coatings were characterised large and irregular particles (Figs. 4.5-1b & c). It should be pointed out that after oxidation at 1000 ℃, the surface of CrAlTiCN-5# sample was severely damaged as evidenced by extremely coarse oxide particles and cracks (Figure 4.5-1c). It is expected that spallation may have occurred to the surface of oxidised CrAlTiCN-5# sample at 1000 ℃.

Figure 4.5-2 shows the quantitatively measured roughness results, which further support the observations made above based on SEM studies. As shown in Figure 4.5-2, in general the Ra of the oxidised samples increased slowly with oxidation temperature, but no appreciable difference in Ra can be identified among these samples when oxidised from 400 ℃ to 900 ℃. However, after oxidation at 1000 ℃, an abrupt increase can be found in all the coatings. Whist the Ra for 0#-4# coatings showed a similar value around 0.11 μm, the Ra for 5# coating increased to around 0.16 μm, which was caused by the spallation during oxidation at 1000 ℃ (Figure 4.5-1c).

Figures 4.5-3, 4 & 5 show the BSE (back scattered electron) cross-sectional morphologies of the oxide layers formed on the coatings after oxidation for 2 hrs at 400 ℃, 900 ℃, and 1000 ℃ for 0#, 1#, and 5# samples, respectively. In general, for all the samples, the oxide layer became thicker with increasing the oxidation temperature.

After oxidation at 400 ℃, for 0#, 1#, and 5# samples, a relatively flat and clear interface existed between the top coatings (CrAlTiN-0# and CrAlTiCN-1# & 5#) and the protective Ni plating layer. Due to the poor adhesion between the electro-deposited Ni layers and the oxidised coatings, an obvious gap with a dark contrast can be seen in Figures 4.5-3, 4.5-4 and 4.5-5.

For 900 ℃ oxidised samples, an oxide scale was formed and the interface between the top oxide layers and the protective Ni plating layers became zigzagged. It can be seen that the thickness of the oxide layer formed on 0# and 1# samples at 900 ℃ is similar (0.4~0.5 μm).

However, for the higher carbon 5# sample (Figure 4.5-5), the thickness of the top oxide layer was much thicker (around 1.0 μm) and rougher as compared with that of the 0# and 1# samples.

After oxidation at 1000 ℃, a thick and rough oxide layer was observed for 0# and 1# samples (Figs. 4.5-3 & 4). However, an oxide layer with a dark grey colour was formed on the 1000 ℃ oxidised CrAlTiCN-5# sample. It can be deduced from the continuous distribution of the carbide band from the HSS substrate into the oxide layer that this is most probably an oxide layer of HSS formed when the CrAlTiCN surface was spallated from the HSS substrate (Fig. 4.5-5). This will be discussed in more detail in the next section (Fig. 4.5-8).

Figures 4.5-6, 4.5-7, and 4.5-8 show the chemical composition profiles along the lines marked in the cross-sectional images of the CrAlTiN-0#, CrAlTiCN-1#, and 5# coatings after oxidation for 2 hrs at 900 ℃ and 1000 ℃.

In general, the oxide scale formed at 900 ℃ for these three coatings and at 1000 ℃ for 0# and 1# samples contained oxygen, chromium, titanium, and aluminium but the Cr, Ti and Al concentration in the surface oxide scale was lower than that in the as-deposited coatings mainly because of oxidation. The oxygen content in the main coating part is very low implying that oxygen was trapped by the chromium, titanium, and aluminium atoms in the top layer.

However, no Cr, Ti or Al was detected but the surface oxide layer was rich in iron for CrAlTiCN-5# sample (Fig. 4.5-8). This is in line with the observations made in the last section that the surface coating was severely oxidised and most probably came off (i.e. spallation).

4.5.2 Phase identification

Figure 4.5-9 shows the typical XRD reflection patterns of the 0#, 3#, and 5# coatings before and after oxidation at different temperatures. It can be seen that except for 1000 ℃ oxidised CrAlTiCN-5# sample, all other oxidised samples exhibited peaks corresponding to a B1-NaCl (rock-salt) structure, indicating that the fcc (Cr, Al, Ti) (C, N) phase formed in the as-deposited coating was still remained. It is noted that the peak around $2\theta=45°$ is the Fe (110) reflection from the M2 tool steel substrate. In addition, the peaks belonging to the fcc (Cr, Al, Ti) (C, N) became sharp with increasing oxidation temperature. This might imply the crystallinity of the coating is improved and/or the relaxation of the residual stress during the oxidation process.

Oxides appeared in the XRD patterns after oxidation in air at 700 ℃ can be indexed to Al_2O_3 (No. 00-010-0414). After oxidation at 800 ℃, a mixture of Cr_2O_3 (No.00-038-1479), TiO (No. 00-088-0117), and Al_2O_3 (No. 00-010-0414) can be identified. For the CrAlTiCN-5# sample (Fig. 4.5-9c), the coating was completely delaminated from the HSS substrate since only Fe_3O_4 and Fe_2O_3 phases were detected, which is consistent with the SEM and EDX analysis (Fig. 4.5-5c & 4.5-8).

4.5.3 TEM observations

In order to further clarify the microstructural changes of the coatings after thermal oxidation, cross-sectional TEM observations were carried out on 800 ℃ oxidised CrAlTiN-0# and CrAlTiCN-3# coatings.

<u>CrAlTiN-0# sample</u>

As has been discussed in Section 4.2.3, CrAlTiCN-5# sample contained four sublayers (starting from the HSS substrate): a pure chromium interface layer (Sublayer I), a columnar chromium nitrides layer (Sublayer II), a CrAlTiN alternative columnar layer (Sublayer III) and a carbon-containing nano-scale multilayer (Sublayer IV). As discussed in Chapter 3, all the coatings were processed with the same deposition parameters before carbon was introduced (Table 3.2-1). Therefore, it is reasonable to assume that the as-deposited CrAlTiN-0# coating would contain similar sublayers I, II and III as observed in the as-deposited CrAlTiCN-5# coating although Sublayer III is much thicker in the CrAlTiN-0# sample than in the CrAlTiCN-5# coating.

Figure 4.5-10 shows the TEM cross-sectional microstructure of 800 ℃ oxidised CrAlTiN-0# coating, which revealed a four-sublayer structure. Sublayers I, II and III are still distinguishable with a top oxide layer of about 100～120 nm in thickness. Two large holes were found within Sublayer III, which were formed during the FIB thinning process. No obvious crack or delamination was found along the interfaces between these sublayers and between Sublayer I and the substrate.

Figure 4.5-11 shows a bright field TEM micrograph taken from sublayers Ⅰ and Ⅱ. As shown in Fig. 4.5-11a, although sublayers Ⅰ and Ⅱ in the oxidised coating are still columnar structured, the interface between these two layers is blurry and can not be distinguished clearly as compared to the as-deposited coating (Fig. 4.2-9a). The average diameter of columns increased to 200～250 nm, which is around five times as larger as the columns in Sublayer Ⅱ in the as-deposited coating. Figure 4.5-11c shows a selected area diffraction pattern taken from the region "A", which confirmed that the sublayers Ⅰ and Ⅱ are still composed of mixed Cr_2N, Cr, and CrN.

Figure 4.5-12 reveals the microstructure of the Sublayer Ⅲ and the top oxide layer. As can be seen in Figure 4.5-12a, the multilayer feature in Sublayer Ⅲ was preserved with interval thickness of around 5-10 nm even after oxidation at 800 ℃. Many small grains throughout the whole Sublayer Ⅲ can also be observed with the contrast coming from different diffraction conditions of these grains in this case in the TEM bright field mode. Figure 4.5-12b shows an SAD pattern taken from the region of Sublayer Ⅲ, which showed continuous fcc rings.

As shown in Figure 4.5-12a, some fink white lines can be observed at the interface between Sublayer Ⅲ and the top oxide layer as well as along the columnar boundaries in Sublayer Ⅲ, which could be the oxygen diffusion path (see the next chapter). As shown in Figure 4.5-12c, the SAD pattern which contributed from region "A" can be confmed to Al_2O_3 (No. 00-010-0414), Cr_2O_3 (No. 00-038-1479) and TiO (No. 00-088-0117), which is consistent with the XRD results (Figure 4.5-9).

CrAlTiCN-3# sample

In order to investigate the effect of carbon addition on the oxidation resistance of CrAlTiCN coatings, the 800 ℃ oxidised carbon-doped CrAlTiCN-3# sample was also studied using XTEM.

Figure 4.5-13 shows a bright field cross-sectional TEM observation of CrAlTiCN-3# sample, which presented a five-sublayer structure formed on the HSS substrate: a pure chromium interface layer (Sublayer I), a chromium nitrides layer (Sublayer II), a CrAlTiN alternative layer (Sublayer III), a carbon-containing nano-scale layer (Sublayer IV), and a top oxide layer. It can be observed that the microstructure of sublayers Ⅰ, Ⅱ and Ⅲ in the 800 ℃ oxidised CrAlTiCN-3# sample are similar to the corresponding sublayers in the 800 ℃ oxidised CrAlTiN-0# sample (Figs. 4.5-11 & 12). This is in line with the fact that before carbon was introduced, the same deposition conditions were used for all the coatings investigated in the project (see Section 3.2.1).

Figure 4.5-14 shows a bright field TEM micrograph taken from the Sublayer IV and oxide layer of oxidised CrAlTiCN-3# sample. As shown in Figure 4.5-14a, the thickness of the top oxide layer is about 200～230 nm, which is thicker than that (100~120 nm) in the oxidised CrAlTiN-0# sample (Fig. 4.5-12a). The same types of oxides, Cr_2O_3, Al_2O_3, and TiO, were identified from the oxide top layer formed on both oxidised CrAlTiN-0# and CrAlTiCN-3# samples. Therefore, it seems that the doping of carbon will to some extent increase the oxidation rate of CrAlTiN coatings.

Compare with Sublayer Ⅳ in the as-deposited CrAlTiCN-3# coating (Fig. 4.2-12), TEM observations on the oxidation treated Sublayer Ⅳ (Fig. 4.5-14) revealed some microstructural features. Firstly, the interfaces between the nano multilayers in the oxidation treated sublayer became blurred probably because of diffusion at high-temperature. Secondly, the SAD diffraction patterns (Figures 4.5-14b and c) taken from the oxidation treated Sublayer Ⅳ revealed $Cr_{23}C_6$ was formed, which was not found in the Sublayer Ⅳ of the as-deposited CrAlTiCN-3# sample (Figure 4.2-12c). Thirdly, Sublayer Ⅳ (carbon-doped layer) still possessed a single cubic B1 NaCl-type structure as evidenced by the SAD pattern shown in Figure 4.5-14b.

4.5.4 Mechanical properties

The nano-hardness and Young's modulus of oxidised CrAlTiN and CrAlTiCN coatings were measured and the results are plotted as a function of the oxidising temperature in Figure 4.5-15. It can be seen that after oxidation at 300 ℃, the hardness of all the oxidised coatings increased slightly; however, further increase in temperature led to a gradual decrease in hardness for all the oxidised samples. Similar trend was observed for the effect of oxidation temperature on the Young's modulus of the oxidised samples; but it is noted that the Young's modulus of the 900 ℃ oxidised samples was in general slightly higher than that for the 800 ℃ oxidised samples.

The formation of porous oxide layer especially at high temperatures could influence on the hardness and Young's modulus (Figures 4.5-3～4.5-5). It is noticed that in general the

experimental errors increased with increasing the oxidation temperatures, which could be attributed to the increased surface roughness (Fig. 4.5-2).

Dynamic load bearing capacity of 700 ℃ oxidised 0#, 3#, and 5# samples was evaluated by micro scratching under both normal and tangential forces. It can be seen from Figure 4.5-16 that the friction force first increased linearly with the applied normal load before it became fluctuated at a certain load, which is normally defined as the first critical load L_c. Comparison of the friction force-load curves for 0#, 3# and 5# samples revealed that the critical load for these three samples was about 7N, 9N and 11N, respectively (Table 4.5-1).

The scratch tracks produced were studied by SEM observations and the typical damage morphologies are compared in Figure 4.5-17. It can be seen that when the applied normal load was below L_c, the bottom of the scratch track looked smooth without any appreciable damage for all these three samples. During this stage, elastic and plastic deformation occurred in the coating material under the tip. However, some radial cracks were observed along the both edges of the scratch track produced in 0# sample. The length of the smooth scratch track increased in the order of 0#, 3# and 5# samples, which is in good agreement with the L_c values extracted from the friction force-load curves (Table 4.5-1). As shown in Fig. 4.5-17, once the applied load was above L_c, damage of the oxidised coatings occurred. More detailed work was conducted to study the failure modes of these oxidised coating surfaces during scratch.

Figure 4.5-18 shows the typical damage morphologies of 700 ℃/2 hrs oxidised CrAlTiN-0# sample. As shown in Figure 4.5-18b, radial cracks can be clearly seen along the both sides

of the scratch track in the first stage. When the load was further increased to above the critical load L_c, chippings and brittle tensile cracks were observed (Figures 4.5-18c & d). Although obvious cracking and chipping formed during scratching, it seems that the substrate was not exposed, which is evidenced by the fact that only little Fe can be detected even at the end of the scratch track by EDX (Figures 4.5-19, 4.3-20). This implies that the bonding between the coating and the substrate was strong enough to resist such interfacial failure as spallation.

Figures 4.3-21 & 4.3-23 show the scratch tracks of carbon-doped CrAlTiCN-3# & 5# samples under the same scratch conditions. It can be seen from Figs. 4.3-21a & 4.3-23a that no radial cracks but only deformation can be observed in the 3# and 5# samples when the applied load was below the L_c, and buckling has occurred at the critical load; chippings were also found at the last edge of the scratch track, but the size is smaller than that on the 0# coating (Fig. 4.5-18). Figure 4.3-22 & 4.3-24 show the EDX compositional analysis at the end region of the scratch tracks. Only a small amount of Fe could be detected from the scratched surface. This would be an indication of good adhesion between the coatings and the HSS substrate.

Chapter 5: Interpretations and Discussion of Results

5.1 Effect of carbon on coating microstructure

In closed-field unbalanced magnetron sputtering processes, the coatings are deposited in vacuum by condensation from a flux of neutral or ionized atoms of metals, which are ejected mechanically from a target by the impact of ions or energetic neutral atoms [295]. The growth speed, binding state and surface temperature during the deposition of coating depend on the atomic masses of the participating ionized atoms, which are mainly controlled by the voltage and current of targets and thus the ion bombardment of the growing film [296, 297]. In this section, the effect of carbon addition on the microstructure of the carbon-doped CrAlTiCN coatings will be discussed.

5.1.1 Structure & binding state

Crystal structure

As stated in Section 4.2, the carbon-doped CrAlTiCN coatings possessed an fcc structure similar to that of CrN, i.e. B1 (NaCl) structure. As indicated by Shtansky and Loffer [298,299], the Cr-Al-Ti-N-C system has no equilibrium phase. Aluminium and titanium atoms are substituted for chromium atoms in the lattice. These substitutions are attributed to the unbalanced magnetron sputtering ion-plating (MSIP) effect during the deposition. The magnetic and electrical fields and the voltage and current of targets can promote the formation of a metastable (Cr, Al, Ti) (C, N) single phase rather than mixed phases of CrN(C), AlN and TiN(C). Similar substitutions occurred using this MSIP technique has already been demonstrated by other researchers [300,301].

As shown in Figure 4.2-7, the XPS spectra of the Cr-Al-Ti-C-N coatings show the binding energy peak of N1s due to Cr-N bond (Fig. 4.2-7c), but does not show the energy peaks due to Ti-N and Al-N bonds. Similarly, the binding energy peak of C1s due to Cr-C bond can be clearly seen from Fig. 4.2-7b, but no peaks corresponding to Ti-C or Al-C could be detected from the carbon-doped CrAlTiCN coatings. This has further supposed the fact that the carbon containing CrAlTiCN coatings has a similar crystal structure to that of CrN phase with part of Cr being substituted by Al and Ti and part of N with C, i.e. (Cr, Al, Ti) (C, N).

It is noted from Table 4.2-3 that the lattice parameter of the CrAlTiCN coatings is smaller than that of CrN (0.417 nm). Substitution of Cr atoms with Al, Ti atoms and substitution of N atom with C in the B1-NaCl structure of CrN are expected to result in lattice expansion since the atomic radii of the substituting Ti and C atoms are larger than that of Cr and N, as shown in Table 5.1-1. However, a contracted lattice was observed for the carbon-doped CrAlTiCN-1#, 3#, and 5# coatings (Table 4.2-3). A similar trend was also reported by Suzuki et al. [302] that the unit cell parameter of (Cr, Al) N and (Ti, Al) N coatings decrease as the Al to Cr ratio and Al to Ti ratio increased. This decrease in the unit cell parameter with Al is considered to be due to the much smaller ionic radius of Al than Cr and Ti. In addition, the deviations from stoichiometric composition of the (Cr, Al, Ti) (C, N) phase, i.e. with 50 at% (N, C) and 50 at% (Cr, Al, Ti), may have resulted in unoccupied atomic lattice positions, thus distorting the entire lattice and leading to reduction in the lattice parameter of the coatings. Furthermore, it may be also related to the metastable phase formed during the coating process [303]. Therefore, the observed seemingly abnormal lattice contraction could be attributed to the smaller ionic radius of Al and the non-equilibrium nature of magnetic sputtering.

Binding state of C

As observed in Section 4.2.2, when increasing the carbon content, the abundant carbon atoms start to build a disordered and irregular phase. The C-C bonding revealed by XPS (Figure 4.2-7b) with a bonding energy of 284.6 eV should be corresponded to C sitting in a sp^2 dominated graphitic environment.

The electron energy loss spectroscopy (EELS) technique has been employed to provide complementary information on the hybridization state of carbon atoms in the newly developed CrAlTiCN coatings. Figure 5.1-1 shows the near-edge fine structures as observed on the C-K edge after background subtraction and deconvolution from the low-loss part for CrAlTiCN-5# coating. It can be seen that the fingerprints observed in the C-K edge $(1s \rightarrow \pi^*)$ clearly correspond to the π-bonding structure of graphite. Attention should be paid to the $1s \rightarrow \pi^*$ transition peak, lying at the bottom of the conduction band around 285 eV, which is characteristic of sp^2-hybridisation of carbon atoms. The typical feature has also been discovered by other researchers [304,305,306] in carbon based coatings containing sp^2-hybridisation.

In summary, the (Cr, Al, Ti) (C, N) phase has an fcc B1-NaCl structure which is similar to that of CrN. The addition of carbon into CrAlTiN coatings will not cause appreciable change in their crystal structure but carbon will partially substitute N when the carbon content is below its solubility in the coatings; excessive carbon would form a phase dominated by a sp^2 C-C bonding when carbon content exceeds its solubility in the (Cr, Al, Ti) (C, N) coatings.

5.1.2 Formation of nano-composite coatings

The concept of multilayered coatings has been recognised to be useful tool for tailoring and adjusting the properties of thin coatings according to specific application requirement. This is mainly because the multilayer structure can enhance the performance of coatings by stopping or slowing down the propagation of cracks [307]. As evidenced in cross-sectional TEM results (Figures 4.2-10 ～ 4.2-13), nano-scale multilayers have been formed in sublayers III and IV of the newly designed carbon-doped CrAlTiCN coatings.

The formation of such nano-scale multilayers is facilitated by the development of modern PVD technologies. In a typical closed-field unbalanced magnetron sputtering system, such as the UDP 450 system used in this work, targets stand vertically along the circular chamber wall while the substrates mounted on the sample carousel rotate around the central axis of the chamber (three-fold holder rotation) and pass the targets one by one at a chosen distance (Figures 3.2-2 and 3.2-3). The landing of sputtered atoms is interrupted in-between the targets and ion impingement may fluctuate to a large extent [12]. For magnetron sputtering, the mixture of Ar and N_2 gases occurs in the plasma everywhere inside the chamber and provides some of the species for deposition that continuously reach the growing film front from all angles and at any position. The thickness of each single layer is based on the target power, deposition rate, distance between targets and samples, and substrate rotation speed. The influence of a specific rotation on the multilayer structure has been studied by Panjan et al. [308].

As shown in Figures 4.2-10～4.2-14, the multilayers were perpendicular to the coatings growth direction and the inter-multilayer spacing was almost constant, indicating that the

isostructured nano-scale multilayer was formed. This structure, which has tremendous interface density, makes interfacial and surface energies contribution predominant. This is supposed to encourage the stabilization of metastable structures and increase the solubility limit in immiscible system, thus enhancing the mechanical or tribological properties [309,310].

In addition, waviness was observed in the multilayers (Figure 5.1-2) and the further deposition of the multilayers did not result in the enhancement of the waviness. The closed-filed unbalanced magnetron can supply the efficient and highly energetic sources form [311]. However, the relatively low deposition temperature and hence the low adatom mobility on the coating surface did not promote the formation of a flat surface. Therefore, wavy topography was formed in addition to the columnar growth of the coating. The similar feature was also observed by Gubisch et al. in the growth of WC/C multilayers [312].

Close observation of Sublayer III revealed many fine-grained columns (Figure 4.2-10d) which grow perpendicularly to the substrate but do not extend through the entire thickness of the coating. This might be defined by low coating temperature compared to melting point and high-energetic bombardment of the growing coatings [313,314,315].

5.1.3 Growth model

Due to an appropriate choice of the deposition conditions, the stability of the nanocomposite coatings consisting of fcc (Cr, Al, Ti) (C, N) phase and amorphous carbon seems to be fairly high. Although a varying quantity of carbon was introduced in Sublayer IV of carbon-doped

CrAlTiCN 1#-5# coatings, no trace of crystalline carbides could be identified in the SAD patterns taken from 1#, 3#, and 5# samples (Figures 4.2-10~4.2-13). The construction of the nanocomposite is carbon content dependent, the higher the carbon content, the lower the crystalinity and the weaker the preferred orientation of the coatings. A similar relationship was also found in the Ti-Al-N-C coating systems [316]. This phenomenon is most likely related to the position of the carbon atoms within the coating structures during film growth procedures.

On the basis of the microstructural evolution of these carbon-doped CrAlTiCN coatings, a growth model is suggested as in Figure 5.1-3. First, an N-deficit is evident from the (Cr+Al+Ti)/N ratio of the carbon-free nanocrystalline fcc (Cr, Al, Ti) N coating (Table 4.2-2, 0# sample). When a low concentration of carbon, such as CrAlTiCN- 1# sample, was sputtered on to the coating surface, the carbon was resolved in the fcc (Cr, Al, Ti) N phase, resulting in the formation of a metastable single fcc (Cr, Al, Ti) (C, N) phase (Figure 5.1-3a). The nanoscale multilayer period favours the necessary interdiffusion of carbon to (Cr, Al, Ti) N phase.

However, when the total amount of carbon and nitrogen exceeds 50 at%, the coating is not in an N-deficit, such as in CrAlTiCN-3# samples, carbon atoms can start to build nanoclusters or agglomerates as a thin interlayer (Figure 5.1-3b) in addition to being resolved into the (Cr, Al, Ti) (C, N) phase.

When increasing the carbon content further, the size of carbon clusters and the thickness of amorphous carbon layers increase. The growth of (Cr, Al, Ti) (C, N) crystals is interrupted

by these carbon nanolayers, thus decreasing the grain size of (Cr, Al, Ti) (C, N) further (Figure 5.1-3c).

5.2 Mechanical behavior

Enhancing the capabilities of coatings in different applications should start with an analysis of reasons for both positive and negative results. Optimized wear behaviour, is not necessarily achieved with the used of the hardest coating materials, but also depends on the elastic modulus, adhesion, chemical and toughness, the load-bearing capacity and sometimes other physical attributes.

The general mechanical properties of bench-mark CrAlTiN coating and carbon-doped CrAlTiCN nanocomposite coatings have been summarised in Figure 4.3-2 and Tables 4.3-1 and 4.3-2. In general, an increase in carbon content leads to decreasing in the nano-hardness, elastic modulus, and micro mar resistance but increase in toughness of the nanocomposite coatings (Figure 4.3-3).

5.2.1 Hardness and Young's modulus

The deposition parameters significantly influence the chemical composition, carbon amorphous environment, the interconnectivity of the amorphous network and the final mechanical properties of the carbon-doped CrAlTiCN coatings. A softening trend with increasing carbon content has been observed in the present CrAlTiCN coatings, and the similar trend was reported in TiAlNC coatings deposited by the same magnetron sputtering PVD technique [317].

It can be seen from Figure 4.3-2 that the addition of a small amount of carbon into the CrAlTiN coating (CrAlTiCN-1# sample) led to marginal decrease in hardness only; however, significant decrease in hardness occurred once the total amount of carbon and nitrogen exceeded 50 at% for CrAlTiCN-2# and CrAlTiCN-3# samples; but further increase in carbon content caused very mild reduction in hardness for CrAlTiCN-4# and CrAlTiCN-5# samples.

The above change in hardness could be related to the evolution of the microstructure of the carbon-doped coatings as a function of the carbon content in the coatings. As discussed in the preceding section, when the total amount of nitrogen and carbon is below 50 at%, the doped carbon is dissolved in the solid solution of (Cr, Al, Ti) (C, N) phase. This has led to marginal decrease in hardness most probably because of the relatively weak affinity between Cr and C than between Cr and N [318].

Once the carbon content exceeds 50 at%, amorphous carbon clusters and thin layers form in between nanocrystalline (Cr, Al, Ti) (C, N). This will reduce the cohesion between nanocrystalline (Cr, Al, Ti) (C, N) grains because of the formation of relatively weak phase boundaries between the nanocrstalline and amorphous phases [319]. This is evidenced by a much lower hardness of CrAlTiCN-2# as compared with CrAlTiCN-1#. Further increase in carbon content significantly increased the volume fraction of the amorphous phase and the inter-spacing between the nanocrystalline (Cr, Al, Ti) (C, N) compounds. Consequently, the coating hardness decreased significantly from 24.5 GPa for bench-mark CrAlTiN-0# to 18.2 GPa for CrAlTiCN-3#. The similar hardness values for CrAlTiCN-4# and CrAlTiCN-5#

could be explained by the fact that their microstructure has been dominated by amorphous carbon phase embedded by nanocrystalline (Cr, Al, Ti) (C, N) particles.

This softening trend with increasing carbon content in the CrAlTiCN coatings agrees well with previous observations [320, 321, 322]. For example, Stueber et al. have reported that in the Ti-Al-N-C system, the hardness of the coatings decrease with the carbon content because of the formation of amorphous phase. However, Veprek has proposed a hardening mechanism for the coating based on the ternary Ti-Si-N system and attributed the superhardness to the formation of a thin amorphous phase of α-Si_3N_4 between the nanocrystalline TiN grains (i.e. formation of n-TiN/ α-Si_3N_4 nanocomposite coatings). The different roles of amorphous phase could be attributed to the difference in the nature of the amorphous phases formed in these two different systems. In the present work, the amorphous carbon phase has a sp^2 binding state and is in the graphitic environment and therefore low-hardness is expected. The imperative for coating tribologists has been, for many years, the development of ever harder (and stiffer) coatings; however, it is increasingly recongised that except for abrasive wear, hardness is not necessarily the prime requirement for wear resistance, which will be discussed in detail in the next section.

As has been shown in Figure 4.3-2, in general the Young's modulus (E) and hardness (H) follow a similar trend with the carbon content. This is understandable because the formation of sp^2 amorphous carbon would reduce the stiffness of the carbon-doped coatings. However, quantitative calculation has revealed that both the H/E ratio (which is related to the elastic strain to failure) and $H^3/E*^2$ (related to the resistance against plastic deformation) (where E* $=E/(1-v^2)$ is the effective Young's modulus and v is the poisson's ratio) slightly decreased

with increasing the carbon content (Table 5.2-1). This implies that more elastic/plastic deformation could occur to the carbon-doped CrAlTiCN coatings before they fracture, which is related to the toughness [323].

5.2.2 Cracking and toughness

In essence, toughness is the ability of a material to absorb energy during deformation up to fracture. According to this definition, toughness encompasses energy required both to create the crack and to enable the crack to propagate until fracture. It is difficult to directly measure the toughness of thin coatings using conventional methods for bulk materials, and hence indentation is most widely used for the assessment of thin film toughness.

As reported in Section 4.3.2, micro-indentation method has been used to study the effect of carbon addition on the toughness of CrAlTiCN coatings. Ring cracks were observed for both CrAlTiN and carbon-doped CrAlTiCN coatings (Figure 4.3-3). However, it has been noted that although radial cracks were observed at each corner of the indentation in the bench-mark CrAlTiN coating (Fig. 4.3-3a), the number and length of the radial cracks formed in the carbon-doped CrAlTiCN coatings were reduced with the carbon (Figures 4.3-3b to 4.3-3e) and almost no appreciable radial cracks could be found for CrAlTiCN-5# coating which contained the highest carbon content (Fig. 4.3-3f).

Marshall and Lawn [324], Anstis et al. [325] developed a quantitative relationship between the toughness K_{1c} and the radial crack dimension C as follows:

$$K_{1c} = \chi \left(\frac{E}{H} \right)^{1/2} \frac{P}{C^{3/2}} \qquad (5.2-1)$$

where E and H are the Young's Modulus and hardness of the material. For Berkovich and Vickers indenters, $\chi=0.016$.

Notwithstanding the fact that quantitatively Eq. 5.2-1 is not fully applicable to the present results since the length of the radial cracks are much shorter than the diagonals of the indentations, the equation indicates that the toughness of hard coatings increases when the radial length reduces. It thus follows that the toughness of the carbon-doped CrAlTiCN coatings is higher than that of the bench-mark CrAlTiN coating since the radial cracks are shorter in the former than in the latter.

It can be deduced from Eq. 5.2-1 that the toughness of a thin coating is, to some extent, also related to the E/H ratio of the coating. As discussed earlier, the H/E ratio reduced (hence the E/H ratio increased) with increasing the carbon content in the CrAlTiCN coatings (Table 5.2-1). It is known that the E/H ratio is a measure of plasticity and increased E/H promotes plastic deformation [342,343]. Therefore, the energy dissipation through plastic deformation can release the elastic energy stored, thus delaying the formation of cracks (i.e. fracture). Hence, the enhanced toughness of the carbon doped CrAlTiCN coatings could be partially attributed to the increased E/H ratio.

From microstructure point-of-view, the toughening of the developed nanocomposite coatings can be achieved via two different scales, namely by restraining the formation of columns on a microscale and through manipulating the nanostructure on a nanoscale [326].

First, it has been frequently observed that columnar boundaries act as sites for crack initiation and preferential crack propagation [344, 345]. In the present research, the microstructure of the coatings changed by doping carbon from columnar structures (as schematically shown in Figure 5.1-3a) to multilayer structures with amorphous carbon (Figures 5.1-3b and 5.1-3c). Therefore, the formation and propagation of cracks along the columnar boundaries can be reduced; the amorphous carbon phase could also eliminate crack initiation and help to divert and arrest macro-crack development [327, 328]. Consequently, enhanced toughness by carbon doping is expected.

Second, the carbon-doped CrAlTiCN coatings developed from this research is nano-multilayer structured especially for medium and high carbon-doped coatings. As introduced in Section 2.2.3.3, multilayers can play a significant role in controlling the residual strain and the stress within the coatings and enhancing their toughness by allowing layers or phases to slide over each other when they are deflected under load. In addition, the nanostructured multilayer coatings generate a high density of interfaces to assist in crack deflection and termination of crack propagation. In a homogenous single layer coating, the cracks will easily propagate perpendicular to the substrate along the columnar grain contrast; however, these cracks in a multilayer coating will change their propagation direction at layer interfaces.

Finally, the enhanced toughness of the carbon-doped CrAlTiCN coatings has also been supported by V-shaped cross-sectional profiles of the indentations shown in Figure 4.3-4. Although the ring cracks formed in CrAlTiN coating (Figure 4.3-3a) and the carbon-doped CrAlTiCN coatings (Figures 4.3-3c and 4.3-3f) seem to similar from the surface images, it

is clear from the cross-sections of the indentations (Figure 4.3-4) that the cracking is much more severe in the CrAlTiN coating than in the carbon-doped CrAlTiCN coatings as evidenced by the zigzags appearing on the side lines of the V-shaped indentation.

5.3 Tribological behaviour

The tribological process takes place as the two surfaces are moving in relation to each other, and both physical and chemical changes occur in accordance with the physical and chemical laws with respect to the input data. As a function of time, the tribolgical process causes changes in both the geometry and the material composition and results in friction and wear [329]. In this section the effect of carbon addition on the tribolgical characteristics in terms of friction and wear of the newly developed CrAlTiCN coatings is discussed based the results present in Section 4.4.

5.3.1 Friction coefficient

As described in Section 4.4, the doped carbon can effectively reduce the coefficient of friction of the developed CrAlTiCN coatings. As listed in Table 4.4-1, the coefficient of friction can be reduced from 0.655 for the bench-mark CrAlTiN (0# without carbon) to as low as 0.350 for the carbon-doped CrAlTiCN-5# coating. The friction-reduction behaviour of the nano-composite coatings can be mainly attributed to the tribological characteristics of the amorphous carbon phase formed in the carbon-doped nanocomposite CrAlTiCN coatings.

It is generally accepted that the low friction of most carbon coatings is largely due to the fact that these materials are chemically inert and consequently they exert very little adhesive force during sliding against other materials [69]. Therefore, carbon containing coatings could more or less reduce the adhesive component of friction. In addition, alike sp^2 dominated carbon-based coatings have low shear strength.

According to classic friction theory, during dry sliding, the force F is required to displace an asperity of the softer material with shear strength S on a real area of contact A [330] while the applied W is supported by the real area of contact with a compressive strength of P:

$$F = AS \qquad (5.3\text{-}1)$$

$$W = AP \qquad (5.3\text{-}2)$$

According to Amonton's friction law, the coefficient of friction f is defined by the ratio of friction force F to the applied load W [348],

$$f = \frac{F}{W} = \frac{S}{P} \qquad (5.3\text{-}3)$$

It can be deduced from Eq. 5.3-3 that a material with a low shear strength and a high compressive strength should exhibit a low friction when contact with a counterpart during sliding. This tribological principle has been successfully used to explain the low-friction behaviour of such lamellar, low shear strength solid lubricant materials as graphite and MoS_2 [331].

Basically, carbon exists in the present nanocomposite CrAlTiCN coatings as an amorphous network. This network consists of strongly cross-linked carbon atoms with mainly graphite-like bonds (Figures 4.2-7 and 5.1-1). Therefore, it is reasonably assumed that alike graphite, the amorphous carbon in the nanocomposite CrAlTiCN coatings should have low shear strength. As discussed in Section 5.1, the amount of the amorphous phase in the nanocomposite coatings increased with the doped carbon, and therefore the friction coefficient of the nanocomposite CrAlTiCN coatings would reduce with increasing the carbon content.

In order to advance the understanding of the friction-reduction mechanism involved, cross-sectional TEM analysis of the wear surface has been conducted. Focused ion beam (FIB) was used to extract a cross-sectional TEM thin foil from the worn surfaces. Figure 5.3-1 shows the SEM wear track morphologies of the tested CrAlTiCN-5# sample and FIB sampling position.

The bright-field TEM micrographs of cross section of the wear surface on tested CrAlTiCN-5# sample are shown in Figure 5.3-2. The cross section of the worn surface, as shown in Figure 5.3-2a, comprises (from the bottom to the top) CrAlTiCN layer, a thin tribofilm layer, and a dark Tungsten protective layer. Closer inspection (figure 5.3-2b) revealed a bright feature-less layer on the top of the nano-scale multilayered CrAlTiCN coatings. High resolution TEM (Figure 5.3-3) and EDX compositional analysis (Figure 4.4-5) indicated that the tribofilm is amorphous with a thickness ranging from 50 to 100 nm, which contains a high amount of oxygen and carbon. It is believed that this thin amorphous tribofilm might have played an important role in reducing the friction of the carbon-doped CrAlTiCN coatings.

5.3.2 Wear resistance

In view of their potential tribological applications, the wear properties of the bench-mark CrAlTiN and carbon-doped CrAlTiCN coatings have been investigated under three different motion conditions: unidirectional sliding, reciprocating sliding and fretting.

5.3.2.1 Carbon effect

As has been shown in Figure 4.4-1a, when tested at room temperature under unidirectional sliding conditions, the wear volume lost of CrAlTiCN coatings was found to decrease with increasing their carbon content; but experimental results have also indicated that the hardness of the CrAlTiCN coatings reduced with the carbon content. It is thus of interest to note that the wear resistance of the carbon-doped CrAlTiCN coatings increased with decreasing their hardness. Furthermore, coarse and deep parallel grooves have been observed for the bench-mark CrAlTiN coating (Figure 4.4-2) and low-carbon CrAlTiCN-1# coating (Figure 4.4-3), indicative of severe abrasive wear; on the other hand, relatively smooth wear tracks with shallow and fine grooves were formed in high-carbon, low-hardness CrAlTiCN-5# coating (Figure 4.4-5).

Clearly, the above abnormal results cannot be explained using classical abrasive wear theory. This is because, as discussed in Chapter 2, the abrasive wear resistance of a surface mainly depends on its hardness. In the present study, the hard bench-mark CrAlTiN-0# coating and the low-carbon CrAlTiCN-1# coating showed more severe abrasive wear than the high-carbon, low-hardness CrAlTiCN-5# coating.

When a WC-Co counterface and the coating come into contact, the contact takes place only on high asperities and the real area of contact is a small fraction of the apparent area of contact. Figure 5.3-4 illustrates the two-body and three-body contact of tough surfaces [332]. During sliding, the collision of the asperities from the wearing surfaces results in their fragmentation especially for the hard bench-mark CrAlTiN coating because of its brittleness as discussed in Section 5.2.2. The hard and brittle wear debris trapped at the interface

between the two contact surfaces will cause severe abrasive wear to the WC-Co counterface and the coating surface. Because the WC-Co counterface is in constant contact with the coating surface during unidirectional sliding and the hardness of the WC-Co is very similar to that of CrAlTiN coating, rapid wear is expected to occur to the WC-Co counterball. Once the WC-Co counterface is damaged, it will in turn cause severe abrasive wear to the coating surface.

In the contrast, the high-carbon CrAlTiCN coating are softer (Section 5.2.1) and tougher (Section 5.2.2) with a much higher plasticity (Table 5.2-1) as compared with the low-carbon CrAlTiCN coatings. Therefore, less wear debris will form during the collision of the asperities from the two contact surfaces during sliding because of the reduced brittleness of the high-carbon CrAlTiCN coatings. Moreover, the high-carbon CrAlTiCN coatings are much softer than the WC-Co counterface and therefore it can only cause mild, if any, abrasive wear to the WC-Co counterface. Furthermore, it is known from the previous discussion that the amorphous carbon wear debris could act as a solid lubricant rather than abrasives. Consequently, the high-carbon, low-hardness CrAlTiCN coatings possess a better wear resistance than the low-carbon high-hardness counterparts.

5.3.2.2 Unidirectional vs reciprocating sliding wear

As has been discussed above, the wear resistance of the carbon-doped CrAlTiCN coatings increased with the carbon content under unidirectional sliding conditions. However, as shown in Figure 4.4-1b, under reciprocating sliding conditions no difference in wear resistance could be observed for the CrAlTiCN coatings doped with different levels of

carbon. The experimental results indicate clearly that the test conditions have a strong effect on the performance of the coatings.

As shown in Table 5.3-1, the material of the counterball, contact pressure and contact area are same for both unidirectional and reciprocating sliding tests. Therefore, the difference in the effect of carbon on the wear of the carbon-doped CrAlTiCN coatings could be attributed to the different types of motion. Indeed, it is recognised that wear is not an intrinsic but a systems property [333] and the behaviour of materials in wear situations depends on the type of motion, the levels of stresses and the nature of environment [334].

During unidirectional sliding tests, since the wear track is a closed circle, the wear debris formed is confined within the wear track, whereas in reciprocating motion, detached material are pushed towards both end regions of the wear track (Figures 4.4-6~4.4-8).

As discussed in the preceding section, wear debris has played an important role in determining the wear behaviour of the carbon-doped CrAlTiCN coatings. When sliding against a WC-Co counterface, hard wear debris from the low-carbon CrAlTiCN coatings can act as hard abrasives to damage the WC-Co counterface, which in turn cause severe abrasive wear of the hard and brittle CrAlTiCN coatings. However, such detrimental effect of hard wear debris could be reduced during reciprocating sliding wear since such wear debris is pushed towards both ends of the wear track. Similarly, the benefit effect of soft, self-lubricating carbon debris is also reduced during reciprocating sliding wear because such carbon wear debris is pushed towards both ends of the wear track. Hence, the combination

of the above effects may have led to the similar wear resistance of the CrAlTiCN coatings under reciprocating sliding wear.

5.3.2.3 Fretting wear behaviour

The fretting wear properties of carbon-doped CrAlTiCN nanocomposite coatings at room temperature and 350 ℃ were investigated in the present study and the results have been reported in Section 4.4.3. It is of interest to find that when tested at room temperature, the fretting wear of these carbon-doped CrAlTiCN nanocomposite coatings increase with carbon content; however, when tested at 350 ℃ the opposite trend was observed. Clearly, the test temperature has played an important role in the fretting wear of the carbon-doped CrAlTiCN nanocomposite coatings.

It can be found by comparing Fig. 4.4-9a with Fig. 4.4-1 that the effect of carbon on the fretting wear of the carbon-doped CrAlTiCN nanocomposite coatings at room temperature is, to some extent, similar to that on the unidirectional wear of these coatings. Therefore, similar discussion given in Section 5.3.2.1 could be used to understand the effect of carbon content on the fretting wear of these carbon-doped CrAlTiCN nanocomposite coatings at room temperature.

It is well-known that fretting wear is not a basic but a complex wear process involving adhesion, abrasive and oxidation. The carbon-doped, lubricous nanocomposite coatings could reduce the friction and abrasive wear between the fretting surfaces. Consequently, the fretting wear of the carbon-doped CrAlTiCN nanocomposite coatings was reduced when increasing the carbon content. However, it is also noted that the effect of the doped carbon

on the fretting wear is not as significant as on the unidirectional sliding wear of the carbon-doped CrAlTiCN nanocomposite coatings (Figs. 4.4-9a vs. 4.4-1a). This is mainly because, as discussed in Section 5.3.2.1, the effect of the doped carbon on the sliding wear of the carbon-doped CrAlTiCN nanocomposite coatings also depends on the type of motion. While the carbon-rich wear debris can retain in the wear track during unidirectional sliding, the wear debris formed during fretting is normally pushed to the both ends of the wear track because fretting is essentially a reciprocating process. However, the amplitude of fretting is normally much smaller than that for conventional reciprocating sliding. Therefore, some carbon-rich wear debris may still be trapped in the fretting surfaces although some would be removed away by the reciprocating action.

However, the beneficial effect of carbon on the fretting wear of the carbon-doped CrAlTiCN nanocomposite coatings becomes detrimental at elevated temperatures. As has been shown in Figure 4.4-9b, the fretting wear of these carbon-doped CrAlTiCN nanocomposite coatings increases with the carbon doped when tested at 350 ℃. This should be related to the oxidation of the carbon-doped CrAlTiCN nanocomposite coatings. Firstly, some researchers have reported that amorphous carbon films will lose their superior lubricous characteristics at elevated temperatures [353, 354]. It is thus reasonable to assume that when tested at 350 ℃, the desirable lubricous features of the amorphous carbon within the nanocomposite coating diminished or disappeared. Secondly, it can be seen from Figure 4.5-15a that the hardness of these carbon-doped coatings at 300 and 400 ℃ decreased with the carbon content. Therefore, it is expected that this will increase the abrasive wear component of the fretting wear as fretting wear is a complex wear process involving adhesion, abrasion and oxidation.

Another interesting observation on the fretting behaviour of the carbon-doped CrAlTiCN nanocomposite coatings is that, except for CrAlTiCN-5# sample, more fretting wear occurred when tested at room temperature than 350 ℃ (Figure 4.4-9). This difference could be attributed to the beneficial effect of oxidation at elevated temperature because it is well-known that oxide films can reduce friction and adhesion between the fretting surfaces. This is supported by the high oxygen measured from the 350 ℃ tested surface (58.71 at% O in Fig. 4.4-16) than from room temperature tested one (47.55 at% in Fig. 4.4-12).

5.3.2.4 Comparing among CrAlTiN, CrAlTiCN and GLC coatings

As reviewed in Chapter 2, CrAlTiN coatings are characterised by high hardness and wear resistance but high coefficient of friction; on the other hand, carbon-based coatings have high wear resistance and low coefficient of friction but poor performance at elevated temperatures. Therefore, it is worthwhile to compare the tribological properties of the newly developed carbon-doped CrAlTiCN nanocomposite coatings with bench-mark CrAlTiN and amorphous graphite-like carbon (GLC) coatings. Table 5.3-2 summarises the tribological properties of these three types of coatings in terms of coefficient of friction and wear volume lost measured by pin-on-disc unidirectional sliding wear at room temperature and fretting wear at room temperature and 350 ℃.

It can be seen that when tested at room temperature, the GLC coating can exhibit the best tribological properties under both unidirectional sliding and fretting wear conditions among these three types of coatings. This is mainly because GLC coatings share many of the properties of graphite: a significant proportion of sp^2 bonding, chemical inertness and low-

friction; but unlike graphite, GLC coatings are amorphous and have a much higher hardness and wear resistance than graphite.

However, when fretted at 350 ℃, both CrAlTiN and carbon-doped CrAlTiCN nanocomposite coatings outperformed the GLC coating. This is largely because the amorphous carbon films could not retain their superior characteristics at a higher temperature because of the irreversible changes in the structure, which limits the application of these films at high temperature [335, 336]. In order to further understand the poor wear performance of the GLC coating at 350 ℃, thermal stability tests at 350 ℃ for the same dwell time have been carried out. Figures 5.3-5 and 5.3-6 show the surface morphology and EDX compositional analysis of as-deposited and oxidised GLC coating respectively. It can be seen that the as-deposited coating is quite smooth and dominated by C and Cr with a very small amount of O (Fig. 5.3-5). After thermal stability tests at 350 ℃, flake-like loose oxide layers with cracks were formed and the GLC coating was destroyed as evidenced by the high content of Fe from the steel substrate (Fig. 5.3-6). This is also strongly supported by the rapid increase in the surface roughness (Fig. 4.5-2). Clearly, GLC coatings will easily oxidise and loss their attractive tribological properties at high temperature.

The experimental results shown in Table 5.3-2 clearly indicate that although the fretting wear of the newly carbon-doped CrAlTiCN nanocomposite coatings at room temperature is slightly higher than that of the GLC coating, the former possesses a much lower fretting wear than the latter at 350 ℃. Therefore, newly carbon-doped CrAlTiCN nanocomposite coatings can significantly outperform the GLC coating at elevated temperatures.

Table 5.3-2 also demonstrates that compared with the bench-mark CrAlTiN coating, the newly carbon-doped CrAlTiCN nanocomposite coatings possess better tribological properties in terms of significantly reduced friction and wear under both unidirectional sliding and fretting wear at room temperature.

In short, at room temperature the newly carbon-doped CrAlTiCN nanocomposite coatings can outperform the bench-mark CrAlTiN coating, in particular the significantly reduced coefficient of friction; at elevated temperature the newly carbon-doped CrAlTiCN nanocomposite coatings are superior to GLC coatings.

5.4 Oxidation behavior

Some engineering components are subjected to elevated temperature in service and some components (such as cutting tools) suffered from friction heating, particularly at high sliding speeds under larger contact loads. Therefore, thermal stability and oxidation behaviour are important properties for the coatings developed for tribological applications to this end, the thermal stability of the carbon-doped CrAlTiCN nanocomposite coatings are compared with CrAlTiN and GLC coatings and its oxidation mechanism is discussed in this section.

5.4.1 Thermal stability

As shown in Figures 4.5-1, 4.5-2, and 4.5-15, when annealed in air at temperatures up to 400 ℃ for 2h, no significant changes in the surface roughness and hardness occur to all carbon-doped nanocomposite CrAlTiCN as well as the bench-mark CrAlTiN coatings. On the other hand, the surface roughness of GLC coating increases rapidly when oxidised at temperature above 300 ℃. Clearly, the thermal stability of the newly developed carbon-doped nanocomposite CrAlTiCN coatings is similar to that of bench-mark CrAlTiN coating but much better than the GLC coating.

When increasing the oxidising temperatures from 400 to 700 ℃, the surface roughness of all carbon-doped nanocomposite CrAlTiCN and CrAlTiN coatings increased (Figure 4.5-2) and the surface hardness (Figure 4.5-15) decreased gradually with the oxidation temperature. This implies that the carbon-doped nanocomposite CrAlTiCN coatings may have similar

thermal stability to the bench-mark CrAlTiN coating within this temperature range. This is supported by the fact that after oxidation at 700 ℃ for 2h the scratch critical load of the carbon-doped 3# and 5# CrAlTiCN coatings is slightly higher than that of the bench-mark CrAlTiN coating.

Differences in surface oxide layer thickness were observed for the bench-mark CrAlTiN coating and the carbon-doped CrAlTiCN coatings when oxidised under temperatures at 800 ℃ or above. After 800 ℃/2h annealing in air, the thickness of the surface oxide film formed on the CrAlTiCN-3# coating (Figure 4.5-14a) is 200～230 nm, which is twice as thick as that (100～120 nm) formed on the bench-mark CrAlTiN coating (Figure 4.5-12a); similarly, after 900 ℃/2h annealing in air, the thickness formed on the bench-mark CrAlTiN coating is about 0.5 μm (Fig. 4.5-3), which is about half that (around 1 μm) formed on CrAlTiCN-5# coating (Fig. 4.5-5). This implies that the thermal stability of the newly developed carbon-doped CrAlTiCN coatings may be inferior to the bench-mark CrAlTiN coating at temperatures above 800 ℃.

The thermal stability of the carbon-doped CrAlTiCN coatings also depends on their carbon content. For example, when oxidised at 1000 ℃ the surface roughness of CrAlTiCN-5# coating increased dramatically (Fig. 4.5-2) and delamination of the surface coating occurred as evidenced in Figures 4.5-1c, 4.5-5c and 4.5-9c. Clearly, the CrAlTiCN-5# coating cannot be used at temperatures above 900 ℃.

5.4.2 Oxidation mechanism

As discussed in Section 5.1.1.1, because of the unbalanced magnetic field and intensive deposition conditions, aluminium and titanium atoms are substituted for chromium atoms in the lattice of CrN phase to form a metastable (Cr, Al, Ti) (C, N) single phase rather than a mixture of phases of CrN(C), AlN and TiN(C) for the carbon-doped CrAlTiCN coatings. The XRD and cross-sectional TEM analyses have revealed that oxides Cr_2O_3, TiO and Al_2O_3 were formed during the oxidation of these carbon-doped CrAlTiCN coatings in air. Therefore, the following reaction might be suggested for the oxidation of these carbon-doped CrAlTiCN coatings:

$$2(CrAlTi)(CN) + 6O_2 \rightarrow Cr_2O_3 + Al_2O_3 + 2TiO + N_2 \uparrow +2CO_2 \uparrow$$
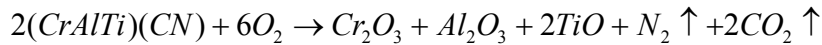
However, these oxides were formed gradually at different temperature. As evidenced in Figure 4.5-9, Al_2O_3 phase was detected from 700℃ oxidised samples while Cr_2O_3 and TiO were found from the samples oxidised at temperatures at 800 ℃ and above. This could be attributed the difference in affinity of oxygen to aluminium, chromium and titanium, which could be estimated by the standard Gibbs free energy of formation of these oxide phases:

$$\Delta_f G^0_{Cr2O3} = -1012411 + 215.37T(J/mol) \text{ for } Cr_2O_3 \text{ [337]}$$

$$\Delta_f G^0_{Al2O3} = -1682900 + 323.24T(J/mol) \text{ for } Al_2O_3 \text{ [338]}$$

$$\Delta_f G^0_{TiO} = -542950 + 100.5T(J/mol) \text{ for } TiO \text{ [339]}$$

The standard Gibbs free energy for formation of Al_2O_3, Cr_2O_3 and TiO [340] at 700℃ are calculated to be -1368.4 KJ/mol, -802.9 KJ/mol, and -444.9 KJ/mol, respectively, and therefore Al_2O_3 would preferably form. However, a continuous Al_2O_3 layer did not form, which means that the Al activity in CrAlTiCN coatings is not high enough in the present work (Table 4.2-2). When oxidised at 800℃ or above, Cr_2O_3 and TiO were formed but the former may dominate in view of its high percentage and thus its activity.

The good thermal stability of the carbon-doped CrAlTiCN coatings with low-to-medium carbon content under oxidative conditions observed in this work could be mainly attributed to the abundant Cr_2O_3. This stable oxide film can act as an oxygen diffusion barrier, thus protecting the coatings underneath from oxidation at temperatures below 900 ℃. This is in line with the findings by other researchers [341, 342] that Cr content determined the oxidation resistance of the coating and 30 at% Cr was found to be optimal. In the present research, despite of different carbon amounts used, the Cr content is still more than 30 at% in all the coatings (Table 4.2-2).

5.4.3 Carbon effect

Although all designed CrAlTiCN coatings showed good oxidation resistance in general, the carbon content still has a strong effect on the oxidation behaviour. The CrAlTiCN-5# coating, which has been doped with the highest level of carbon in the present research (Table 4.2-2), was completely destroyed at 1000 ℃ (Figure 4.5-9c).

As has been schematically shown in Figure 5.1-3, the microstructure of the designed carbon-doped CrAlTiCN coatings depends on the amount of carbon doped. When doped with low-to-medium level of carbon, the microstructure consists mainly of alternating layers of amorphous carbon and (Cr, Al, Ti) (C, N) crystals. When oxidised in air, dense and stable oxide film dominated by Cr_2O_3 formed, which stops or retards the inwards diffusion of oxygen and thus protect the underneath coating from oxidation. However, the microstructure of the high-carbon CrAlTiCN-5# coating is dominated by amorphous carbon with (Cr, Al, Ti) (C, N) phase imbedded into the carbon matrix. Therefore, it is impossible to form a continue oxide film to act as an oxygen diffusion barrier. In addition, the phase boundaries between the (Cr, Al, Ti) (C, N) and amorphous carbon can serve as the short-circuit for oxygen diffusion. Consequently, rapid oxygen diffusion and severe oxidation occur at high-temperature.

Furthermore, the formation of amorphous carbon phase may accelerate the oxidation rate. Yanez-Limon [343] reported that annealing in the air of sputtered amorphous carbon films with predominantly sp^2 bonds led to their low temperature crystallization. The catalytic effect of oxygen in the crystallization process was explained in terms of the generation of a porous structure in the carbon coating due to the vaporization of carbon oxide. With the porous structure and micro-cracks inside the oxide layer, the oxidation diffusion mechanism for oxygen transport changed from atomic diffusion to mass transfer [344]. Therefore, oxygen can easily diffuse inwardly accompanied by faster growth of Cr_2O_3, Al_2O_3, and TiO.

This mechanism is supported by the oxidation results of Cr doped amorphous GLC coating. As shown in Figures 5.4-1 and 5.4-2, the GLC coating was destructed at 400°C and almost

fully destroyed at 700 ℃ as evidenced by the very high iron and oxygen content measured.

Indeed, after oxidation at 1000 ℃, the surface roughness of the high-carbon CrAlTiCN-5# coating is very close to that of GLC (Figure 4.5-2). Therefore, a large amount of amorphous carbon will reduce the thermal stability of carbon-doped CrAlTiCN coatings.

Chapter 6: Summary and Conclusions

The evidence produced throughout this project and the discussion presented in the last chapter can be summarised as follows:

Design and synthesis of new Cr-Al-Ti-C-N coatings:

(1) It is possible to generate novel carbon-doped CrAlTiCN coatings with the carbon content up to 24.34 at % by closed-field unbalanced magnetron sputtering of graphite target.

(2) The carbon content in the CrAlTiCN coatings increased with the current of the graphite target used during the deposition of these carbon-doped coatings.

Characterisation of new Cr-Al-Ti-C-N coatings:

(3) An fcc structured metastable phase (Cr, Al, Ti) (C, N) has been identified by XRD in the all CrAlTiCN coatings developed from the project. The lattice parameters of the (Cr, Al, Ti) (C, N) is smaller than that of CrN.

(4) As designed in this project, the new coating system consists of (from the substrate to the surface) a pure chromium interface layer, a chromium nitrides layer, a CrAlTiN layer and a new CrAlTiCN top layer. The microstructure of the top carbon containing CrAlTiCN layer mainly depends on the graphite target current and thus the carbon content.

(5) When the carbon content is low (between 2.34 and 3.96 at %), carbon atoms are mainly dissolved in the crystal lattice of (Cr, Al, Ti) N to partially substitute nitrogen, thus forming fcc structured metastable phase (Cr, Al, Ti) (C, N).

(6) When the carbon content of the top layer ranges from 9.65 to 12.53 at %, the excessive carbon atoms will begin to form amorphous carbon layer, thus producing multilayered nanocomposite coating with alternating amorphous carbon and nano-crystalline (Cr, Al, Ti) (C, N) layers.

(7) When the carbon content of the top layer reaches 24.34 at %, the top carbon-containing layer consists of (Cr, Al, Ti) (C, N) grains embedded in an amorphous carbon matrix.

(8) XPS and EELS analyses indicate that the amorphous free carbon in the top layer of medium-to-high carbon doped CrAlTiCN coatings has a C-C bond state and is in a sp^2 dominated graphitic environment.

Mechanical properties of new Cr-Al-Ti-C-N coatings:

(9) The addition of a small amount of carbon into the CrAlTiN coating (CrAlTiCN-1# sample) can lead to only marginally decrease in hardness and Young's modulus; however, significant decrease will occur once the total amount of carbon and nitrogen exceeded 50 at% (for CrAlTiCN-2# and CrAlTiCN-3# samples) because of the formation of amorphous layers.

(10) The toughness of CrAlTiCN coatings increase effectively with the carbon doped mainly because of the formation of amorphous carbon, the nano-multilayer structure and the increased plasticity.

Tribological behaviour of new Cr-Al-Ti-C-N coatings:

(11) The doping of carbon can effectively reduce the coefficient of friction of the developed CrAlTiCN coatings. The coefficient of friction can be reduced from 0.655 for the non-doped bench-mark CrAlTiN coating to as low as 0.350 for the carbon-doped CrAlTiCN-5# coating because of the amorphous phase formed in the coatings.

(12) When tested at room temperature under unidirectional sliding conditions, the wear resistance of the CrAlTiCN coatings increase with increasing their carbon content most probably due to the reduced damage to the counterface and the retained lubricous wear debris. However, no obvious difference in wear resistance could be observed for the CrAlTiCN coatings doped with different levels of carbon different under reciprocating sliding conditions.

(13) It is of interest to find that when tested at room temperature, the fretting wear of these carbon-doped CrAlTiCN nanocomposite coatings increase with carbon content; however, when tested at 350 ℃ the opposite occurs.

(14) When tested at room temperature, amorphous graphite-like carbon (GLC) coatings possess a better wear resistance than the carbon-doped CrAlTiCN nanocomposite coatings;

however, when fretted at 350°C, the carbon-doped CrAlTiCN nanocomposite coatings can outperform the GLC coating owing to its oxidation-induced degradation.

Thermal stability and oxidation resistance:

(15) When oxidised in air at temperatures up to 400 ℃ for 2h, no significant changes in the surface roughness and hardness occur to all carbon-doped nanocomposite CrAlTiCN. The thermal stability of the newly developed carbon-doped nanocomposite CrAlTiCN coatings is similar to that of bench-mark CrAlTiN coating but much better than the GLC coating.

(16) The carbon-doped nanocomposite CrAlTiCN coatings have very similar thermal stability to the bench-mark CrAlTiN coating at temperatures ranging from 400 to 900 ℃ mainly because of the formation of protective Cr_2O_3 as well as Al_2O_3 films.

(17) The CrAlTiCN-5# coating, which has been doped with the highest level of carbon in the present research, was completely destroyed at 1000 ℃ because the amorphous carbon matrix cannot form any protective films during the oxidation.

Chapter 7: Proposals for Future Work

This study has clearly shown that a novel low-friction, wear and oxidation resistant multilayered nanocomposite Cr-Al-Ti-C-N coatings can be generated using closed-field unbalanced magnetron ion plating technique. To realise their potential for high-speed dry machine and other high temperature applications, the following topics are proposed for the future studies:

Friction properties and wear tests:

More work could be conducted to reduce the frictional coefficient further.

In order to identify the application window, more laboratory wear tests could be conducted under different test conditions such as higher temperatures and higher sliding speeds. If feasible, the new coatings could be evaluated using real cutting or drilling trials.

Oxidation mechanisms:

The good oxidation resistance seems to be intrinsic to (Cr, Al, Ti) N based coatings but the oxidising process and anti-oxidation mechanisms of the new multilayered nanocomposite Cr-Al-Ti-C-N coatings deserve further attention.

Potential for both sp^2 and sp^3 carbon:

The coating hardness of high-carbon Cr-Al-Ti-C-N coatings could be increased by changing the deposition conditions to form carbon-based phases with both sp^2 and sp^3 hybridisations.

References

[1] A. A. Voevodin, J. S. Zabinski, C. Muratore, Recent advances in hard, tough, and low friction nanocomposite coatings, Tsinghua Science and Technology, 10 (2005) 665-679

[2] R. Buhl, H. K. Pulker, E. Moll, TiN coatings on steel, Thin Solid Films 80 (1981) 265-270

[3] G. Paller, B. Matthes, W. Herr and E. Broszeit, Tribological properties of r.f.-sputtered titanium based hard coatings and their behaviour under plastics processing conditions, Materials Science and Engineering, A140 (1991), 647–654.

[4] S. Y. Lee, S. D. Kim, Y. S. Hong, Application of the duplex TiN coatings to improve the tribological properties of Electro Hydrostatic Actuator pump parts, Surface and Coatings Technology, 193 (2005) 266-271

[5] X. T. Zeng, Unbalanced magnetron sputtered carbon composite coatings, Journal of Vacuum Science and Technology, A 17 (1999) 1991

[6] J. J. Nainaparampil, J. S. Zabinski, A. Korenyi-Both, Formation and characterization of multiphase film properties of (Ti–Cr)N formed by cathodic arc deposition, Thin Solid Films, 333 (1998) 88-92

[7] W. D. Munz, itanium aluminum nitride films: A new alternative to TiN coatings, Journal of Vacuum Science and Technology, A 4 (1986) 2717-2725

[8] H. A. Jehn, S. Hofmann, W. D. Munz, Surface and interface characterization of heat- treated (Ti, Al)N coatings on high speed steel substrates, Thin Solid Films, 153 (1987) 45-53

[9] I. A. Polonsky, T. P. Chang, L. M. Keer, W. D. Sproul, A study of rolling-contact fatigue of bearing steel coated with physical vapor deposition TiN films: Coating response to cyclic contact stress and physical mechanisms underlying coating effect on the fatigue life, Wear, 215 (1998) 191-204

[10] S. Hofmann, Formation and diffusion properties of oxide films on metals and on nitride coatings studied with Auger electron spectroscopy and X-ray photoelectron spectroscopy, Thin Solid Films, 193 (1990) 648-664

[11] X. T. Zeng, S. Zhang, L. S. Tan, Multilayered (Ti, Al) ceramic coating for high-speed machining applications, Journal of Vacuum Science and Technology, A 19 (2001) 1919-1923

[12] T. Ueda, M. A. Huda, K. Yamada, K. Nakayama, H. Kudo, Temperature measurement of CBN tool in turning of high hardness steel, CIRP Annals Manufacturing Technology, 48 (1999) 63-66

[13] M. Kawate, A. Kimura, T. Suzuki, Microhardness and lattice parameter of $Cr_{1-x}Al_xN$ films, Journal of Vacuum Science and Technology, A 20 (2002) 569-571

[14] A. E. Reiter, V. H. Deflinger, B. Hanselmann, T. Bachmann, B. Sartory, Investigation of the properties of $Al_{1-x}Cr_xN$ coatings prepared by cathodic arc evaporation, Surface and Coatings Technology, 200 (2005) 2114-2122

[15] R. Lamni, E. Martinez, S. G. Springer, P. E. Schmid, Optical and electronic properties of magnetron sputtered ZrN_x thin films, Thin Solid Films, 447 (2004) 316-321

[16] B. C. Schramm, H. Scheerer, H. Hoche, E. Broszeit, E. Abele, C. Berger, Tribological properties and dry machining characteristics of PVD-coated carbide inserts, Surface and Coatings Technology, 188 (2004) 623-629

[17] X. Z. Ding, X. T. Zeng, Y. C. Liu, F. Z. Fang ,G. C. Lim, $Cr_{1-x}Al_xN$ coatings deposited by lateral rotating cathode arc for high speed machining applications, Thin Solid Films, 516 (2008) 1710-1715

[18] T. Sato, Y. Tada, M. Ozaki, T. Hoke, T. Besshi, A crossed-cylinders testing for evaluation of wear and tribological properties of coated tools, Wear, 178 (1994) 95-100

[19] G. Berg, C. Friedrich, E. Broszeit, C. Berger, Development of chromium nitride coatings substituting titanium nitride, Surface and Coatings Technology, 86 (1996) 184-191

[20] B. Navinsek, P. Panjan, I. Milosev, Industrial applications of CrN (PVD) coatings, deposited at high and low temperatures, Surface and Coatings Technology, 97 (1997) 182-191

[21] M. Kawate, A. K. Hashimoto, T. Suzuki, Oxidation resistance of $Cr_{1-X}Al_XN$ and $Ti_{1-X}Al_XN$ films, Surface and Coatings Technology, 165 (2003) 163-167

[22] S. Yang, D. G. Teer, Properties and performance CrTiAlN of multilayer hard coatings deposited using magnetron sputter ion plating, Surface Engineering, 18 (2002) 391-396

[23] K. E. Cooke, S. Yang, C. Selcuk, A. Kennedy, D. G. Teer, D. Beale, Development of duplex nitrided and closed field unbalanced magnetron sputter ion plated CrTiAlN-based coatings for H13 aluminium extrusion dies, Surface and Coatings Technology, 188 (2004) 697-702

[24] S. G. Harris, E. D. Doyle, A. C. Vlasvels, J. Audy, J. M. Long, D. Quick, Influence of chromium content on the dry machining performance of cathodic arc evaporated TiAlN coatings, Wear, 254 (2003) 185-194

[25] L. Bai, X. Zhu, J. Xiao, J. He, Study on thermal stability of CrTiAlN coating for dry drilling, Surface and Coatings Technology, 201 (2007) 5257-5260

[26] X. Wen, Master thesis, Xi'an university of technology, 2005

[27] Q. Yanf, L. R. Zhao, F. Cai, S. Yang, D. G. Teer, Wear, erosion and corrosion resistance of CrTiAlN coating deposited by magnetron sputtering, Surface and Coatings Technology, 202 (2008) 3886-3892

[28] A. J. Hermann, Multicomponent and multiphase hard coatings for tribological applications, Surface and Coatings Technology, 131 (2000) 433-440

[29] K. Enke, H. Dimigen, H. Hubsch, Frictional properties of diamondlike carbon layers, Appllied Physics Letters, 36 (1980) 291-292

[30] T. Le. Huu, H. Nery, H. Zaidi, D. Paulmier, Tribologogical behaviour of hard carbon coatings deposited on steel substrates by plasma-assisted chemical vapour deposition, Diamond Related Materials, 3 (1994) 1028-1033

[31] S. Yang, D. Camino, A. H. S. Jones, D. G. Teer, The deposition and tribological behaviour of sputtered carbon hard coatings. Presented at the International Conference on Metallic Coatings and Thin Films, ICMCTF'99, San Diego, Surface and Coatings Technology, (1999) 12-15

[32] Teer Coatings Ltd. Technical Data Sheet, Graphit-iC. Teer Coatings Ltd., 290 Hartlebury Trading Estate, Hartlebury, Kidderminster, Worcestershire DY 10 4JB, UK

[33] M. Lindquist, O. Wilhelmsson, U. Jansson, U. Wiklund, Tribofilm formation and tribological properties of TiC and nanocomposite TiAlC coatings, Wear, 266 (2009) 379-387

[34] L. Bai, P.hD thesis, Xi'an Jiaotong university , 2006

[35] H. Peter. Jost.: Tribology—origin and future, Wear, 136 (1990) 1-17

[36] P. J. Blau, 'Glossary of terms', in ASM international (ed): ASM Handbook, Vol 18. Friction Lubrication and Wear Technology, The Society, Metals Park, Ohio, pp 1-21

[37] K. Holmberg, H. Ronkainen, A. Laukkane, K. Wallin, Friction and wear of coated surfaces — scales, modelling and simulation of tribomechanisms, Surface and Coatings Technology, 202 (2007) 1034-1049

[38] P. J. Blau, Friction and Wear Transitions of Materials-Break-in, Run-in, Wear-in, Noyes Publications, Park Ridge, New Hersey, USA, 1989, pp 476

[39] B. Bhushan, Priciples and Applications in Tribology, John Wiley & Sons, New York, 2001, pp 205

[40] K. Kato, K. Adashi, in: B. Bhushan (Ed.), Modern Tribology Handbook, CRC Press, New York, 2001, pp 273

[41] F. P. Bowden, D. Tabor, Friction and Lubrcation of Solids, Clarendon, Oxford, 1950, pp 299

[42] D. Dowson: History of Tribology, Longman, London, 1979, pp 67

[43] P. J. Blau, Appendix: static and kinetic friction coefficient for selected materials, in ASM international (ed): ASM Handbook, Vol 18, Friction Lubrication and Wear Technology, The Society, Metals Park, Ohio, pp 70-75

[44] J. Larsen-Basse, Basic theory of solid friction, in ASM international (ed): ASM Handbook, Vol 18, Friction, Lubrication and Wear Technology, The Society, Metals Park, Ohio, pp 27-38

[45] A. W. J. Gee, Friction and wear as related to the composition, structure, and properties of metals, International Metals Review, 24 (1979) 57-67

[46] H. Uetz, K. Sommer, Investigations of the effect of surface temperatures in sliding contact, Wear, 43 (1977) 375-388

[47] T. F. J. Quinn, The role of oxidation in the mild wear of steel, British Journal of Applied Physics, 13 (1962) 33-37

[48] T. F. J. Quinn, W. O. Winer, The thermal aspects of oxidation wear, Wear, 102 (1985) 67-80

[49] T. F. J. Quinn, Oxidation wear, in ASM international (ed): ASM Handbook, Vol 18, Friction Lubrication and Wear Technology, The Society, Metals Park, Ohio, pp 280-289

[50] J. F. Archard, The temperature of rubbing surface, Wear, 2 (1959) 438-455

[51] S. C. Lim, M. F. Ashby, Overview no. 55 Wear-mechanism maps, Acta Metallurgica, 35 (1987), pp 1-24

[52] D. A. Rigney, Fundamentals of friction and wear of materials, ASM book, 1981, pp 187

[53] J. N. Michael, Tribology handbook, Elsevier, 1995, pp 234

[54] S. C. Lim, M. F. Ashby, Wear mechanism maps, Acta Metallurgica, 35 (1987) 1-5

[55] M.B. Peterson, Wear control handbook, American Society of Mechanical Engineers, 1980, pp 105

[56] P. M.B Walker, N. S. T. J. Braithwait, P. R. Lewis, K. Reynolds, G. W. Weidmann, Materials science and technology dictionary. Chambers, 1993, pp 268

[57] N. H. Macmillan, On the need for a generally accepted terminology consistent with the complexities of wear, Wear, 78 (1982) 385-388

[58] S. L. Rice, H. Nowotny, S. F. Wayne, A survey of the development of subsurface zones in the wear of materials, Key Engineering Materials, 33 (1989) 77-100

[59] C. R. Gagg, P. R. Lewis, Wear as a product failure mechanism—Overview and case studies, Engineering Failure Analysis, 14 (2007) 1618-1640

[60] J. T. Burwell Jr, Survey of possible wear mechanisms, Wear, 1 (1957) 119-141

[61] H. Czichos, Tribology—a System Approach to the Science and Technology of Friction, Lubrication and Wear, Elsevier, Amsterdam

[62] C. S. Yust, Tribology and wear, International metals Reviews, 30 (1985) 141-154

[63] H. Czichos, Importance of properties of solids to friction and wear behavious, in NASA (ed): Tribology in the 80's, Vol 1, NASA Conference Publication 2300, pp 71-106

[64] B. Bhushan, Principles and applications of tribology. New York: Wiley; 1999

[65] I. M. Hutchings, Lubrication and wear, Amsterdam, Elsevier, 1982, pp 423

[66] R. Divakar, P. J. Blau, Wear testing of advanced materials. ASTM, 1992

[67] T. S. Eyre, Wear characteristics of metals, Tribology International, 9 (1976) 203-212

[68] T. F. J. Quinn, Review of oxidational wear Part Ⅰ,: The origins of oxidational wear, Tribology International, 16 (1983) 257-271

[69] T. A. Stolarski, Tribology in machine design, A Butterworth-Heinemann, 1999, pp 13-14

[70] E. Rabinowicz, The determination of the compatibility of metals through static friction tests, Tribology Transaction, 14 (1971) 198-205

[71] E. Rabinowicz, The influence of compatibility on tribological phenomenon, Tribology Transaction, 14 (1975) 206-212

[72] D. A. Ringney, L. H. Chen, M. G. S. Naylor, A. R. Rosenfield, Wear processes in sliding systems, Wear, 100 (1984) 195-219

[73] J. Halling, R. D. Arnell, Ceramic coatings in the war on wear, Wear, 100 (1984) 367-380

[74] J. Halling, K. A. Nuri, The elastic contact of rough surface and its importance in the reduction of wear, Proceedings of Institute of Mechanical Engineers, 199 (1985) 139-144

[75] J. A. Greenwood, J. B. P. Williamson, Contact of nominally flat surface, Proceedings of Royal Society of London, A 295, pp 300-319

[76] J. C. Rich., The Materials and Methods of Sculpture, Courier Dover Publications, 1988, pp129

[77] K. G. Budiski, Incipient galling of metals, Wear, 74 (1981) 93-105

[78] R. Gohar, H. Rahneiat, Fundamentals of Tribology, Imperial College Press, USA, pp 213

[79] G.. W. Rowe, Introduction Survey of Lubrication and Wear, Lubrication and Lubrications, Braithwaite, E. R. (Eds), Elsevier, New York, 1967

[80] J. B. Peace, Solid Lubricants, Lubrication and Lubricants, E. R. Braithwaite (Eds), Elasevier, New York, 1969

[81] J. K. Lancaster, Solid Lubricants, CRC Handbook of Lubrication, Vol. 2, Theory of Lubrication, E. R. (Eds), CRC Press, New York, 1984, pp 269

[82] I. M. Hurching, Tribology: Friction and Wear of Engineering Materials, Edward Arnell, London, 1992

[83] B.Bhushan, B. K. Gupta, Handbook of Tribology, McGraw-Hill, New York, 1991

[84] T. Bell, Surface engineering: past, present, and future, Surface Engineering, 6 (1990) 31-40

[85] T. Bell, Surface engineering of steel to combat wear, Metallurgica, 49 (1990) 103-108

[86] A. Erdemir, in: B. Bhushan (Ed.), Modern Tribology Handbook, Ⅱ, CRC Press, 2001, pp 787-825

[87] M. N. Yoder, in R. E. Clausing et al. (eds.), Diamond and Diamond-like Films and Coatings, Plenum Press, New York, 1991, pp 1

[88] C. Donnet, A. Erdemir, Historical developments and new trends in tribological and solid lubricant coatings, Surface and Coatings Technology, 180 (2004) 76-84

[89] K. Holmberg, A. Matthews, in: D. Dowson (Ed.), Coatings Tribology, Elsevier, 1994, pp 1-6

[90] C. Donnet, Condensed Matter News, 4 (1995) 9-16

[91] A. Erdemir, in: B. Bhushan (Ed.), Modern Tribology Handbook, Ⅱ, CRC Press, 2001, pp 787-825

[92] P. Sutor, MRS Bull. 16 (1991) 1-17

[93] K. Miyoshi, Surface Desingn Engineering Toward Wear-Resistant, Self-lubricating Diamond Films and Coatings, NASA TM 208905 (1999) 1-17

[94] I. L. Singer, How third-body processes affect friction and wear, MRS Bull, 23 (1998) 37-40

[95] W. E. Jamison, CRC Handbook of Tribology and Lubrication, 3, CRC Press, Boca Raton, FL, 1994, pp 121

[96] T. A. Blanchet, F. E. Kennedy, Notes on contributors, Wear 153 (1992) 229-233

[97] C. D. Martino, F. Demichelis, A. Tagliaferro, Characterisitics of α-C:H:Si films deposited by r.f.sputtering under various deposition conditions, Diamond and Related Materials, 3 (1994) 547-552

[98] V. V. Uglov, N. N. Cherenda, A. Koeniger, W. Bruechner, B. Rauschenbach, V. V. Khodasevich, Structure and phase composition of low friction carbon coatings deposited on aluminum surface, Surface and Coatings Technology, 97 (1997) 322-325

[99] D. I. Jone, A. D. Stewart, Properties of hydrogenated amorphous carbon films and the effects doping, Philosophical Magazine, B 46 (1982) 423-434

[100] E. Teng, C. Jiaa, A. Eltoukhy, Diamond-like carbon overcoat for magnetic thin fim recording disks, Surface and Coatings Technology, 68 (1994) 632-637

[101] K. Taube, M. Grischke, K. Bewilogua, Improvement of carbon-based for use in the cold forming of non-ferrous metals, Surface and Coatings Technology, 68 (1994) 662-668

[102] K. C. Walter, H. Kung, T. Levine, J.T. Tesmer, P. Kodali, B.P. Wood, D.J. Rej, M. Nastasi, J. Koskinen, J.-P. Hirvonen, Characterization and performance of diamond-like carbon films synthesized by plasma- and ion-beam-based techniques, Surface and Coatings Technology, 74-75 (1995) 734-738

[103] K. Enke, H. Dimigen, H. Hubsch, Frictional properties of diamondlike carbon layers, Appllied Physics Letters, 36 (1980) 291-292

[104] T. Le. Huu, H. Nery, H. Zaidi, D. Paulmier, Tribologogical behaviour of hard carbon coatings deposited on steel substrates by plasma-assisted chemical vapour deposition, Diamond Related Materials, 3 (1994) 1028-1033

[105] S. Chowdhury, M. T. Laugier, I. Z. Rahman, Characterization of DLC coatings deposited by rf magnetron sputtering, Journal of Materials Processing Technology, 153 (2004) 804-810

[106] R. Memming, H.J. Tolle, P.E. Wierenga, Properties of polymeric layers of hydrogenated amorphous carbon produced by a plasma-activated chemical vapour deposition process II: Tribological and mechanical properties, Thin Solid Films 143 (1986) 31-41

[107] A. Grill, Review of the tribology of diamond-like carbon, Wear, 168 (1993) 143-153

[108] C. Donnet, Condensed Matter News, 4 (1995) pp 9

[109] A. Grill, B. S. Meyerson, K. E. Spear, J. P. Dismuke, Synthetic diamond: emerging CVD science and technology. New York: John Wiley and Sons, 1994, pp 91

[110] C. Donnet, A. Grill, Friction control of diamond-like carbon coatings, Surface and Coatings Technology, 94 (1997) 456-462

[111] M. K. Arora, A. H. Lettington, D. R. Waterman, Amorphous nitrogen containing carbon films deposited by plasma assisted chemical vapour deposition, Diamond Related Materials, 8 (1999) 623-627

[112] B. Wei, B. Zhang, K. E. Johnson, Nitrogen-induced modifications in microstructure and wear durability of ultrathin amorphous-carbon films, Journal of Appllied Physics, 83 (1998) 2491-2499

[113] K. Miyoshi, Y. Tzeng, M. Yosikawa, Proc 1st Int Conf Appl Diamond Films Relat Mater, Amsterdam, Elsevier Science, 1991, pp 699

[114] T. Le Huu, H. Zaidi, D. Paulmier, Lubricating properties of diamond-like coating, Wear, 181 (1995) 766-770

[115] C. Donnet, T. Le Mogne, L. Pansonnet, Tribology Letters, 4 (1998) 259

[116] A. Gangopadhyay, Tribology Letters, 5 (1998) 25-39

[117] A. Grill, V. Patel, Plasma-deposited diamond-like carbon and related materials Diamond Related Materials, 43 (1999) 1-2

[118] A. H. S Jones, D. Camino, D. G. Teer, Novel high wear resistant diamond-like carbon coatings deposited by magnetron sputtering of carbon targets, Journal of Engineering Tribology, 212 (1998) 301-306

[119] D. Camino, A. H. S. Jones, D. Mercs, D. G. Teer, High performance sputtered carbon coatings of wear resistant applications, Vacuum, 52 (1999) 125-131

[120] S. K. Field, M. Jarratt, D. G. Teer, Tribological properties of graphite-like and diamond-like carbon coatings, Tribological International, 37 (2004) 949-956

[121]   O. Knotek, M. Atzor, H. G. Prengel, On reactively sputtered Ti-Al-V carbonitrides Surface and Coatings Technology, 36 (1988) 265-273

[122]   A. J. Hermann, Multicomponent and multiphase hard coatings for tribological applications, Surface and Coatings Technol, 131 (2000) 433-440

[123]   T. J. Robertson, Diamond-like Amorpjous Carbon, Materials Science and Engineering, R 37 (2002) 129-132

[124]   C. Subramanian, K. N. Strafford, Review of multicomponent and multilayer coatings for tribological applications, wear, 165 (1993) 85-95

[125]   P. Vincenzini, in K. N. Strafford, P. K. Datta and J. Gray (eds.), Surface Engineering Practices: Processes, Fundamentals and Applications in Corrosion and Wear, Ellis Horwood, Chichester, 1990

[126]   W. Grzesik, Advanced Protective Coating for Manufacturing and Engineering, Hanser Gardner, Cincinnati, 2003

[127]   H. G. Prengel, P. C. Jindal, K. H. Wendt, A new class of high performance PVD coatings for carbide cutting tools, Surface and Coatings Technology, 139 (2001) 25-34

[128]   F. Klocke, T. Krieg, K. Gerschwiler, R. Fritsch, Improved cutting processes with adapted coating systems, Ann. CIRP 47 (1998) 65-68

[129]   K. Osakada, R. Matsumoto, Fundamental study of dry metal forming with coated tools, Ann. CIRP 49 (2000) 161-164

[130]   H. Ohnuma, N. Nihira, A. Mitsuo, K. Toyoda, K. Kubota, T. Aiziwa, Effect of aluminum concentration on friction and wear properties of titanium aluminium nitride films, Surface and Coatings Technology, 177 (2004) 623-626

[131]   K. Fujita, Research and development of oxidation, wear and corrosion resistant materials at high temperature by surface modification using ion processing, Surface and Coatings Technology, 196 (2005) 139-144

[132]   M. Braic, M. Balaceanu, V. Braic, A. Vladescu, G. Pavelescu, M. Albulescu, Synthesis and characterization of TiN, TiAlN and TiN/TiAln biocompatible coatings, Surface and Coatings Technology, 200 (2005) 1014-1017

[133]   G. T. Liu, J. G. Duh, K. H. Wang, Mechanical characteristics and corrosion behavior of (Ti, Al)N coating on dental alloys, Surface and Coatings Technology, 200 (2005) 2100-2105

[134]   K. Kutschej, Mayrhofer, M. Kathrein, P. Polcik, Tessardi, C. Mitterer, Structure, mechanical and tribological properties of sputtered $Ti_{1-x}Al_xN$ coatings with $0.5<x<0.75$, Surface and Coatings Technology, 200 (2005) 2358-2365

[135]   G. Erkens, R. Cremer, T. Hamoudi, K. D. Bouzakis, Properties and performance of high aluminium containing (Ti, Al)N based supernitride coating in innovative cutting applications, Surface and Coatings Technology, 177(2004) 727-734

[136]   M. Algren, H. Blomgvist, Influence of bias variation on residual stress and texture in TiAlN PVD coatings, Surface and Coatings Technology, 145 (2001) 60-70

[137]   A. N. Kale, K. Ravindranath, D. C. Kothari, P. M. Raole, Tribological properties of (Ti, Al) N coatings at different bias voltages using cathodic arc technique, Surface and Coatings Technology, 145 (2001) 60-70

137

[138] M. Kathrein, C. Michotte, M. Penoy, P. Polcik, C. Mittere, Multifunctional multi-component PVD coatings for cutting tools, Surface and Coatings Technology, 200 (2005) 1867-1871

[139] K. Kutschej, N. Fateh, P. H. Mayrhofer, M. Kathrein, P. Policik, C. Mitterer, Comparative study of Ti1-xAlxN coatings alloyed with Hf, Nb, and B, Surface and Coatings Technology, 200 (2005) 113-117

[140] H. Holleck, Material selection for hard coatings, Journal of Vacuum Science and Technology, A 4 (1986) 2661-2669

[141] M. Astrand, T. J. Selinder, M. E. Sjostrand, Deposition of Ti1-xAlxN using bipolar pulsed dual magnetron sputtering, Surface and Coatings Technology, 200 (1005) 625-629

[142] L. Donohue, I. J. Smith, W. –D. Munz, I. Petrov, J. E. Greene, Microstructure and oxidation-resistance of $Ti_{1-x-y-z}Al_xCr_yY_zN$ layers grown by combined steered-arc/unbalanced-magnetron-sputter deposition, Surface and Coatings Technology, 94-95 (1997) 226-231

[143] A. Alberdi, M. Marin, B. Diaz, O. Sanchez, R. Escobar Galindo, Wear resistance of titanium–aluminium–chromium–nitride nanocomposite thin films, Vacuum, 81 (2007) 1453-1456

[144] D. V. Shtansky, F. V. Kiryuhantsev-Korneev, A. N. Sheveiko, I. A. Bashkova, O. V. Malochkin, E. A. Levashov, N. B. D'yakonova, I. V. Lyasotsky, Physics of Solid State, 47 (2005) 242

[145] P. C. Yashar, W. D. Sproul, Nanometer scale multilayered hard coatings, Vacuum, 55 (1999) 179-190

[146] G. Hilz, H. Holleck, Proceedings of the 13th International Plansee Seminar, Reutte Tirol, 3 (1993) 267

[147] M. S. Wong, Y. C. Lee, Paper presented at ICMCTF 99, Paper B1-3-5, (1999)

[148] A. A. Voevodin, J. S. Zabinski, Superhard, functionally gradient, nanolayered and nanocomposite diamond-like carbon coatings for wear protection, Diamond Related Materials, 7 (1998) 463-467

[149] M. Lacerda et al., Paper presented at ICMCTE 99, Paper E2-2-8, (1999)

[150] A. E. Santana, A. Karimi, V. H. Derflinger, A. Schutze, Microstructure and mechanical behavior of TiAlCrN multilayer thin films, Surface and Coatings Technology, 177 (2004) 334-340

[151] M. Balaceanu, M. Braic, V. Braic, G. Pavelescu, Properties of arc plasma deposited TiCN/ZrCN superlattice coatings, Surface and Coatings Technology, 200 (2005) 1084-1087

[152] P. Eh. Hovsepian, C. Reinhard, A. P. Ehiasarican, CrAlYN/CrN superlattice coatings deposited by the combined high power impulse magnetron sputtering/unbalanced magnetron sputtering technique, Surface and Coatings Technology, 201 (2006) 4105-4110

[153] E. Lugscheider, K. Bobzin, C. Pinero, F. Klocke, T. Massmann, Development of a superlattice (Ti,Hf,Cr)N coating for cold metal forming applications, Surface and Coatings Technol, 177-178 (2004) 616-622

[154] H. Holleck, V. Schier,: Multilayer PVD coatings for wear protection, Surface and Coatings Technology, 76(1995) 328-336

[155] J. Patscheider,: Nanocomposite Hard Coatings for Wear Protection, MRS Bull. 28 (2003) 180

[156] A. Leyland, A. Matthews, On the significance of the H/E ratio in wear control: a nanocomposite coating approach to optimised tribological behaviour, Wear, 246 (2000) 1-11

[157] J. Musil, P. Zeman, H. Hruby, P. Mayrhofer, Nanocrystalline and nanocomposite CrCu and CrCu–N films prepared by magnetron sputtering, Surface and Coatings Technology, 115 (1999) 32-37

[158] S. A. Barnett, A. Madan, I. Kim, K. Martin, Stability of nanometer-thick layers in hard coating, MRS Bull. 28 (2003) 169-172

[159] A. Savan, E. Pfluger, R. Goller, W. Gissler, Use of nanoscaled multilayer and compound films to realize a soft lubrication phase within a hard, wear-resistant matrix, Surface and Coatings Technology, 126 (1999) 159-165

[160] C. Donnet, J. Fontaine, T. Le Mogne, M. Belin, C. Heau, J. P. Terrat, Diamond-like carbon-based functionally gradient coatings for space tribology, Surface and Coatings Technology, 120 (1999) 548-554

[161] A. A. Voevodin, S. D. Walck, J. S. Zabinski, Architecture of multilayer nanocomposite coatings with super-hard diamond-like carbon layers for wear protection at high contact loads, Wear, 203-204 (1997) 516-527

[162] S. Veprek, The search for novel, superhard materials, Journal of Vacuum Science and Technology, A17 (1999) 2401-2420

[163] H. Holleck, H. Leiste, M. Stuber, S. Ulrich, Nachrichten Forsch. Karlsr. 31 (1) (1999) 13

[164] S. Hogmark, S. Jacobson, M. Larsson, Design and evaluation of tribological coatings, wear, 246 (2000) 20-33

[165] H. S. Heshmat, C. A. Heshmat, Tribl. Trans. 42 (1999) 640

[166] R. M. Gresham, in: E. R. Booser (Ed.), CRC Handbook of Lubrication: Theory and Practice of Tribology, Ⅲ, CRC Press, 1997, pp 167-181

[167] K. Holmberg, A. Matthews, Coatings Tribology-Properties, Techniques and Applications in Surface Engineering, Tribology Series 28, Elsevier, Amsterdam, 1994, pp 442

[168] O. Knotek, F. Loffler and G. Kramer, Arc-deposited Ti-Zr-N coatings on cemented carbides for use in interrupted cutting, Surface and Coatings Technology, 49 (1991) 325-329

[169] W. D. Munz, F. J. M. Hauzer, D. Schulze and B. Buil, A new concept for physical vapor deposition coating combining the methods of arc evaporation and unbalanced-magnetron sputtering, Surface and Coatings Technology, 49 (1991) 161-167

[170] R. Buhl, H. K. Pulker and E. Moll, TiN coatings on steel Thin Solid Films, 80 (1981) 1256-270

[171] H. Ehrich, B. Hasse, M. Mausbach and K. G. Muller, The anodic vacuum are & its application to coating, Joutnal of Vacuum Science and Technology, A 8 (1990) 2160-2164

[172] P. S. Mcleod, L. D. Hartsough, Hig-rate sputtering of aluminum for metallization of integrated circuits, Joutnal of Vacuum Science and Technology, A 14 (1977) 263-265

[173] R. K. Waits, Joutnal of Vacuum Science and Technology, A 15 (1978) 179-87

[174] B. Window, N. Savvides, Charged particle fluxes from planar magnetron sputtering sources, Journal of Vacuum Science and Technology, A 4 (1986) 196-202

[175] B. Window, N. Savvides, Joutnal of Vacuum Science and Technology, A 4 (1986) 453-456

[176] N. Savvides, B. Window, Unbalanced DC Magnetron as Sources of Hig Ion Fluxes, Joutnal of Vacuum Science and Technology, A 4 (1986) 504-508

[177] D. G. Teer, Technical note: A magnetron sputter ion-plating system, Surface and Coatings Technology, 39 (1989) 565-572

[178] W. D. Sproul, P. J. Rudnick, M. E. Graham, S. L. Rohde, High rate reactive sputtering in an opposed cathode closed-field unbalanced magnetron sputtering system, Surface and Coatings Technology, 43 (1990) 270-278

[179] R. J. Bunshah, R. S. Juntz, Activated Reactive Evaportation Process for High Rate Deposition of Compounds, Joutnal of Vacuum Science and Technology, 9 (1972) 1404-1408

[180] R. J. Hecht, J. R. Mullaly, Deposition rate and substrate temperature effects on the structure and properties of bulk-sputtered OFHC Cu and Cu-0.15 Zr, Joutnal of Vacuum Science and Technology, 12 (1975) 836-841

[181] P. J. Kelly, R. D. Arnell, The production and characterisation of chemically reactive porous coatings of zirconium via unbalanced magnetron sputtering, Surface and Coatings Technology, 86 (1996) 200-206

[182] D. G. Teer. UK patent No. 2 258 343, USA patent No. 5 554 519, European patent No. 0 521 045

[183] W. -D. Munz, F. J. M. Hauzer, D. Schulze, B. Buil, A new concept for physical vapor deposition coating combining the methods of arc evaporation and unbalanced-magnetron sputtering, Surface and Coatings Technology, 49 (1991) 161-167

[184] B. Window,: Recent advances in sputter deposition, Surface and Coatings Technology, 71 (1995) 93-97

[185] J. Musil, Basic properties of low pressure plasma, in: A. Paoleti, A. Tucciarone (Eds.), Proceedings of the International School of Physics "Enrico Fermi", Course CSSSV, IOS Press, Amsterdam 1997, pp 145-177

[186] J. Musil, Low-pressure magnetron sputtering, Invited paper at the 7th Joint Vacuum Conference, May 26-29, 1997, Debrecen, Hungary, Vacuum, 50 (1998) 363-367

[187] J. Musil, Recent advances in magnetron sputtering technology, Surface and Coatings Technology, 100-101 (1998) 280-286

[188] B. North, Six issues for the hard coatings community, Surface and Coatings Technology, 106 (1998) 129-134

[189] J.-E. Sundgren, H. T. G. Hentzell, Structure and properties of nitride thin films grown by magnetron sputter deposition: effects of ion irradiation during growth, Journal of Vacuum Science and Technology, A 6 (1986) 1694-1695

[190] M. M. Khruschov, In: Proc. Conference on Lubrication and Wear. London: Institution of Mechanical Engineers; 1957. pp 655

[191] M. M. Khruschov, Principles of abrasive wear, Wear, 28 (1974) 69-88

[192] N. Axen, S. Jacobason, S. Hogmark, Influence of hardness of the counterbody in three-body abrasive wear-an overlooked hardness effect, Tribology International, 27 (1994) 233-241

[193] A. G. Evans, D. B. Marshall, Wear mechanisms in ceramics, Fundamentals of Friction and Wear Materials, ed. D. A. Rigney. ASM International, 1981, pp 439-452

[194] A. Broese van Groenou, Tribology of magnetic storage systems: a short review. JMMM 95 (1991), pp 289-312

[195] J.-E. Sundgren, H. T. G. Hentzell, A review of the present state of art in hard coatings grown from the vapor phase. Journal of Vacuum Science and Technology, A 5 (1986) 2259-2279

[196] W.-D. Munz, Titanium aluminum nitride films: A new alternative to TiN coatings, Journal of Vacuum Science and Technology, A 4 (1986) 2717-2725

[197] O. Knotek, M. Bohmer, T. Leyendecker, On structure and properties of sputtered Ti and Al based hard compound films, Journal of Vacuum Science and Technology, A 4 (1986) 2695-2700

[198] L. A. Donohue, W. –D. Munz, D. B. Lewis, J. Cawley, Large-scale fabrication of hard superlattice thin films by combined steered arc evaporation and unbalanced magnetron sputtering, Surface and Coatings Technol, 93 (1997) 69-87

[199]   P. Eh. Hovsepian, W. –D. Munz, Recent progress in large-scale production of nanoscale multilayer/superlattice hard coatings, Vacuum, 69 (2003) 27-36

[200]   F. H. W. Loffler, Systematic approach to improve the performance of PVD coatings for tool applications, Surface and Coatings Technology, 68 (1994) 729-740

[201] D. P. Monaghan, D. G. Teer, K. C. Laing, I. Efeoglu, R. D. Arnell, Deposition of graded alloy nitride films by closed field unbalanced magnetron sputtering, Surface and Coatings Technology, 59 (1993) 21-25

[202] D. Mclntyre, J. E. Greene, G. Hakansson, J.-E. Sundgren, W.-D. Munz, Oxidation of metastabe single-phase polycrystalline TiAlN films: Kinetics and mechanisms, Journal of Vacuum Science and Technology, 67 (1990)1542-1556

[203] C. W. Kim, K. H. Kim, Anti-oxidation properties of TiAlN film prepared by plasma-assisted chemical vapor deposition and roles of Al, Thin Solid Films, 307 (1997) 113-119

[204] S. Hogmark, P. Hedenqvist, S. Jacobson, Tribological properties of thin hard coatings: demands and evaluation, Surface and Coatings Technology, 90 (1997) 247-257

[205] S. Hogmark, S. Jacobson, J. STLE Lubrication Eng. 1992, pp 401

[206] X. Z. Ding, X. T. Zeng, Structural, mechanical and tribological properties of CrAlN coatings deposited by reactive unbalanced magnetron sputtering, Surface and Coatings Technology, 200 (2005) 1372-1376

[207] S. G. Kim, Y. L. Sang, H. H. Jun, Synthesis of CrN/AlN superlattice coatings using closed-field unbalanced magnetron sputtering process, Surface and Coatings Technology, 171 (2003) 91-95

[208]   A. Grill, Tribology of diamondlike carbon and related materials: an updated review, Surface and Coatings Technol, 94 (1997) 507-513

[209] C. Donnet, Recent progress on the tribology of doped diamond-like and carbon alloy coatings: a review, Surface and Coatings Technology, 100 (1998) 180-186

[210] A. Gangorpadhyay, Tribology Letters, 5 (1998) 25

[211] A. Grill, Diamond-like carbon: state of the art, Diamond and Related Materials, 8 (1999) 428-434

[212] E. C. Cutiongco, D. Li, Y. W. Chung, C. S. Bhatia, Trans. ASME 1996, 118, 543

[213]   K.-R. Lee K. Y. Eun, Tribology of diamond-like carbon coated VCR head drums, Materials Science and Engineering, A 209 (1996) 264-269

[214] J. Guttler, J. Reschke, Metal-carbon layers for industrial application in the automotive industry, Surface and Coatings Technology, 60 (1993) 531-535

[215] W. C. Oliver, G. M. Pharr, An improved technique for determining hardness and elastic modulus using load and displacement sensing indentation experiments. Journal of Materials Research, 7 (1992) 1564-1583

[216] M. Dao, N. Chollacoop, K. J. Van Vliet, T. A. Venkatesh, S. Suresh, Computational modeling of the forward and reverse problems in instrumented sharp indentation, Acta Materialia, 49 (2001) 3899-918

[217] Y. T. Cheng, C. M. Cheng, Scaling, dimensional analysis, and indentation measurments, Materials Science and Engineering, R 44 (2004) 91-149

[218] A. C. Fischer-Cripps, Critical review of analysis and interpretation of nanoindentation test data, Surface and Coatings Technology, 200 (2006) 4153-4165

[219] J. L. Bucaille, S. Stauss, E. Felder, J. Michler, Determination of plastic properties of metals by instrumented indentation using different sharp indenters, Acta Materialia, 51 (2003) 1663-1678

[220] N. Chollacoop, M. Dao, S. Suresh, Depth-sensing instrumented indentation with dual sharp indenters, Acta Materialia, 51 (2003) 3713-3729

[221] W. C. Oliver, G. M. Pharr, Measure of hardness and elastic modulus by instrumented indentation: Advances in understanding and refinements to methodology, Journal of Materials Research, 19 (2004) 3-20

[222] A. J. Perry, The adhesion of chemically vapour deposited hard coatings to steel-the scratch test, Thin Solid Films, 78 (1981)77-93

[223] H. E. Hintermann, Adhesion, friction and wear of thin hard coatings, Wear, 100 (1984) 381-97

[224] S. J. Bull, D. S. Rickerby, New developments in the modeling of the hardness and scratch adhesion of thin films, Surface and Coatings Technology, 42 (1990)149-164

[225] P. Benjamin, C. Weaver, Measurement of adhesion of thin films, Proceeding of Royal Society of London, A 254 (1960) 163-176

[226] S. J. Bull, Spallation failure maps from sceatch testing. High Temperature Materials and Processes, 13 (1995) 169-174

[227] S. J. Bull, Failure mode maps in the thin film scratch adhesion test, Tribology International, 30 (1997) 491-498

[228] S. J Bull, Scratch adhesion tesing and its significance for coating performance, in: Proceedings of the Second Australia International Confeenceon Surface Engineering, Adelaide, Australia, 1994

[229] F. Ramos, M. T. Vieira, Adhesion improvement of RF-sputtered alumina coatings as determined by the scratch test, in: K. L. Mittal (Ed.), Adhesion Measurement of Films and Coatings, VSP, Utrecht, 1995, pp 115-126

[230] B. Bhushan, J. N. Israelachvili, U. Landman, Nanotribology: Friction, Wear and Lubrication at the Atomic Scale, Nature, 374 (2004) 13-18

[231] B. Bhushan, Friction, Acratching/Wear, Indentation and Lubrication on Micro- to Nnaoscales, Micro/Nanotribology and its Application, edited by B Bhushan, Kluwer Academic Publishers, pp 169-191

[232] B. Bhushan, Nanoscale Tribophysics and Tribomechanics, Wear, 225 (1999) 465-492

[233] B. Bhushan, Nano-to-Microscale Wear and Mechanical Characterisation Using Scanning Probe Microscopy, Wear, 251 (2001) 1105-1123

[234] R. D. Ott, C. Ruby, F. Huang, M. L. Weaver, J. A. Barnard, Nanotribology and Surface Chemistry of reactively Sputtered Ti-B-N Hard Coatings, Thin Solid Films, 377 (2000) 601-606

[235] L. Y. Huang, K. W. Xu, Lu J, B. Guelorget, H. Chen, Nano-Scratch and Fretting Wear Study of DLC Coatings for Biomedical Application, Diamond and Related Materials, 10 (2001) 1448-1456

[236] T. W. Scharf, J. A. Barbard, Nanotribology of Ultrathin SiC/SiC-N Overcoats Using a Depth Sensing Nanoindentation Multiple Sliding Technique, Thin Solid Films, 308 (1997) 340-344

[237] V. D. McGinniss, Developing abrasion-resistance coatings. Paint and Coatings Industry, 22 (1994) 34-39

[238] D. C. Andrei, J. L. Keddie, J. N. Hay, S. G. Yeates, H. J. Briscoe, D. Parsonage, Nano-mechancial properties and topography of thermosetting acrylic powder coatings, Journal of Coatings Technology, 73 (2001) 65-73

[239] P. Bertrand-Lambotte, J. L. Loubet, C. Verpy, S. Pavan, Understanding of automotive clear coats scratch resistance, Thin Solid Films, 420 (2002) 281-286

[240] U. Schulz, V. Wachtendorf, T. Klimmasch, P. Alers, The influence of weathering on scratches and on scratch and mar resistance of automotive coatings. Prog Org Coat, 42 (2001) 38-48

[241] W. Shen, L. Mi, B. Jiang, Characterization of mar/scratch resistance of coatings with a Nano-indenter and a scanning probe microscope, Tribology International, 39 (2006) 146-158

[242] W. Shen, C. Ji, F. Jones, M. P. Everson, R. A. Rynt, Measuring scratch resistance and microharness of crosslinked coatings with a scanning force microscope, Polymeric Materials Science and Engineering, 74 (1996) 346-347

[243] W. Shen, C. Ji, F. Jones, M. P. Everson, R.A. Ryntz, Measurement by scanning force microscopy of the scratch and mar resistance of surface coatings, Surface Coatings International, 79 (1996) 253-256

[244] W. Shen, S. M. Smith, F. N. Jones, C. Ji, R. A. Ryntz, M. P. Everson,: Use of a scanning probe microscope to measure marring mechanisms and microhardness of cross linked coatings, Journal of Coatings Technology, 69 (1997) 123-128

[245] X. Zeng, S. Zhang, J. Hsieh, Development of graded Cr–Ti–N coatings, Surface and Coatings Technology, 102 (1998) 108-112

[246] X. Z. Ding, X. T. Zeng, Structural, mechanical and tribological properties of CrAlN coatings deposited by reactive unbalanced magnetron sputtering, Surface and Coatings Technology, 200 (2005) 1372-1376

[247] S. G. Harries, E. D. Doyle, A. C. Vlasveld, J. Audy, J. M. Long, D. Quick, Influence of chromium content on the dry machining performance of cathodic arc evaporated TiAlN coatings, Wear, 254 (2003) 185-194

[248] H. L. Coldwell, R. C. Dewes, D. K. Aspinwall, N. M. Renevier, D. G. Teer, The use of soft/lubricating coatings when dry drilling BS L168 aluminium alloy, Surface and Coatings Technology, 177 (2004) 716-726

[249] J. J. Nainaparampil, J. S. Zabinski, A. Korenyi-Both, Formation and characterization of multiphase film properties of (Ti–Cr)N formed by cathodic arc deposition, Thin Solid Films, 333 (1998) 88-94

[250] S. Ulrich, S. Sattel, Influence of low energy ion implantation on mechanical properties of magnetron sputtered metastable (Cr,Al)N thin films, Thin Sold Films, 437 (2003) 164-169

[251] J. H. Park, W. S. Chung, Y. R. Cho, K. H. Kim, Synthesis and mechanical properties of Cr–Si–N coatings deposited by a hybrid system of arc ion plating and sputtering techniques, Surface and Coatings Technology, 188 (2004) 425-430

[252] B. Rother, H. Kappl, Effects of low boron concentrations on the thermal stability of hard coatings, Surface and Coatings Technology, 96 (1997) 163-168

[253] J. Almer, M. Oden, G. Hakansson, Microstructure, stress and mechanical properties of arc-evaporated Cr–C–N coatings, Thin Solid Films, 385 (2001) 190-197

[254] F. Regent, J. Musil, Magnetron sputtered Cr-Ni-N and Ti-Mo-N films: comparison of mechanical properties, Surface and Coatings Technology, 142 (2001) 146-151

[255] M. Kawate, A. K. Hashimoto, T. Suzuki,- Oxidation resistance of $Cr_{1-X}Al_XN$ and $Ti_{1-X}Al_XN$ films, Surface and Coatings Technology, 165 (2003) 163-167

[256] K. E. Cooke, S. Yang, C. Selcuk, D. G. Teer, A. Kennedy, D. Beale, Development of duplex nitrided and closed field unbalanced magnetron sputter ion plated CrTiAlN-based coatings for H13 aluminium extrusion dies, Surface and Coatings Technology, 188 (2004) 697-702

[257] S. G. Harris, E. D. Doyle, A. C. Vlasvels, J. Audy, J. M. Long, D. Quick, Influence of chromium content on the dry machining performance of cathodic arc evaporated TiAlN coatings, Wear, 254 (2003) 185-194

[258] J. A. Heimberg, K. J. Wahl, I. L. Singer, A. Erdemir, Superlow friction behaviour of diamond-like carbon coatings: time and speed effects, Applied Physics Letters, 78 (2001) 2449-2451

[259] X.Y. Li, Y. Sun, A. Bloyce, XTEM characterisation of low temperature plasma nitrided AISI316 austenitic stainless steel, Institute of Physics Conference Series, 153 (1997) 633-636.

[260] D. Rafaja, V. Klemm, G. Schreiber, M. Knapp, J. Appl. Crystallogr. 37 (2004) 613

[261] D. Rafaja, V. Klemm, M. Dopita, Int. Union. Crystallogr. 34 (2007) 7 http: www.iucr-cpd.org/newsletters.htm

[262] W. C. Oliver, G. M. Pharr, An improved technique for determining hardness and elastic modulus using load and displacement sensing indentation experiments, Journal of Materials Research, 7, pp 1564-1583

[263] W. Shen, B. Jiang, S. M. Gasworth, H. Mukamal, Study of tribological properties of coating/substrate system in micrometer and nanometer scales with a scanning probe microscope, Tribology International, 34 (2001) 135-142

[264] T. Bell, Y. Sun, Glow discharge depth profiling-a powerful analytical technique in surface engineering, Proceedings of the 5th IHSTSE Seminar, Isfahan, Iran, 26-28 Sept 1995

[265] T. Asam, Glow discharge potical spectroscopy depth profile analysis of conductive and non-conductive samples in a commercial service laboratory, Surface and Coatings Technology, 116 (1999) 310-312

[266] A. Vysa, Y. G. Shen, Z. F. Zhou, K. Y. Li, Nano-structurred CrN/CNx multilayer films deposition by magnetron sputtering, Composites Science and Technology, 68 (2008) 2922-2929

[267] D. Rafaja, M. Dopita, M. Růžička, V. Klemm, D. Heger, G. Schreiber, M. Šíma, Microstructure development in Cr-Al-Si-N nanocomposites deposited by cathodic arc evaporation, Surface and Coatings Technology, 201 (2006) 2835-2843

[268] D. Rafaja, A. Poklad, V. Klemm, G. Schreiber, D. Heger, M. Šíma, Microstructure and hardness of nanocrystalline $Ti_{1-x-y}Al_xSi_yN$ thin films, Material Science and Engineering, A 462 (2007) 279–282

[269] S. M. Aouadi, K. C. Wong, K. A. R. Mitchel, F. Namavar, E. Tobin, D. M. Mihut, S. L. Rohde, Characterization of titanium chromium nitride nanocomposite protective coatings, Applied Surface Science, 229 (2004) 387-394

[270] V. M. Vishnyakov, V. I. Bachurin, K. F. Minnebaev, R. Valizadeh, D. G. Teer, J. S. Colligon, V. V. Vishnyakov, V. E. Yurasova, Ion assisted deposition of titanium chromium nitride, Thin Solid Films, 497 (2006) 189-195

[271] X. Feng, Y. Bai, B. Lu, C. Wang, Y. Liu, G. Geng, L. Li, Easy synthesis of TiC nanocrystallite, Journal of Crystal Growth, 264 (2004) 316-319

[272] D. V. Shtansky, Ph. V. Kiryukhantsev-Korneev, A. N. Sheveyko, B. N. Mavrin, C. Rojas, A. Fernandez, E. A. Levashov, Comparative investigation of TiAlC(N), TiCrAlC(N), and CrAlC(N) coatings deposited by sputtering of MAX-phase $Ti_{2-x}Cr_xAlC$ targets, Surface and Coating Technology, 203 (2009) 3595-3609

[273] E. Damond, P. Jacquot, J. Pagny, TiC_xN_{1-x} coatings by using the arc evaporation technique, Materials Science and Engineering, A 140 (1991) 838-841

[274] B. Stypula, The characterization of passive films on chromium electrodes by XPS, Corrosion Science, 36 (1994) 2159-2167

[275] P. Marcus, M.E. Bussell, XPS study of the passive films formed on nitrogen-implanted austenitic steels, Applied Surface Science 59 (1992) 7-21

[276] C. Cardinaud, G. Lemperiere, M. C. Peignon, P. Y. Jouan, Characterisation of TiN coatings and of the TiN/Si interface by X-ray photoelectron spectroscopy and Auger electron spectroscopy, Applied Surface Science, 68 (1993) 595-603

[277] A. Vyas, Y. G. Shen, Z. F. Zhou, K. Y. Li, Nano-structured CrN/CN_x multilayer films deposited by magnetron sputtering, Composites Science and Technology, 68 (2008) 2922-2929

[278] S. Grouderva-Zotova, R. G. Vitchev, B. Blanpain, Phase composition of Cr-C thin films deposited by a double magnetron sputtering system, Suface and Interface Analysis, 30 (2000) 544-548

[279] J. T. Titantah, D. Lamoen, Carbon and nitrogen 1s energy levels in amorphous carbon nitride systems: XPS interpretation using first-principles, Diamond and Related Materials, 16 (2007) 581-588

[280] J. L. Vossen, W. Kern, Thin Film Processes, Academic Press, 1978 pp 15

[281] R. Wuhrer, W. Y. Yeung, A comparative study of magnetron co-sputtered nanocrystalline titanium aluminium and chromium aluminium nitride coatings, Scripta Materialia, 50 (2004) 1461-1466

[282] D. V. Shtansky, K. Kaneko,Y. Ikuhara, E. A. Levashov, Characterization of nanostructured multiphase Ti–Al–B–N thin films with extremely small grain size, Surface and Coatings Technology, 148 (2001) 206-215

[283] K. Kutschej, P. H. Mayrhofer, M. Kathrein, P. Polcil, R. Tessadri, C. Mitterer, Structure, mechanical and tribological properties of sputtered $Ti_{1-x}Al_xN$ coatings with $0.5 \leq x \leq 0.75$, Surface and Coatings Technology, 200 (2005) 2358-2365

[284] R. Sanjines, P. Hones, F. Levy, Hexagonal nitride coatings: electronic and mechanical properties of V_2N, Cr_2N and δ-MoN Thin Solid Films, 332 (1998) 225-229

[285] I. Milosev, H. -H. Strehblow, B. Navinsek, XPS in the study of high-temperature oxidation of CrN and TiN hard coatings Surface and Coatings Technology, 74 (1995) 897-902

[286] I. Ikemoto, K. Ishii, S. Kinoshita, H. Kuroda, M. A. A. Franco, J. M. Thomas, X-ray photoelectron spectroscopic studies of CrO_2 and some related chromium compounds, Journal of Solid State Chemistry, 17 (1976) 425-430

[287] M. J. Goldbery, J. G. Clabes, C. A. Kovac, Metal-polymer chemistry; Chromium-polyimide interface reactions and related organometallic chemistry, Journal of Vacuum Science and Technology, A 6 (1988) 991-996

[288] B. F. Dzhuriuskii, D. Gati, N. P. Sergushin, V. I. Nefedov, Y. A. V. Salyn, Simple and coordination compunds, Russion Journal of Inorganic Chemistry, 20 (1975) 2307-2314

[289] Y. Shi, S. Y. Long, S. C. Yang, F. S. Pan, Structural and tribological properties of CrTiAlN coatings on Mg alloy by closed-field unbalanced magnetron sputtering ion plating, Applied Surface Science, 254 (2008) 7342-7350

[290] S. Logothetidis, C. Charitidis, Elastic properties of hydrogen-free amorphous carbon thin films and their relation with carbon–carbon bonding, Thin Solid Films, 353 (1999) 208-213

[291] T. Pachler, R.M. Souza, A.P. Tschiptshin, Finite element analysis of peak stresses developed during indentation of ceramic coated steels, Surface and Coatings Technology, 202 (2007) 1098-1102

[292] J. L. Mo, M. H. Zhu, B. Lei, Y. X. Leng, N. Huang, Comparsion of tribological behaviours of AlCrN and TiAlN coatings—Deposited by physical vapor deposition, wear, 365 (2007) 1423-1429

[293] P. L. Tam, Z. F. Zhou, P. W. Shum, K. Y. Li, Structural, mechanical, and tribological studies of Cr-Ti-Al-N coating with different chemical compositions, Thin Solid Films, 516 (2008) 5725-5731

[294] G. Zhang, A. K. Schlarb, Correlation of the tribological behaviors with the mechanical properties of poly-ether-ether-ketones with different molecular weights and their filled composites, wear, 266 (2009) 1-2

[295] C. V. Budtz-Jorgensen, J. Bottiger, P. Kronghoj, Energetic ion bombardment of the grounded anode in pulsed DC-glow discharges   Surface and Coatings Technology, 137 (2001) 104-110

[296] S. M. Rossnagel, J. J. Cuomo, Ion beam bombardment effects during films position, Vacuum 38 (1988) 73-81

[297] J. S. Colligon, Journal of Vacuum Science and Technology A, 13 (1995) 1649-1657

[298] D. V. Shtansky, P. V. KiryuRhantsev-Korneev, A. N. Sheveyko, B. N. Mavrin, C. Rojas, A. Fernandez, E. A. Levashov, Conparative inverstigation of TiAlC(N), TiCrAlC(N), and CrAlC(N) coatings by spyttering of Max-phase $Ti_{2-x}Cr_xAlC$ targets, surface and Coatings Technology, 203 (2009) 3595-3609

[299] F. H. W. Loffler, Formation of non-equilibrium phases in the PVD process, Vacuum, 43 (1992) 397-401

[300] L. A. Donohue, J. Cawley, J. S. Brooks, W. –D. Munz, Deposition and characterisation of TiAlZrN films produced by unbalanced magnetron sputtering technique, 74 (1995) 123-134

[301] X. Z. Ding, X. T. Zeng, Structural, mechanical and tribological properties of CrAlN coatings deposited by reactive unbalanced magnetron sputtering, 200 (2005) 1372-1376

[302] A. Kimura, M. Kawate, H. Hasegawa, T. Suzuki, Anisotropic lattice expansion and shrinkage of hexagonal TiAlN and CrAlN films, 169 (2003) 367-370

[303] F. H. W. Loffler, Formation of non-equilibrium phases in the PVD process, Vacuum, 43 (1992) 397-401

[304]   S. D. Bergerand, D. R. Mckenzie, EELS analysis of vacuum arc-deposited diamond-like films, Philosophical Magazine Letters, 57 (1988) 285-190

[305]   R. F. Egerton, M. J. Whelan, The electron energy loss spectrum and band structure of diamond Philosophical Magazine Letters, 30 (1974) 739-749

[306]   X. Weng, P. Rez, H. Ma, Carbon *K*-shell near-edge structure: Multiple scattering and band-theory calculations Physical Review B, 40 (1989) 4175-4178

[307]   D. Galvan, Y. T. Pei, J. Th. M. De Hosson, Deformation and failure mechanism of nano-composite coatings under nano-indentation, Surface and Coatings Technology, 200 (2006) 6718-6726

[308] M. Panjan, T. Peterman, M. Cekada, P. Panjan, Simulation of a multilayer structure in coatings prepared by magnetron sputtering, 204 (2009) 850-853

[309] H. Holleck, V. Schier, Multilayer PVD coatings for wear protection, Surface and Coatings Technology, 76 (1995) 328-336

[310] P. E. Hovsepian, D. B. Lewis, W. –D. Munz, Recent progress in large scale manufacturing of multilayer/superlattice hard coatings, Surface and Coatings Technology, 133 (2000) 166-175

[311] D. G. Teer, Technical note: A magnetron sputter Ion-plating system, Surface and Coatings Technology, 39 (1989) 565-572

[312]   M. Gabisch, Y. Liu, L. Spiess, H. Romans, S. Krischok, G. Ecke, J. A. Schaefer, Ch. Knedlik, Nanoscale multilayer WC/C coatings developed for nanopositioning: Part I. Microstructures and mechanical properties, Thin Solid Films, 488 (2005) 132-139

[313]   J. A. Thornton, Influence of apparatus geometry and deposition conditions on the structure and topography of thick sputtered coatings, Journal of Vacuum Science and Technology Archives, 11 (1974) 666-670

[314]   D. S. William, Multilayer, multicomponent, and multiphase physical vapor deposition coatings for enhanced performance, Journal of Vacuum Science and Technology A, 4 (1986) 3059-3061

[315]   M. Panjan, S. Sturm, P. Panjan, M. Cekada, TEM investigation of TiAlN/CrN multilayer coatings prepared by magnetron sputtering, Surface and Coatings Technology, 202 (2007) 815-819

[316] M. Stueber, P. B. Barna, M. C. Simmonds, U. Albers, H. Leiste, C. Ziebert, H. Holleck, P. Hovsepian, I. Gee, Constitution and microstructure of magnetron sputtered nanocomposite coatings in the system Ti–Al–N–C, Thin Solid Films, 493 (2005) 104-112

[317] M. Stueber, U. Albers, H. Leiste, S. Ulrich, H. Holleck, P. B. Barna, A. Kovacs, P. Hovsepian, I. Gee, Multifunctional nanolaminated PVD coatings in the system Ti–Al–N–C by combination of metastable fcc phases and nanocomposite microstructures, Surface and Coatings Technology, 200 (2006) 6162-6171

[318] C. Uebing, Formation of surface compunds on Fe-15%Cr (100) single crystals, 225 (1990) 97-106

[319] J. Patscheider, T. Zehnde, M. Diserens, Structrure-performance relations in nanocomposite coatings, Surface and Coatings Technology 146 (2001) 201-208

[320]   O. Knotek, R. Breidenbach, F. Jungblut, Superhard Ti-B-C-N coatings, Surface and Coatings Technology, 43 (1990) 107-115

[321] C. Mitterer, M. Rauter, Sputter deposition of ultrahard coatings within the system Ti-B-C-N, Surface and Coatings Technology, 41 (1990) 351-363

147

[322] W. Gissler, Structure and properties of Ti-B-N coatings, Surface and Coatings Technology, 68 (1994) 556-563

[323] D. Galvan, Y. T. Pei, J. Th. M. De Hosson, Deformation and failure mechanism of nano-composite coatings under nano-indentation, Surface and Coatings Technology, 200 (2006) 6718-6726

[324] D. B. Maeshall, B. R. Lawn, P. Chantikul, Residual stress effects in sharp contact cracking, Journal of Materials Science, 60 (1997) 86

[325] G. R. Anstis, P. Chantikul, B. R. Lawn, D. B. Manshall, A critical evaluation of indentation techniques for measuring fracture toughness: I, direct crack measurement, Journal of the American Ceramic Society. 64 (1981) 533

[326] Y. T. Pei, D. Galvan, J. T. M. De Hosson, Nanostructure and properties of TiC/a-C:H composite coatings, Acta Materialia, 53 (2005) 4505-4521

[327] S. Veprek, The search for novel, superhard materials, Journal of Vacuum Science and Technology A, 17 (1999) 2401-2420

[328] J. Musil, Hard and superhard nanocomposite coatings, Surface and Coatings Technology, 125 (2000) 322-330

[329] Kenneth Holmberg, Allan Matthews, Helena Ronkainen, РП: S0301-679X(98)00013-9

[330] M. M. Khonsari, E. R. Boo, Applied tribology: bearing design and lubrication, 1885, pp 56

[331] I. L. Singer, R. N. Bolster, J. Wegand, S. Fayeulle, B. C. Stupp, Role of third bodies in friction and wear, Applied Physics Letters, 57 (1990) 995-999

[332] B.t Bhushan, M. Nosonovsky, Comprehensive model for scale effects in friction due to adhesion and two- and three-body deformation (plowing), Acta Materialia, 52 (2004) 2461-2474

[333] E. F. Finkin, what happens when parts wear, Mach. Des., 42 (1970) 148

[334] M. M. Tenenbaum, Abrasive wear of construction materials and machine parts, Izd-Vo Macinostroyeniye, Moscow, 1996

[335] J. C. Knight, T. F. Page, H. W. Chandler, Thermal instability of the microstructure and surface mechanical properties of amorphous carbon films, Surface and Coatings Technology, 49 (1991) 519-529

[336] T. A. Friedmann, K. F. Mecarty, J. C. Barbour, M. P. Siegal, B. C. Dibble, Thermal stability of amorphous carbon films grown by pulsed laser deposition, Applied Physics Letters, 68 (1996) 1643-1649

[337] M. W. Choose, C. A. Davies, J. R. Dourey, D. J. Frury, R. A. McDorald, A. N. Syverud, Journal of Physcial and Chemical Reference Data, 21 (1985) 941-1004

[338] F. Shao, Z. Liu, Y. Wan, Matching of Al_2O_3 Ceramic Tools with Workpiece Materials Bases of Thermodynamics, 2009 International. Conference on Interlligent Human-Machine Systems and Cybernetics. Ihmsc, vd. 1, pp 221-224

[339] A. Kostov, B. Friedrich, Selection of crucible oxides in molten titanium and titanium aluminum alloys by thermo-chemistry calculations, Journal of Mining and Metallurgy, 41 B (2005) 113-125

[340] Y. K. Yao, Stoichiometry and Themodynamic of Metallurgical Processes, Cambridge University Press, Cambridge, 1985

[341]   Q. Luo, W. M. Rainforth, W. D. Munz, TEM observations of wear mechanisms of TiAlCrN and TiAlN/CrN coatings grown by combined steered-arc/unbalanced magnetron deposition, Wear 225 (1999) 74-82

[342]   P. E. Hovsepian, D. B. Lewis, W. D. Munz, Recent progress in large scale manufacturing of multilayer/superlattice hard coatings, Surface and Coatings Technology 133 (2000) 166-175

[343] J. M. Yanez-Limon, F. Ruiz, J. Gonzalez-Hernandez, B. S. Chao, S. R. Ovshinsky, Journal of Applied Physics, 78 (1995) 3015-3019

[344] J. Lin, B. Mishra, J. J. Moore, W. D. Sproul, Structure and properties of Ti–B–C–N nanocomposite coatings synthesized using pulsed closed field unbalanced magnetron sputtering (P-CFUBMS), Surface and Coatings Technology, 203 (2008) 588-593

Table 2.2-1: Carbides, nitrides, oxides and borides employed to combat corrosion and wear.

Resource: Ref [125]

Carbides	Nitrides	Oxides	Borides
Corrosion-resistant ceramics			
SiC	Si_3N_4, Sialon	Al_2O_3	TiB_2
HfC	HfN	SiO_2	MoB
ZrC	ZrN	TiO_2	WB
	TiN	ZrO_2	NbB_2
		SnO_2	TaB_2
		$MgAl_2O_4$	ZrB_2
		MgO	HfB_2
		Cr_2O_3	
Tribological ceramics			
TiC	TiN	Al_2O_3	TiB_2
HfC	HfN	SiO_2	MoB
ZrC	Si_3N_4	TiO_2	WB
SiC	BN	ZrO_2	NbB_2
B_4C	ZrN	Ta_2O_5	TaB_2
B_2C	TaN	Cr_2O_3	ZrB_2
W_2C	AlN	HfO_2	HfB_2
Cr_7C_3	VN	V_2O_3	VB
Cr_2O_3	NbN		
$Cr_{23}C_6$			
TaC			
VC			
NbC			
WC			

Table 2.2-2: Various compounds used as coating materials for tribological applications.

Data from various sources

	IV B			V B			VI B			III A		IV A	
	Ti	Zr	Hf	V	Nb	Ta	Cr	Mo	W	B	Al	Si	
B	●	●				●							
C	●	●	●	●	●	●	●		●	●		●	
N	●	●	●	●	●	●	●	●		●	●	●	
O	●	●					●				●		
CN	●	●											
ON	●												
OCN	●												

Table 2.2-3: Ternary and quaternary hard compounds used as tribological coatings.

Data from various sources

	Ti											
	Zr	Hf	V	Nb	Ta	Cr	Mo	W	Al	Si	AlV	AlZr
B												
C												
N	●	●	●	●	●	●			●	●		
O									●		●	●
CN			●						●	●	●	
ON									●			
OCN									●			

Table 2.2-4: Classification of various hard materials. Data from various sources

Metallic	Covalent	Ionic
Borides	borides	oxides of Al, Zr, Ti, Be
carbides	carbides	
nitrides of the transition metals	nitrides of Al, Si, B, diamond	
e.g. TiB, TiC, TiN, VC, WC	e.g. B_4C, SiC, BN	e.g. Al_2O_3, ZrO_2, BeO

Table.2.2-5: Properties and bahaviour of various groups of hard materials.

Data from various sources

Properties and behaviour of carious groups of hard materials (M=Metallic; C=Covalent; I=Ionic)

Level	Hardness	Brittleness	Marking Point	Stability $-\triangle G$	Thermal Expansion Co-efficient	Adherence to Metallic Substrates	Interaction tendency	Multilayer Suitability
High	C	I	M	I	I	M	M	M
↓	M	C	C	M	M	I	C	I
Low	I	M	I	C	C	C	I	C

Table 3.1-1: Chemical composition of M2 High speed steel

Element	C	Si	Mn	Cr	Mo	V	W	Fe
Composition (wt%)	0.78-0.88	0.20-0.40	0.20-0.40	3.75-4.50	4.50-5.50	1.60-2.20	5.50-6.75	balance

Table 3.2-1: Typical deposition conditions for carbon-doped CrAlTiCN coatings

by the CUMSIP system

| Variable	CrAlTiN-0#	CrAlTiCN-1#	CrAlTiCN-2#	CrAlTiCN-3#	CrAlTiCN-4#	CrAlTiCN-5#
Cr/Al/Ti target current	4.5/3.5/3.5A	4.5/3.5/3.5A	4.5/3.5/3.5A	4.5/3.5/3.5A	4.5/3.5/3.5A	4.5/3.5/3.5A
C target current	0 A	1 A	2 A	3 A	4 A	5 A
Bias				70 V		
Base pressure				$< 3.0 \times 10^{-3}$ Pa		
Substrate rotation speed				5 rpm		
Typical coatings thickness				$\sim$4.5 μm		

Table 3.3-1: XRD settings

Variable	Value
Scan-Detector arrangement	θ-2θ
Step size (2θ)	$0.02°$
Scan step time (s)	1.00 s
Scan type	Continuous
Anode material	Cu
Generator settings	40 KV, 40 mA
Used wavelength ($K_{\alpha 1}$)	1.540 Å

Table 3.3-2: AFM settings

Tip	
Height	2.5 μm-3.5 μm
Front and side angles	$35°$
Tip radius	20 nm

Cantilever	
Material	Silicon nitride
Top layer	Au (60 nm)
Shape	Triangular
Length	180 μm
Width	33 μm
Elastic constant	0.12 N/m

Table 3.3-3: Stylus profilometer settings for different measurements

Parameter	Roughness	Wear track
Filter	Gaussian	2CR
λ_c	0.8 mm	2.5 mm
Length	5.0 mm	2.5 mm
Standard	ISO/BS	ANSI/JIS 82
Data	$R_a/R_y/R_z$	PPFL
Tip radius	2 µm	2 µm

Table 4.2-1: Surface roughness of CrAlTiN and carbon-doped CrAlTiCN coatings

Sample	CrAlTiN-0#	CrAlTiCN-1#	CrAlTiCN-2#	CrAlTiCN-3#	CrAlTiCN-4#	CrAlTiCN-5#
Roughness (μm)	0.0303 ±0.0013	0.0315 ±0.0015	0.0378 ±0.0018	0.0372 ±0.0028	0.0405 ±0.0035	0.0388 ±0.0022

Table 4.2-2: Elemental concentration of CrAlTiN and carbon-doped CrAlTiCN coatings using EDX and WDX

Sample	Element (at %)						
	WDX		EDX				
	N	C	Al	Ti	Cr	N	C
CrAlTiN-0#	45.98		6.87	6.07	40.53	46.53	
CrAlTiCN-1#	44.12	2.34	6.96	6.45	40.13	43.54	2.92
CrAlTiCN-2#	47.02	3.96	6.58	5.09	37.35	46.29	4.69
CrAlTiCN-3#	44.79	9.65	5.91	5.87	33.78	45.69	8.75
CrAlTiCN-4#	41.87	12.53	6.09	5.33	34.18	42.14	12.26
CrAlTiCN-5#	33.16	24.34	5.78	5.35	31.37	35.18	22.32

Table 4.2-3: Lattice parameters and grain sizes of carbon-doped coatings from GAXRD

Sample	Stress-free lattice parameter	Crystallite size
CrAlTiCN-1#	(0.4135 ± 0.004) nm	(3.0 ± 0.5) nm
CrAlTiCN-3#	(0.4152 ± 0.003) nm	(3.0 ± 0.6) nm
CrAlTiCN-5#	(0.4141 ± 0.004) nm	(2.5 ± 0.4) nm

Table 4.3-1: Micro-mar resistance of CrAlTiN and carbon-doped CrAlTiCN coatings

Sample	CrAlTiN-0#	CrAlTiCN-1#	CrAlTiCN-2#	CrAlTiCN-3#	CrAlTiCN-4#	CrAlTiCN-5#
MMR (GPa)	634	527	503	491	375	357

Table 4.3-2: Critical load of scratch obtained on as-deposited coatings

Sample	CrAlTiN-0#	CrAlTiCN-3#	CrAlTiCN-5#
Critical Load (L_c) (N)	42	36	33

Table 4.4-1: Coefficient of friction of CrAlTiN and carbon-doped CrAlTiN coatings

Sample	CrAlTiN-0#	CrAlTiCN-1#	CrAlTiCN-2#	CrAlTiCN-3#	CrAlTiCN-4#	CrAlTiCN-5#
Cof	0.655 ±0.003	0.420 ±0.003	0.410 ±0.006	0.375 ±0.003	0.400 ±0.001	0.350 ±0.002

Table 4.5-1: Critical load of scratch obtained on 700 ℃/2 hrs oxidised coatings

Sample	CrAlTiN-0#	CrAlTiCN-3#	CrAlTiCN-5#
Critical Load (L_c) (N)	7	9	11

Table 5.1-1: Atomic radius and ionic radius

Data from various sources

Element	Cr	Al	Ti	C	N
Atomic radius ($\times 10^{-12}$ m)	128	125	140	70	65
Ionic radius ($\times 10^{-12}$ m)	90.5 (2+ ion) 75.5 (3+ ion)	53.5 (3+ ion)	100 (2+ ion) 81 (3+ ion)		

Table 5.2-1: H/E and H^3/E^{*2} ratios

	CrAlTiN-0#	CrAlTiCN-1#	CrAlTiCN-2#	CrAlTiCN-3#	CrAlTiCN-4#	CrAlTiCN-5#
H^3/E^{*2} 10^{-2}	16.44	15.50	13.40	9.97	9.27	9.08
H/E 10^{-3}	86.49	84.86	81.85	77.11	75.15	74.61

Table 5.3-1: Elastic contact stress of wear tests

Test	Contact load (N)	Ball diameter (mm)	Contact radius (μm)	Hertz stress (GPa)
Pin-on-disc (WC-Co)	20	5	59.84	2.668
Reciprocating (WC-Co)	50	8	94.99	2.667
Fretting (Cobalt-Chromium)	100	40	495.90	0.194

Table 5.3-2: Comparison of friction coefficient and wear volume lost

Sample	Cof	Worn volume		
			Fretting	
	Unidirectional sliding		Room temperature	350 ℃
GLC coating	0.273	3.5×10^6 μm^3	5.8×10^5 μm^3	8.3×10^5 μm^3
CrAlTiN-0#	0.655	7.8×10^6 μm^3	7.0×10^5 μm^3	4.8×10^5 μm^3
CrAlTiCN-5#	0.350	5.1×10^6 μm^3	6.2×10^5 μm^3	6.5×10^5 μm^3
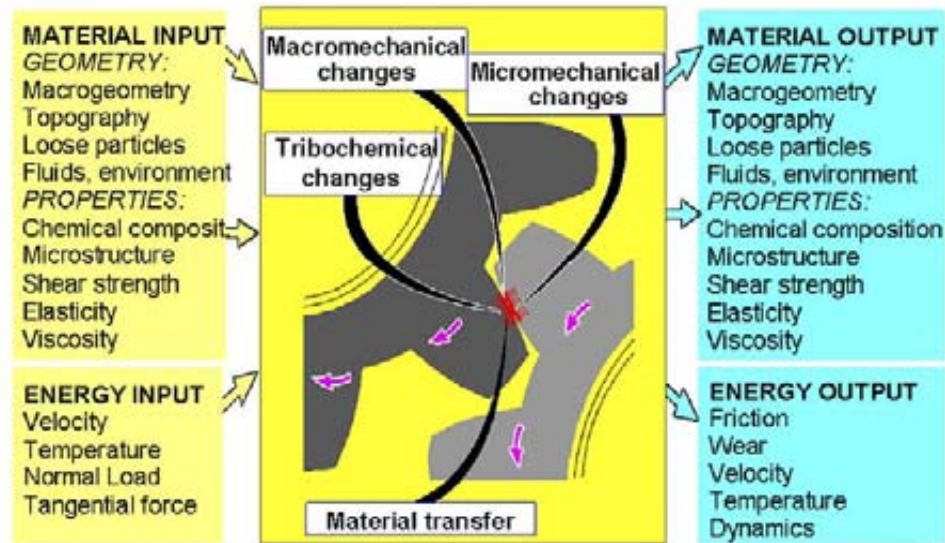
Figure 2.1-1: The tribological contact process is determined by a number of geometry, material and energy related parameters, including changes that can be described on e.g. macro- micro- and nano-level and results in friction, wear and changed contact conditions. Source: Ref [37]
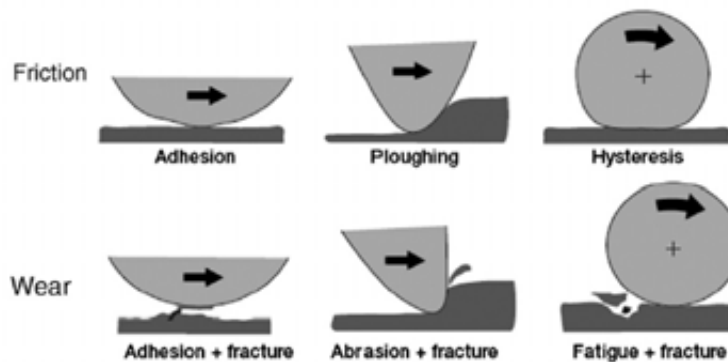
Figure 2.1-2: The basic friction and wear mechanisms are related to adhesion, ploughing and hysteresis. In the case of wear these contact mechanisms results in material fracture, detachment and removal. Source: Ref [38-40]
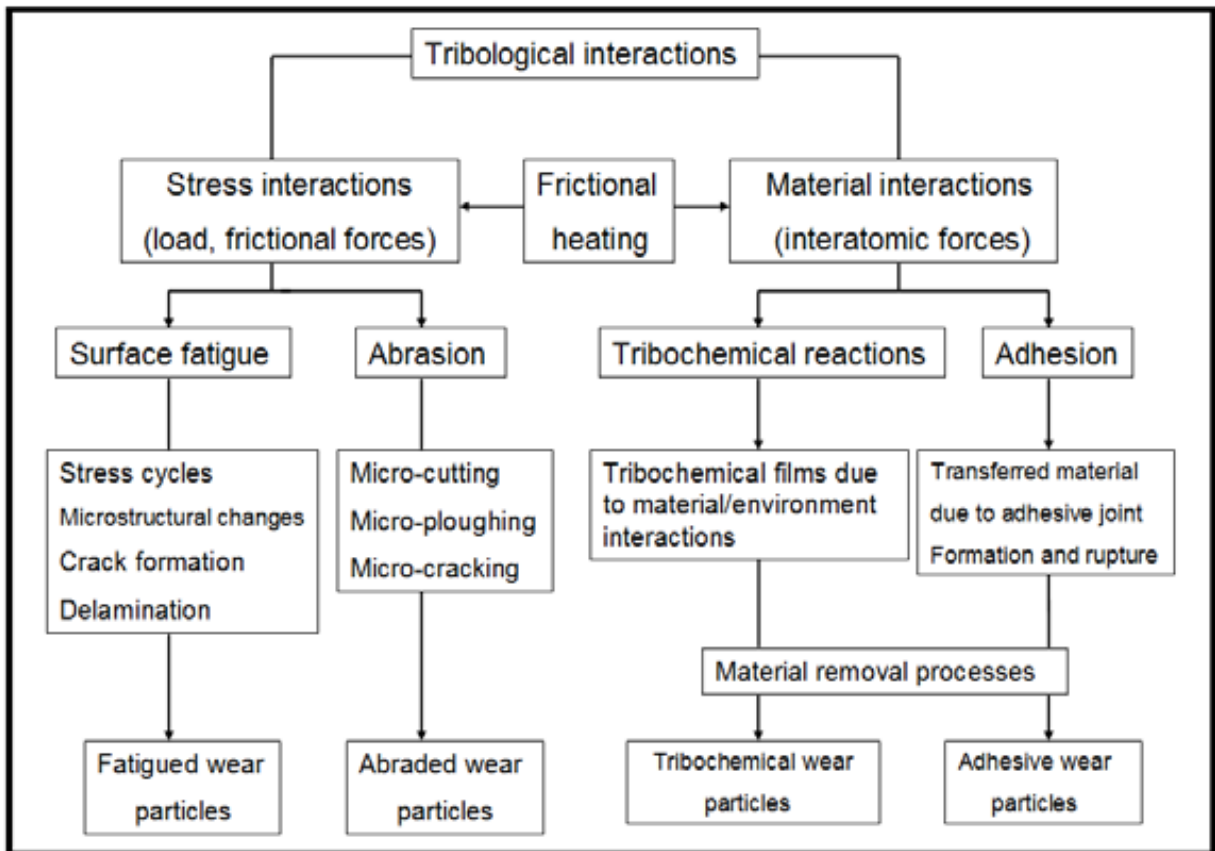
Figure 2.1-3: Tribological interactions and wear mechanisms. Source: Ref [63]

$$W_V = k \cdot s \cdot F_N/H$$
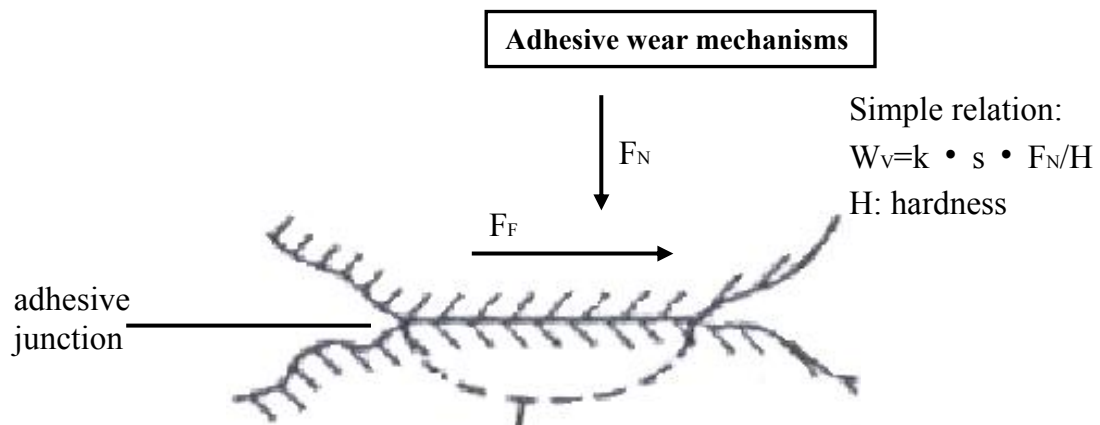
Adhesive wear model:

(1) asperity contact deformation;

(2) removal of surface films;

(3) formation of adhesive junctions;

(4) fracture of junctions and transfer of material;

(5) modification of transferred fragments (e.g. strain energy storage, tribochemical effects);

(6) removal of transferred/backtransferred fragments (e.g. by frtigue, fracture, abrasion)

Figure 2.1-4: Adhesive wear model. Source: Ref [55]
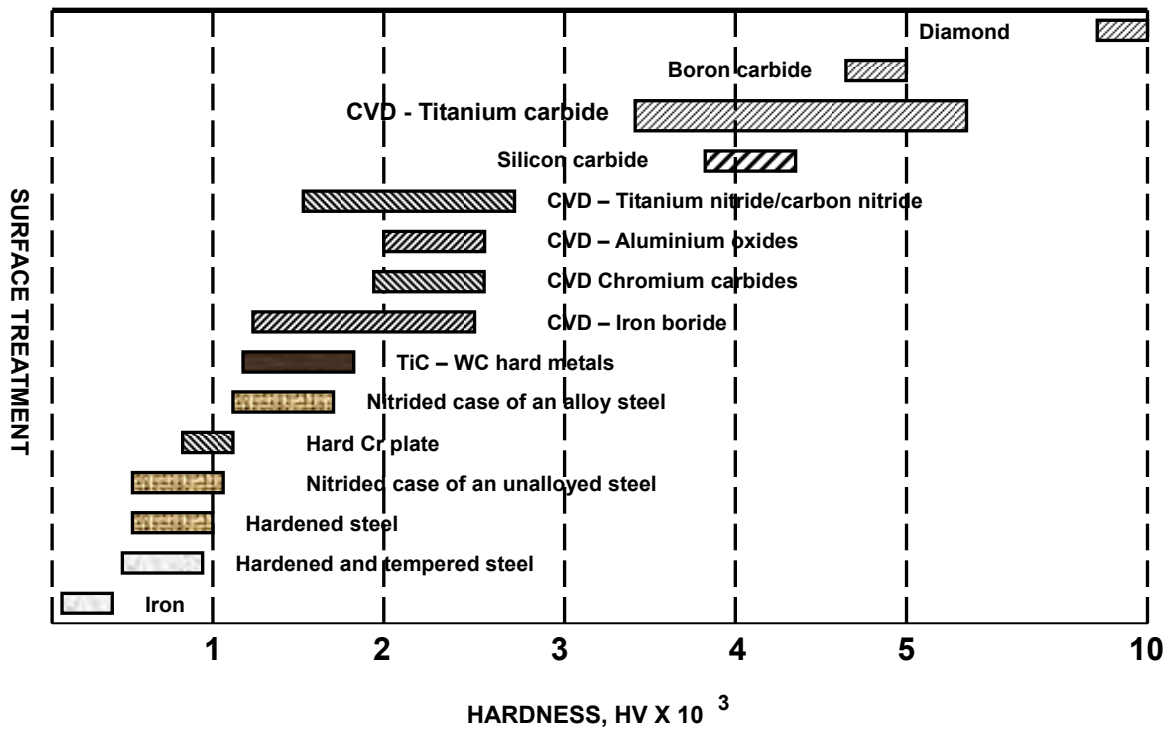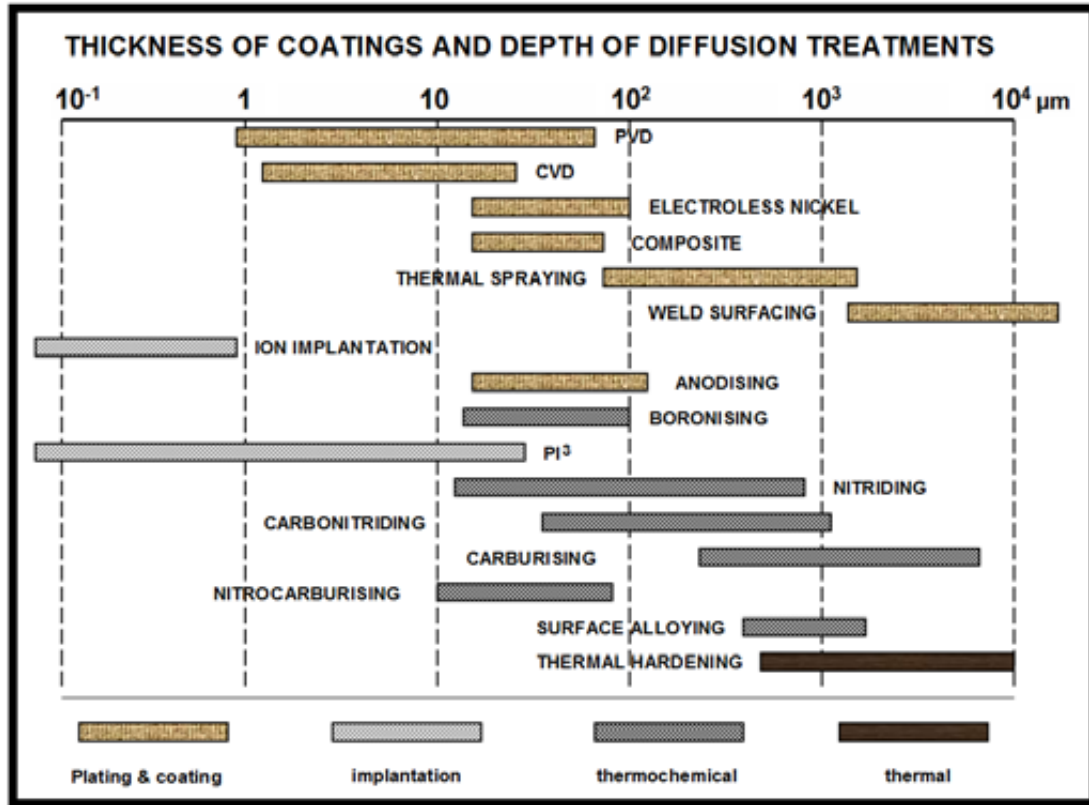
Figure 2.1-5: typical thickness and hardness of surface engineered layers.

Source: Ref [84,85]
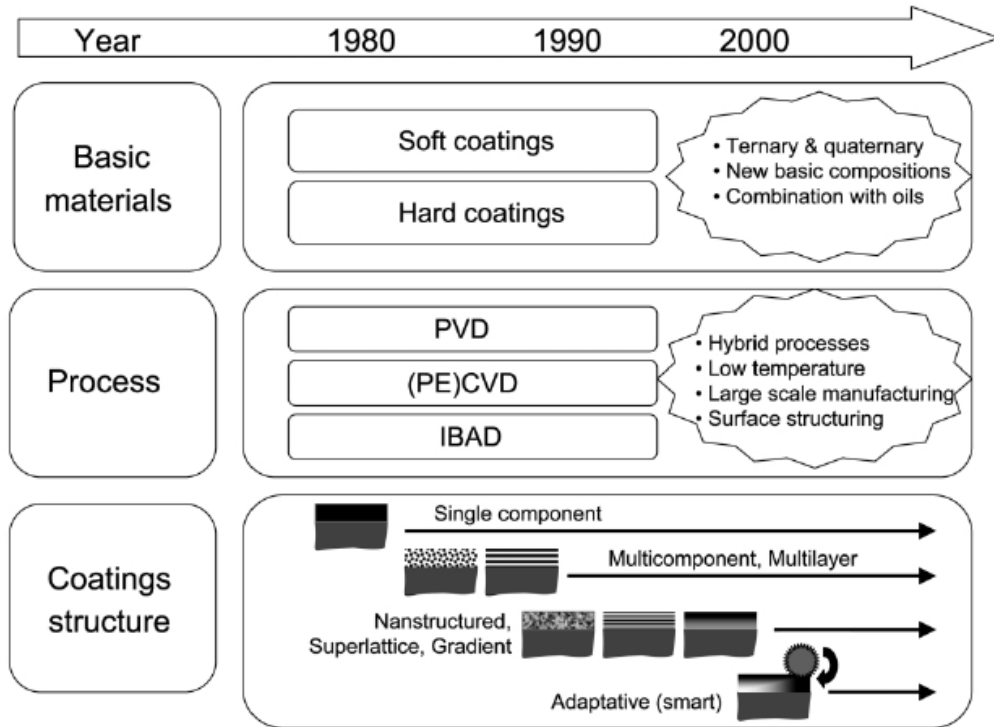
Figure 2.2-1: Historical development of tribological coatings and solid films.

Source: Ref [88]
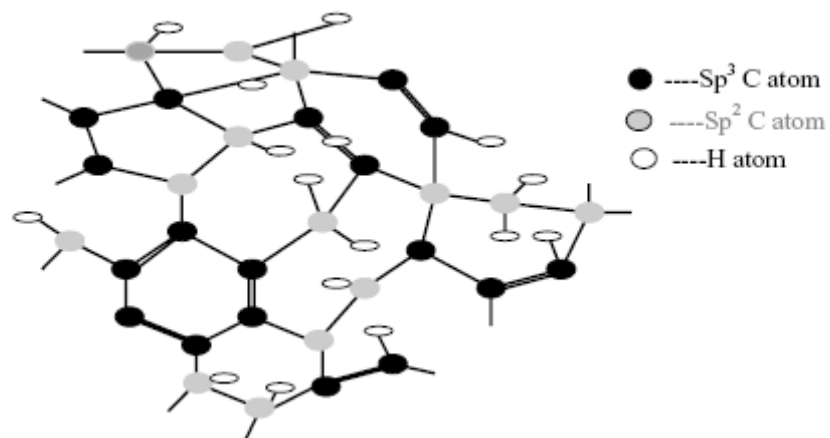
Figure 2.2-2: In DLC sp2-bonded carbon interconnected by a random network of sp3-

bonded atomic sites. Source: Ref [105]
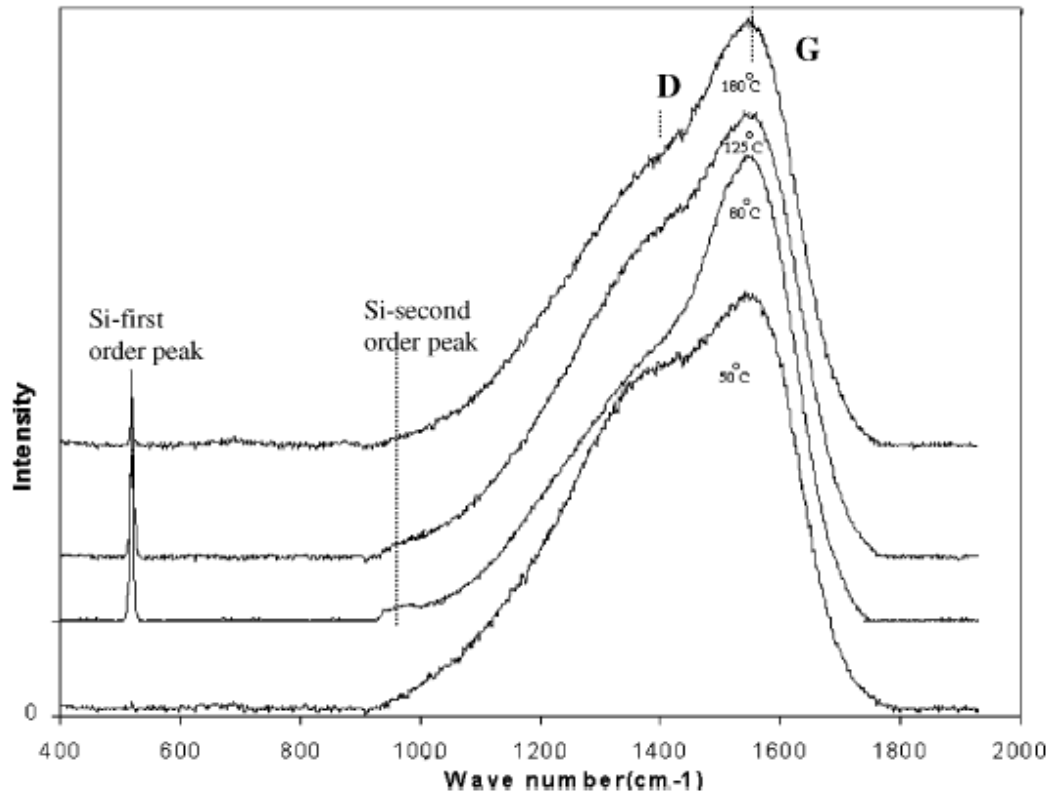
Figure 2.2-3: Raman spectra of DLC films at different temperature. Source: Ref [107]
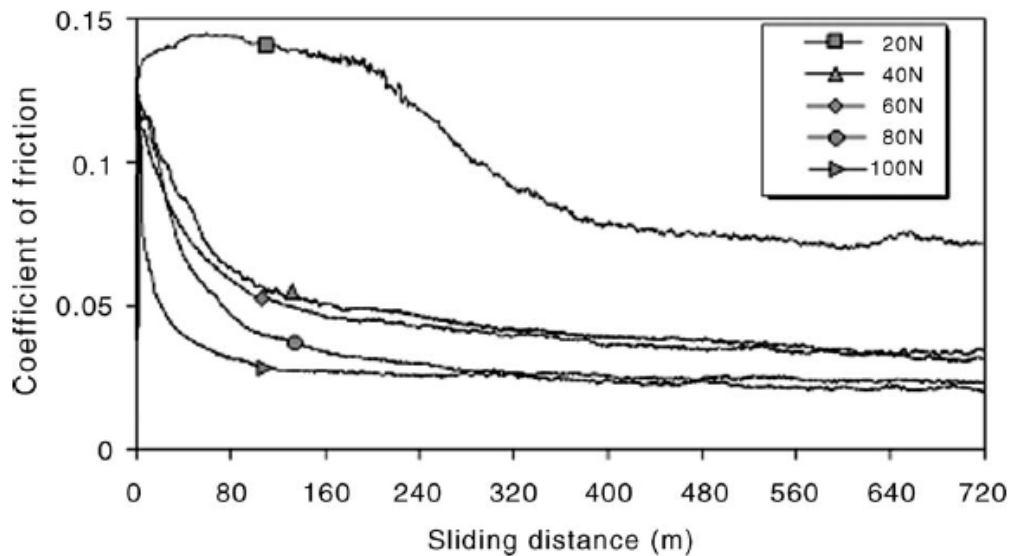
Figure 2.2-4: Fiction coefficient of GiC coating as a function of the sliding distance using

applied normal loads equal to 20, 40, 60, 80 and 100 N. Source: Ref [120]
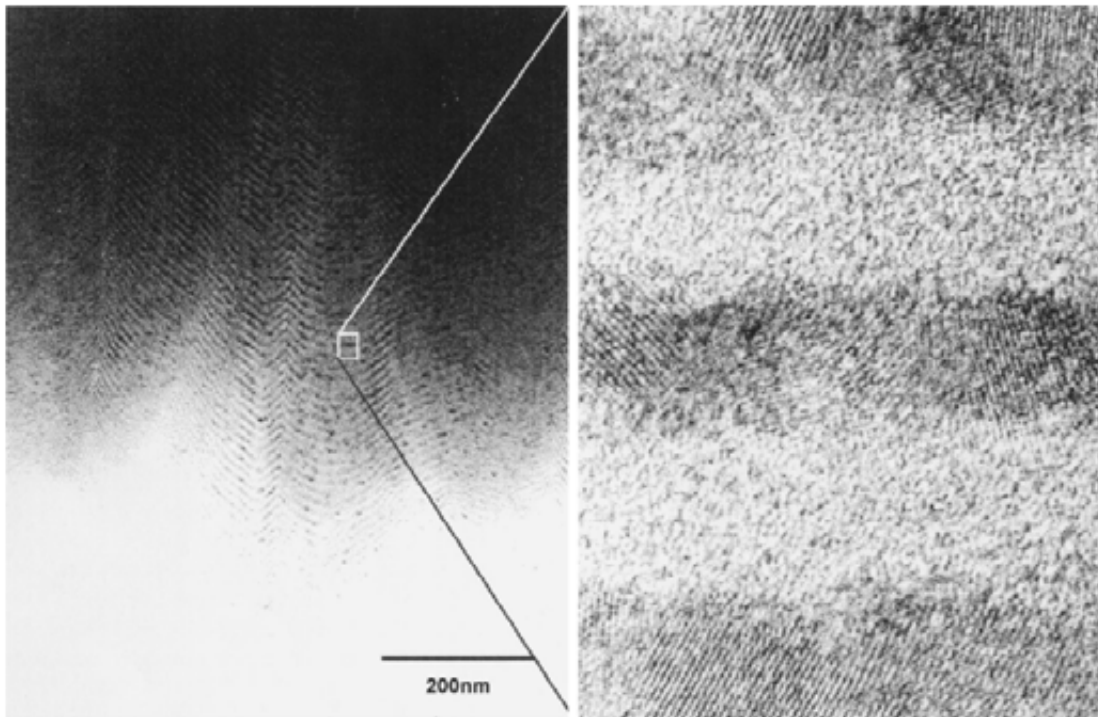
Figure 2.2-5: Bright field and HRTEM of TiN/CN$_x$ layers deposited by reactive magnetron

sputtering. Source: Ref [149].
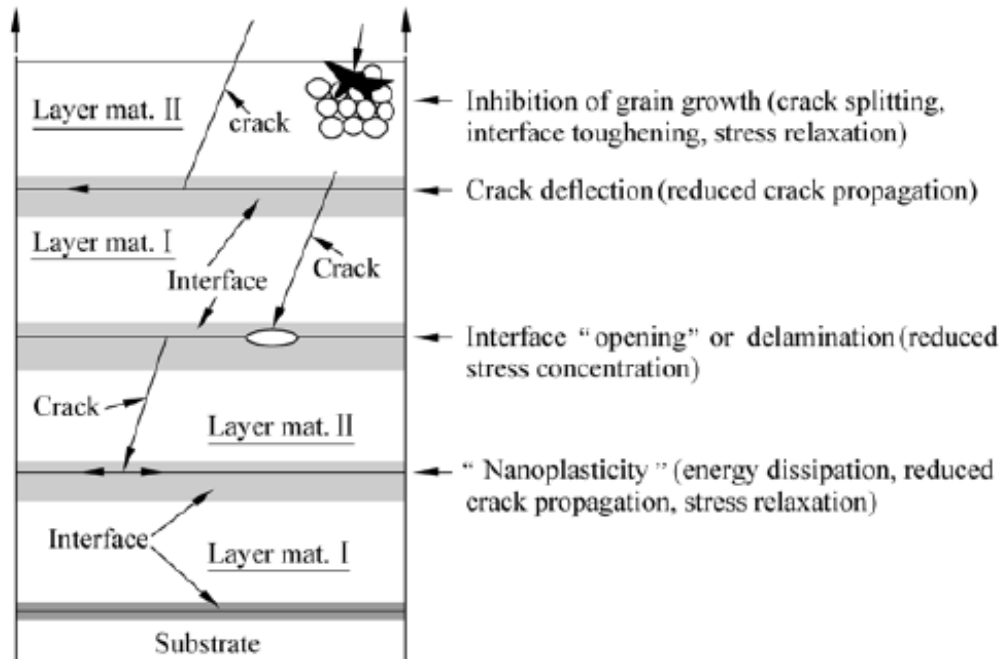
Figure 2.2-6: Mechanisms of toughness enhancement in hard ceramic multilayers.

Source: Ref [154]
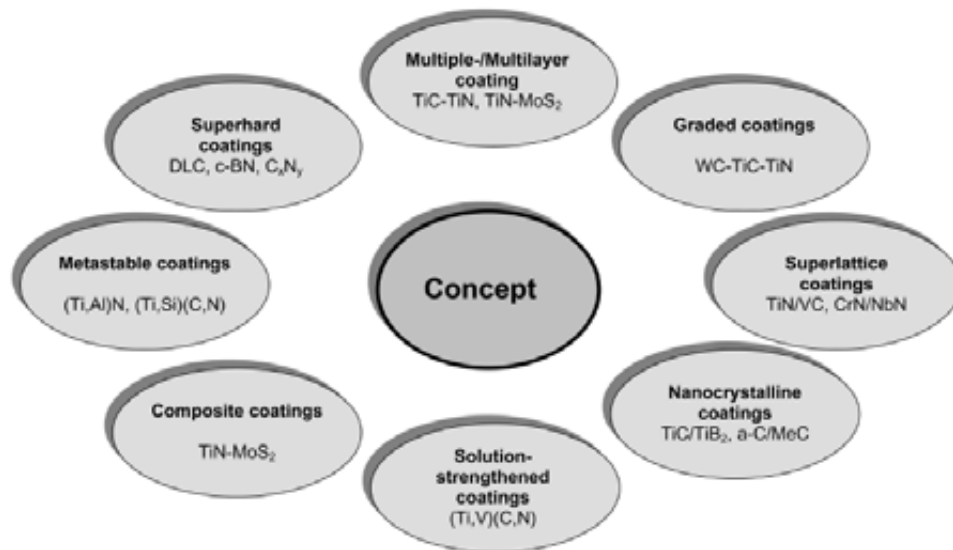
Figure 2.2-7: Realized concepts for hard and protecting coatings. Source: Ref [163]
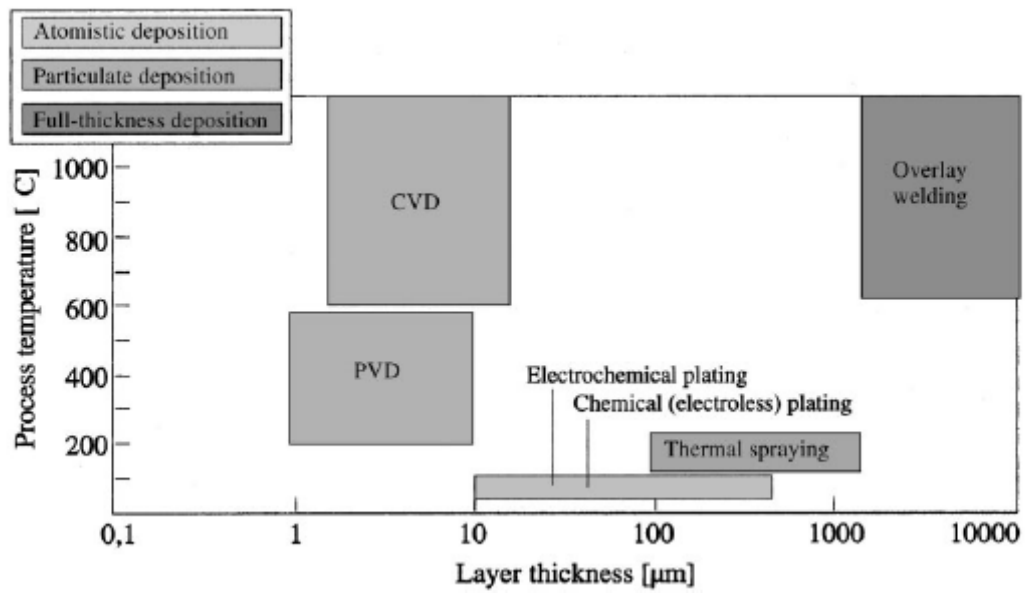
Figure 2.2-8: Typical values of coating thickness and process temperature (temperature at the substrate surface) of today's tribological coating methods. Source: Ref [164]
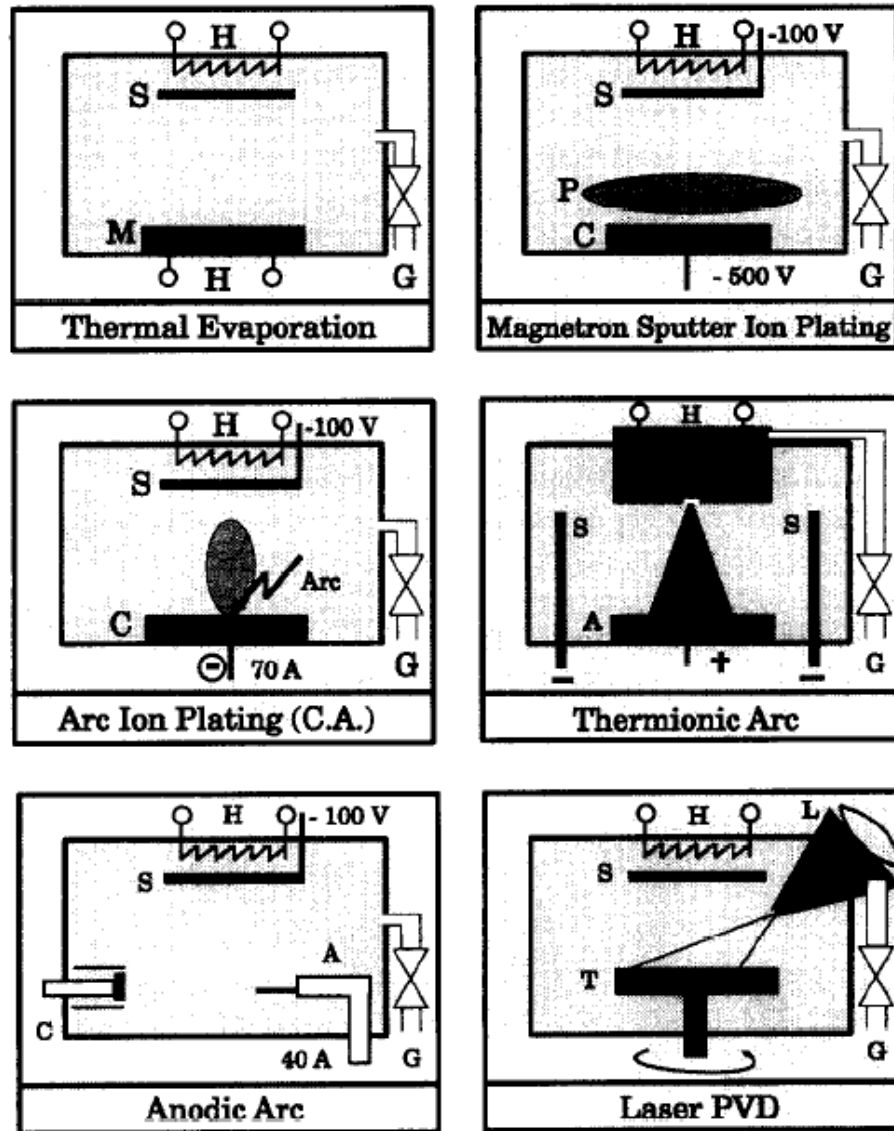
Figure 2.2-9: PVD processes. Source: Ref [168-171]
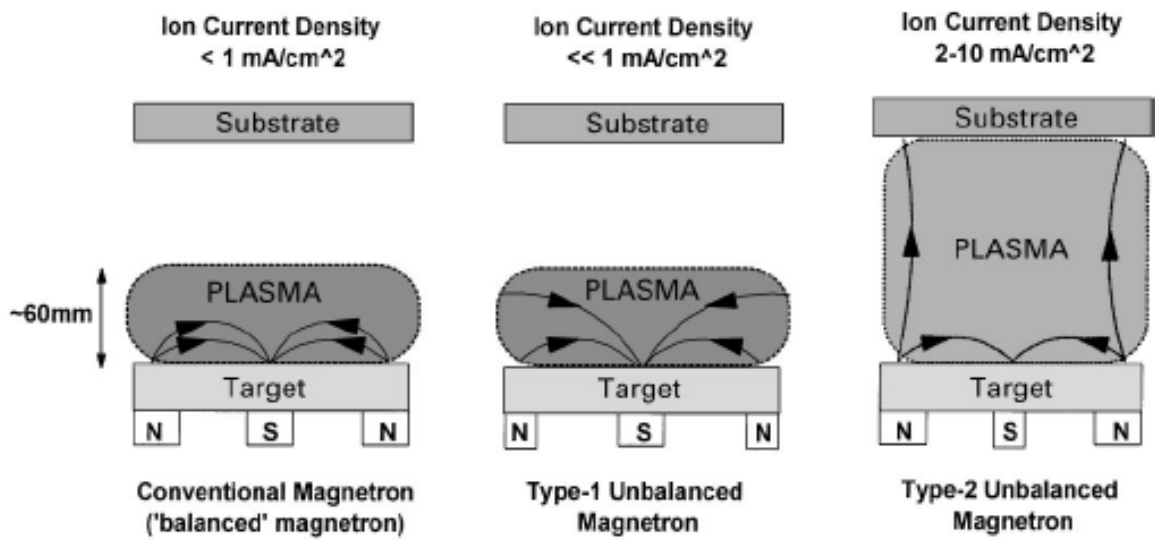
Figure 2.2-10: Schematic representation of the plasma confinement observed

in conventional and unbalanced magnetron. Source: Ref [178]
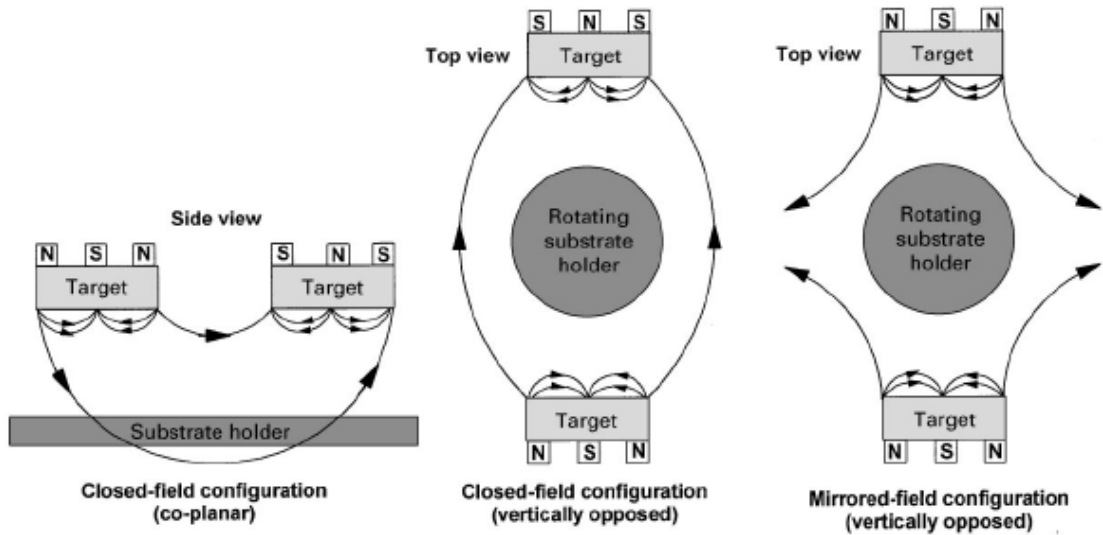
Figure 2.2-11: Dual unbalanced magnetron configurations. Source: Ref [182]
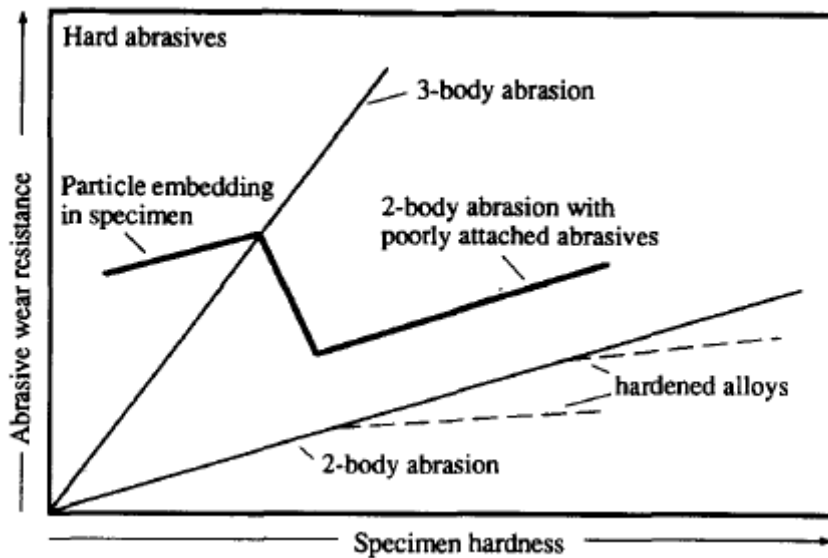
Figure 2.3-1: Schematic illustration of the dependence of specimen hardness on the wear

resistance in three-body abrasion with hard abrasives. Source: Ref [192]
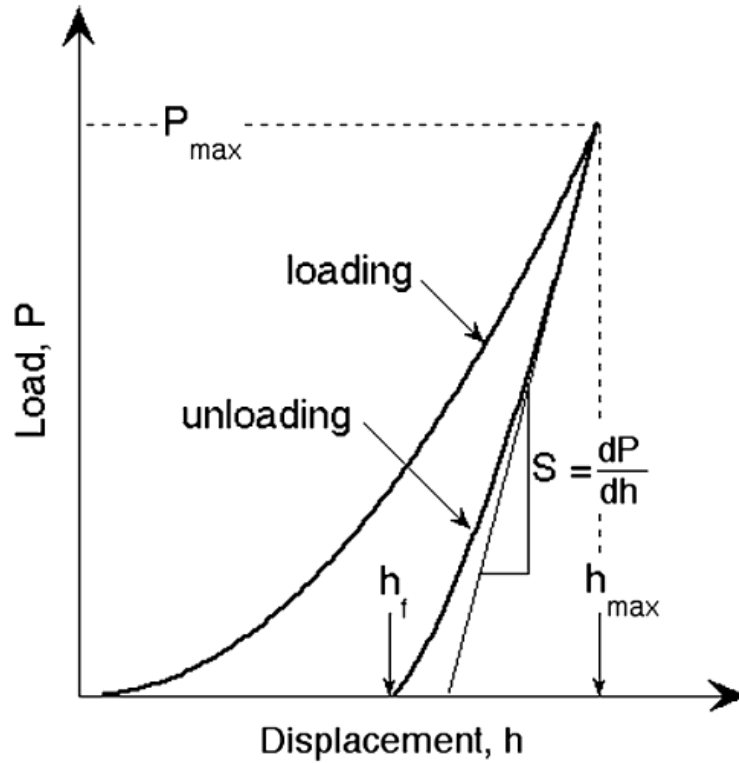
Figure 2.3-2: Schematic illustration of indentation load-displacement data

showing important measured parameters. Source: Ref [222]
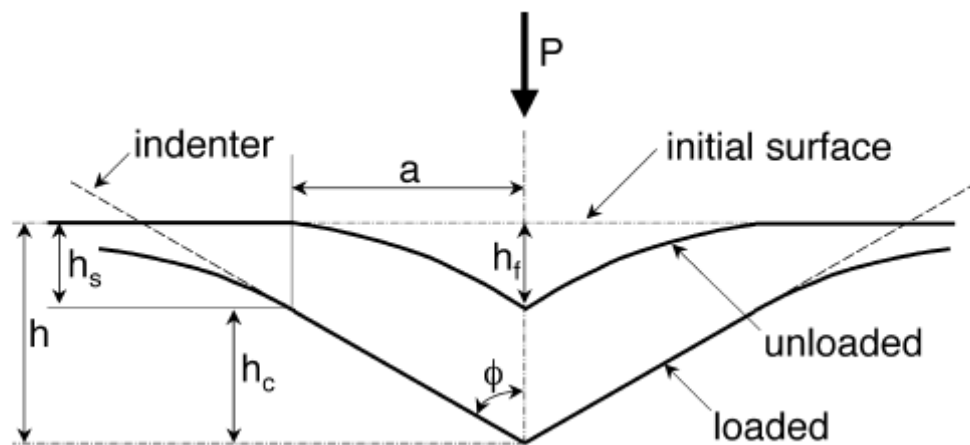
Figure 2.3-3: Schematic illustration of the unloading process showing parameters

characterizing the contact geometry. Source: Ref [222]
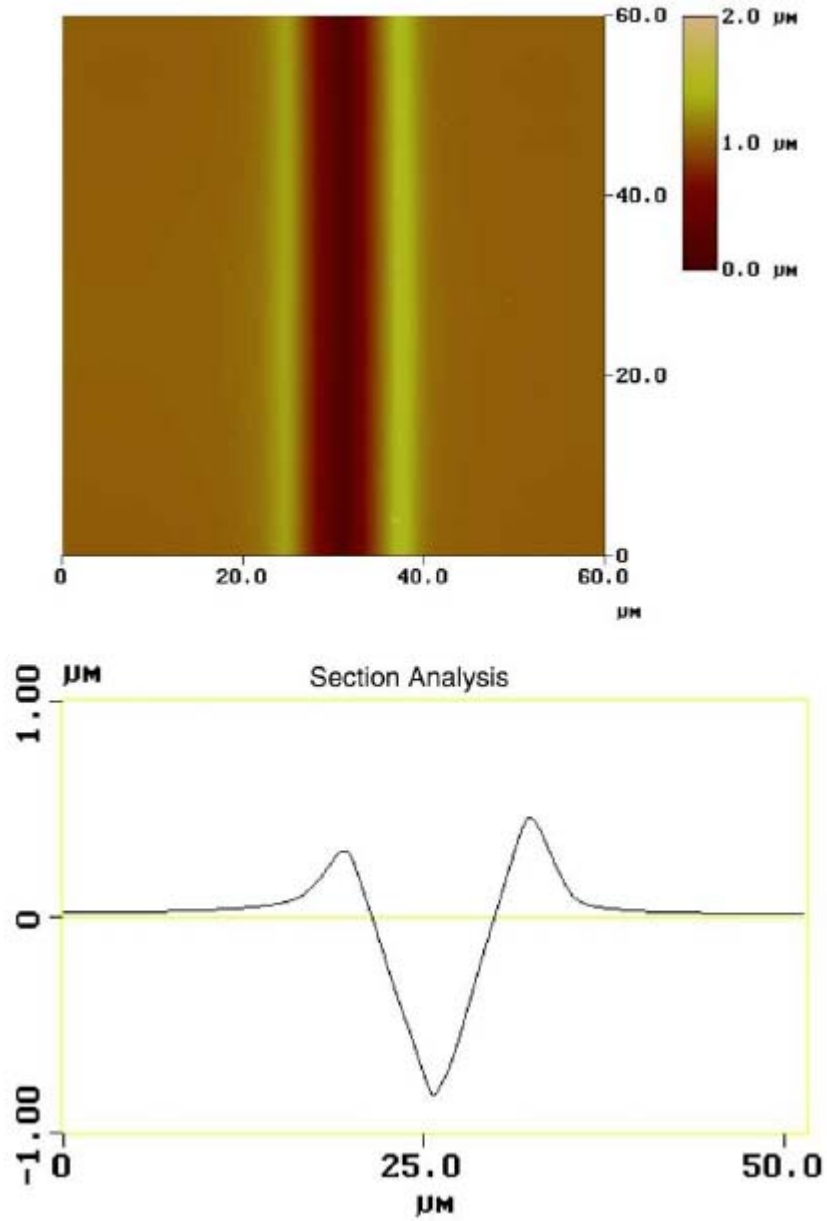
Figure 2.3-4: Cross-section profile of a typical mar under a constant load.

Source: Ref [242]
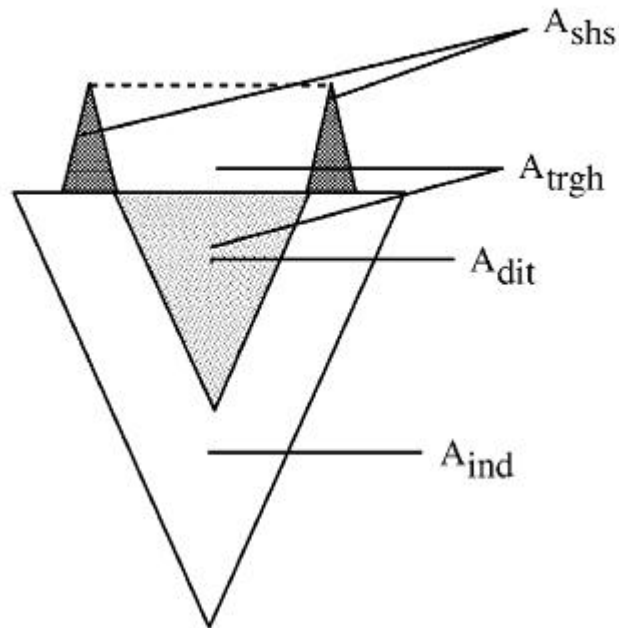
A_{ind}: Cross-section area of the indentation

A_{dit}: Cross-section area of the ditch

A_{shs}: Cross-section area of the two shoulders

A_{trgh}: Cross-section area of the trough

Micro Mar Resistance: $(A_{ind} - A_{dit}) / A_{ind} * \%$

Plastic Deformation: $A_{shs} / A_{ind} * \%$

Abrasive Wear: $(A_{dit} - A_{shs}) / A_{ind} * \%$

Figure 2.3-5: Cross-section areas used in calculating responses of a coating to marring stress.

Source: Ref [244]
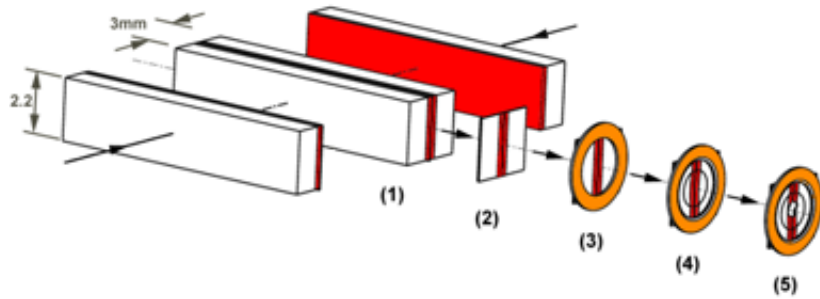
Figure 3.1-1: Schematic view of the steps involved in the preparation of
a Cross-section TEM sample preparation
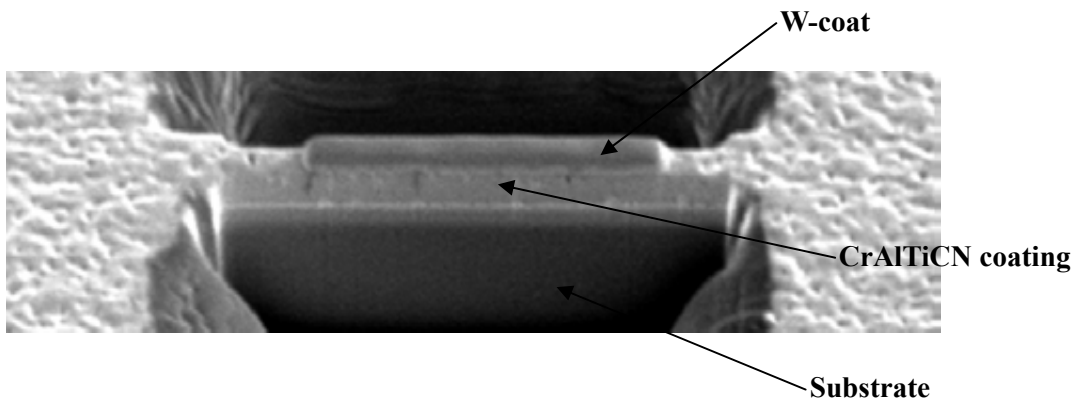
Figure 3.1-2: Secondary electron image of FIB cross-section sample

Figure 3.2-1: UDP 450 closed-field unbalanced magnetron sputtering ion plating system
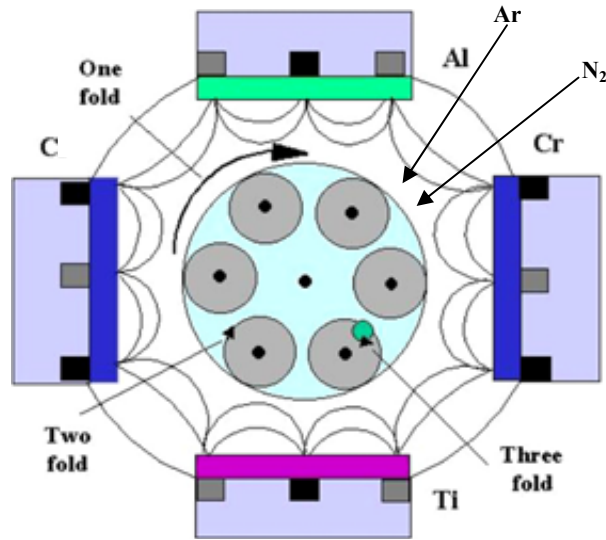
Figure 3.2-2: Cross-section schematic drawing of arrangement of magnetron targets and substrate holder in CFUBMSIP system
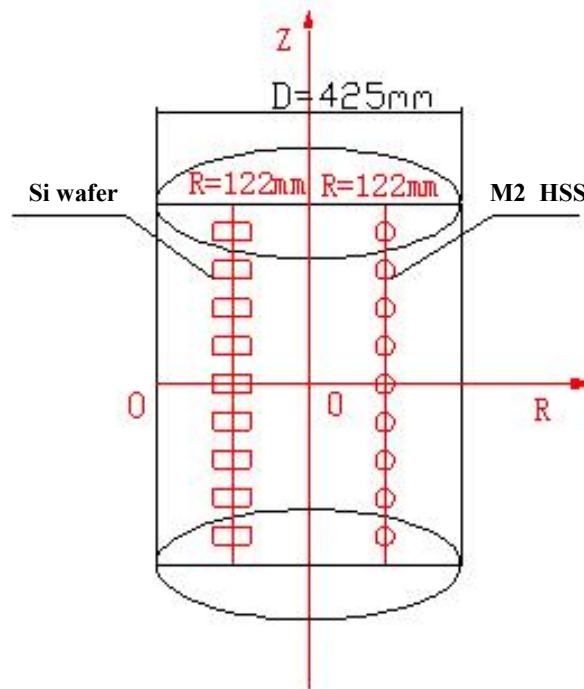
Figure 3.2-3: Schematic illustration of sample arrangement
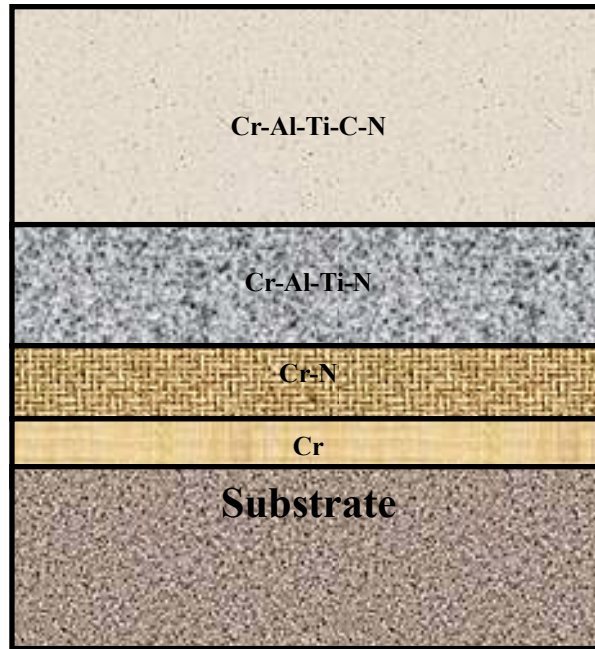
Figure 3.2-4: Schematics of the layer structure of CrAlTiCN coating systems
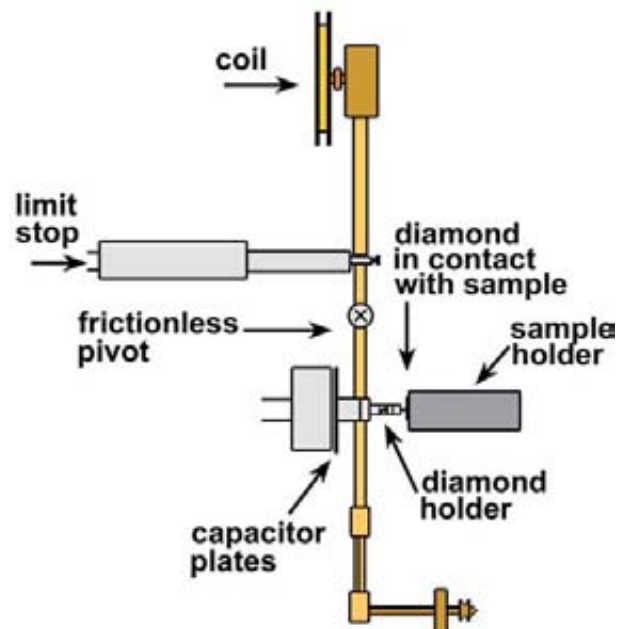
Figure 3.4-1: Schematic view of nano-indentation testing machine
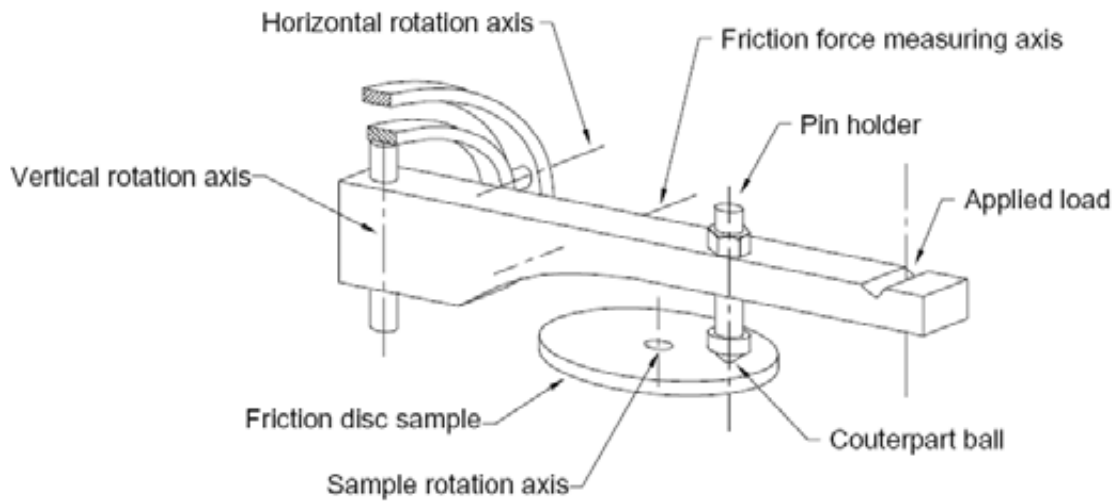
Figure 3.4-2: Schematic view of pin-on-disc tribometer
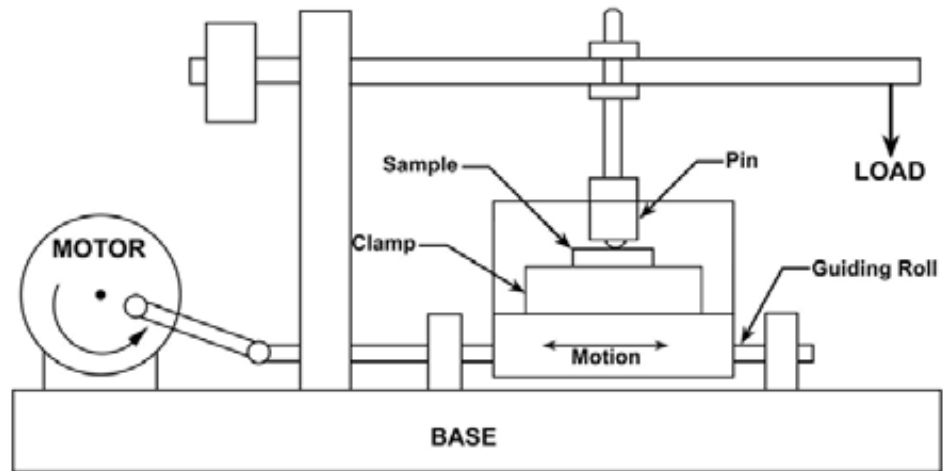
Figure 3.4-3: Schematic view of reciprocating wear tribometer
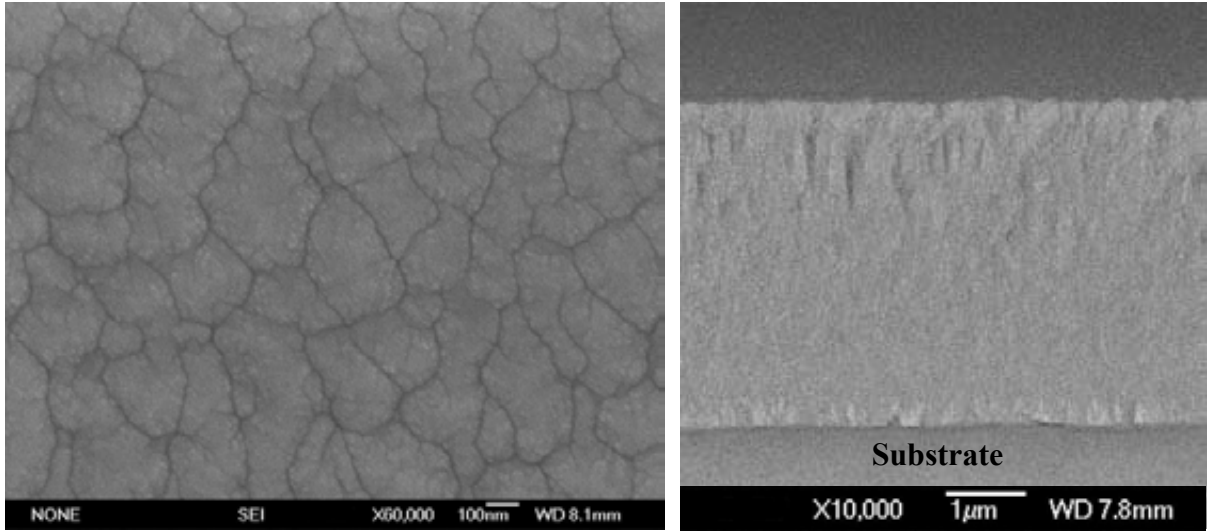
(a) CrAlTiN-0#
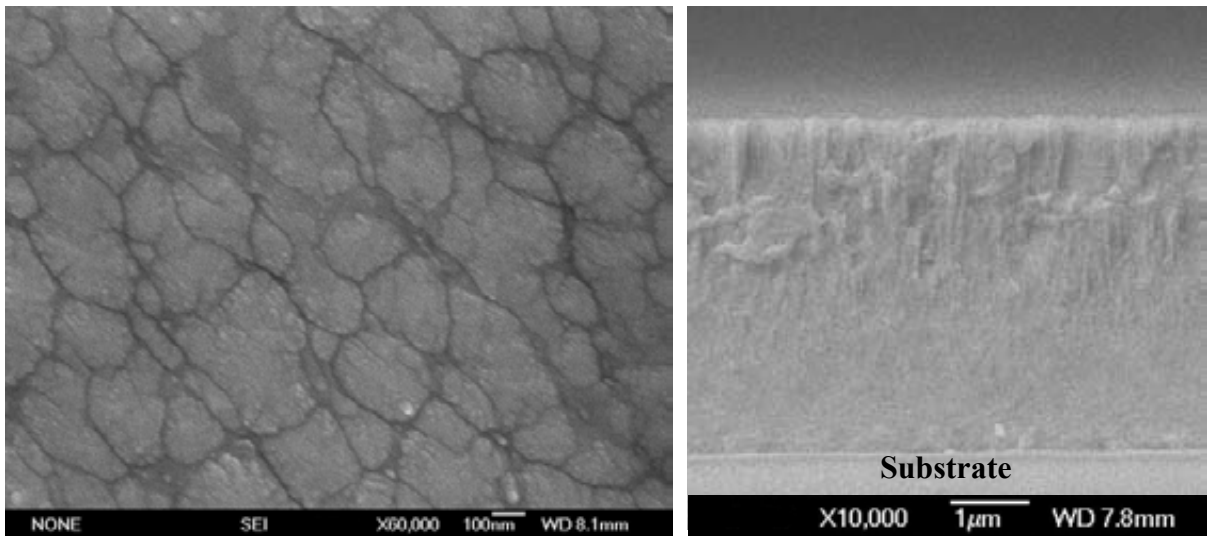
(b) CrAlTiCN-1#
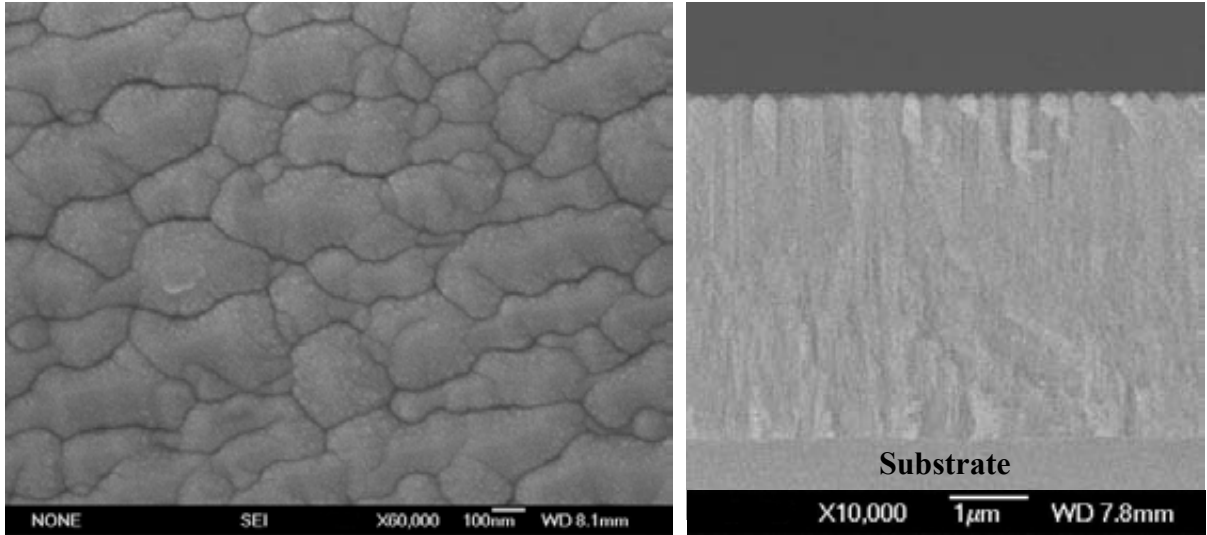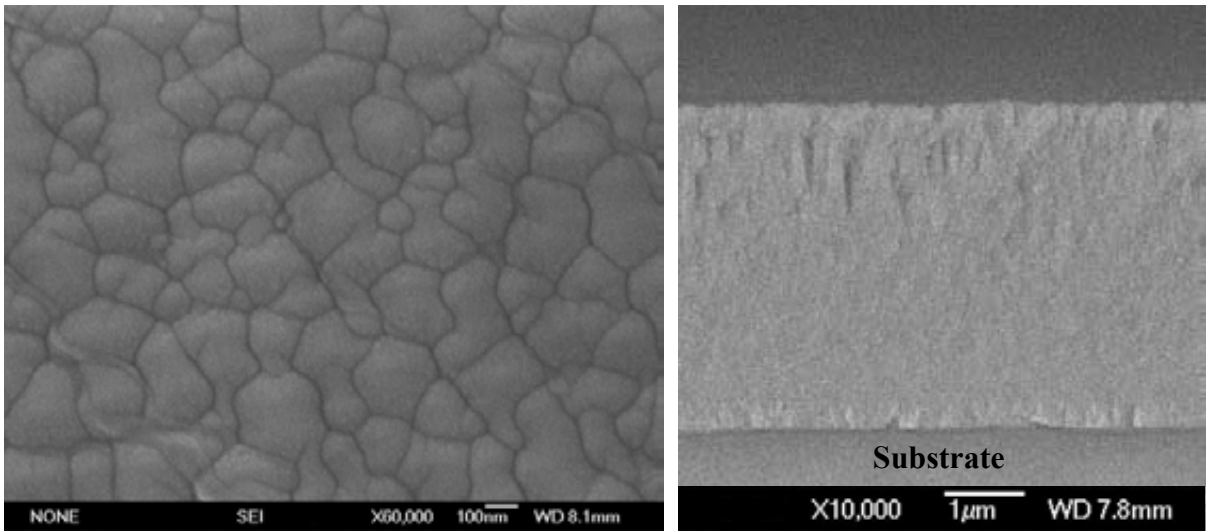
(c) CrAlTiCN-2#
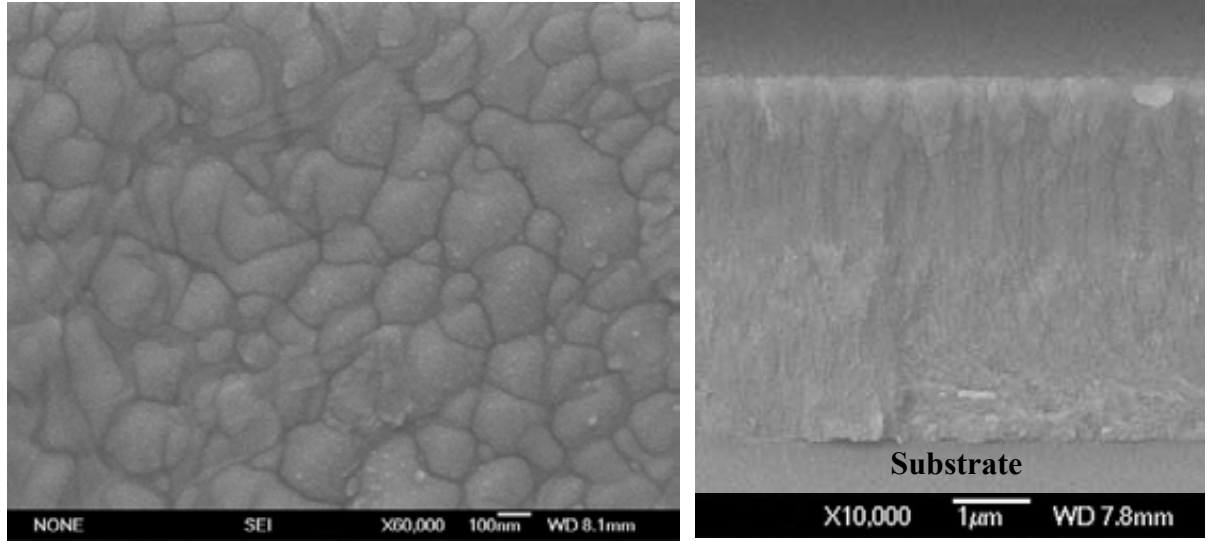
(d) CrAlTiCN-3#
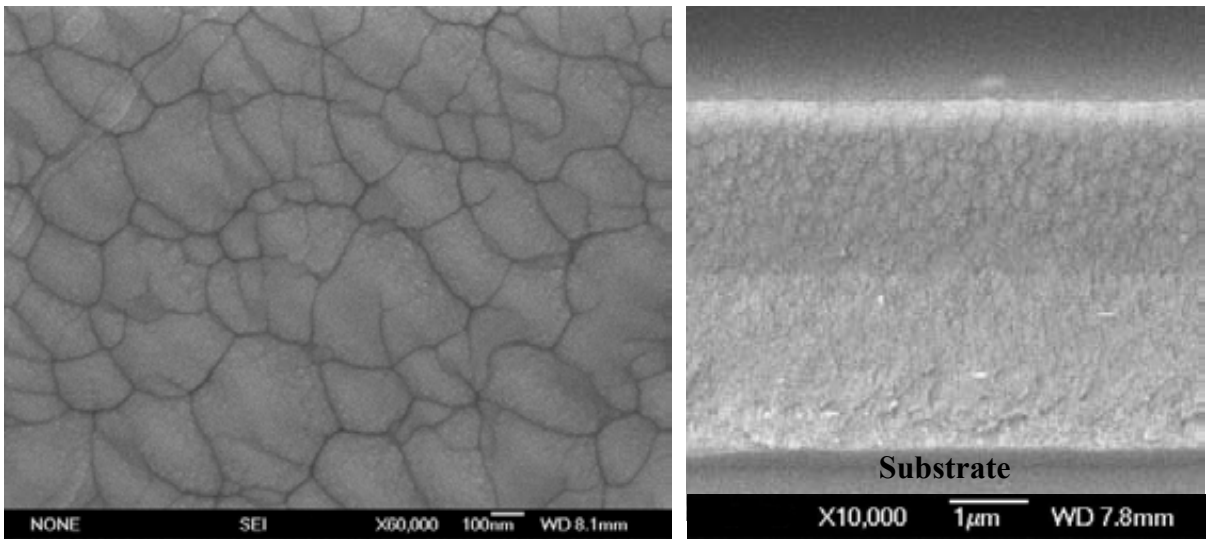
(e) CrAlTiCN-4#

(f) CrAlTiCN-5#

Figure 4.2-1: Surface and cross-sectional SEI SEM micrographs of
(a) CrAlTiN-0#, (b) CrAlTiCN-1#, (c) CrAlTiCN-2#, (d) CrAlTiCN-3#,
(e) CrAlTiCN-4# and (f) CrAlTiCN-5# samples

(a) CrAlTiN-0#

(b) CrAlTiCN-1#

(c) CrAlTiCN-2#

182
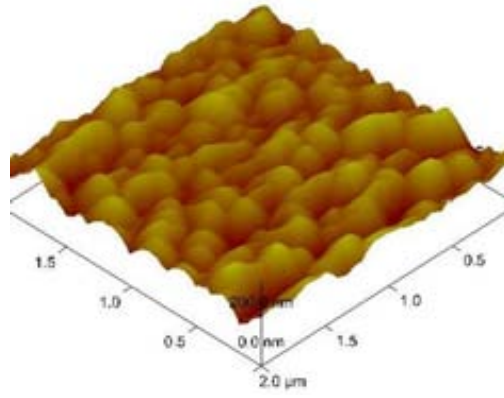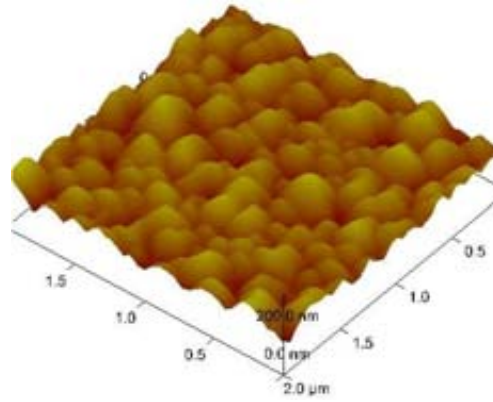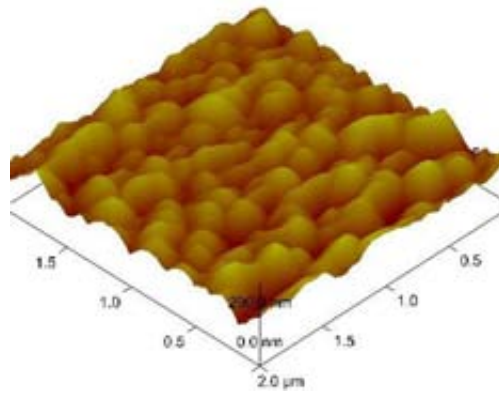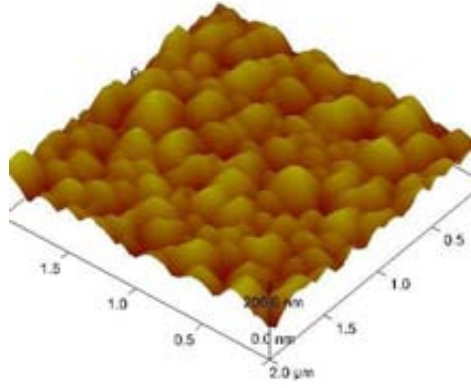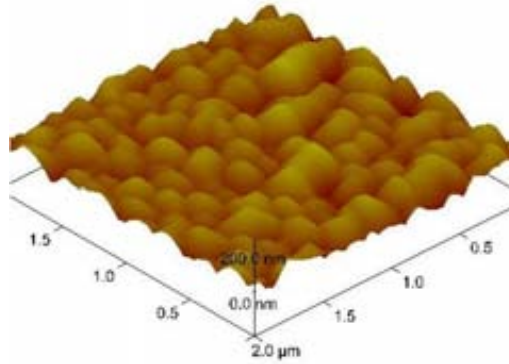
(d) CrAlTiCN-3#
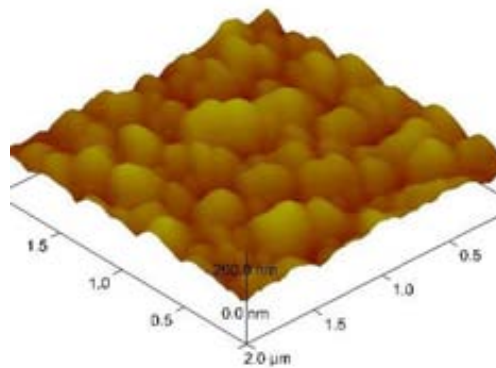
(e) CrAlTiCN-4#

(f) CrAlTiCN-5#

Figure 4.2-2: 3-D AFM images of
(a) CrAlTiN-0#, (b) CrAlTiCN-1#, (c) CrAlTiCN-2#, (d) CrAlTiCN-3#,
(e) CrAlTiCN-4# and (f) CrAlTiCN-5# samples

183
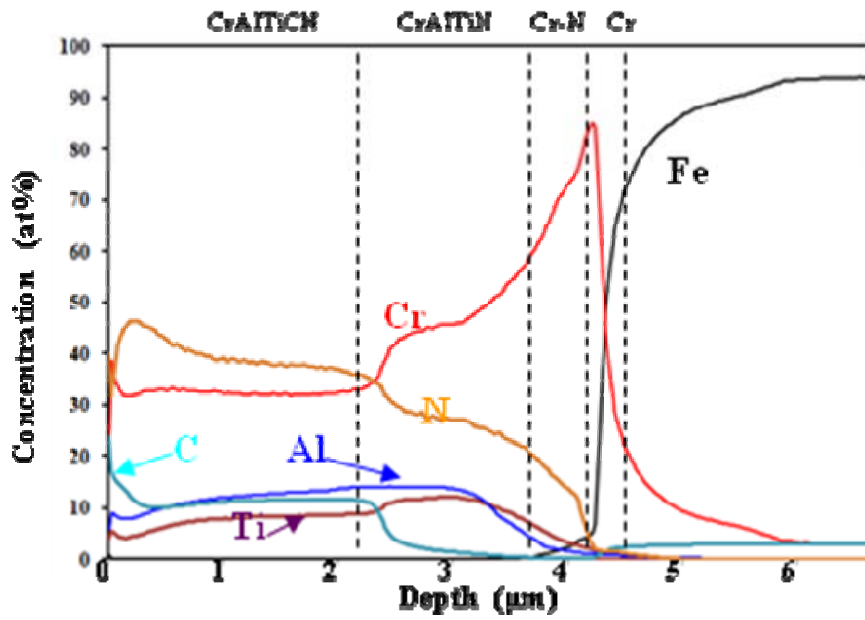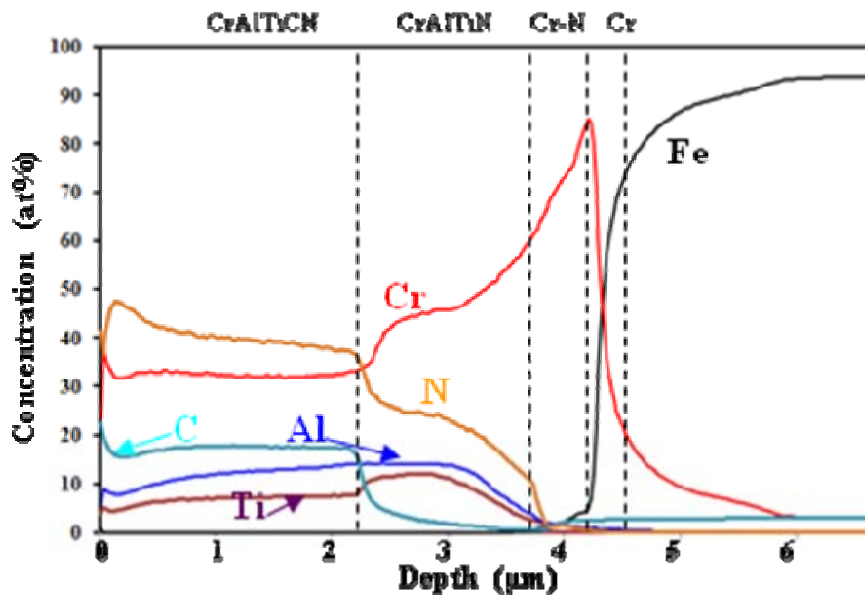
(a) CrAlTiCN-3#

(b) CrAlTiCN-5#

Figure 4.2-3: GDOES composition-depth profiles of:
(a) CrAlTiCN-3# and (b) CrAlTiCN-5# samples
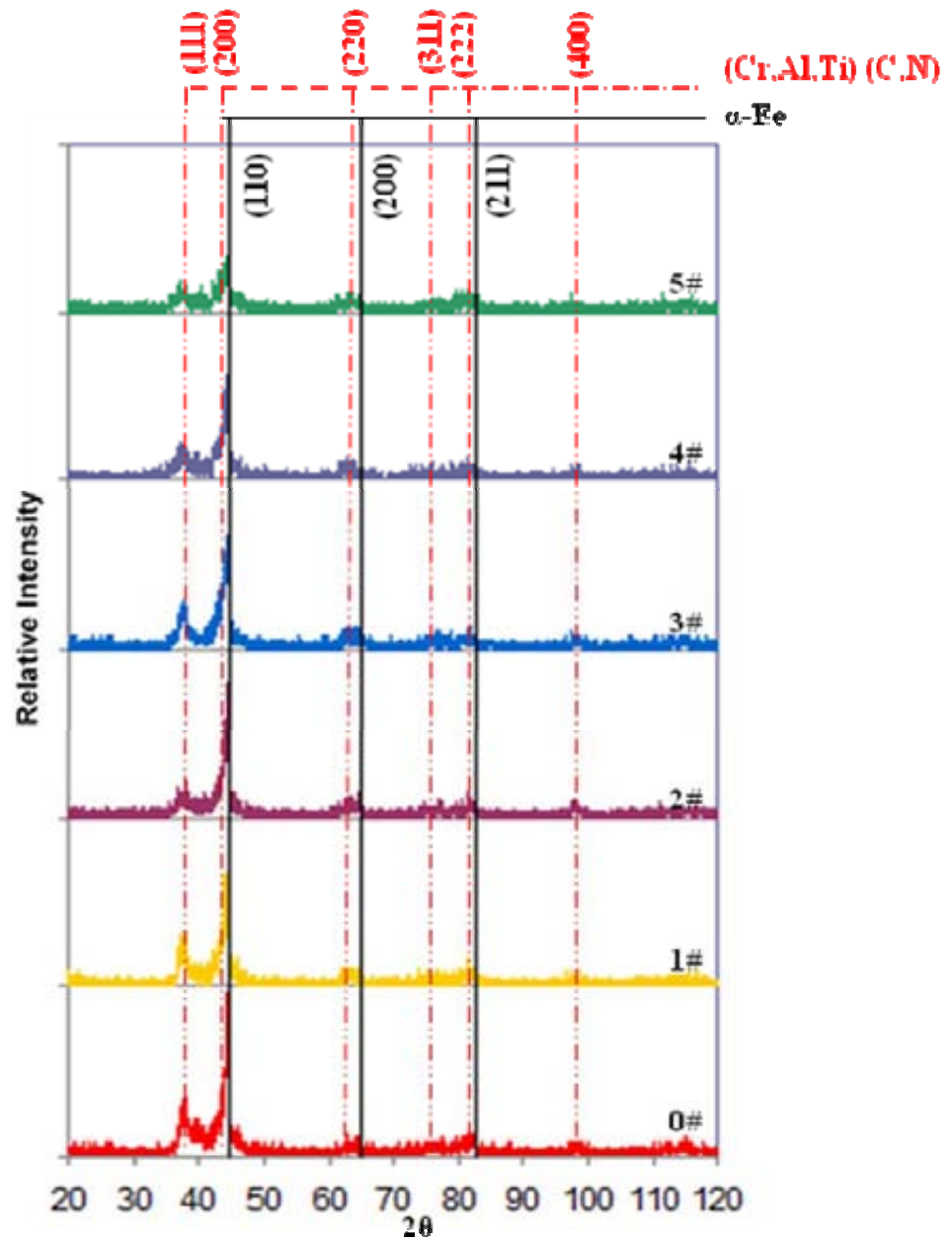
Figure 4.2-4: XRD patterns obtained on CrAlTiN and carbon-doped CrAlTiCN coatings
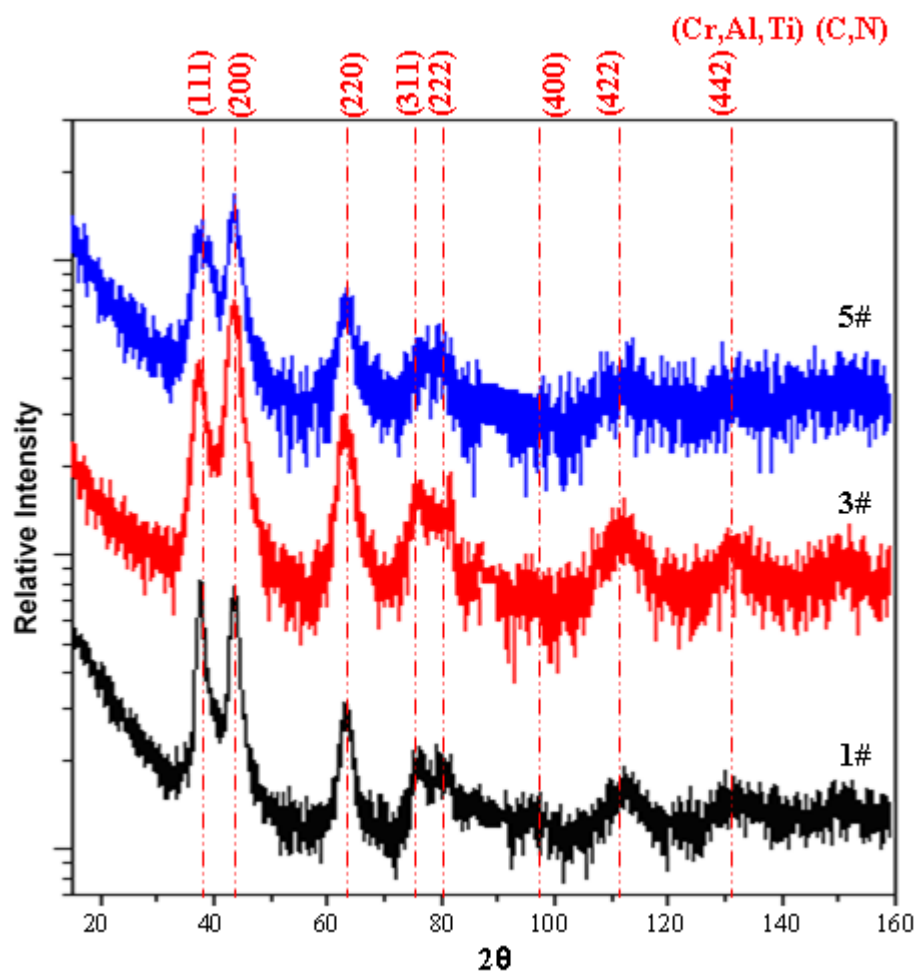
(a)
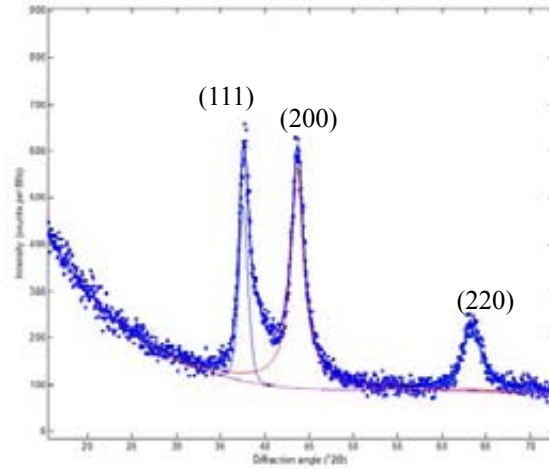
(b) CrAlTiCN-1#
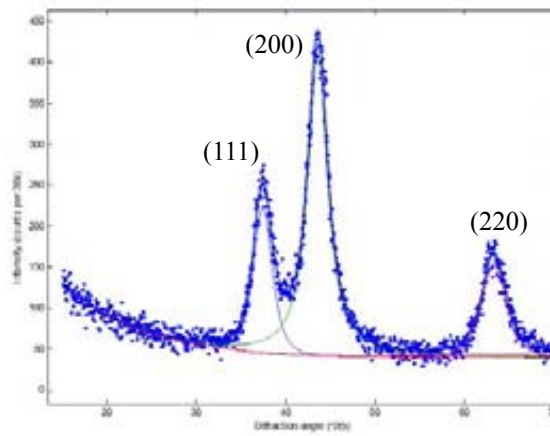
(c) CrAlTiCN-3#
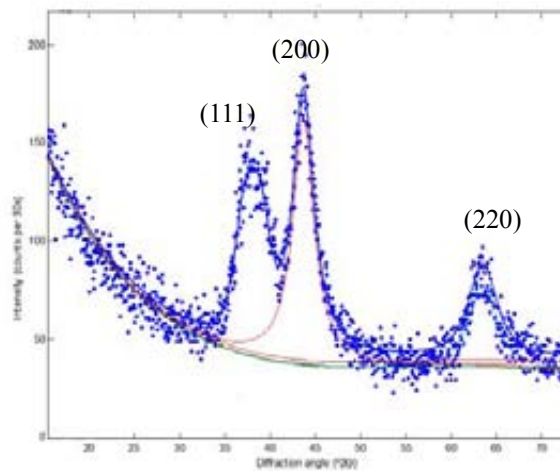
(d) CrAlTiCN-5#

Figure 4.2-5: GAXRD patterns (a) and the line fittings obtained on carbon-doped CrAlTiCN (b) 1#, (c) 3# and (d) 5# coatings
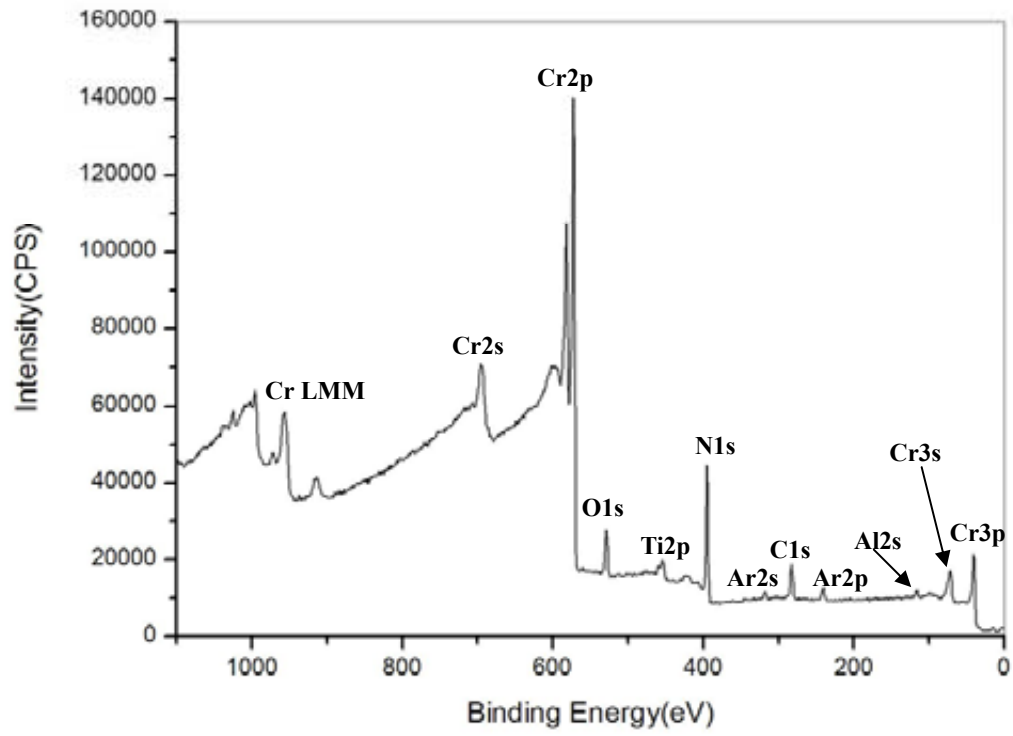
Figure 4.2-6: XPS survey spectra of CrAlTiCN-5# coating
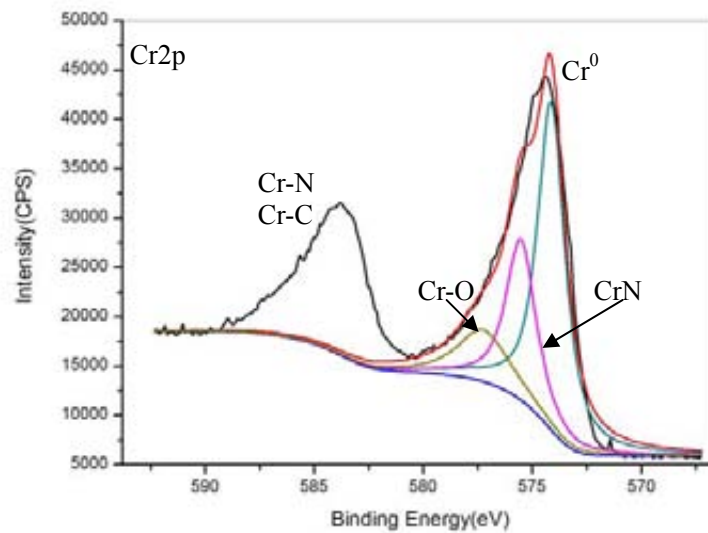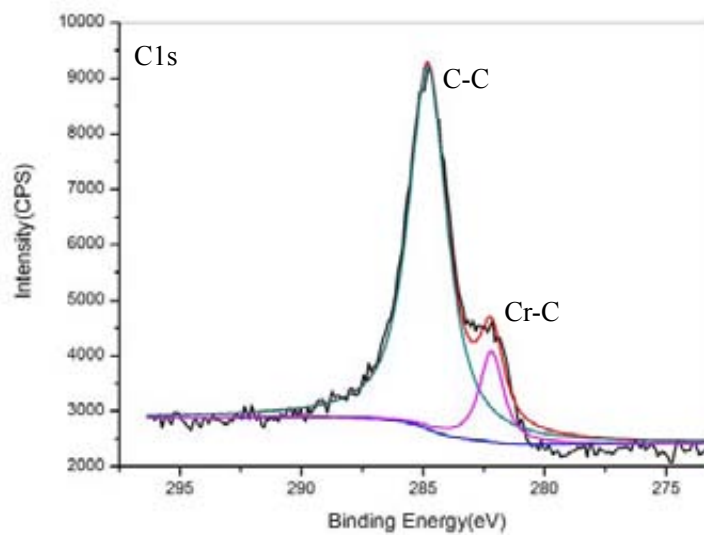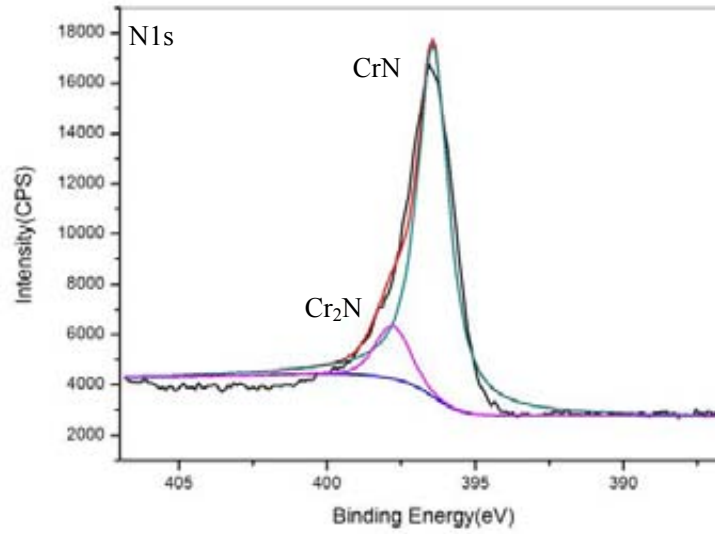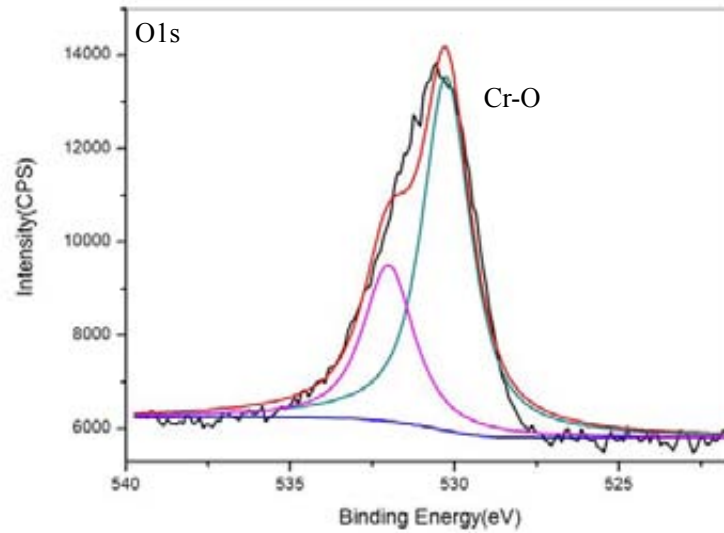
(a) Cr2p

(b) C1s

(c) N1s

(d) O1s

Figure 4.2-7: Fitting spectrum by XPS for carbon-doped CrAlTiCN-5# coating:
(a) Cr2p, (b) C1s, (c) N1s and (d) O1s
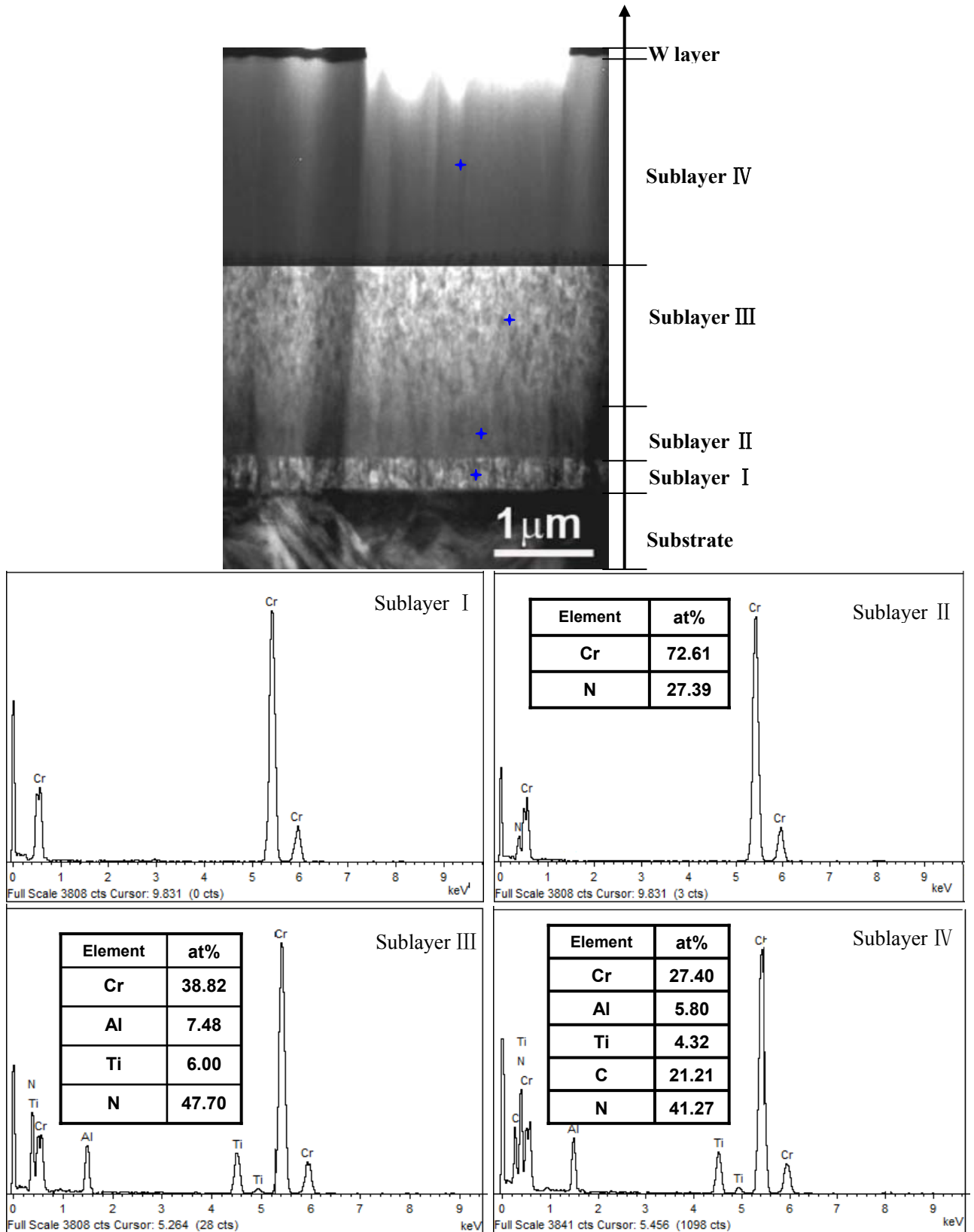
Figure 4.2-8:Cross-sectional TEM micrograph of CrAlTiCN-5# layer structure
and EDX spectrums
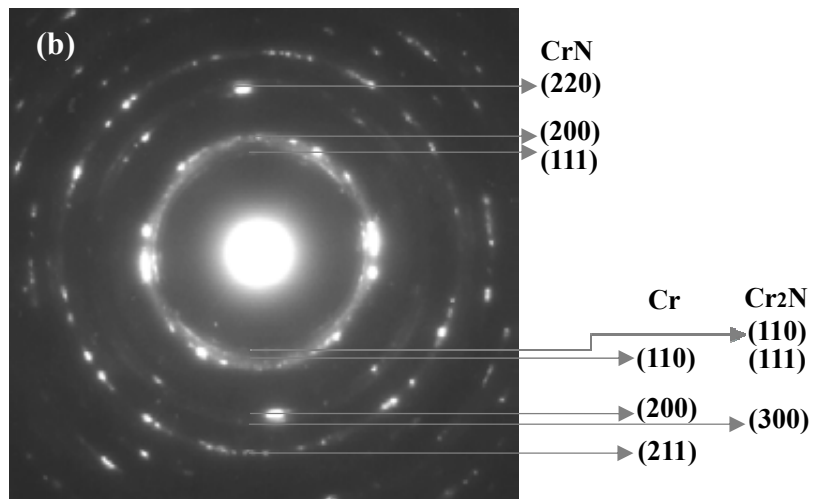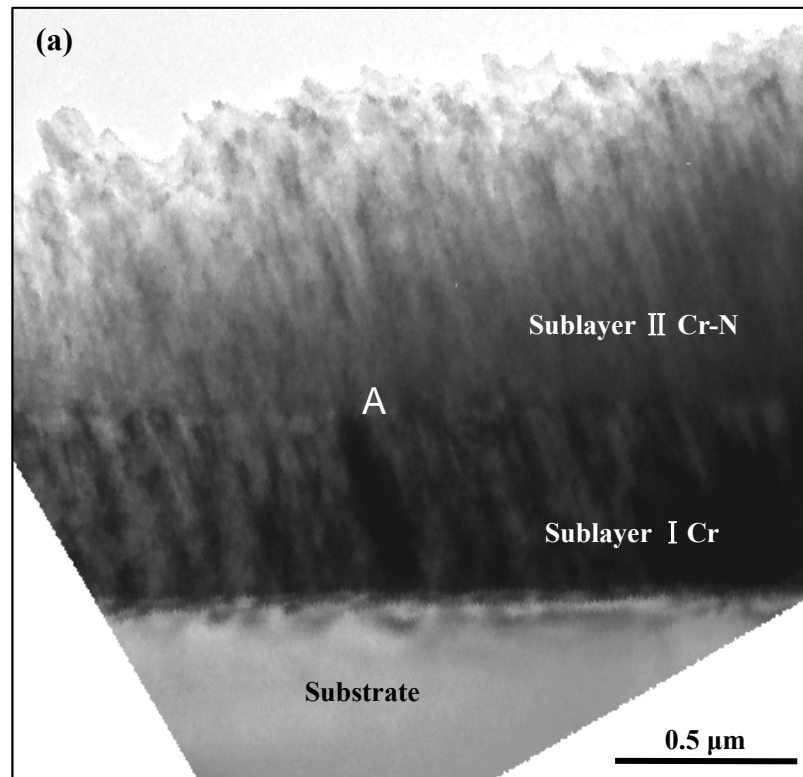
Figure 4.2-9: TEM micrograph and electron diffraction pattern on sublayers Ⅰ and Ⅱ from CrAlTiCN-5# coating
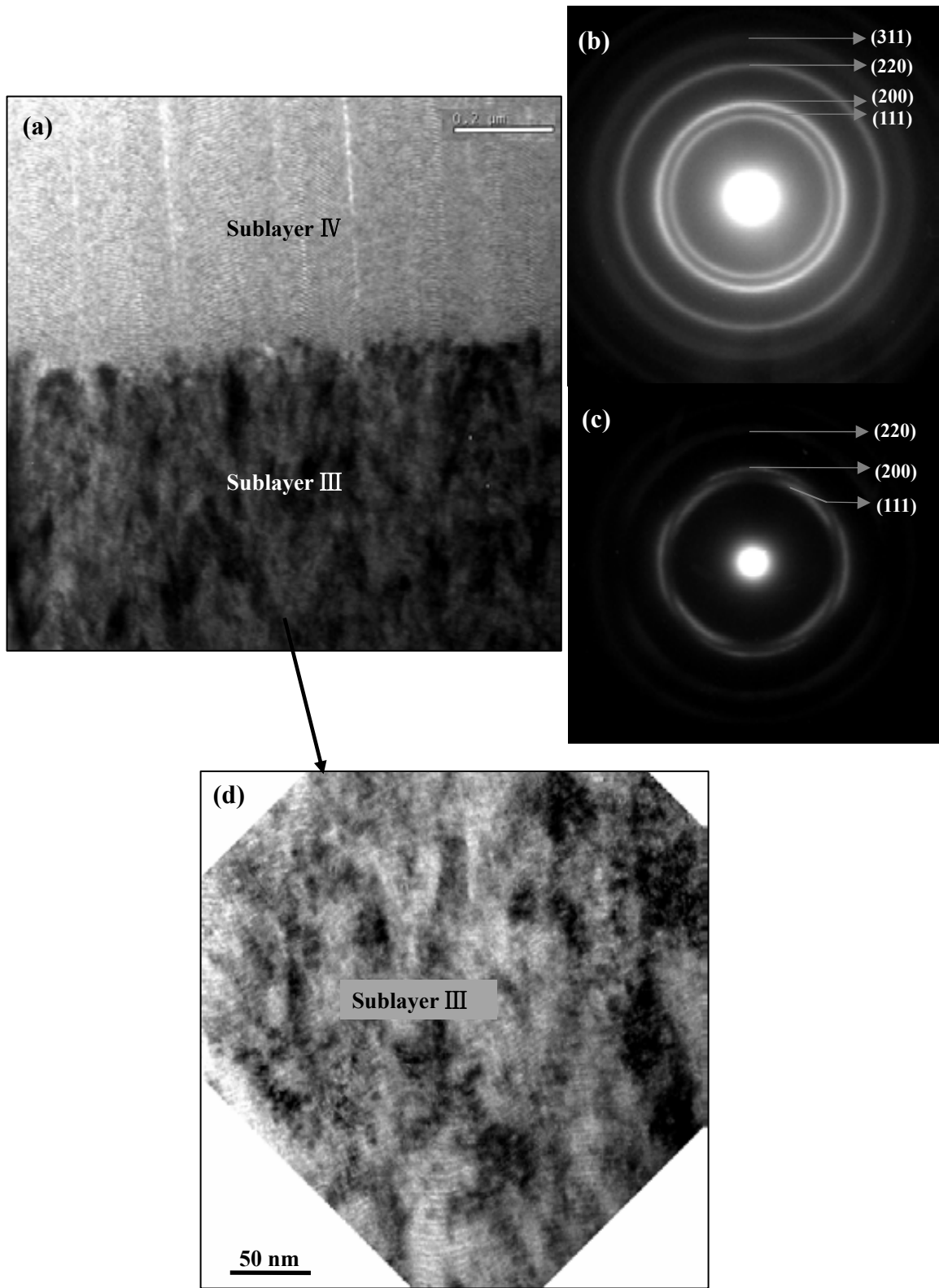
Figure 4.2-10: TEM micrographs and electron diffraction patterns on
sublayers Ⅲ and Ⅳ from CrAlTiCN-5# coating
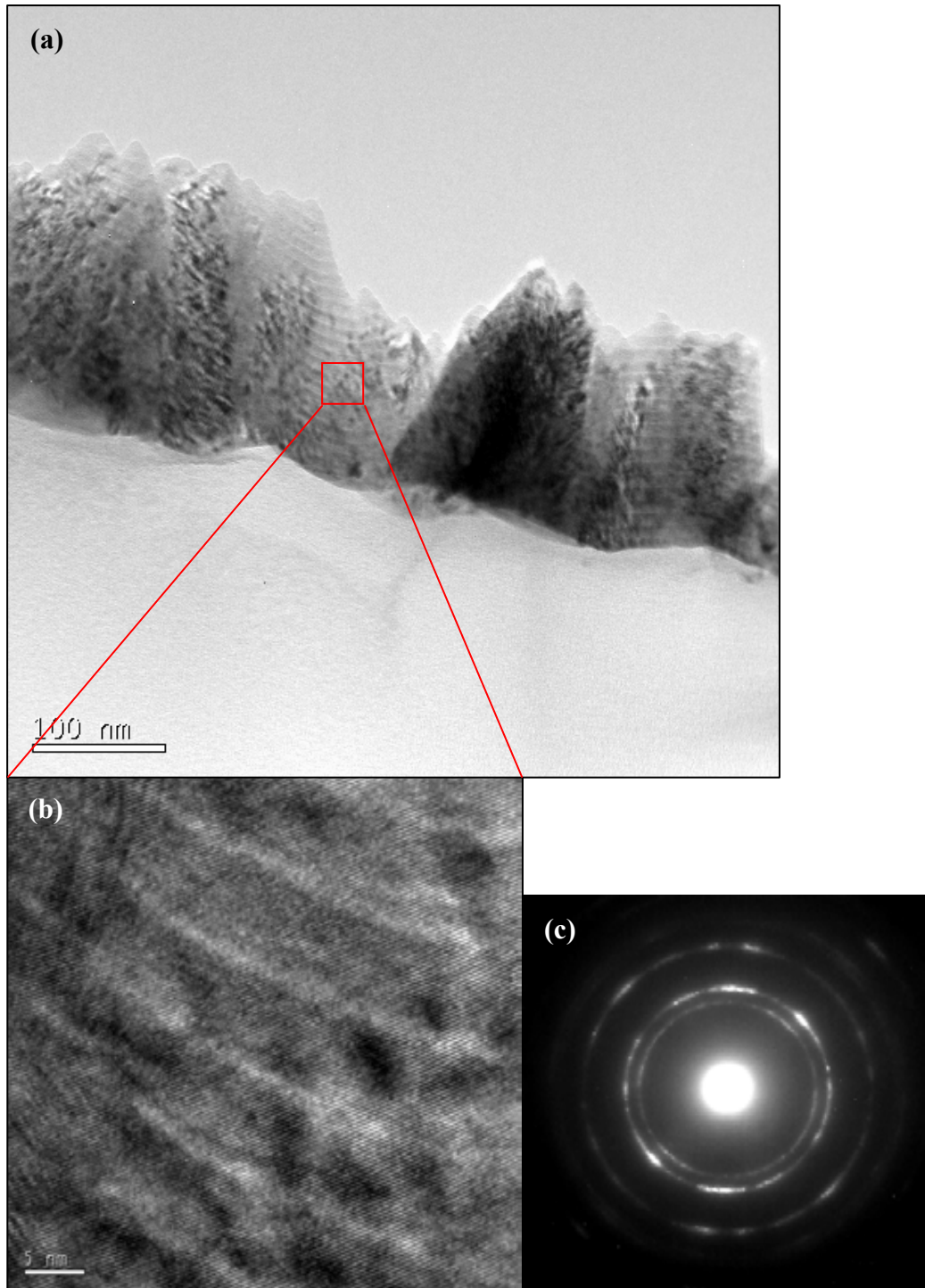
Figure 4.2-11: TEM micrographs and electron diffraction pattern on
Sublayer Ⅳ from CrAlTiCN-1# coating
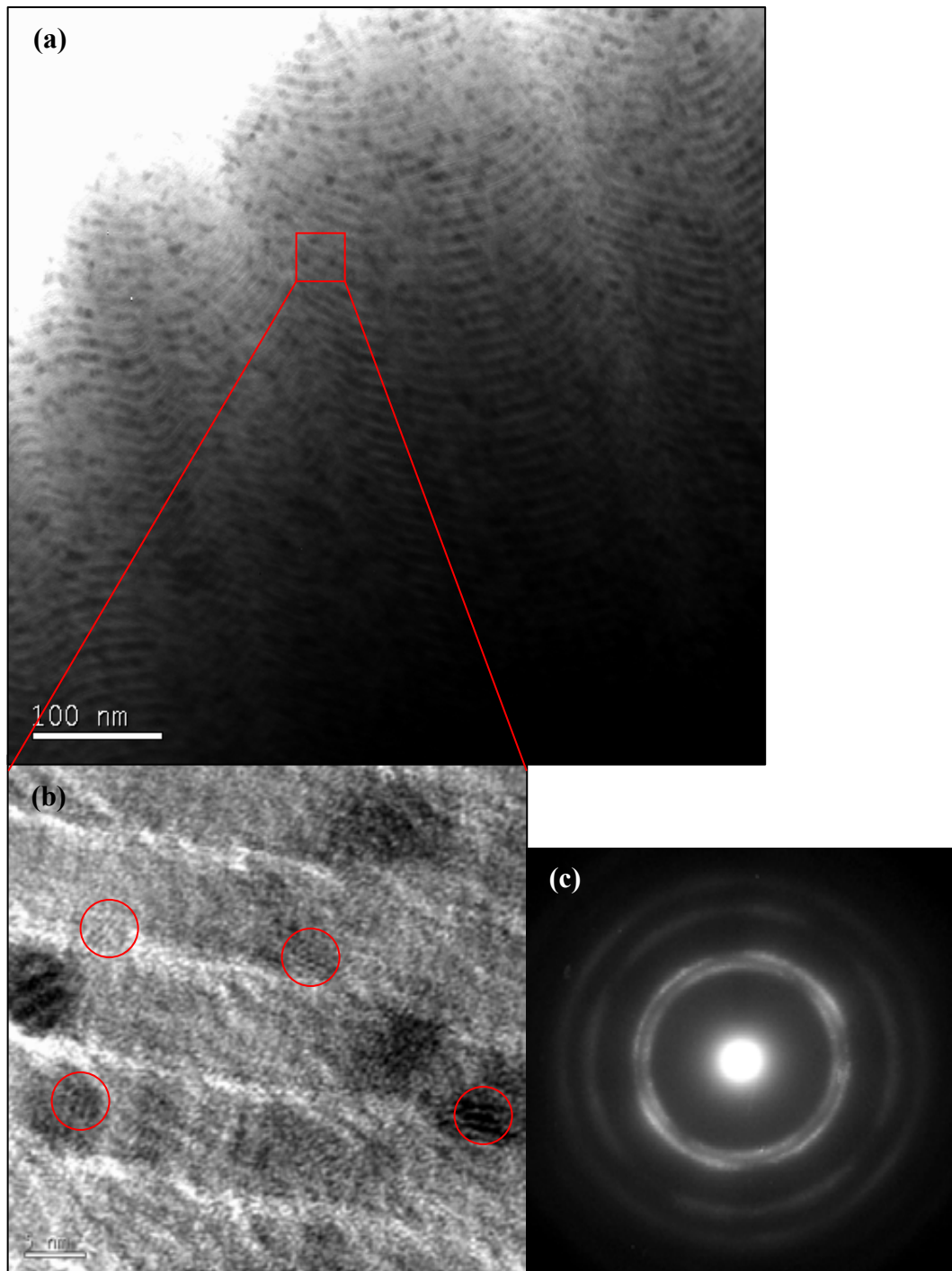
Figure 4.2-12: TEM micrographs and electron diffraction pattern on
Sublayer Ⅳ from CrAlTiCN-3# coating
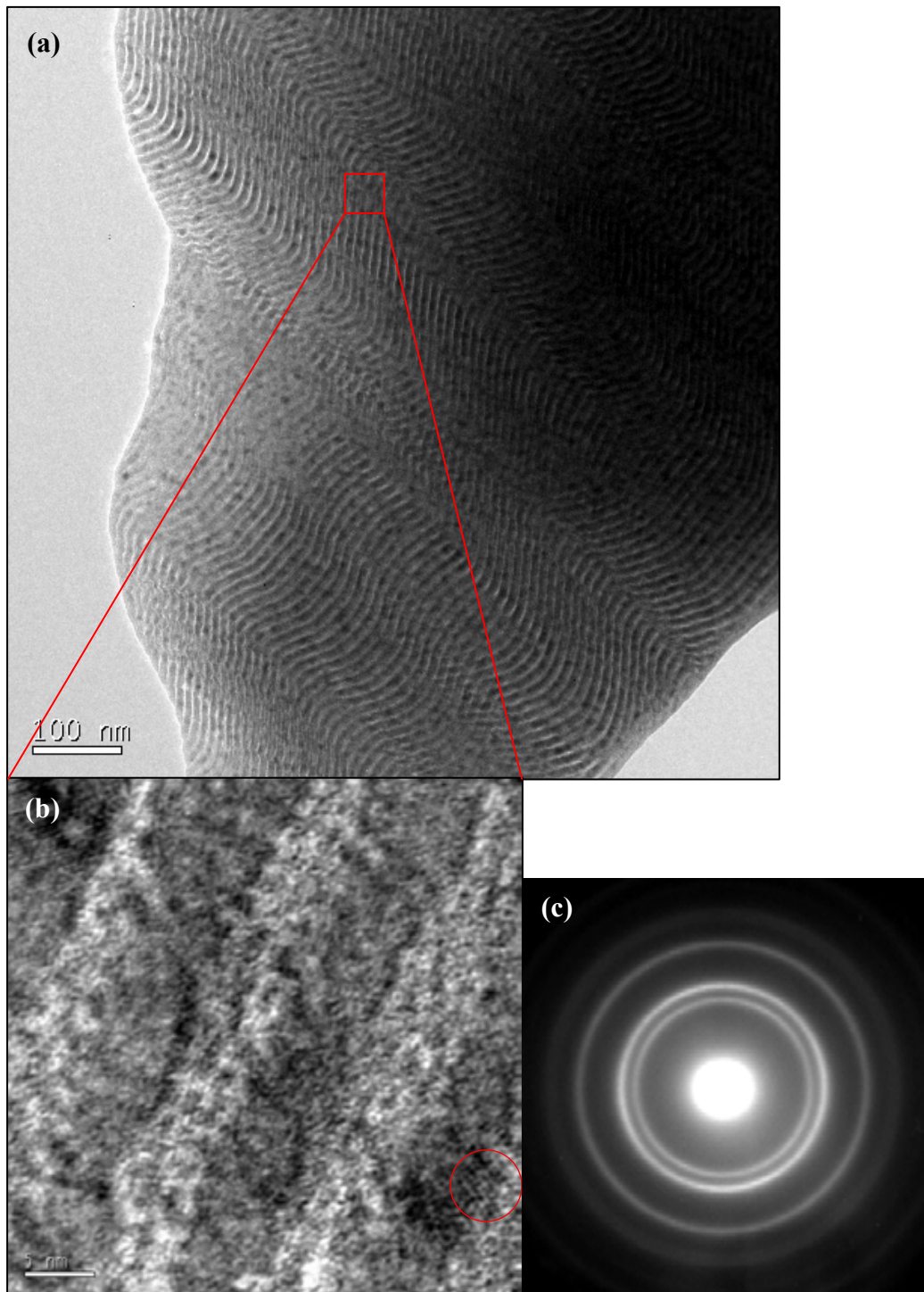
Figure 4.2-13: TEM micrographs and electron diffraction pattern on
Sublayer Ⅳ from CrAlTiCN-5# coating
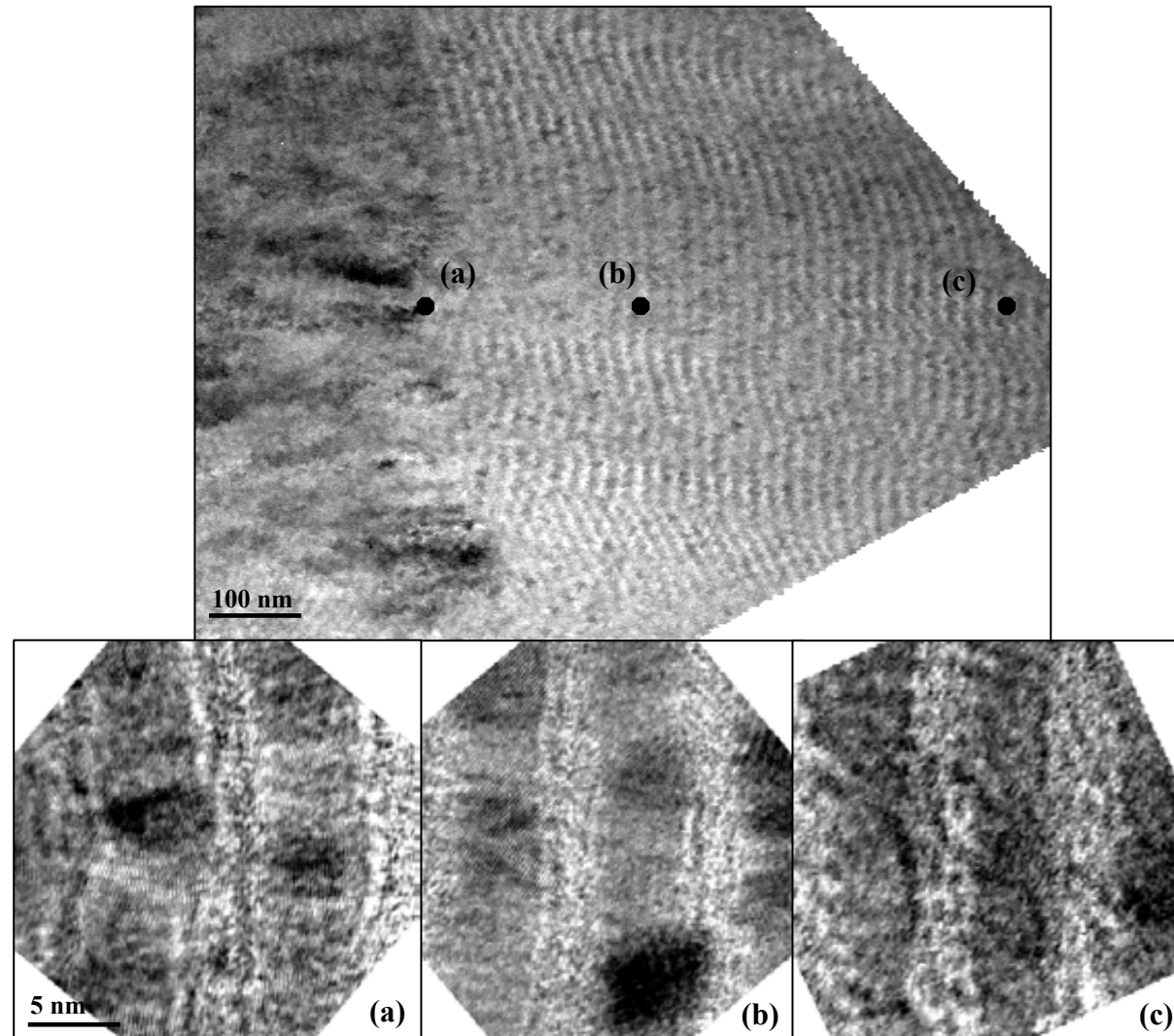
Figure 4.2-14: High-resolution TEM micrographs on Sublayer Ⅳ from CrAlTiCN-5# coating: (a) initial region, (b) middle region and (c) top region
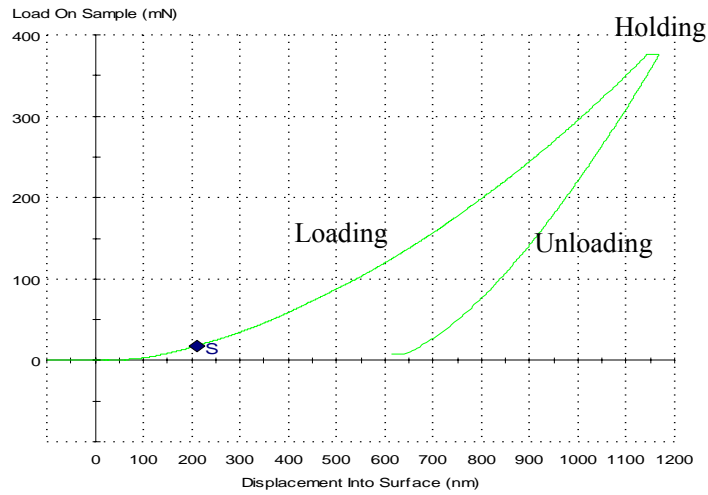
Figure 4.3-1: Typical nano-indentaion load against displacement curve of CrAlTiCN-5# coating
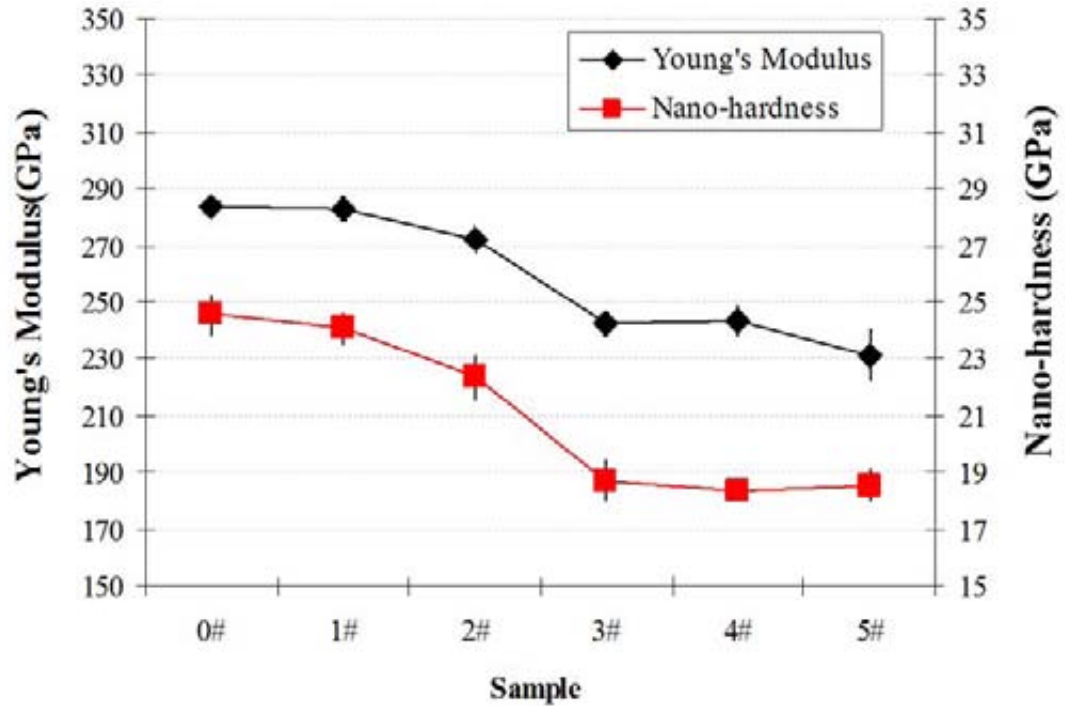
Figure 4.3-2: Nano-hardness and Young's modulus varied with
CrAlTiN and carbon-doped CrAlTiCN coatings
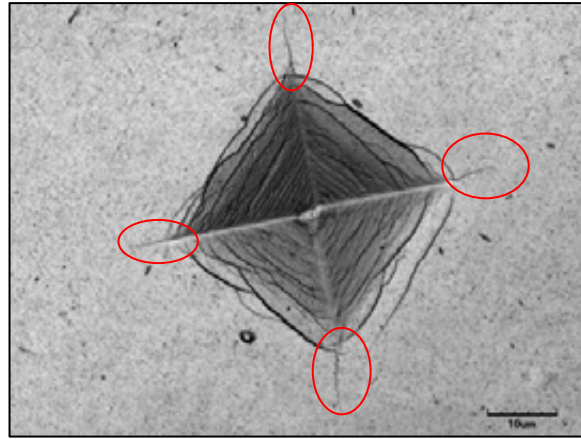
(a) CrAlTiN-0#
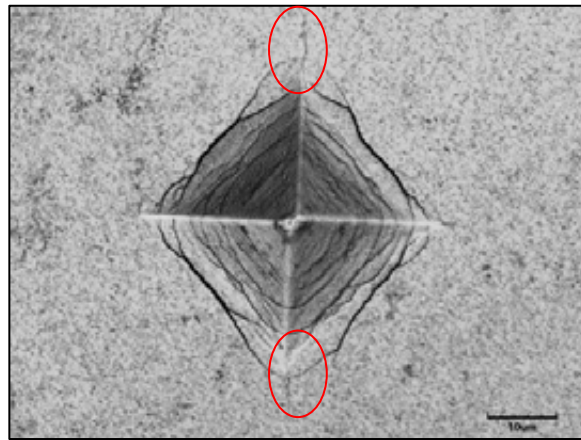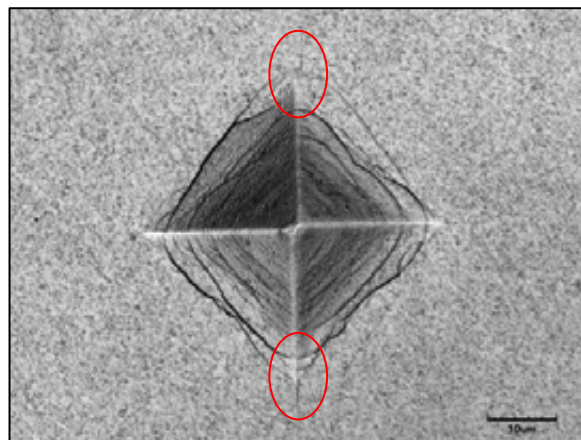
(b) CrAlTiCN-1#
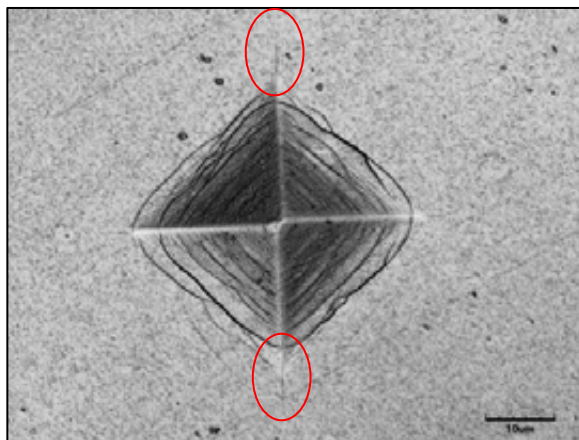
(c) CrAlTiCN-2#
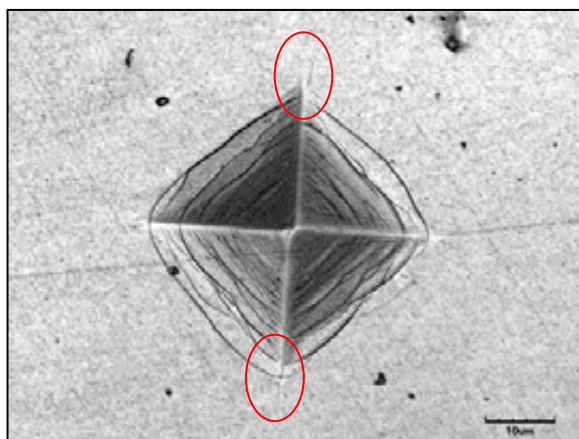
(d) CrAlTiCN-3#
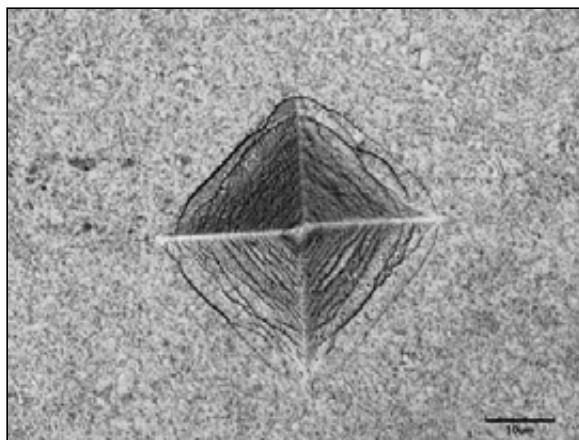
(e) CrAlTiCN-4#

(f) CrAlTiCN-5#
Figure 4.3-3: Laser confocal microscope images of indentations on
(a) CrAlTiN-0#, (b) CrAlTiCN-1#, (c) CrAlTiCN-2#, (d) CrAlTiCN-3#,
(e) CrAlTiCN-4# and (f) CrAlTiCN-5# samples
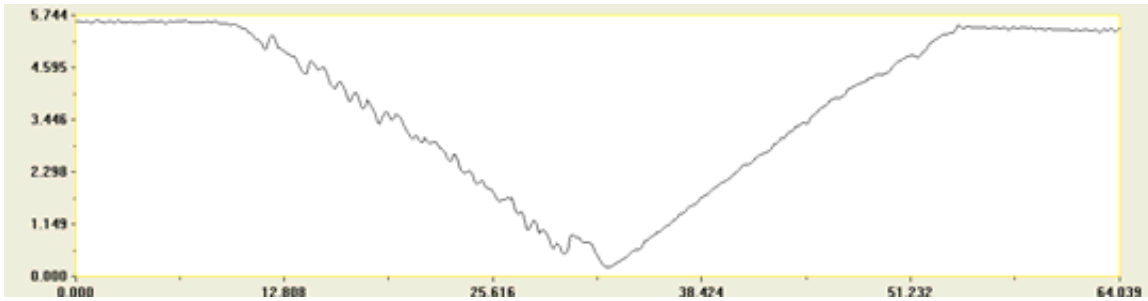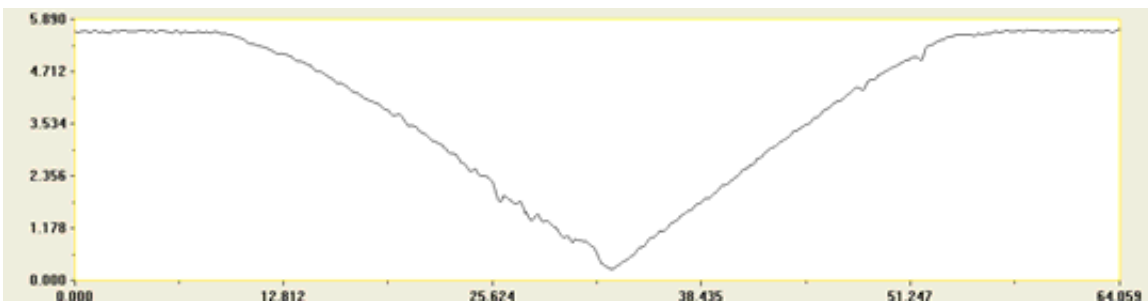
(a) CrAlTiN-0#
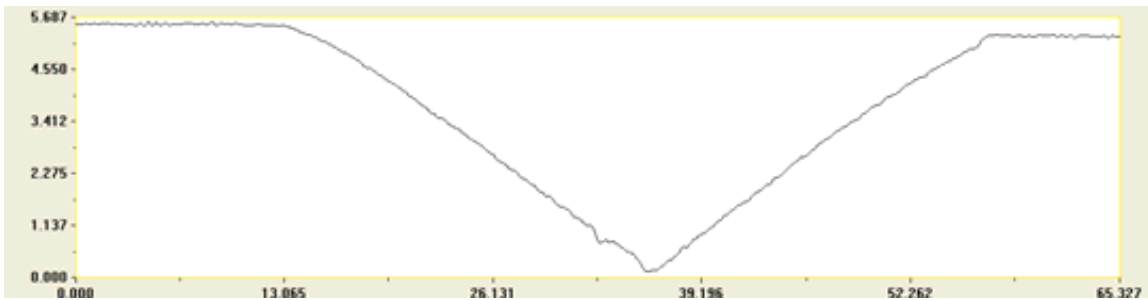
(b) CrAlTiCN-1#

(c) CrAlTiCN-5#

Figure 4.3-4: Typical depth-profiles of the indentations on
(a) CrAlTiN-0#, (b) CrAlTiCN-1# and (c) CrAlTiCN-5# samples

(a) CrAlTiN-0#
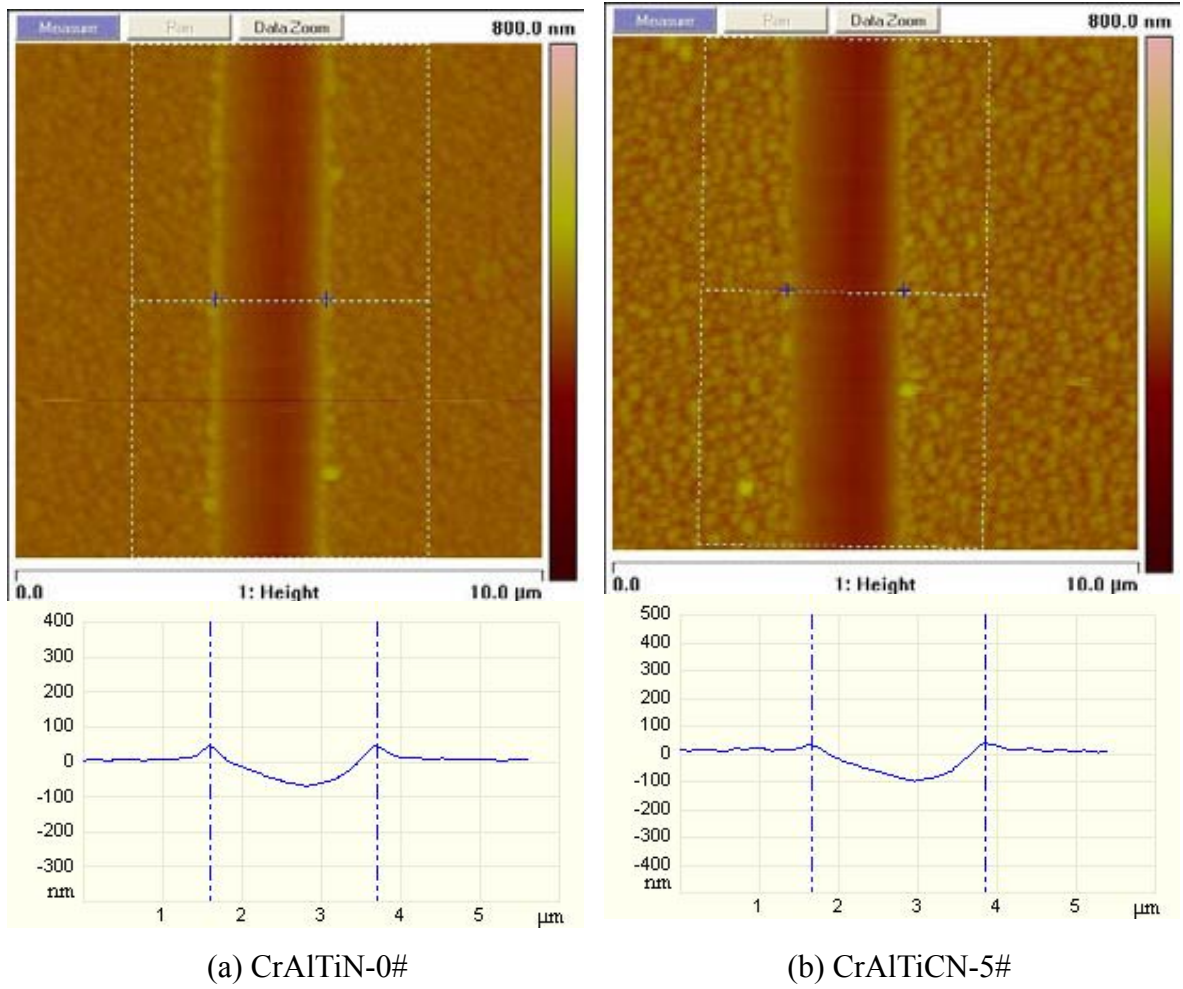
(b) CrAlTiCN-5#

Figure 4.3-5: Typical depth-profiles of micro-mar on
(a) CrAlTiN-0# and (b) CrAlTiCN-5# samples
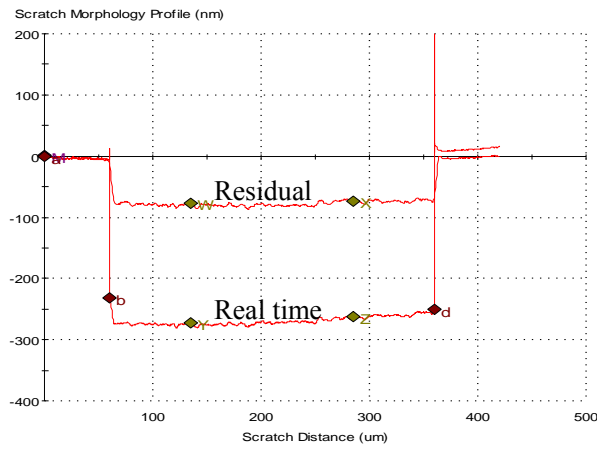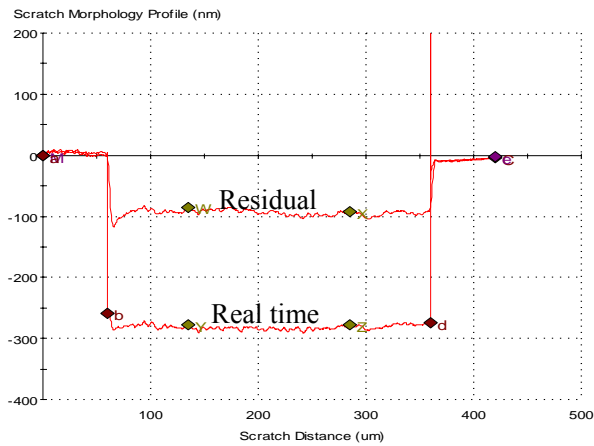
(a) CrAlTiN-0#
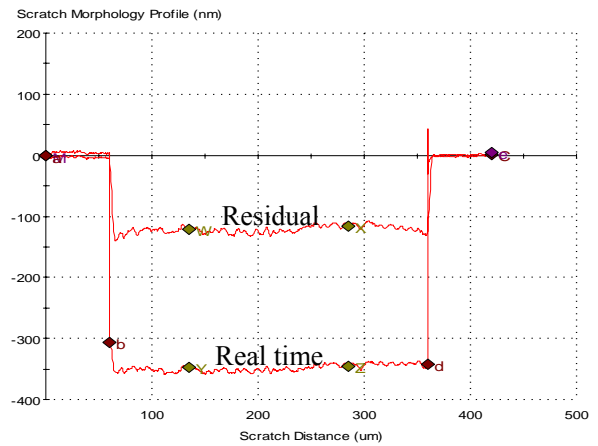
(b) CrAlTiCN-1#

(c) CrAlTiCN-5#

Figure 4.3-6: Depths vs. scratching distance plots after micro-mar resistance tests from (a) CrAlTiN-0#, (b) CrAlTiCN-1# and (c) CrAlTiCN-5# samples
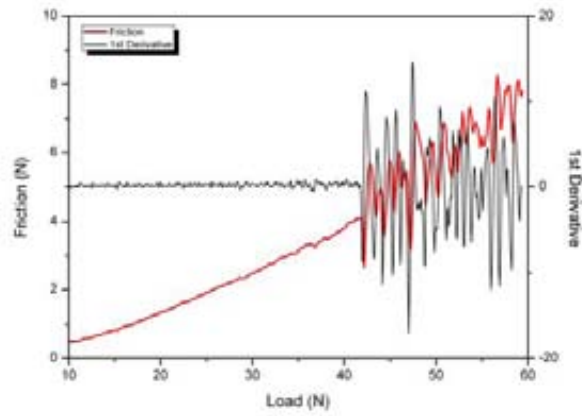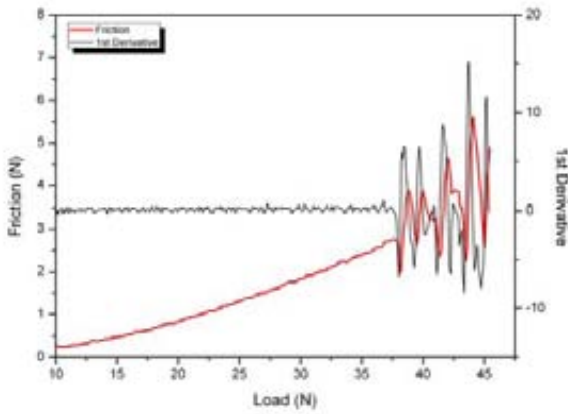
(a) CrAlTiN-0#
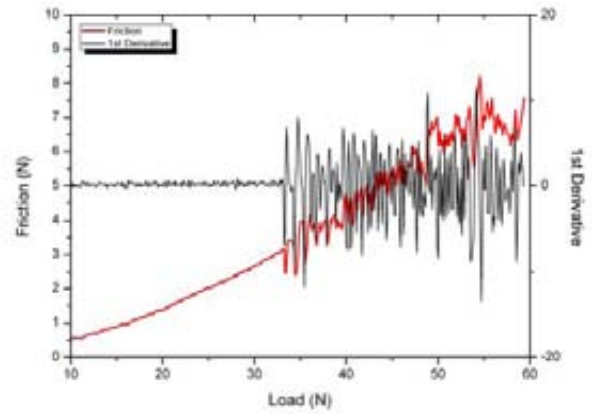
(b) CrAlTiCN-3#

(c) CrAlTiCN-5#

Figure 4.3-7: Friction force and its first derivation against scratch load from (a) CrAlTiN-0#, (b) CrAlTiCN-3# and (c) CrAlTiCN-5# samples
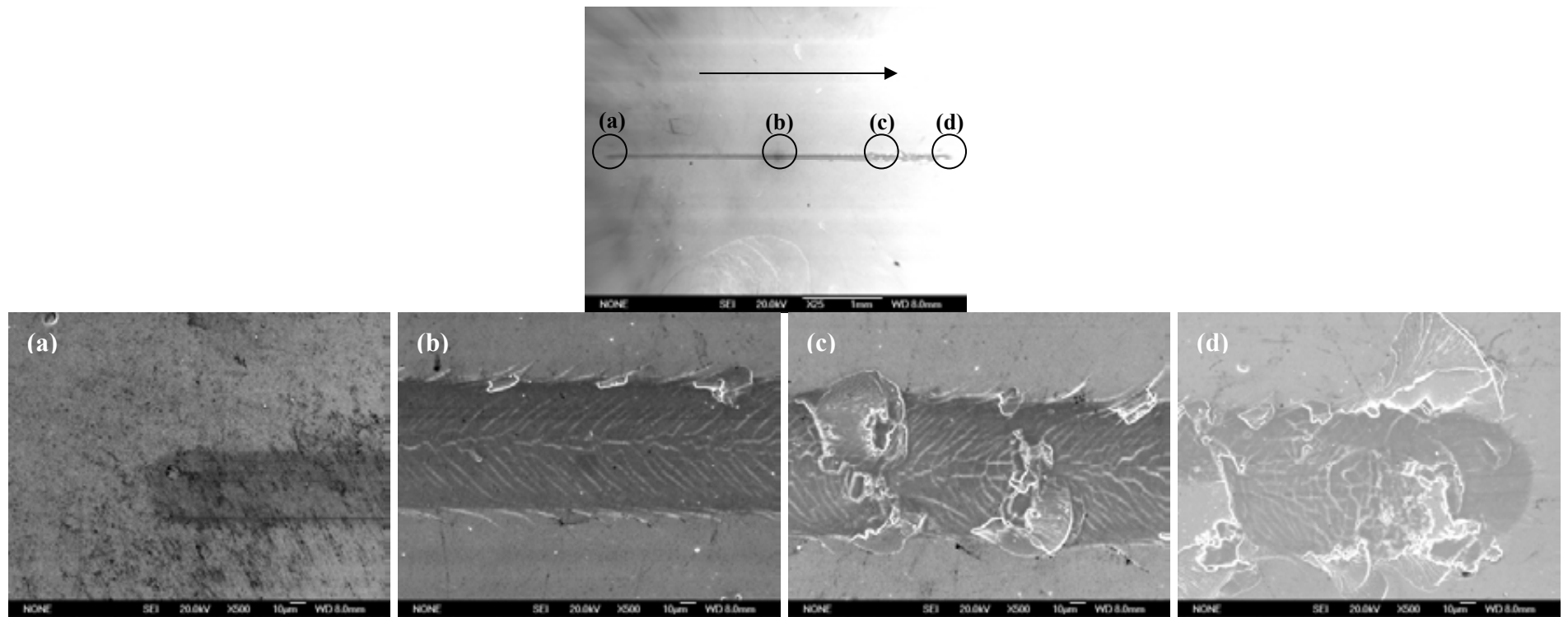
Figure 4.3-8: Typical scratch track SEM morphologies of as-deposited CrAlTiCN-3# sample
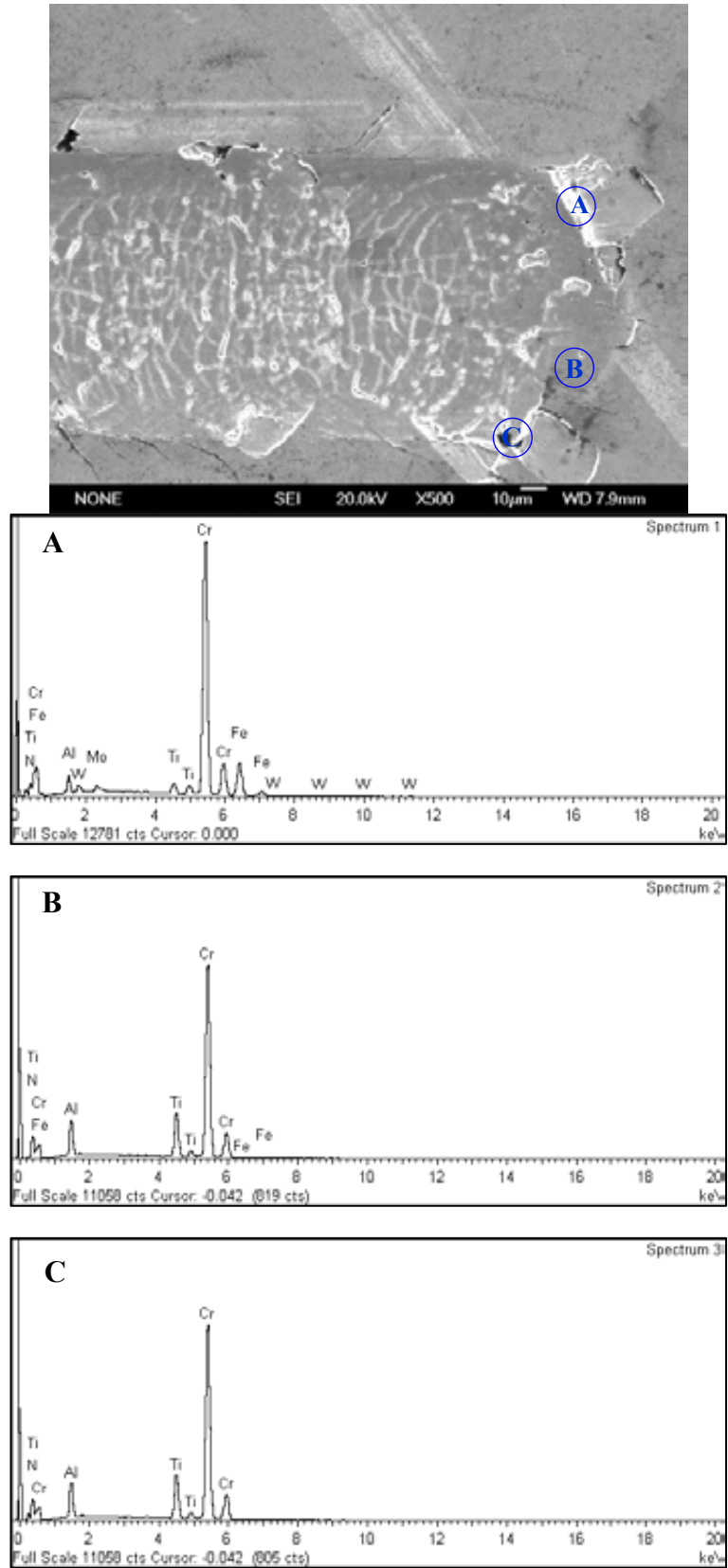
Figure 4.3-9: SEM images of the end region of the scratched track and EDX spectrums from CrAlTiN-0# sample
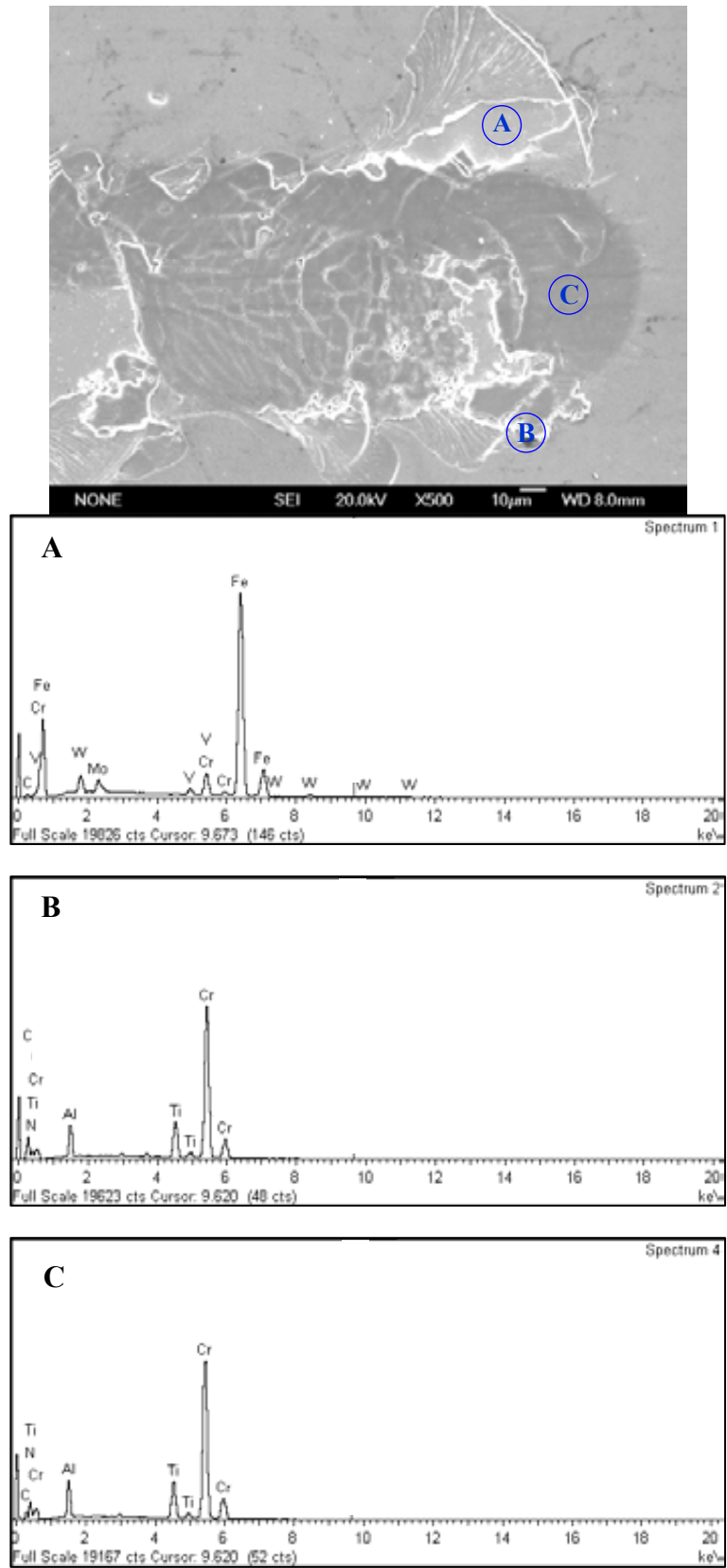
Figure 4.3-10: SEM images of the end region of the scratched track and EDX spectrums from CrAlTiCN-3# sample
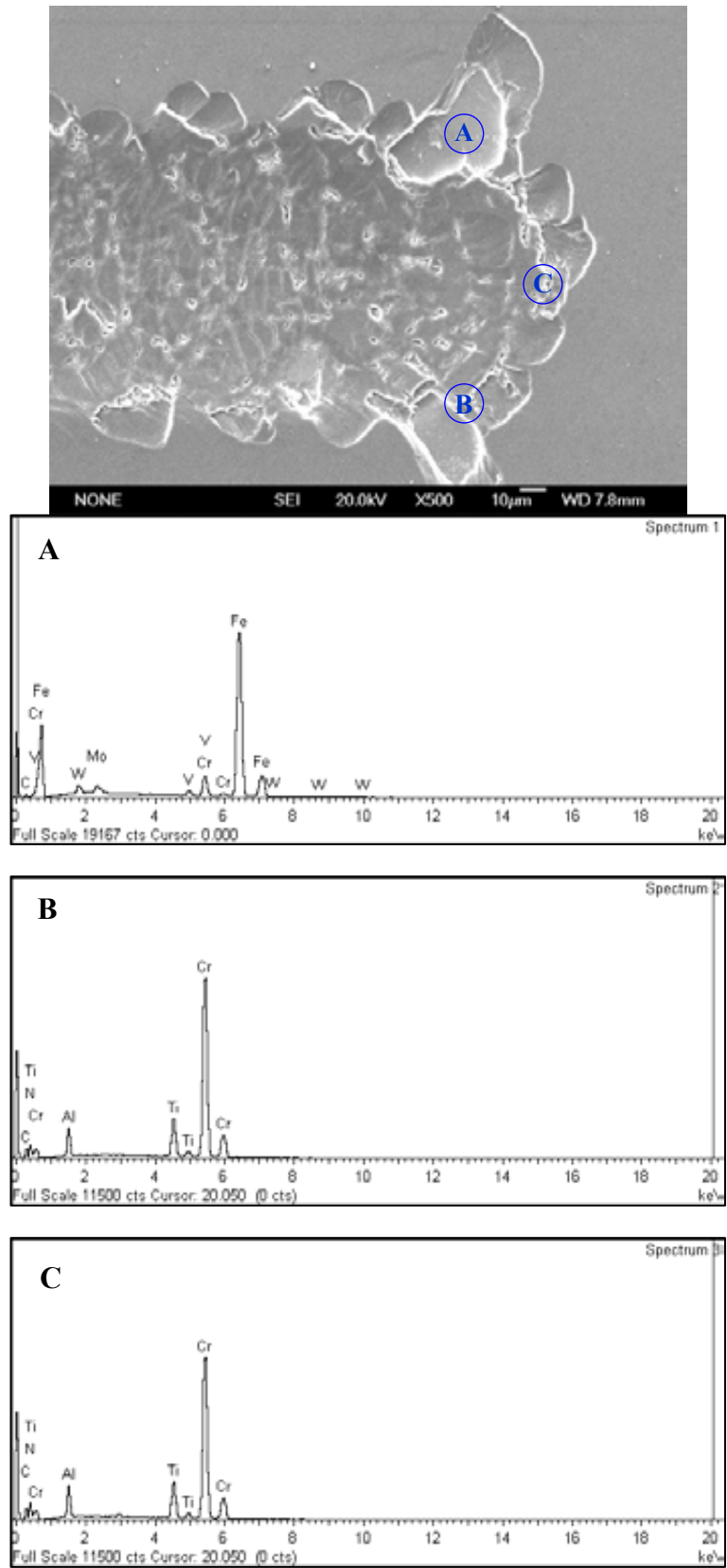
Figure 4.3-11: SEM images of the end region of the scratched track and EDX spectrums from CrAlTiCN-5# sample
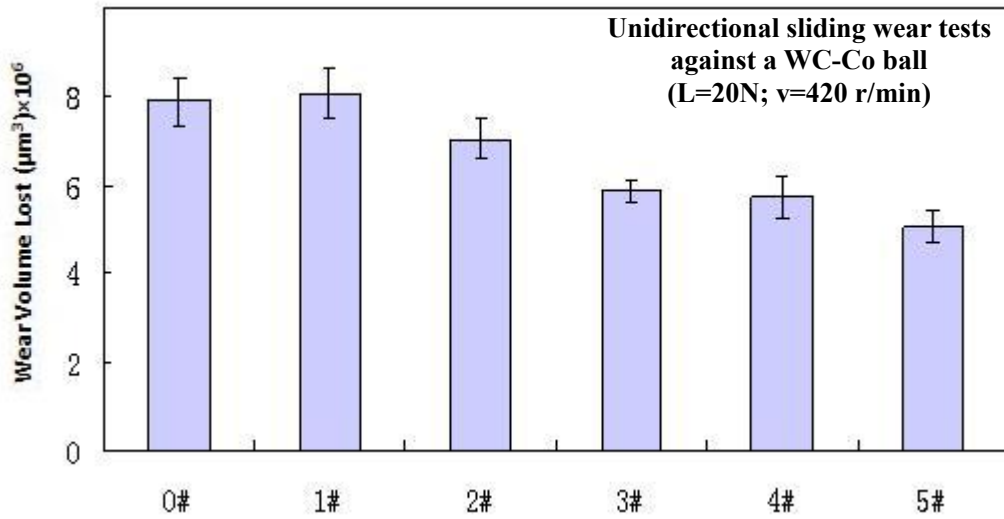
(a)
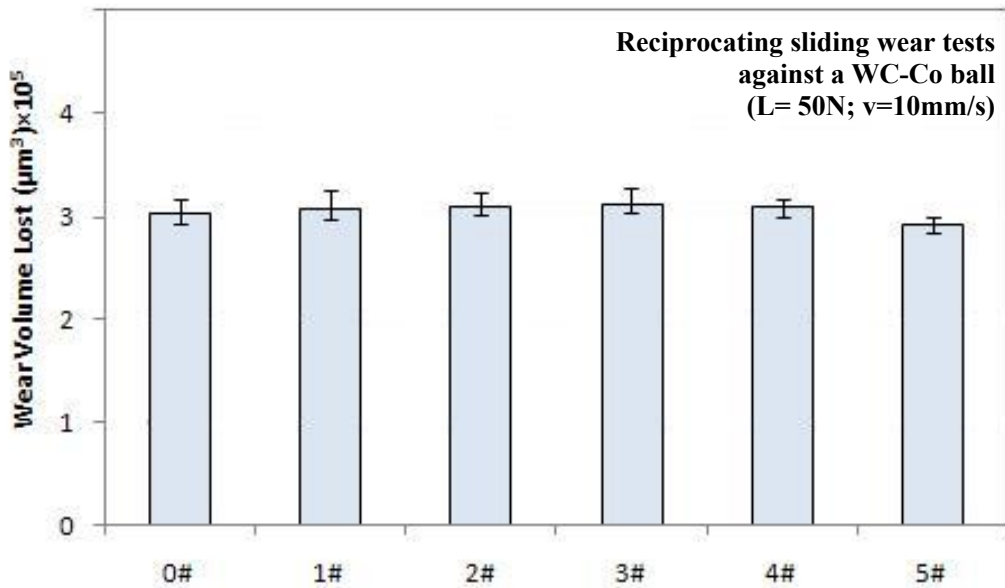
(b)

Figure 4.4-1: Measured worn volume after (a) unidirectional sliding tests and
(b) reciprocating sliding tests
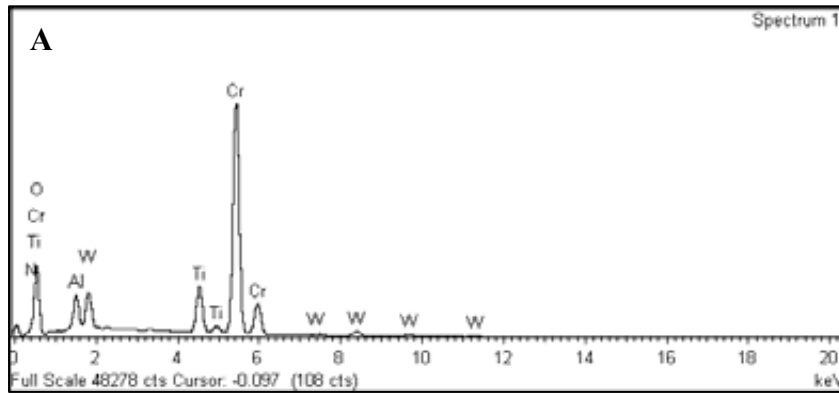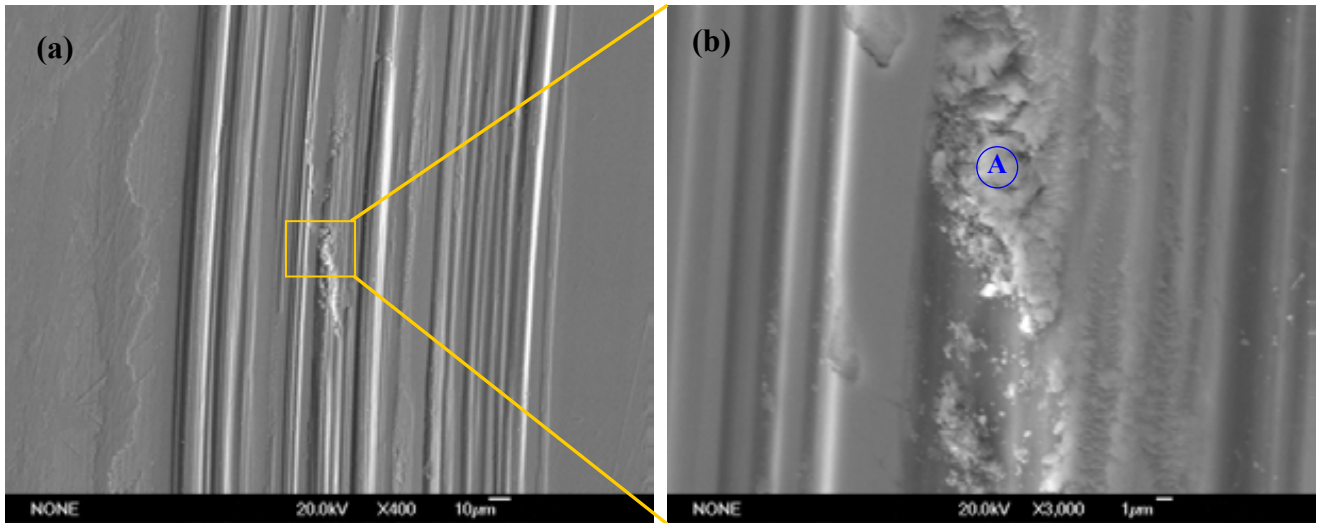
Element	Cr	Al	Ti	N	O	W
at%	38.48±0. 40	5.33±0. 06	5.84±0. 08	1.71±0. 57	45.29±0. 32	3.35±0. 14

Figure 4.4-2: SEM images of unidirectional sliding wear track and EDX spectrum
from CrAlTiN-0# coating
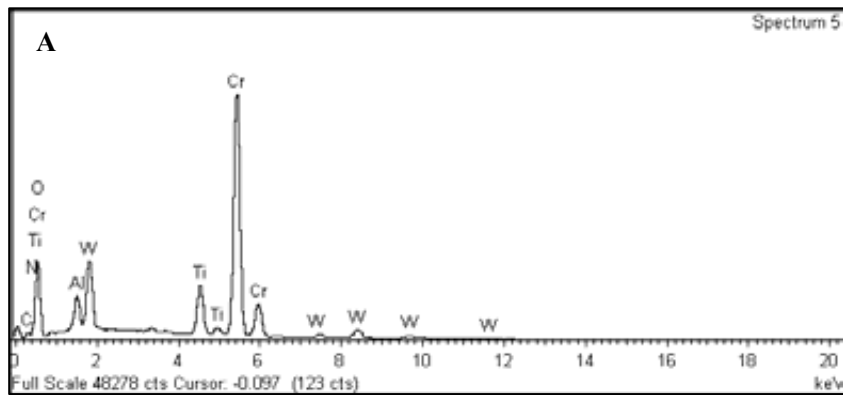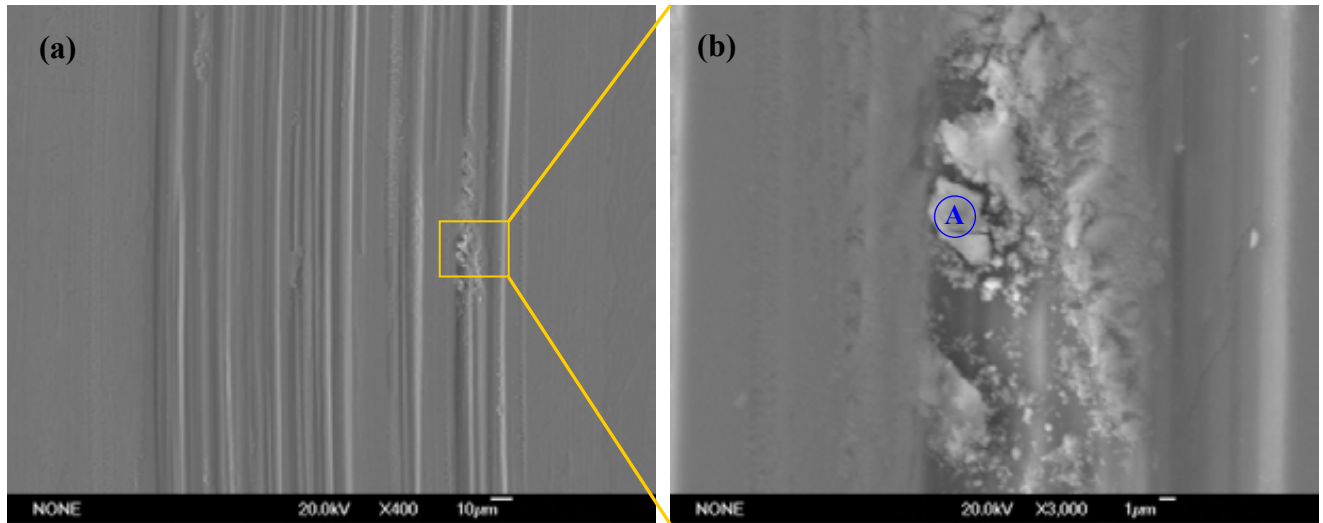
Element	Cr	Al	Ti	N	O	C	W
at%	33.31±0.32	4.53±0.04	5.67±0.07	15.50±0.43	32.64±0.22	7.30±0.21	1.05±0.09

Figure 4.4-3: SEM images of unidirectional sliding wear track and EDX spectrum from CrAlTiCN-1# coating
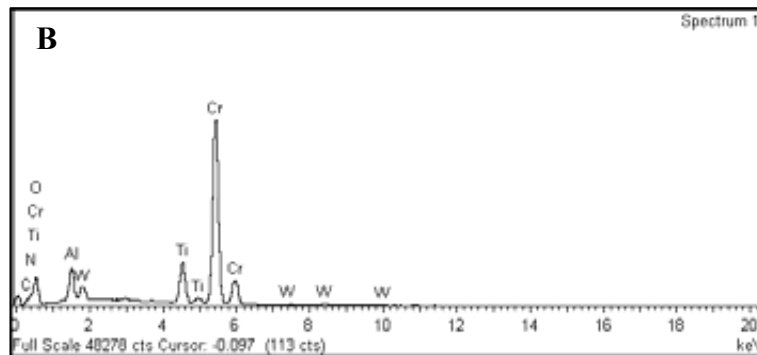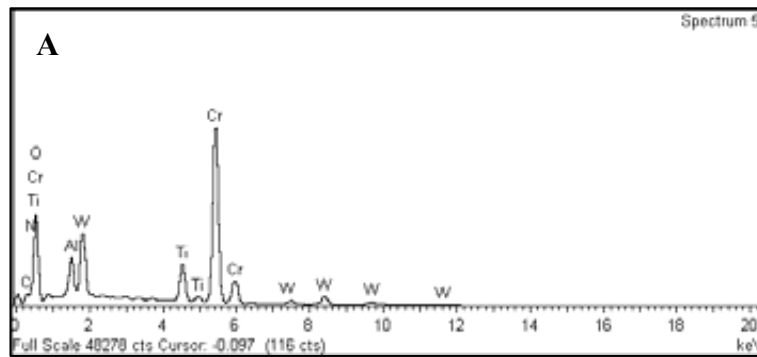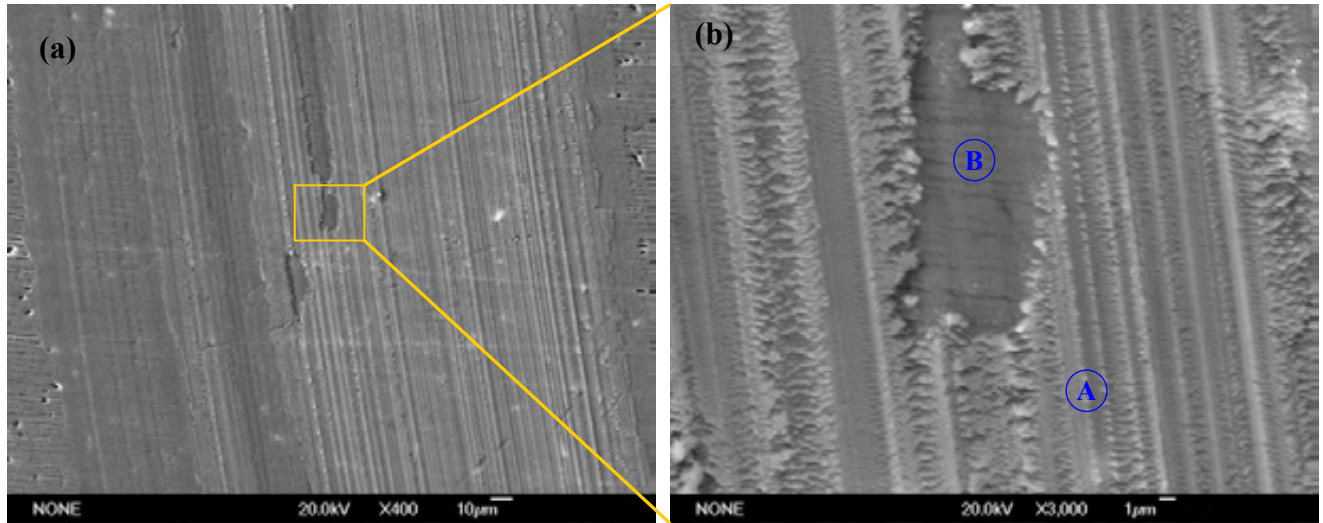
Element	Cr	Al	Ti	N	O	C	W
A (at%)	34.12±0. 36	5. 56±0. 05	5.35±0. 10	5. 43±0. 70	33. 14±0. 39	15.19±0. 29	1.21±0. 17
B (at%)	35.50±0. 55	5. 81±0. 07	5.57±0. 10	35. 12±0. 69	1. 78±0. 39	15.37±0. 35	0.85±0. 13

Figure 4.4-4: SEM images of unidirectional sliding wear track and EDX spectrums
from CrAlTiCN-3# coating
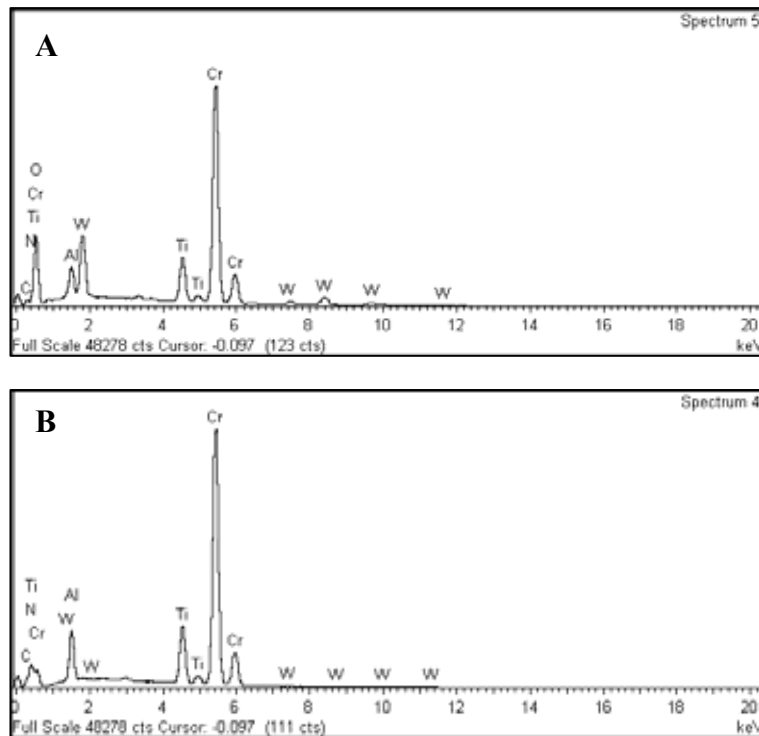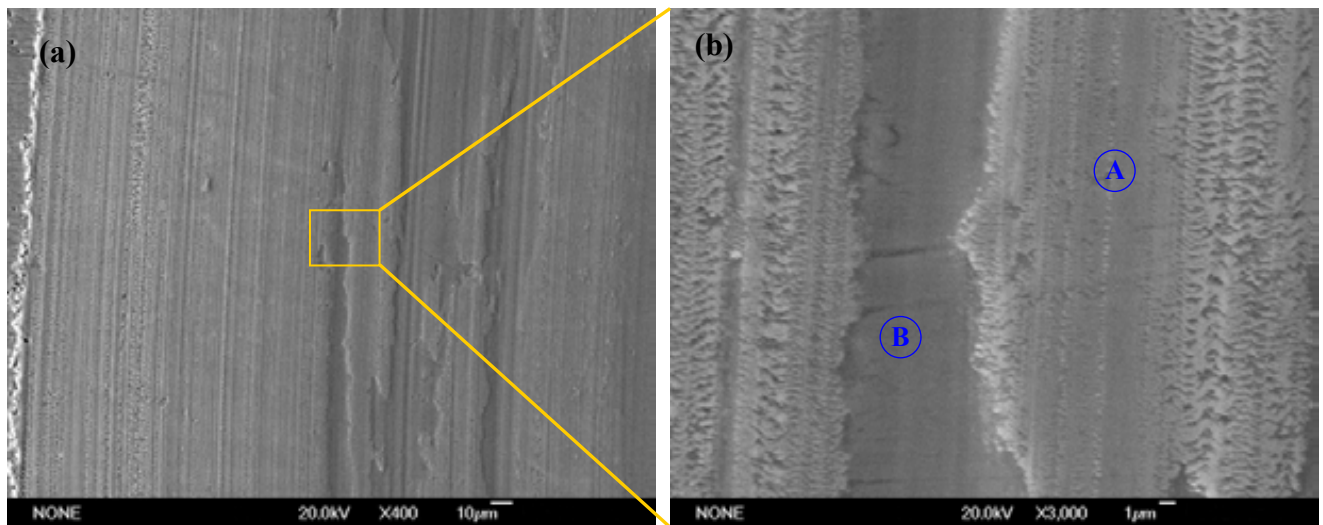
Element	Cr	Al	Ti	N	O	C	W
A (at%)	35. 85±0. 16	4. 66±0. 05	4.74±0. 07	2. 97±0. 58	39. 27±0. 31	11.30±0. 26	1.21±0. 16
B (at%)	38.26±0. 42	7. 43±0. 07	6.23±0. 08	32. 46±0. 47		15.05±0. 32	0.57±0. 09

Figure 4.4-5: SEM images of unidirectional sliding wear track and EDX spectrums
from CrAlTiCN-5# coating
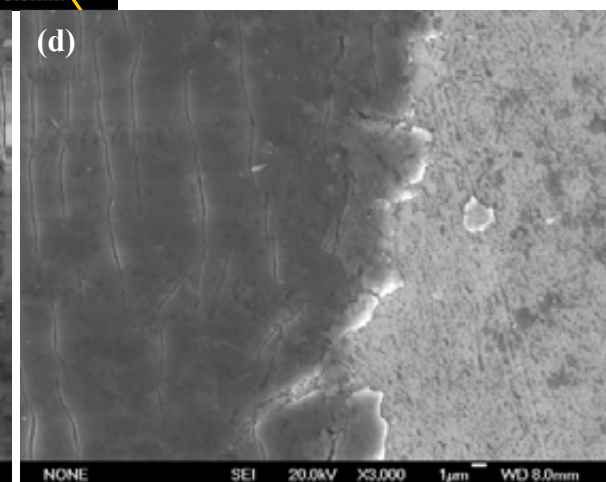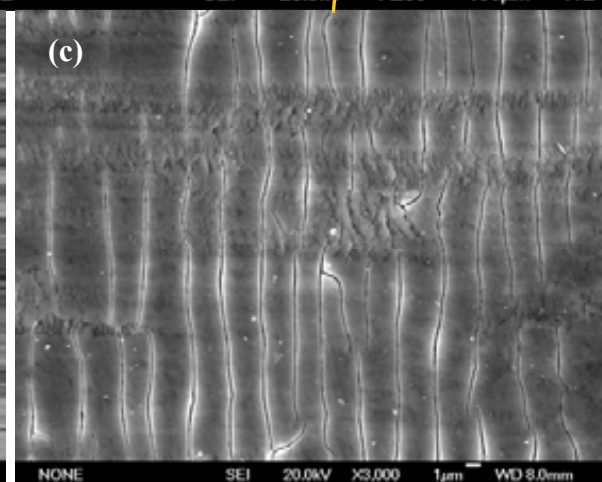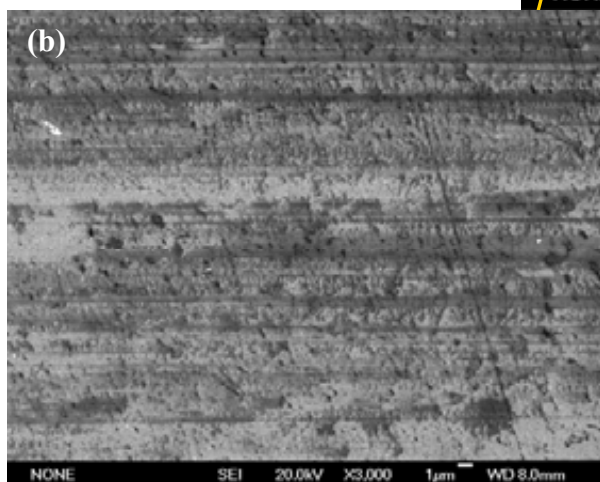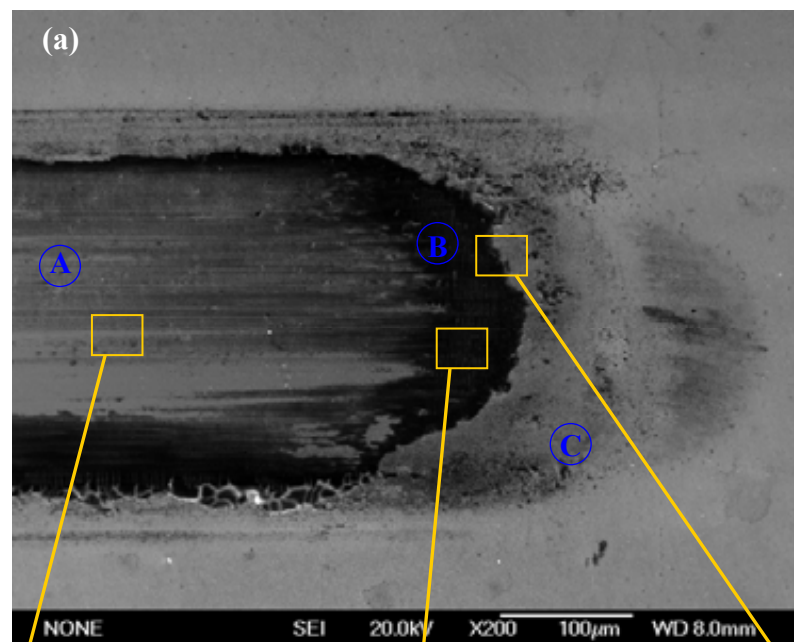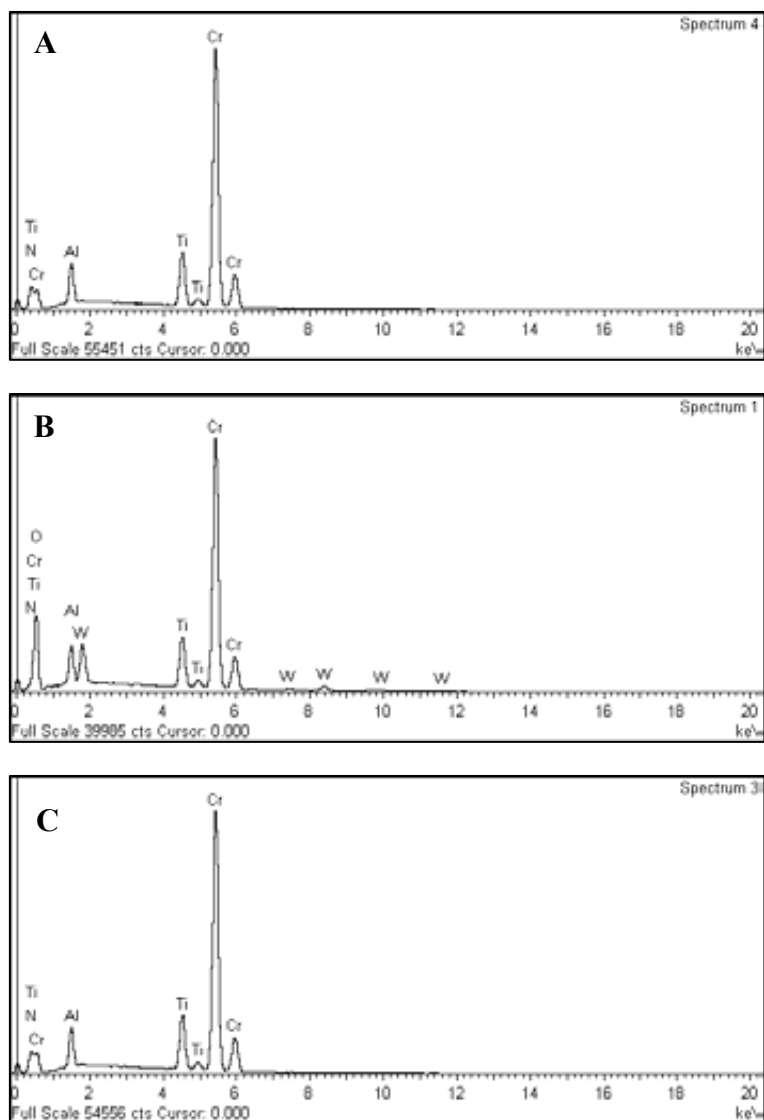
Element	Cr	Al	Ti	O	N	W
A (at%)	52.60±0.34	8.25±0.06	7.60±0.07		31.55±0.40	
B (at%)	38.48±0.40	5.34±0.06	5.84±0.08	45.69±0.08	2.70±0.57	1.95±0.14
C (at%)	54.58±0.35	8.52±0.06	7.83±0.07		29.07±0.41	

Figure 4.4-6: SEM images of reciprocating sliding wear track and EDX spectrums
from CrAlTiN-0# coating

216
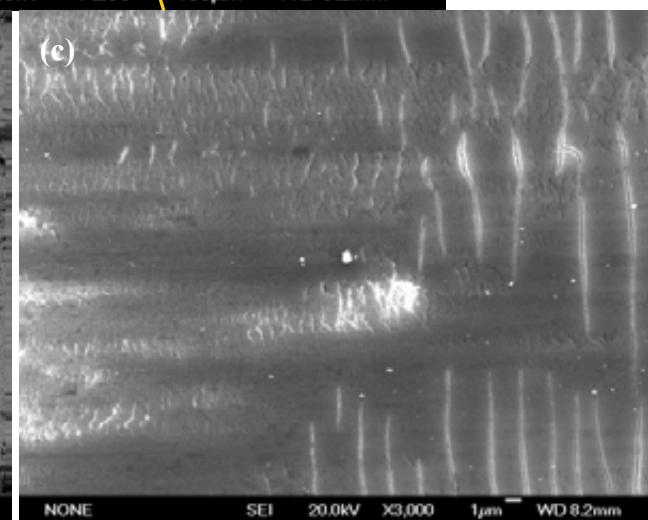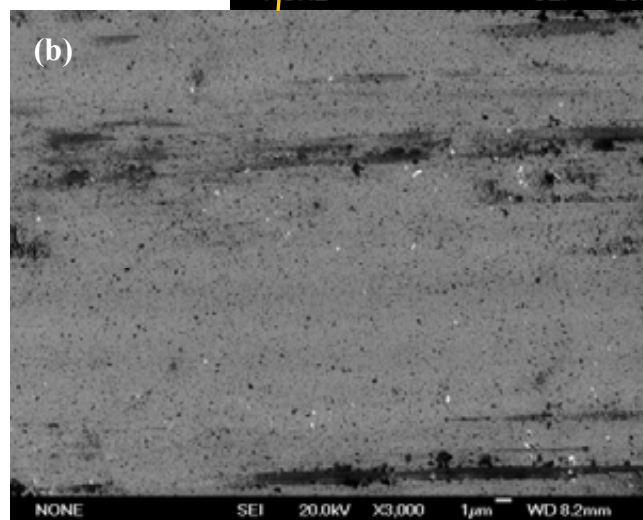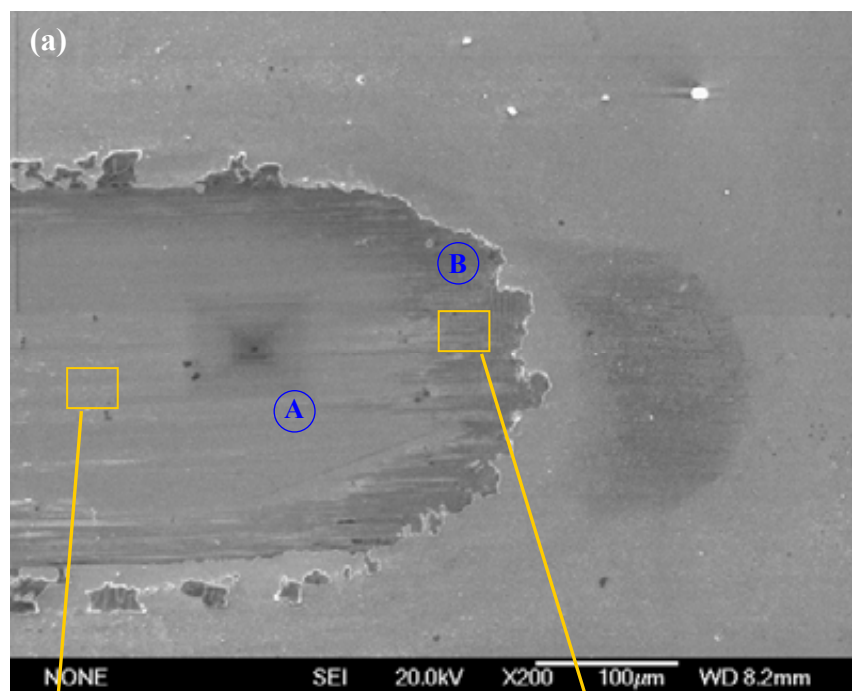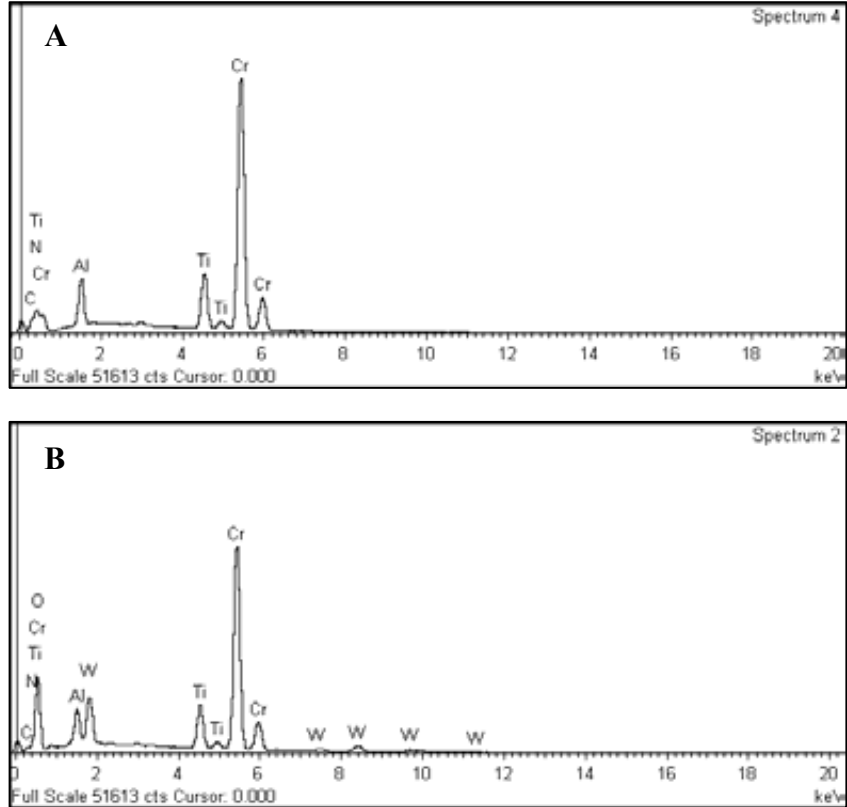
Element	Cr	Al	Ti	O	N	W	C
A (at%)	35.90±0.45	6.24±0.07	5.52±0.08		31.08±0.53		21.26±0.33
B (at%)	29.32±0.40	4.33±0.06	4.75±0.08	45.59±0.35	4.52±0.62	2.17±0.16	9.32±0.35

Figure 4.4-7: SEM images of reciprocating sliding wear track and EDX spectrums from CrAlTiCN-3# coating
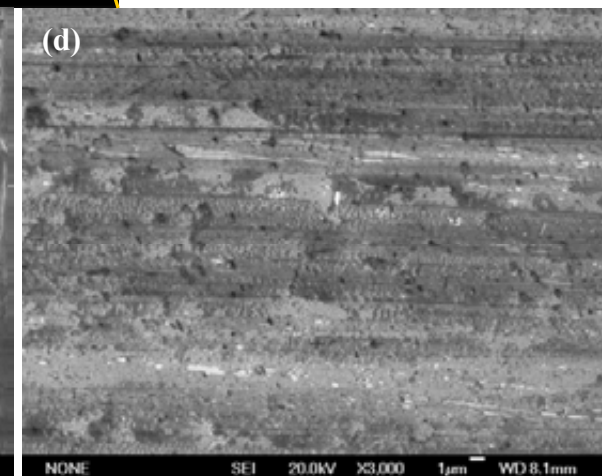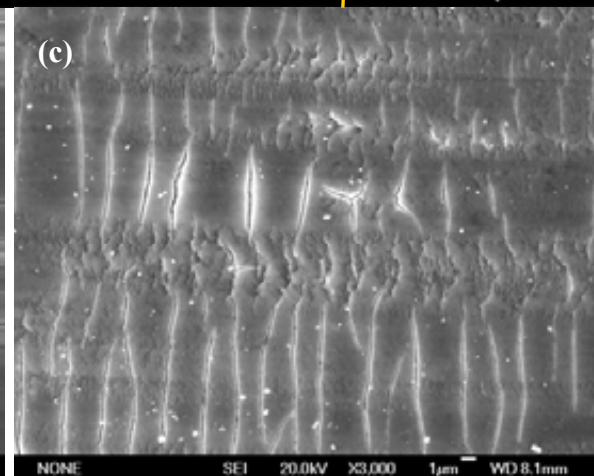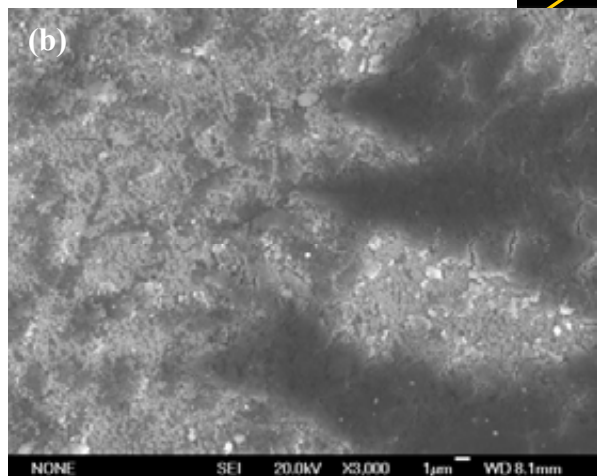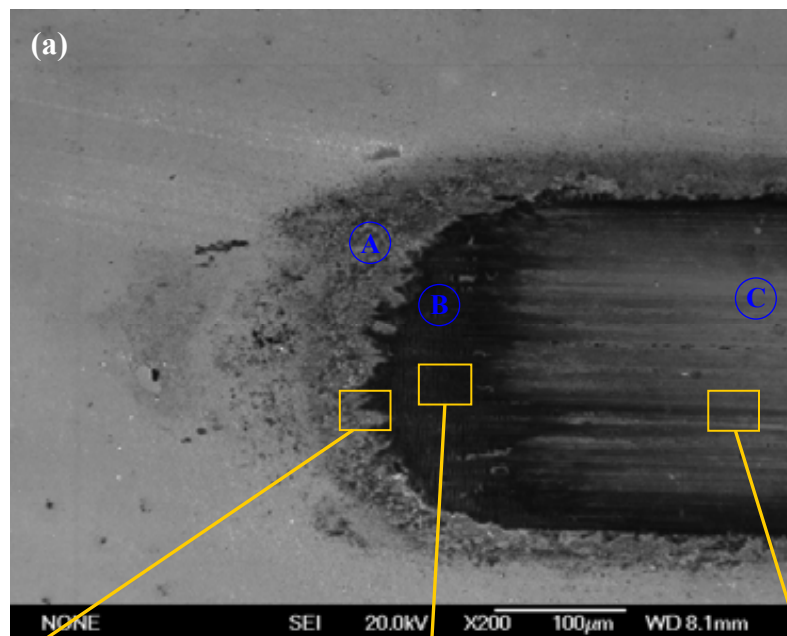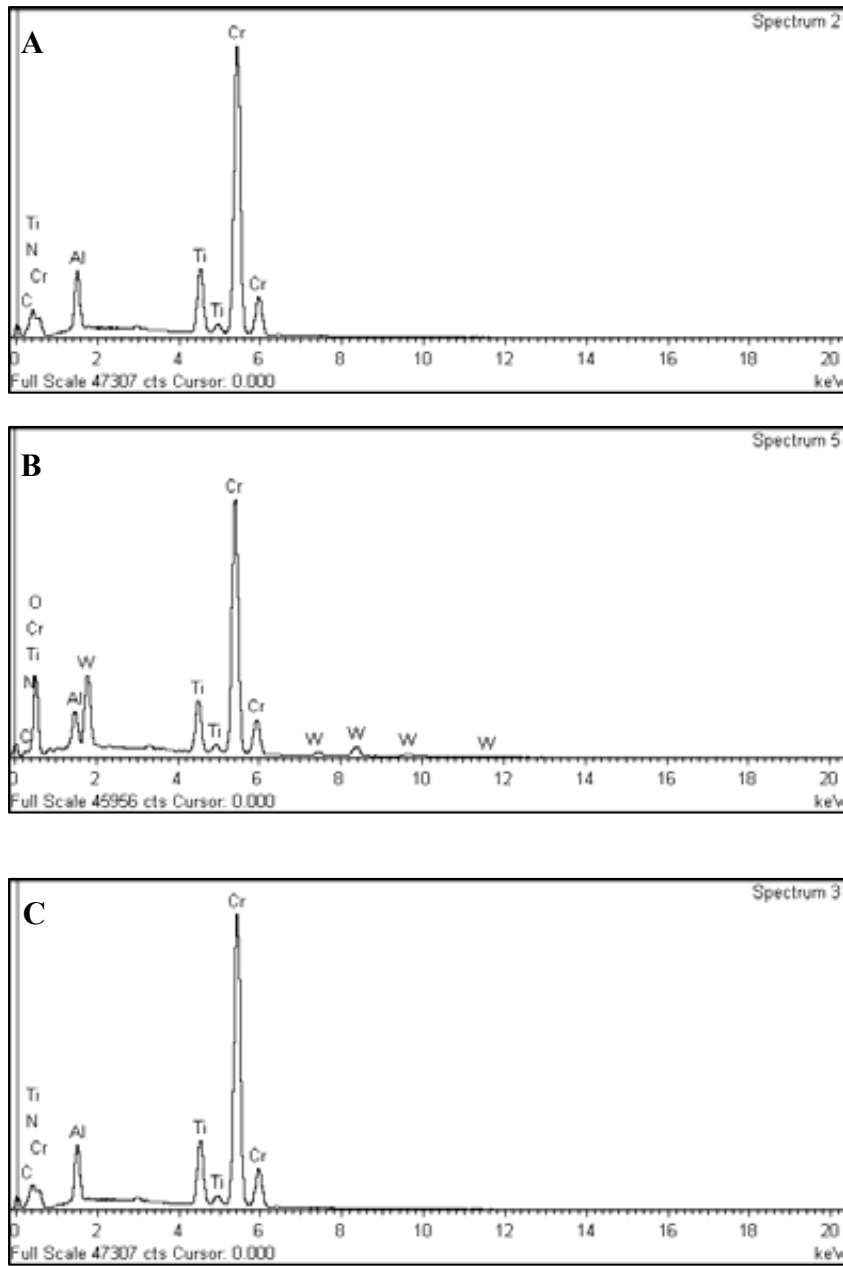
Element	Cr	Al	Ti	O	N	W	C
A (at%)	38.38±0.42	7.43±0.07	5.99±0.08		33.22±0.47		14.98±0.32
B (at%)	30.35±0.37	3.66±0.05	4.74±0.07	43.27±0.31	3.97±0.58	2.71±0.16	11.30±0.26
C (at%)	38.60±0.41	7.31±0.07	6.07±0.08		32.85±0.46		15.17±0.31

Figure 4.4-8: SEM images of reciprocating sliding wear track and EDX spectrums
from CrAlTiCN-5# coating
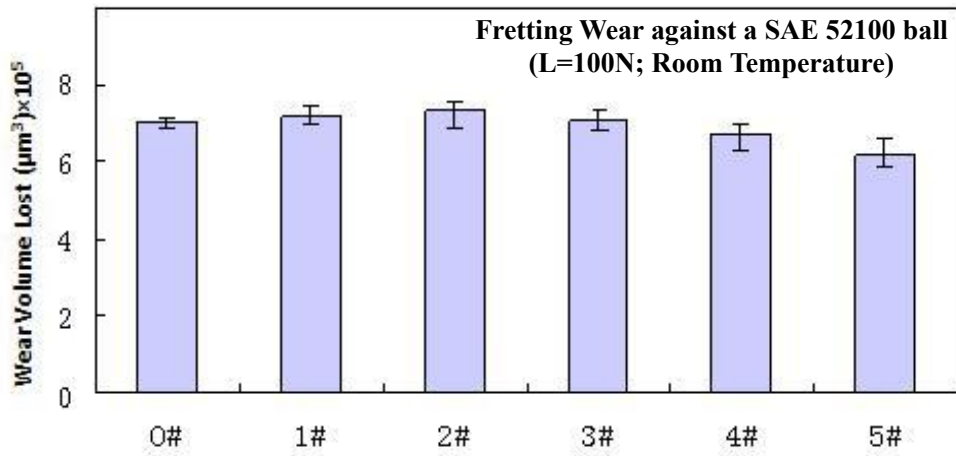
(a)
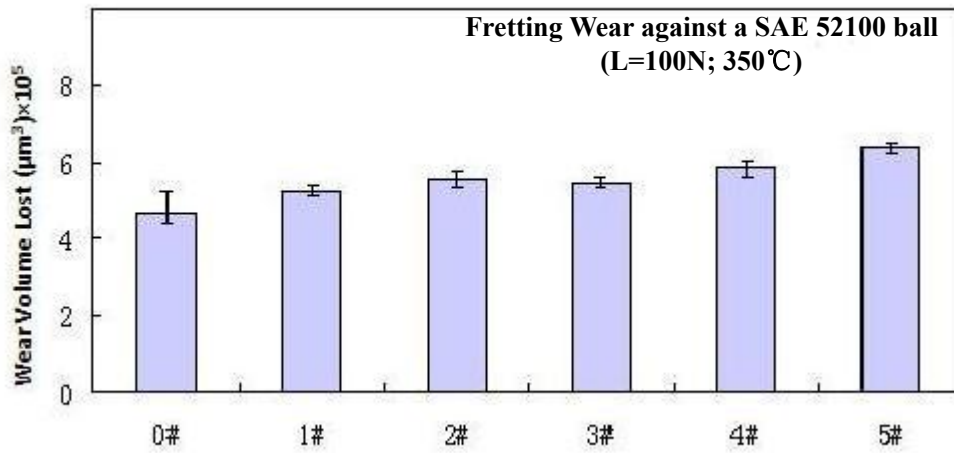
(b)

Figure 4.4-9: Measured worn volume after fretting wear tests at:
(a) room temperature and (b) 350 ℃
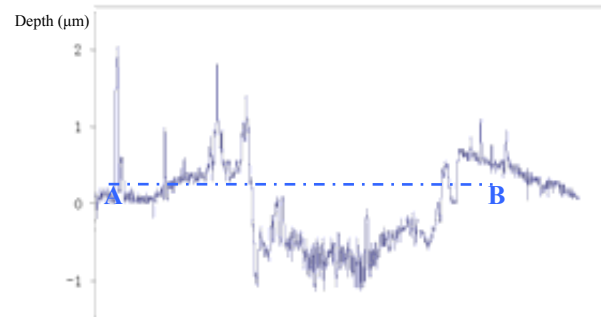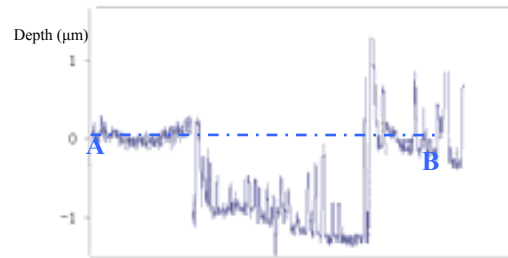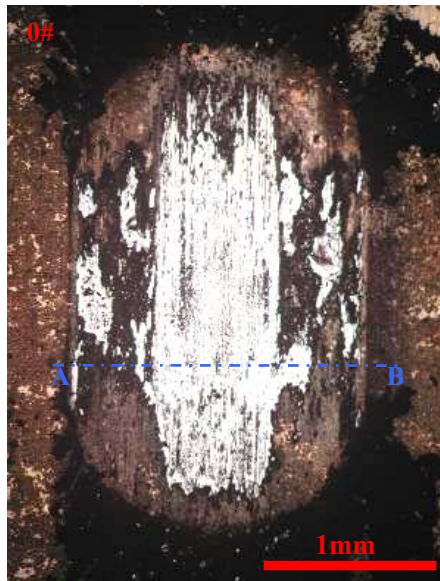
Figure 4.4-10: Optical micrographs of room temperature fretting wear tests on
CrAlTiN-0# and CrAlTiCN-5# samples

(a) Wear scar — Sliding direction — End region — NONE 20.0kV X400 10μm

(b) Wear scar — Middle region — NONE 20.0kV X400 10μm

(c) NONE 20.0kV X3,000 1μm

(d) NONE 20.0kV X3,000 1μm
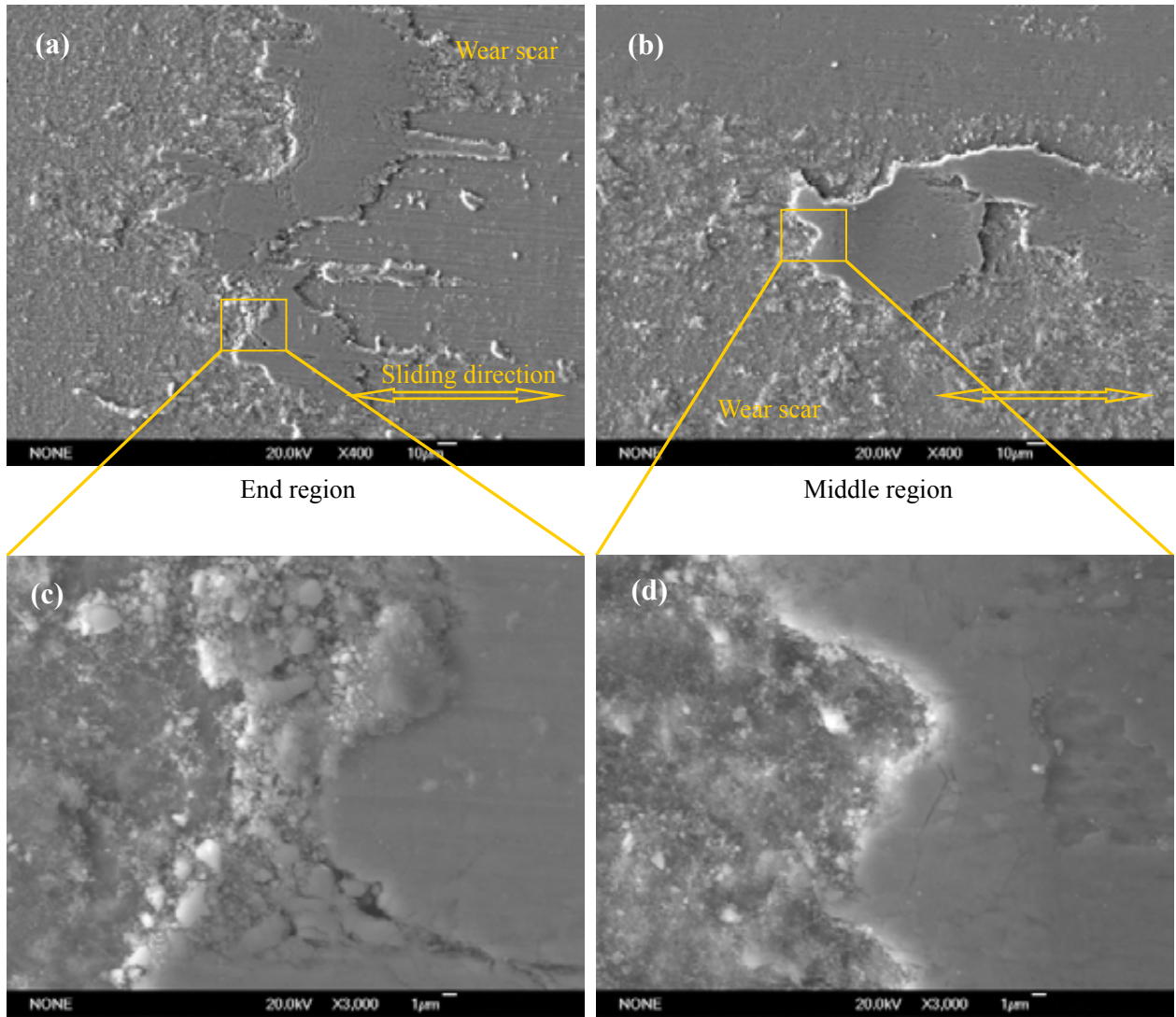
Figure 4.4-11: SEM images of room temperature fretting wear tracks on CrAlTiN-0# sample

Edge region

Middle region
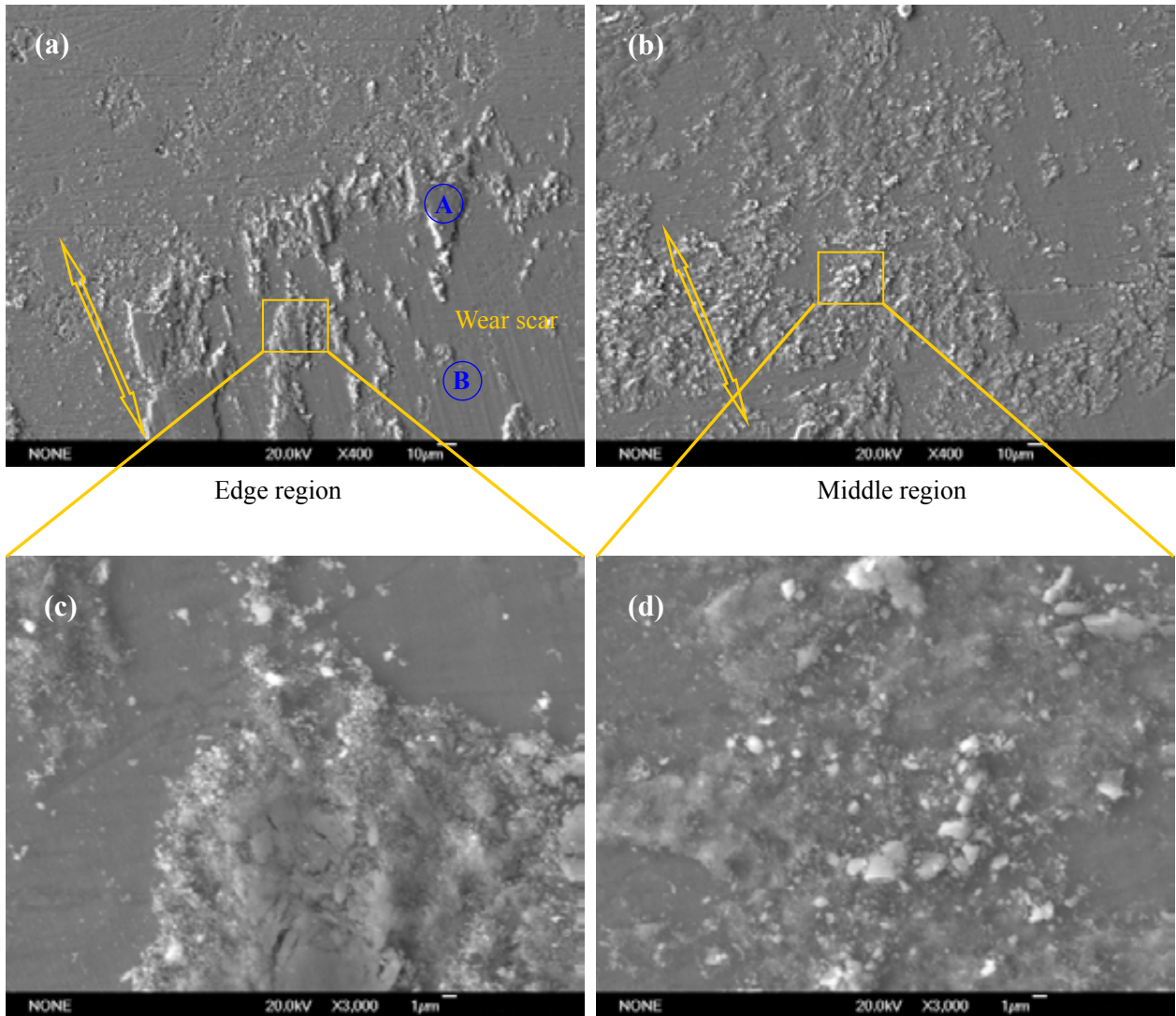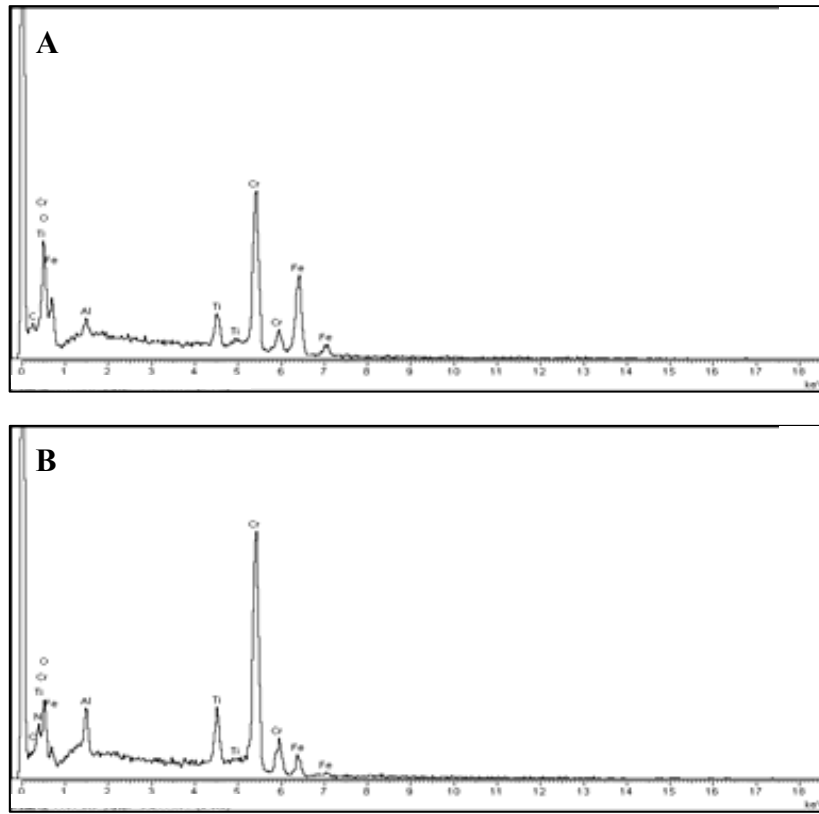
Element	Cr	Al	Ti	N	O	C	Fe
A (at%)	20. 66±0. 15	1. 89±0. 05	3. 34±0. 07		47. 55±0. 31	12.32±0. 39	14.24±0. 06
B (at%)	35. 61±0. 32	5. 81±0. 05	5. 33±0. 08	43. 34±0. 17	2. 07±0. 13	4. 59±0. 32	3.25±0. 08

Figure 4.4-12: SEM images of room temperature fretting wear tracks and EDX spectrums from CrAlTiCN-1# sample
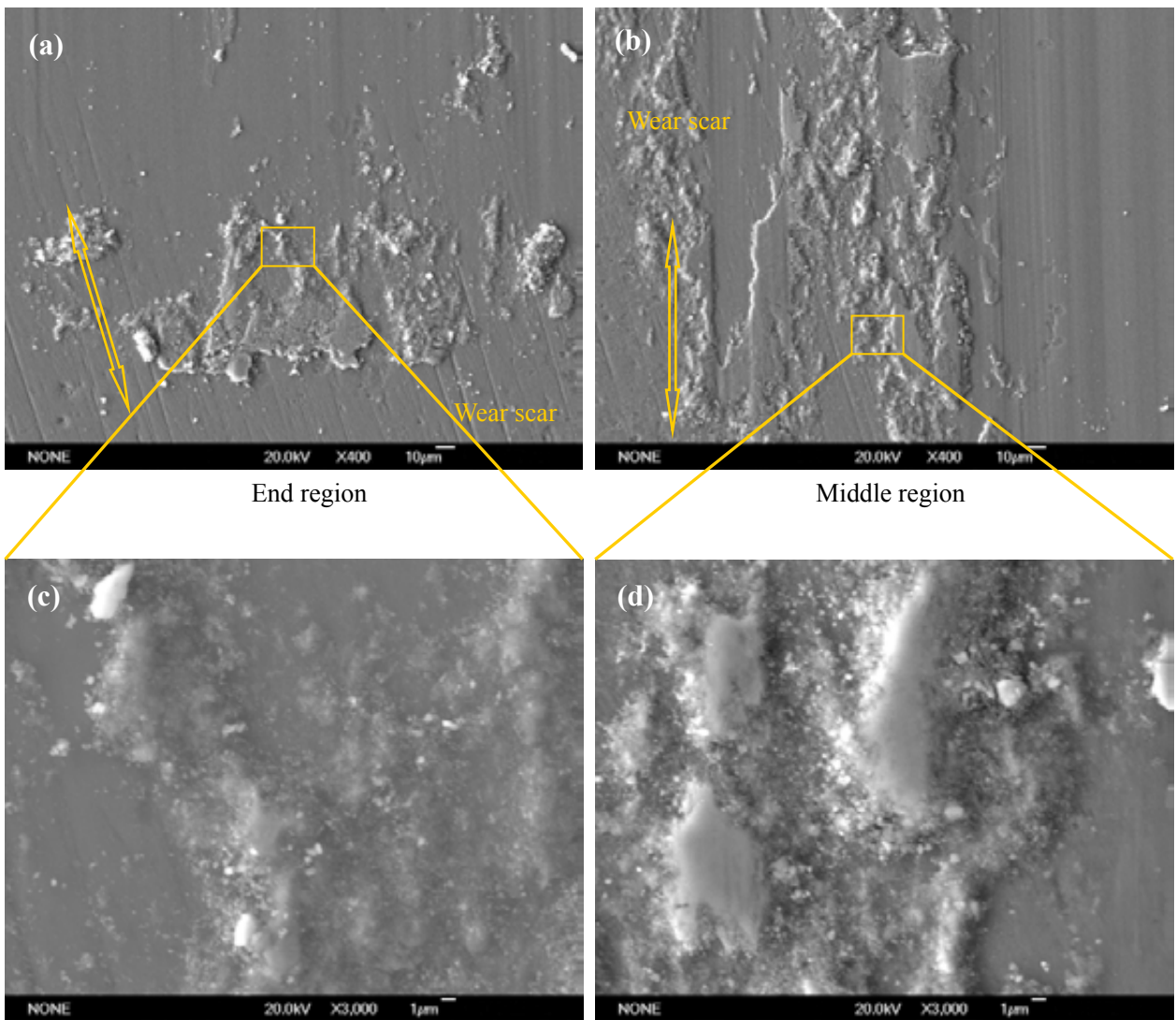
Figure 4.4-13: SEM images of room temperature fretting wear tracks on CrAlTiCN-4# sample
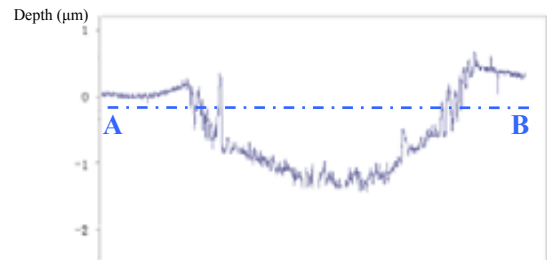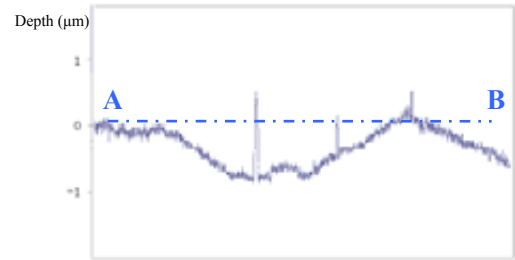
Figure 4.4-14: Optical micrographs of 350 ℃ fretting wear tests on
CrAlTiN-0# and CrAlTiCN-5# samples
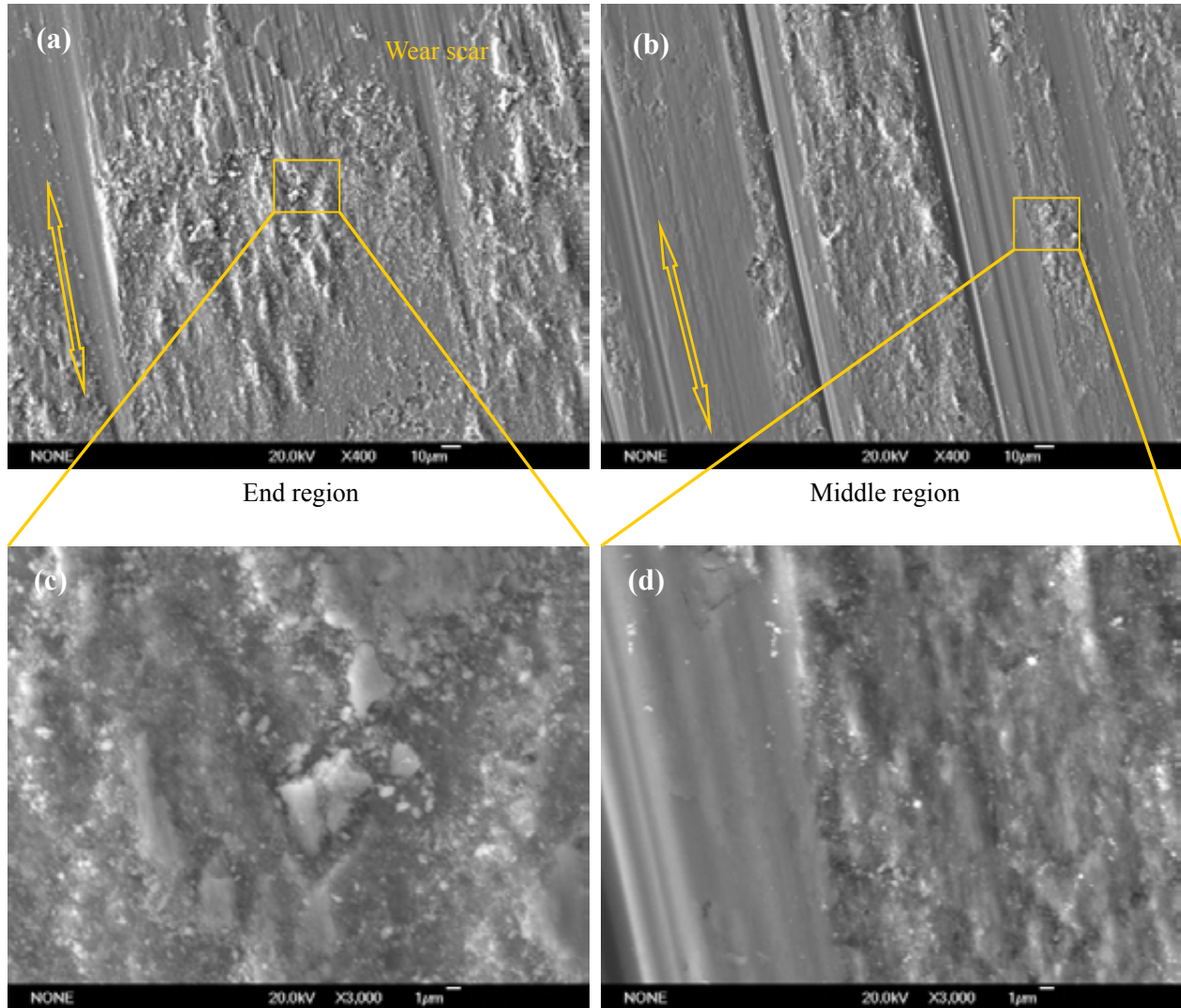
Figure 4.4-15: SEM images of 350℃ fretting wear tracks on CrAlTiN-0# sample

Edge region

Middle region
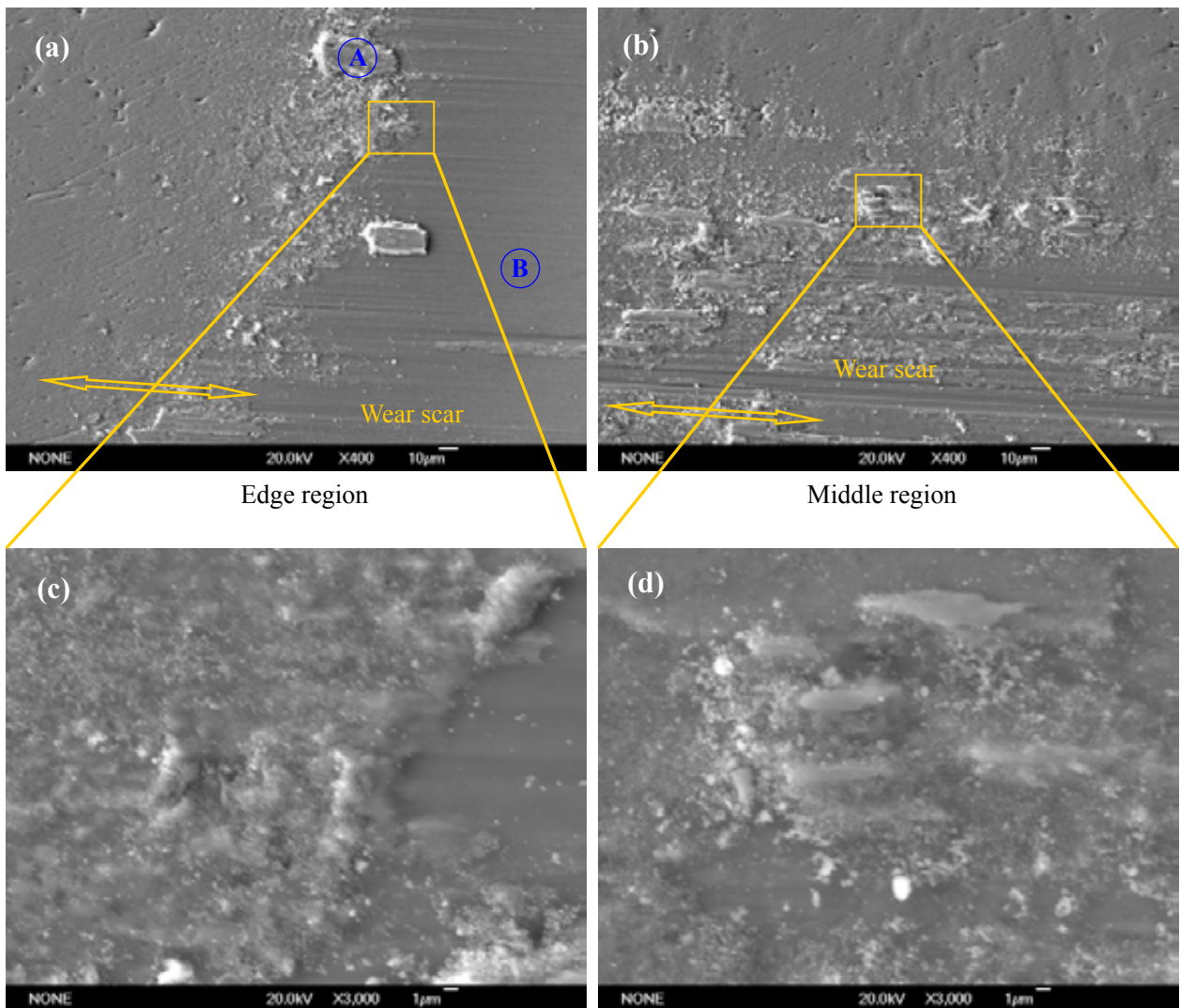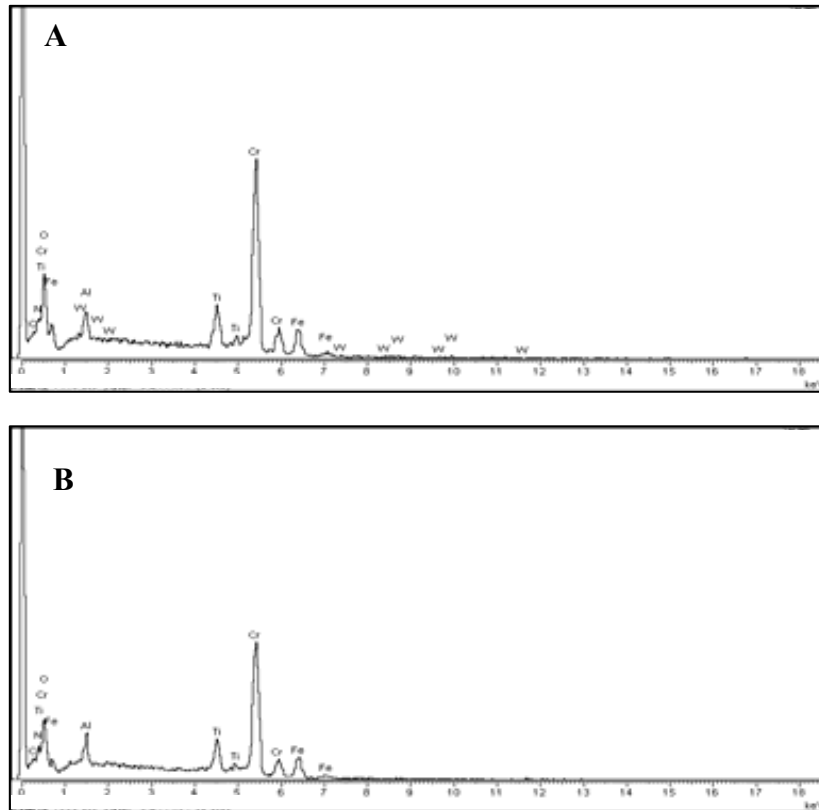
Element	Cr	Al	Ti	N	O	C	Fe
A (at%)	7. 36±0. 13	0. 23±0. 05	1. 47±0. 07	1. 50±0. 06	58. 71±0. 21	9.05±0. 09	20.58±0. 05
B (at%)	27. 47±0. 12	5. 19±0. 07	4. 71±0. 08	42. 58±0. 07	1. 67±0. 13	13. 95±0. 03	4.43±0. 06

Figure 4.4-16: SEM images of 350℃ fretting wear tracks and EDX spectrums
from CrAlTiCN-1# coatings
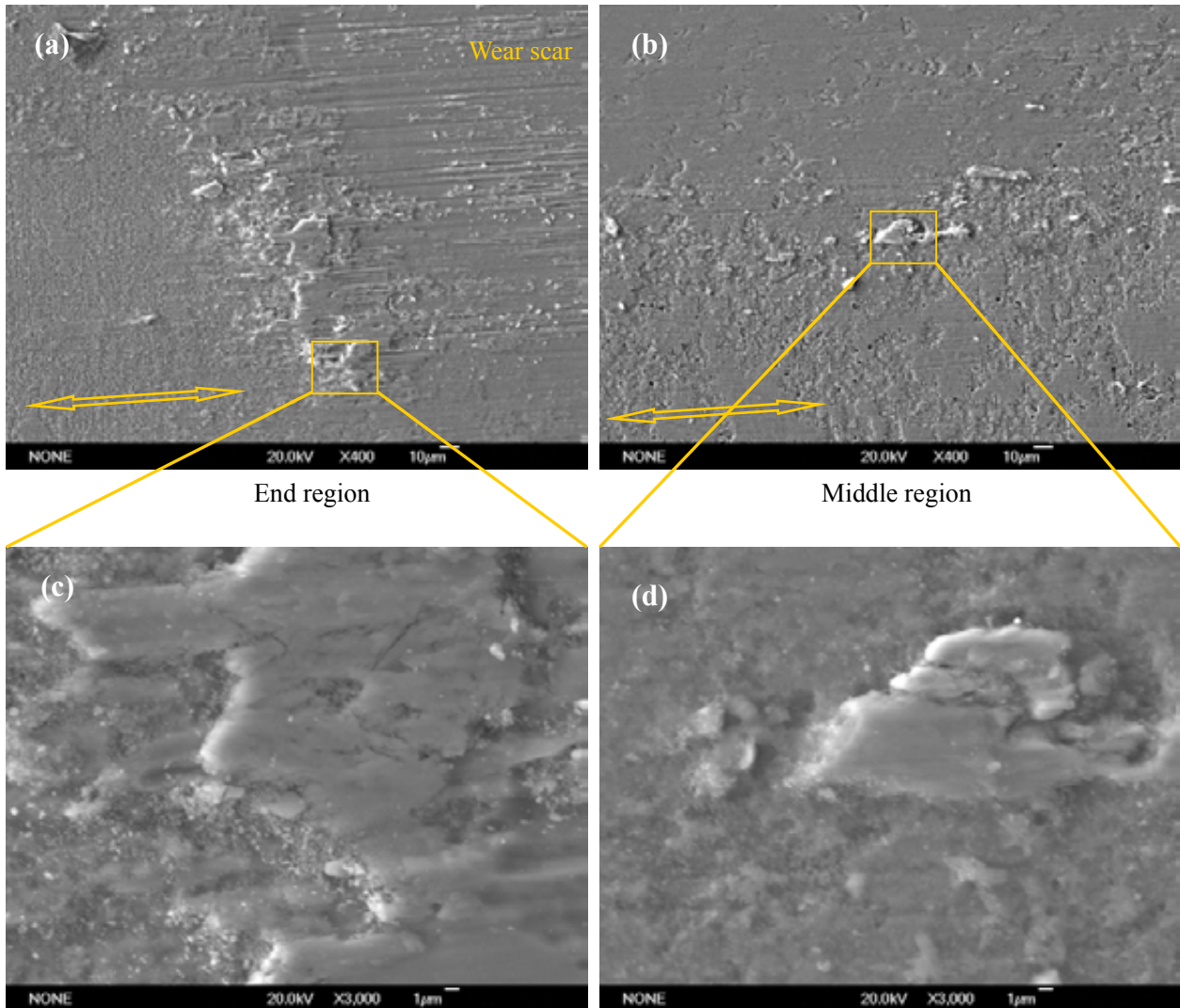
Figure 4.4-17: SEM images of 350℃ fretting wear tracks on CrAlTiCN-4# sample
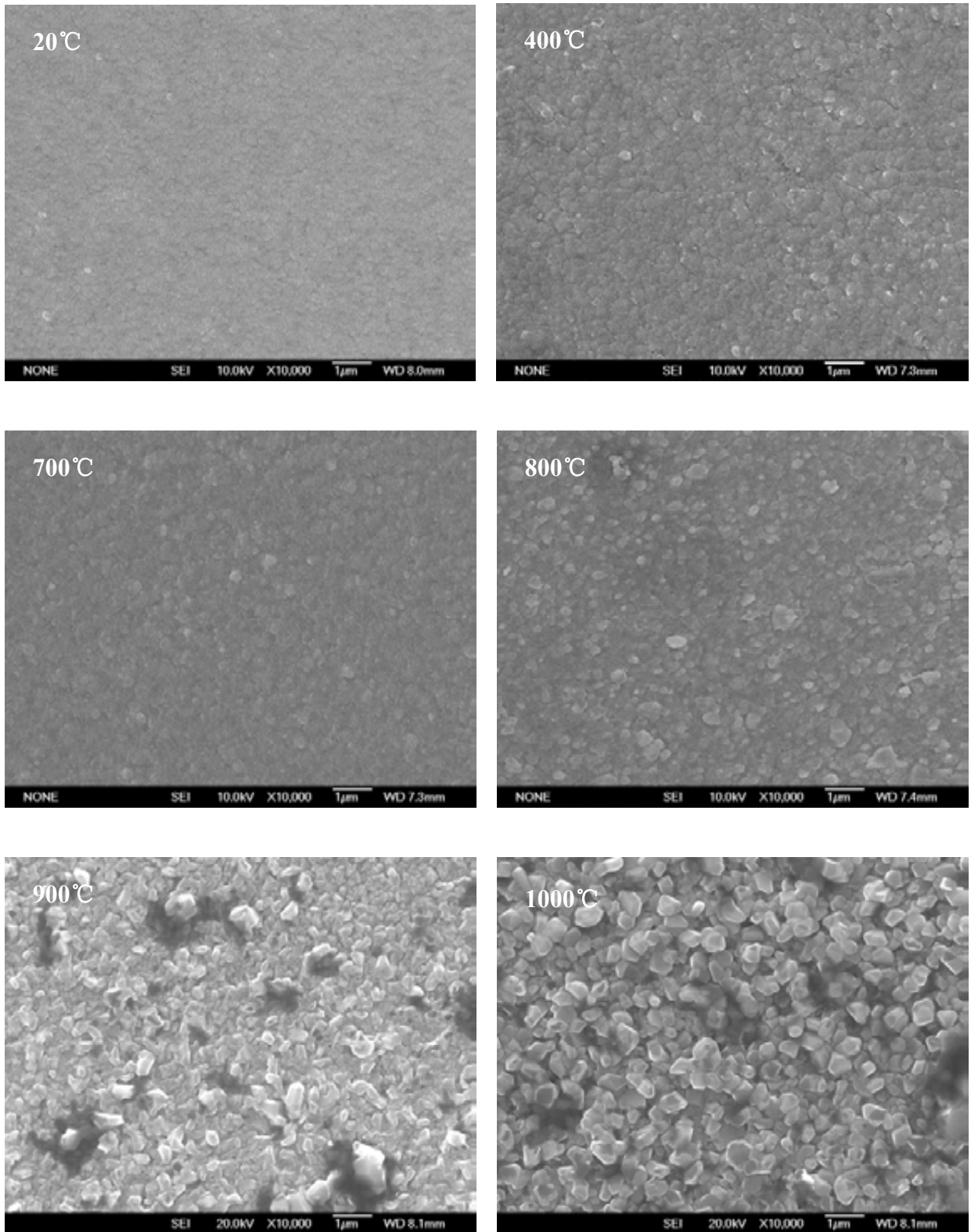
(a) CrAlTiN-0#
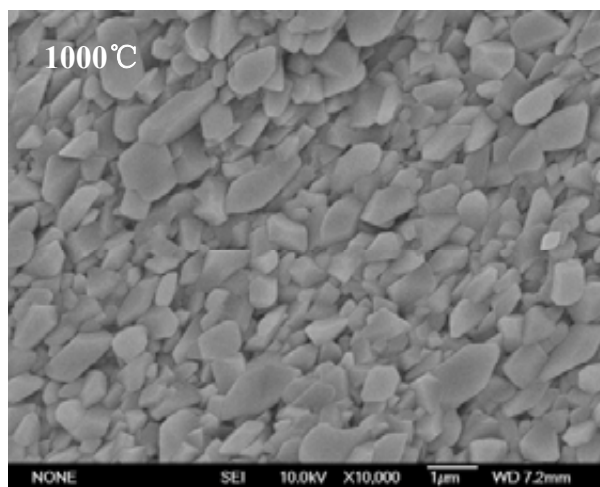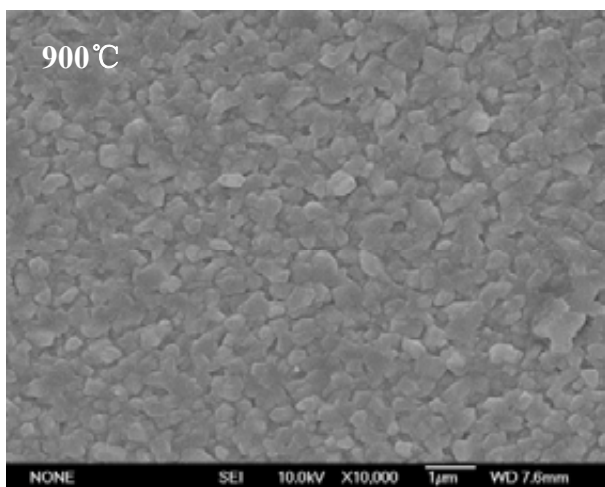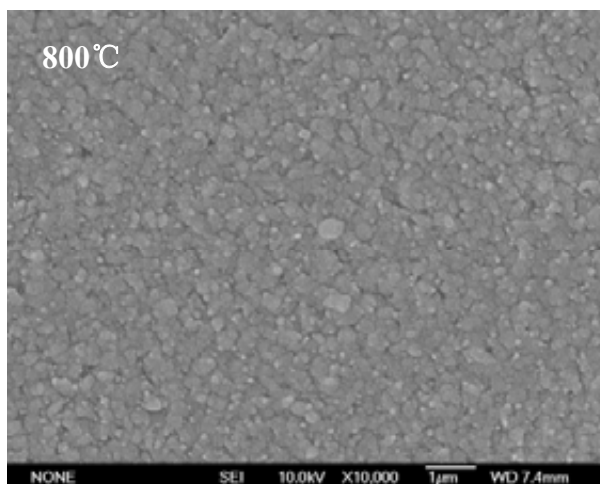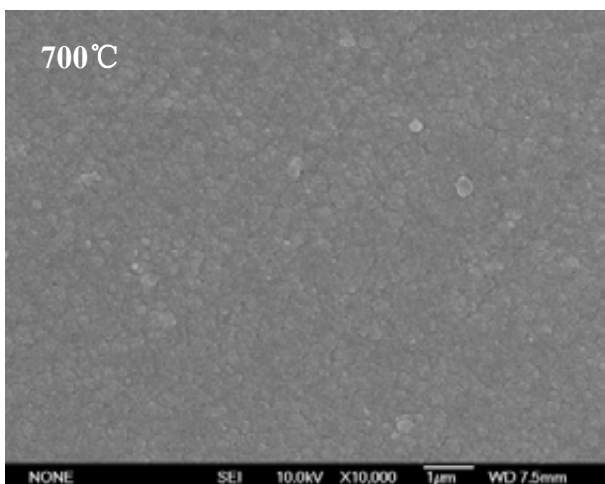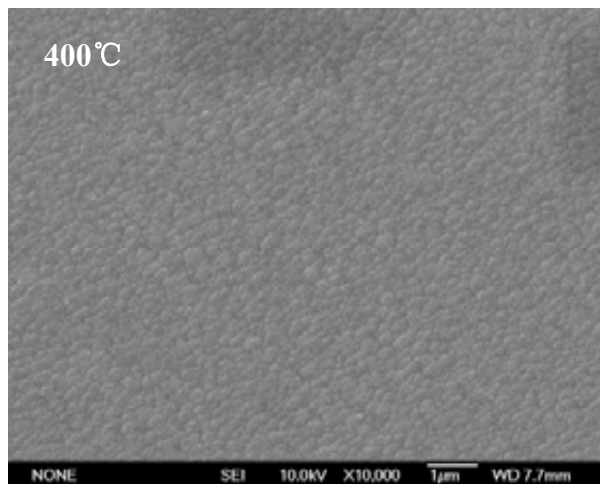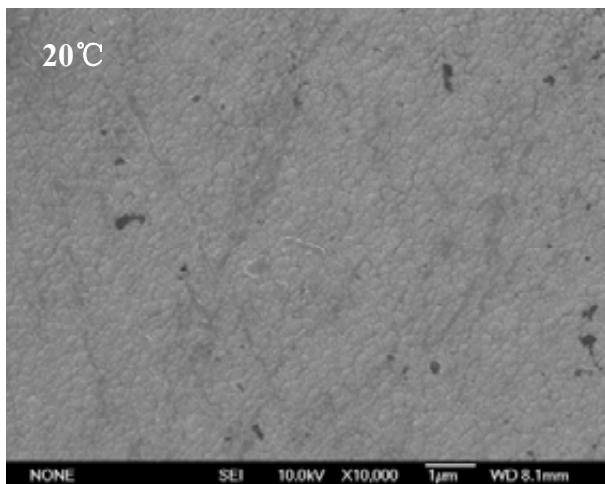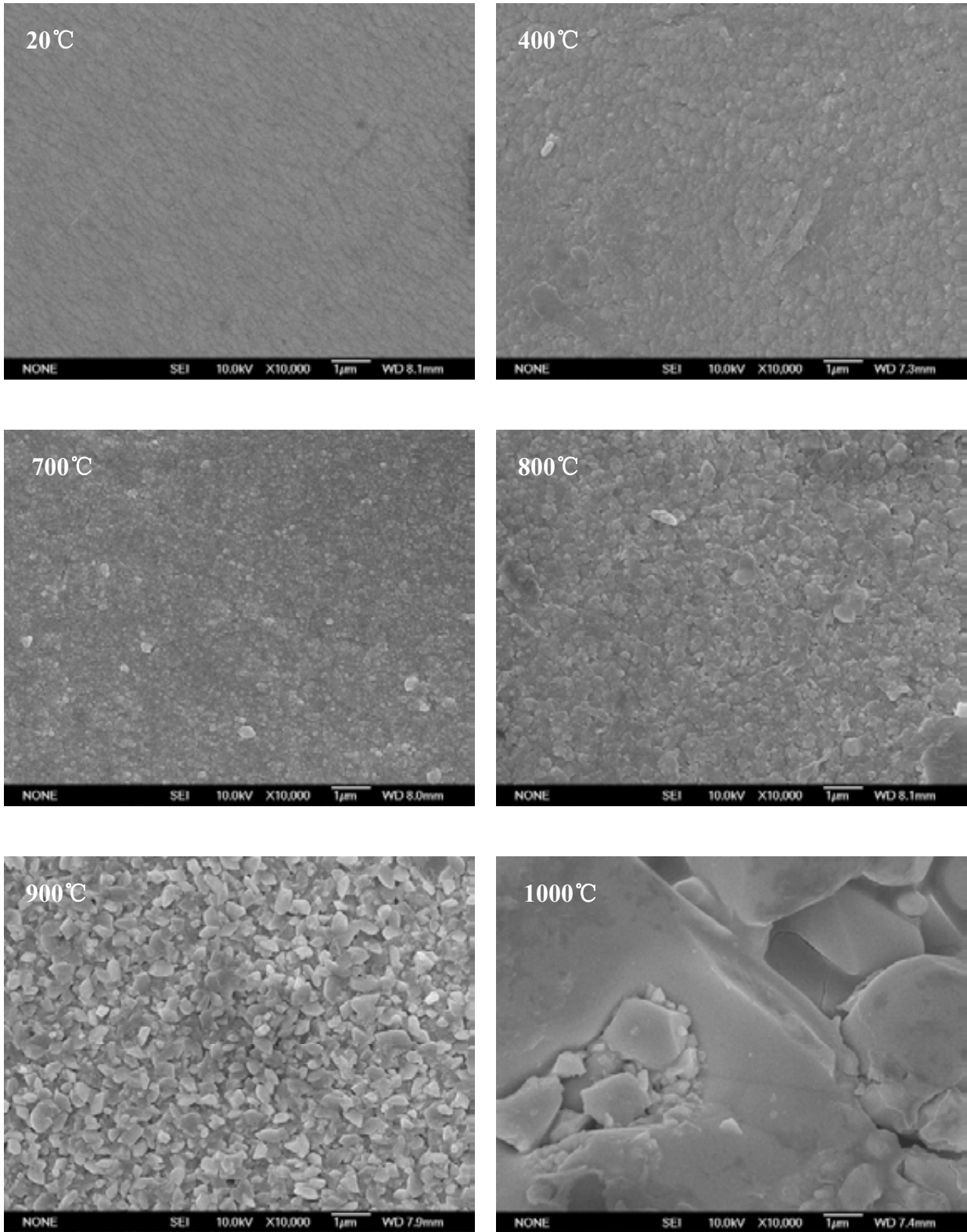
(b) CrAlTiCN-4#

(c) CrAlTiCN-5#

Figure 4.5-1: SEM micrographs of oxidised:
(a) CrAlTiN-0#, (b) CrAlTiCN-4# and (c) CrAlTiCN-5# samples
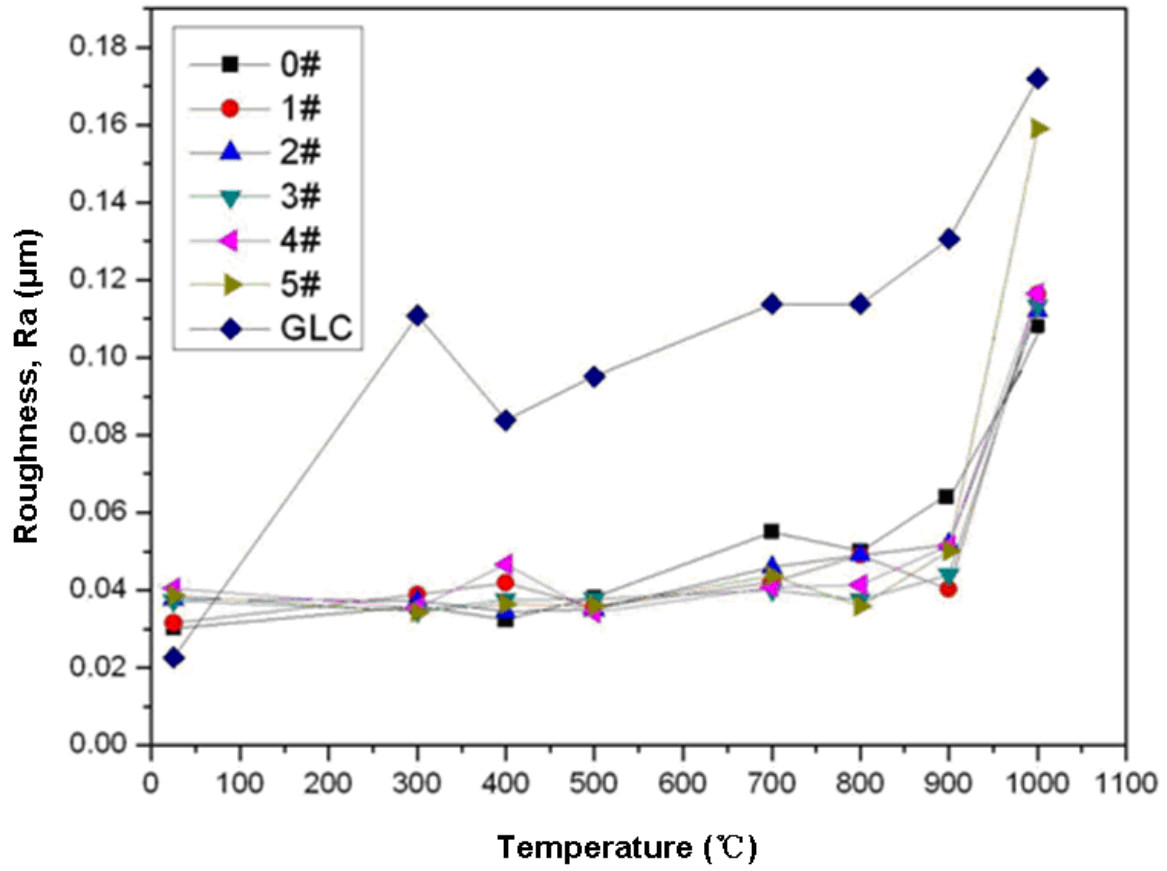
Figure 4.5-2: Surface roughness of oxidised coatings

| HSS | Coating | Ni |

COMPO 20.0kV X6,000 1μm

COMPO 20.0kV X15,000 1μm

(a) 400℃

Oxide layer

| HSS | Coating | Oxide layer | Ni |

COMPO 20.0kV X6,000 1μm

COMPO 20.0kV X15,000 1μm

(b) 900℃

235
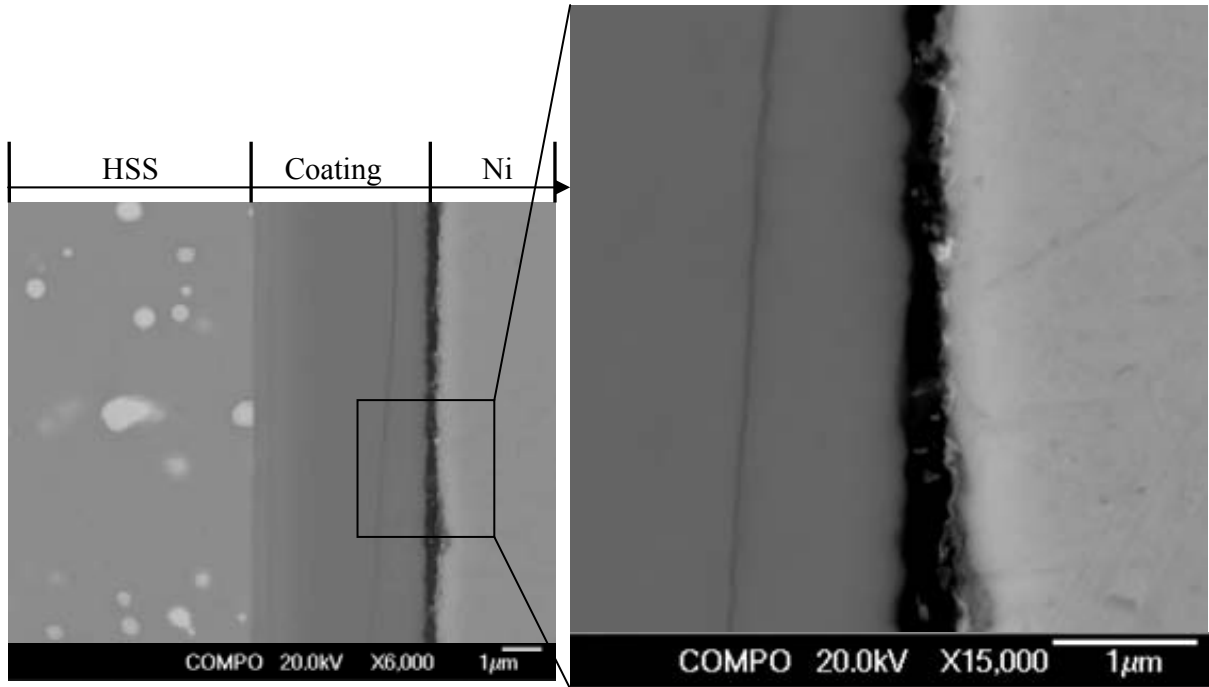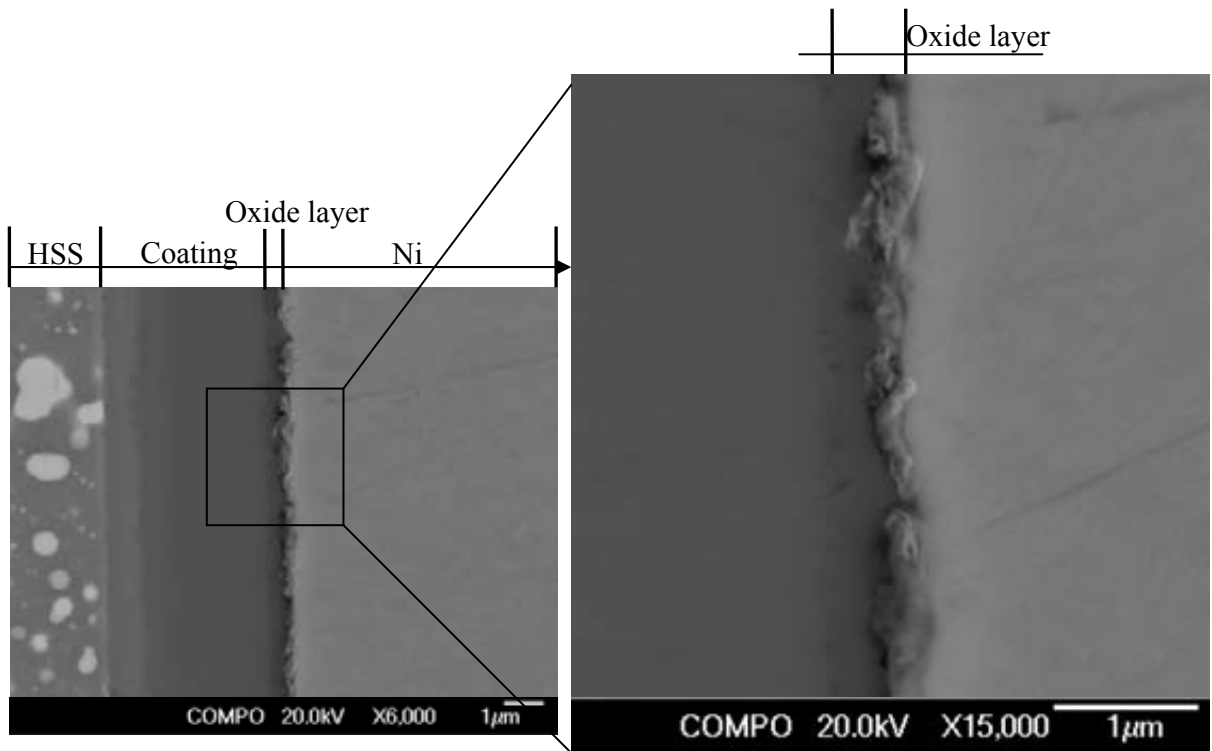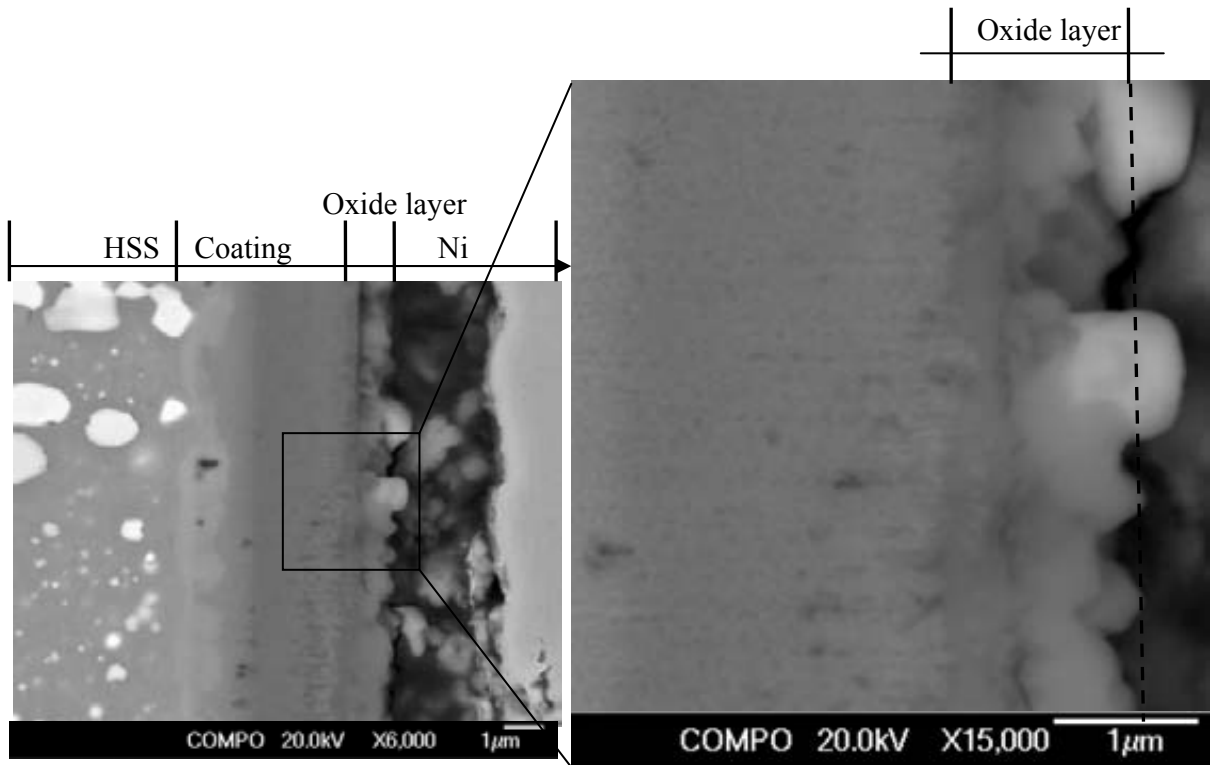
(c) 1000℃

Figure 4.5-3 Cross-sectional SEM BSE micrographs of CrAlTiN-0# sample after oxidation at 400℃, 900℃, and 1000℃
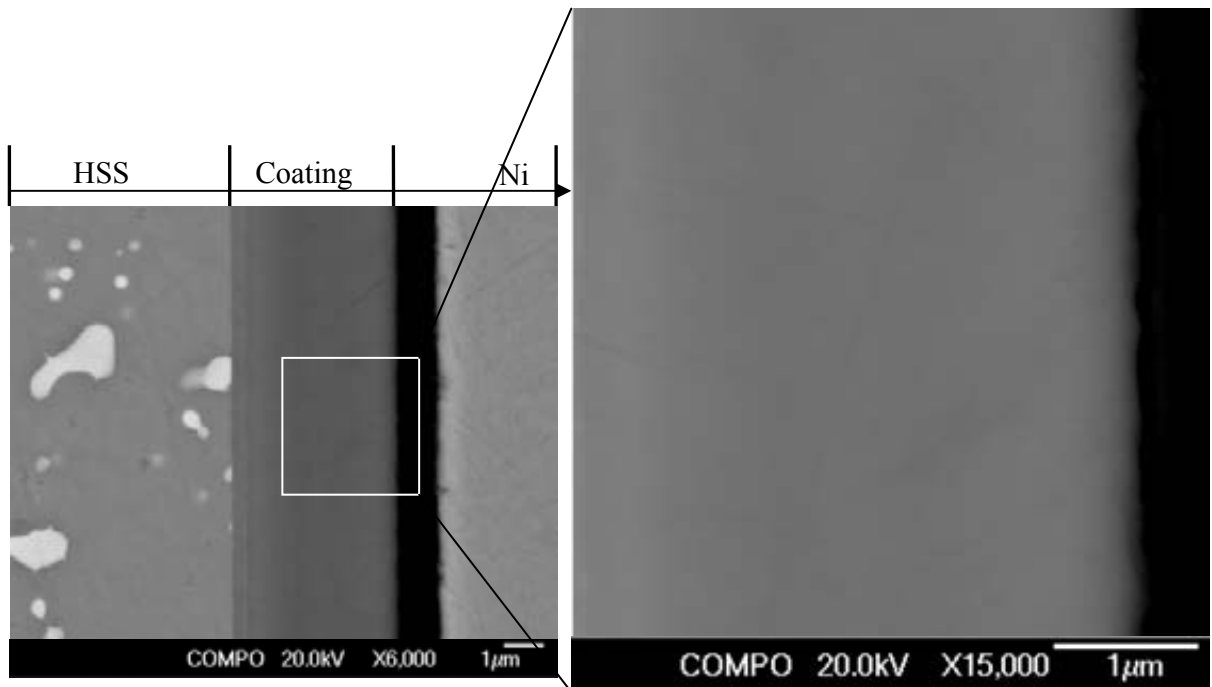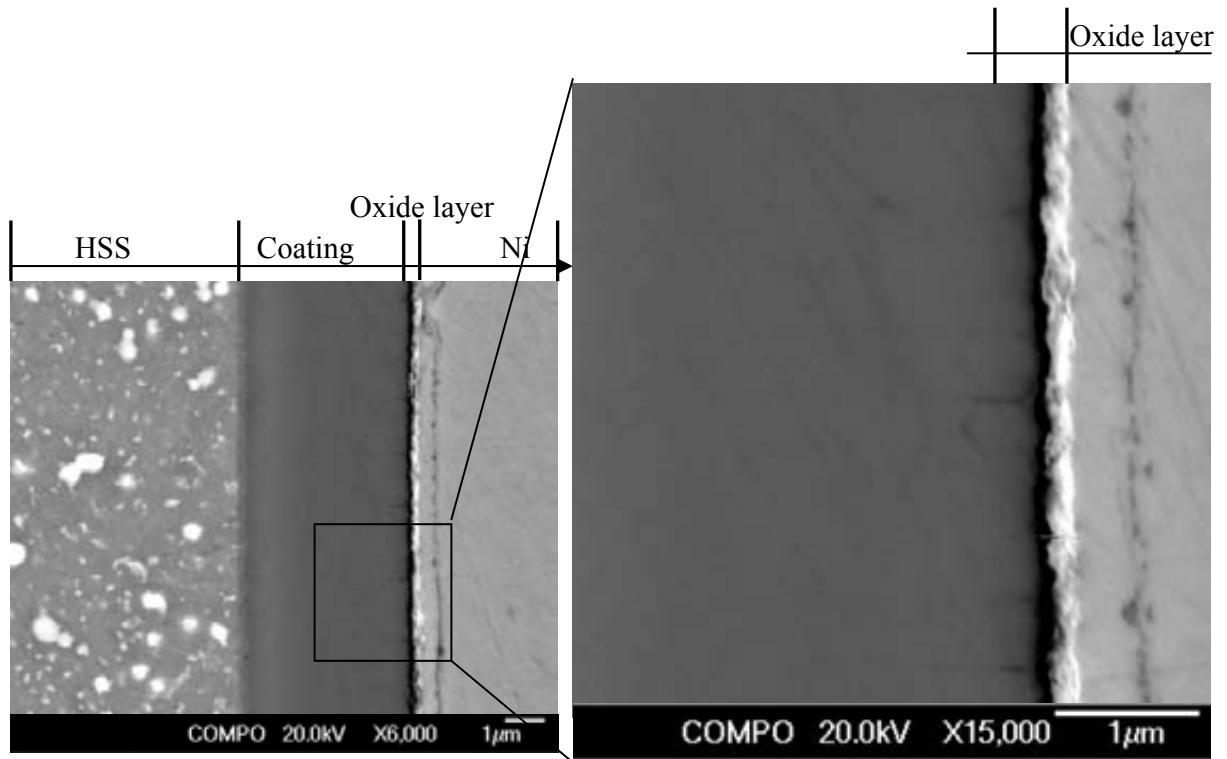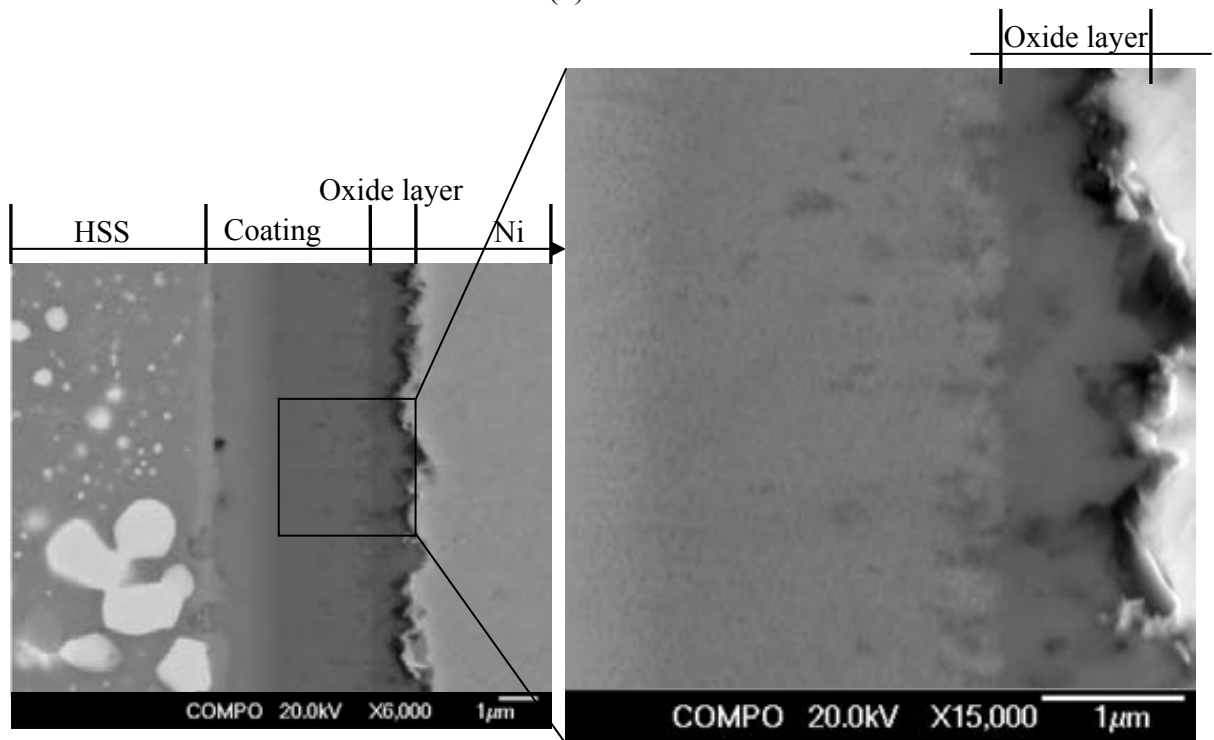
(a) 400℃

(b) 900℃

(c) 1000℃

Figure 4.5-4: Cross-sectional SEM BSE micrographs of CrAlTiCN-1# sample after oxidation at 400℃, 900℃, and 1000℃
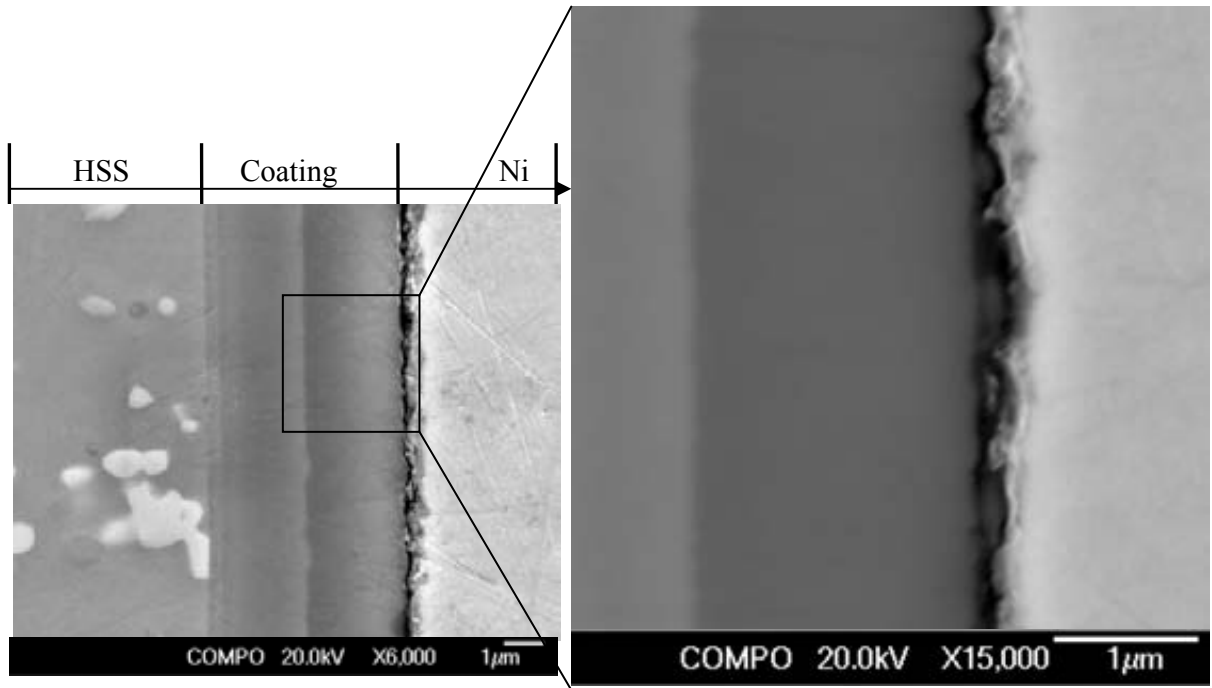
(a) 400℃
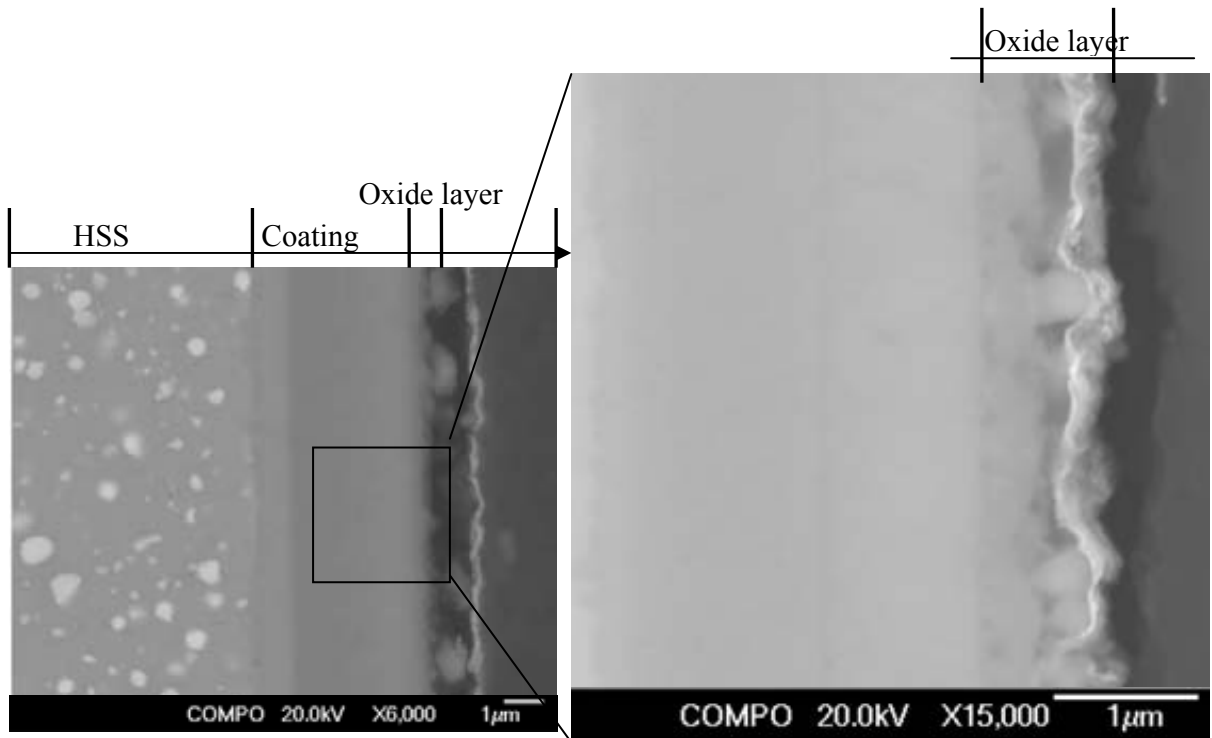
(b) 900℃
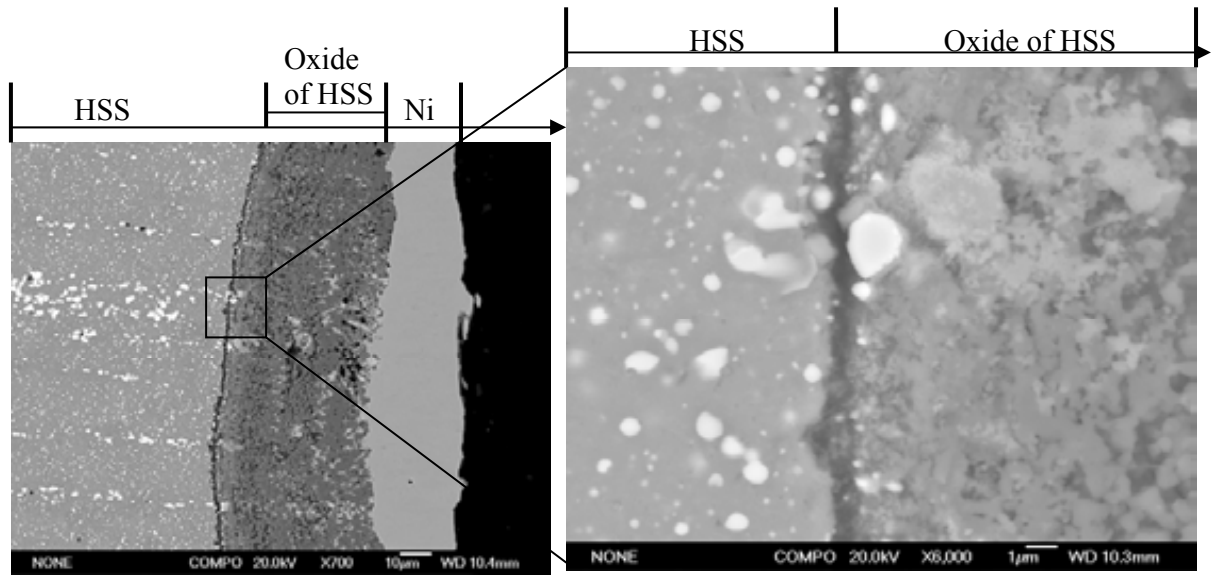
(c) 1000℃

Figure 4.5-5: Cross-sectional SEM BSE micrographs of CrAlTiCN-5# sample after oxidation at 400℃, 900℃, and 1000℃
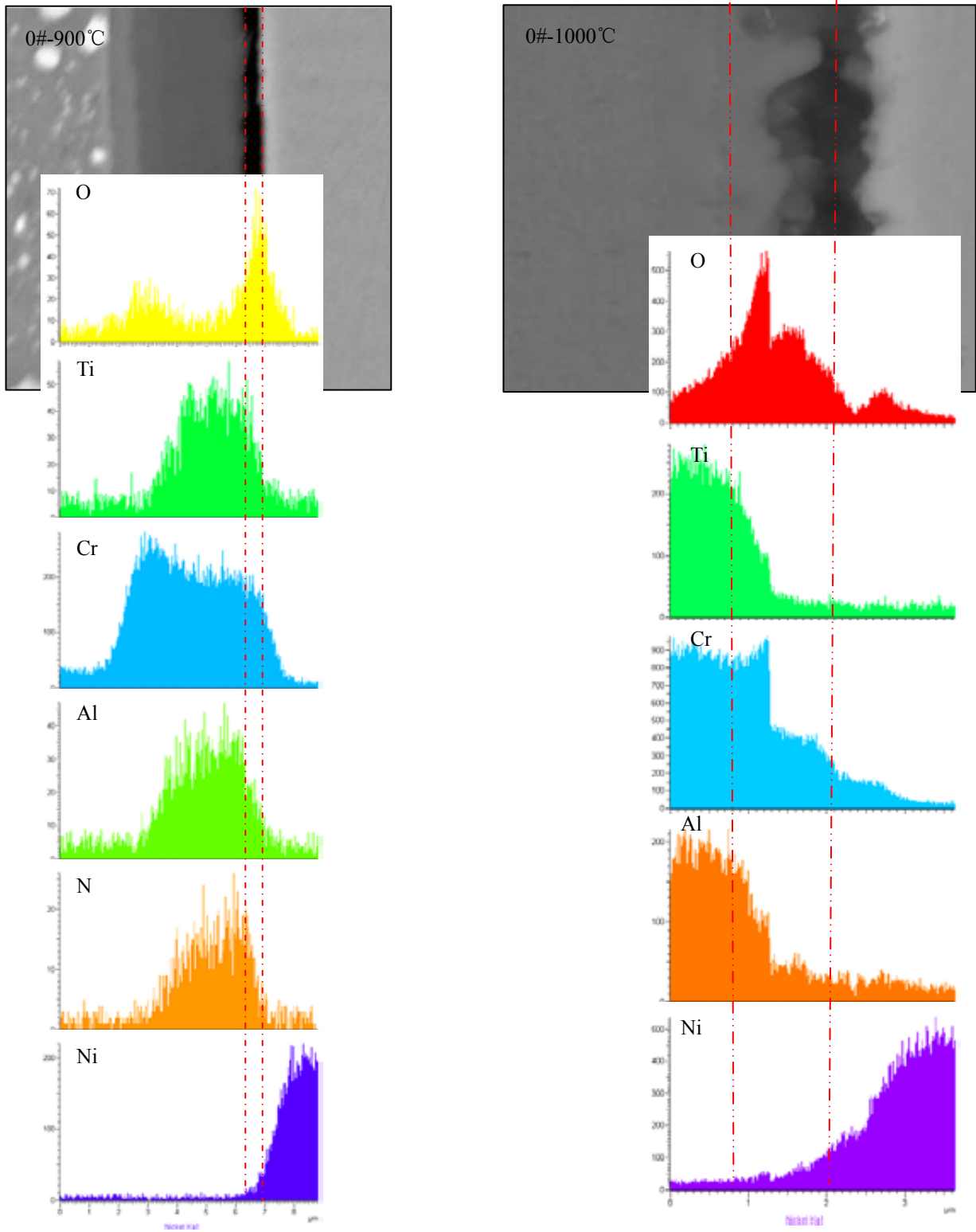
Figure 4.5-6: EDX line scanning of oxidised CrAlTiN-0# sample
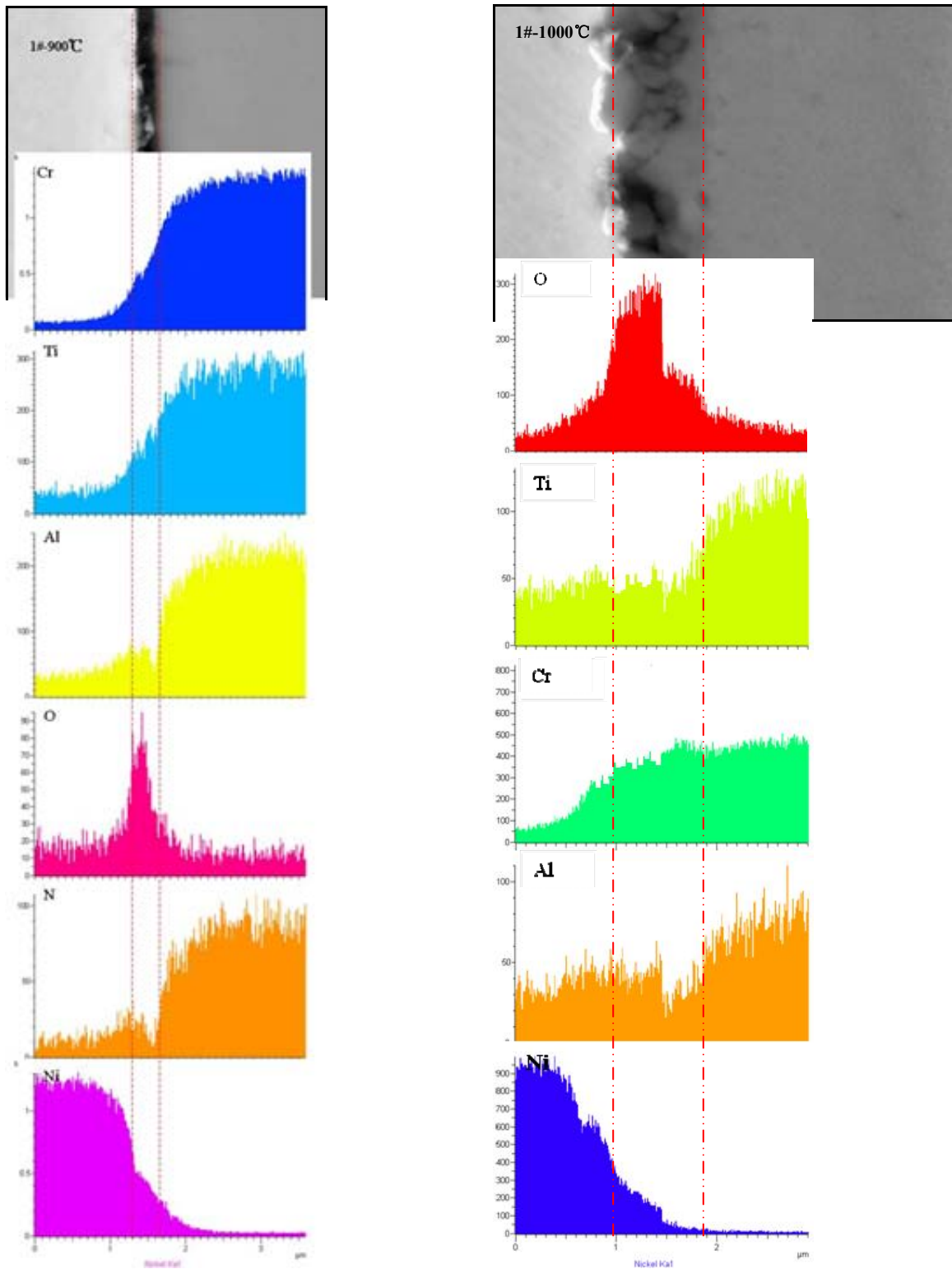
Figure 4.5-7: EDX line scanning of oxidised CrAlTiCN-1# sample
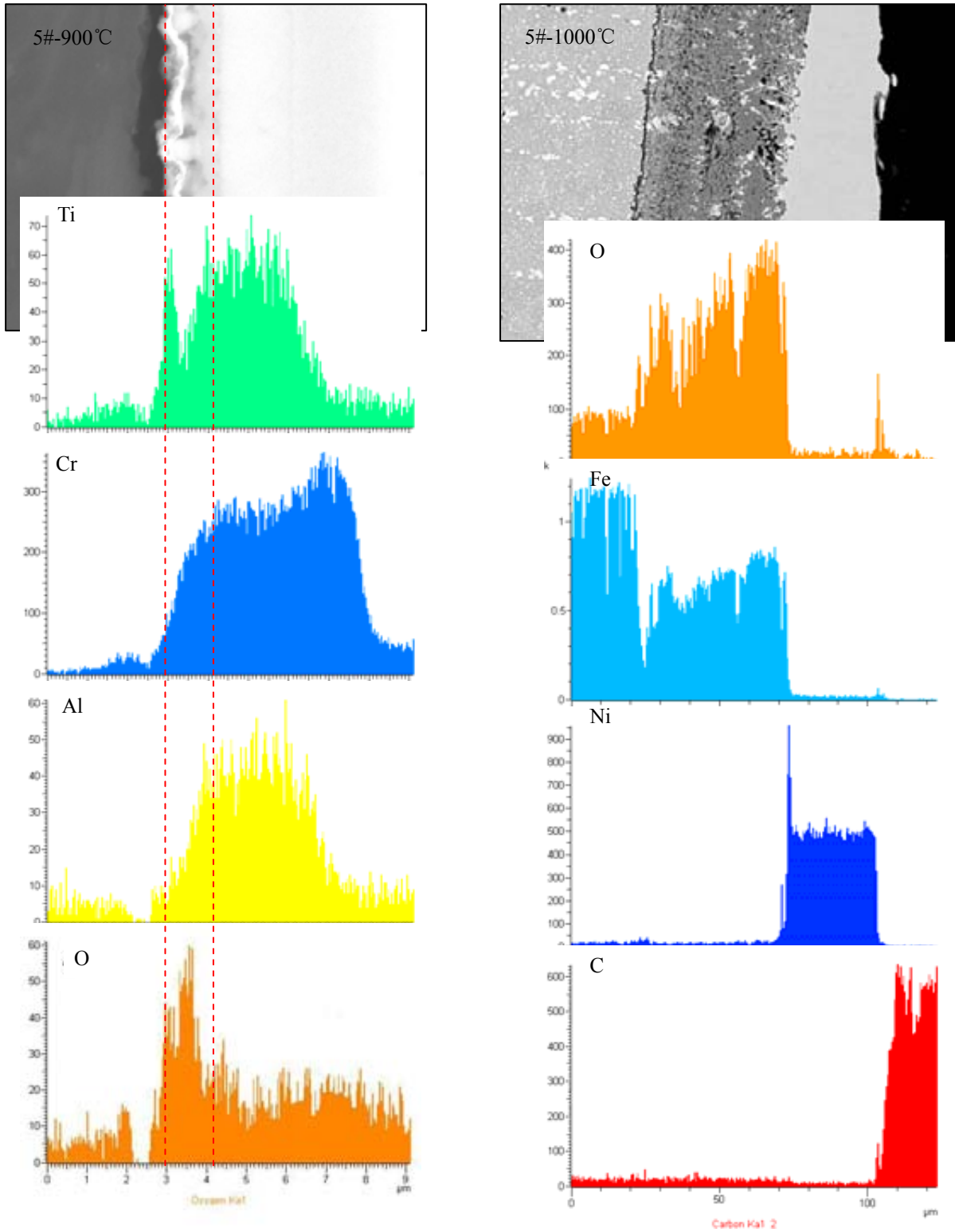
Figure 4.5-8: EDX line scanning of oxidised CrAlTiCN-5# sample
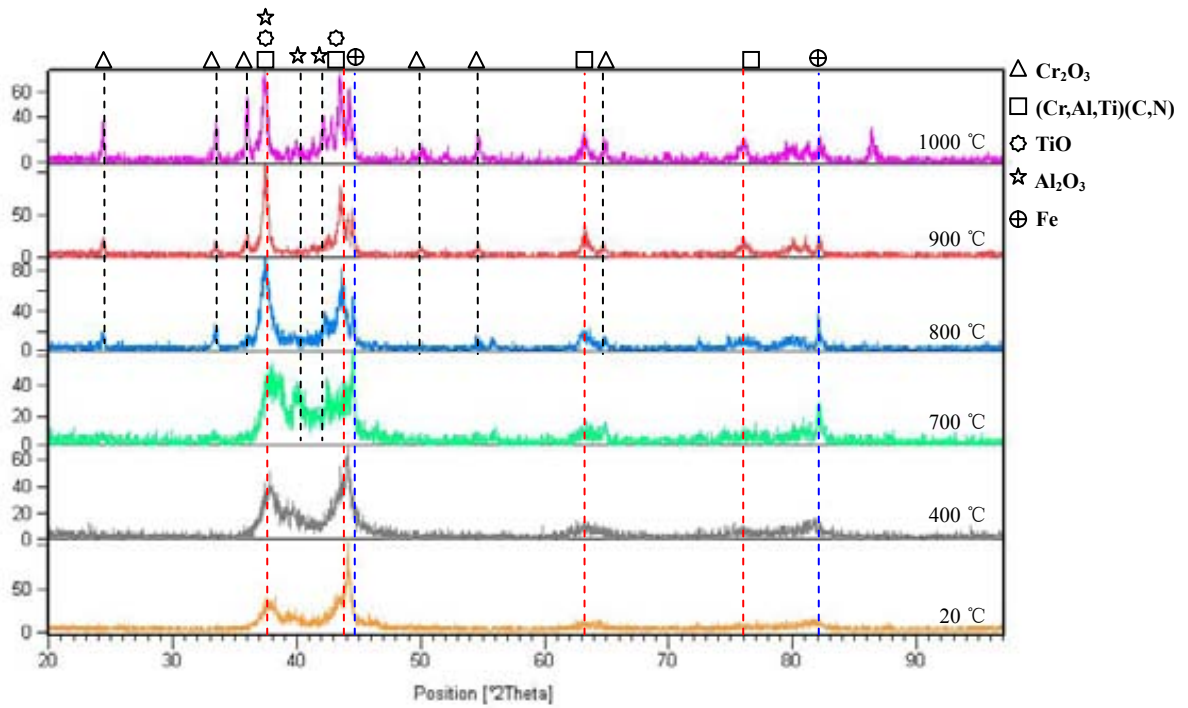
(a) CrAlTiN-0#
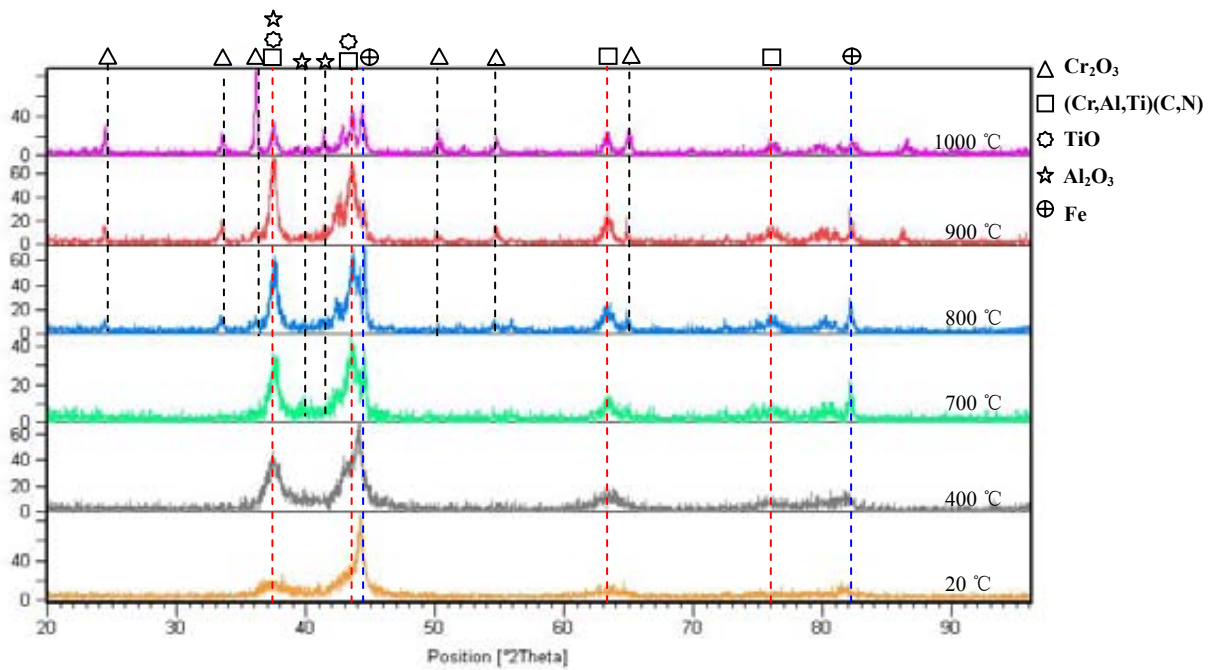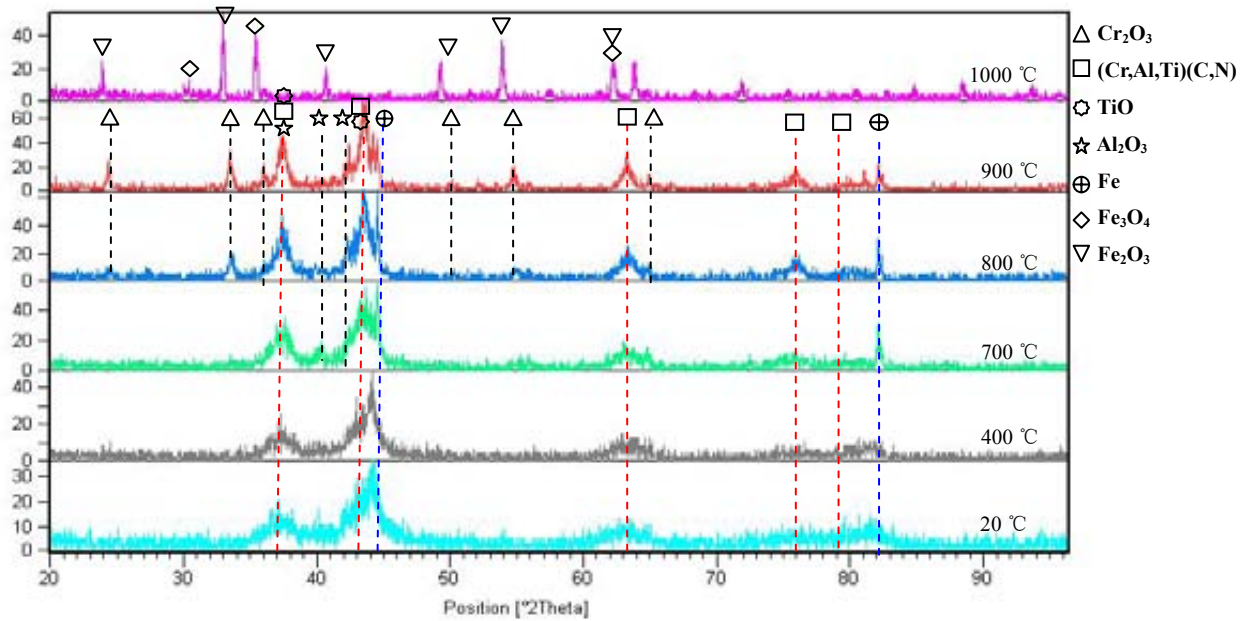
(b) CrAlTiCN-3#

(c) CrAlTiCN-5#

Figure 4.5-9: XRD patterns obtained on oxidised
(a) CrAlTiN-0#, (b) CrAlTiCN-3# and (c) CrAlTiCN-5# samples

HSS Substrate

Sublayer Ⅰ

Sublayer Ⅱ

Sublayer Ⅲ

Oxide layer

0.2μm
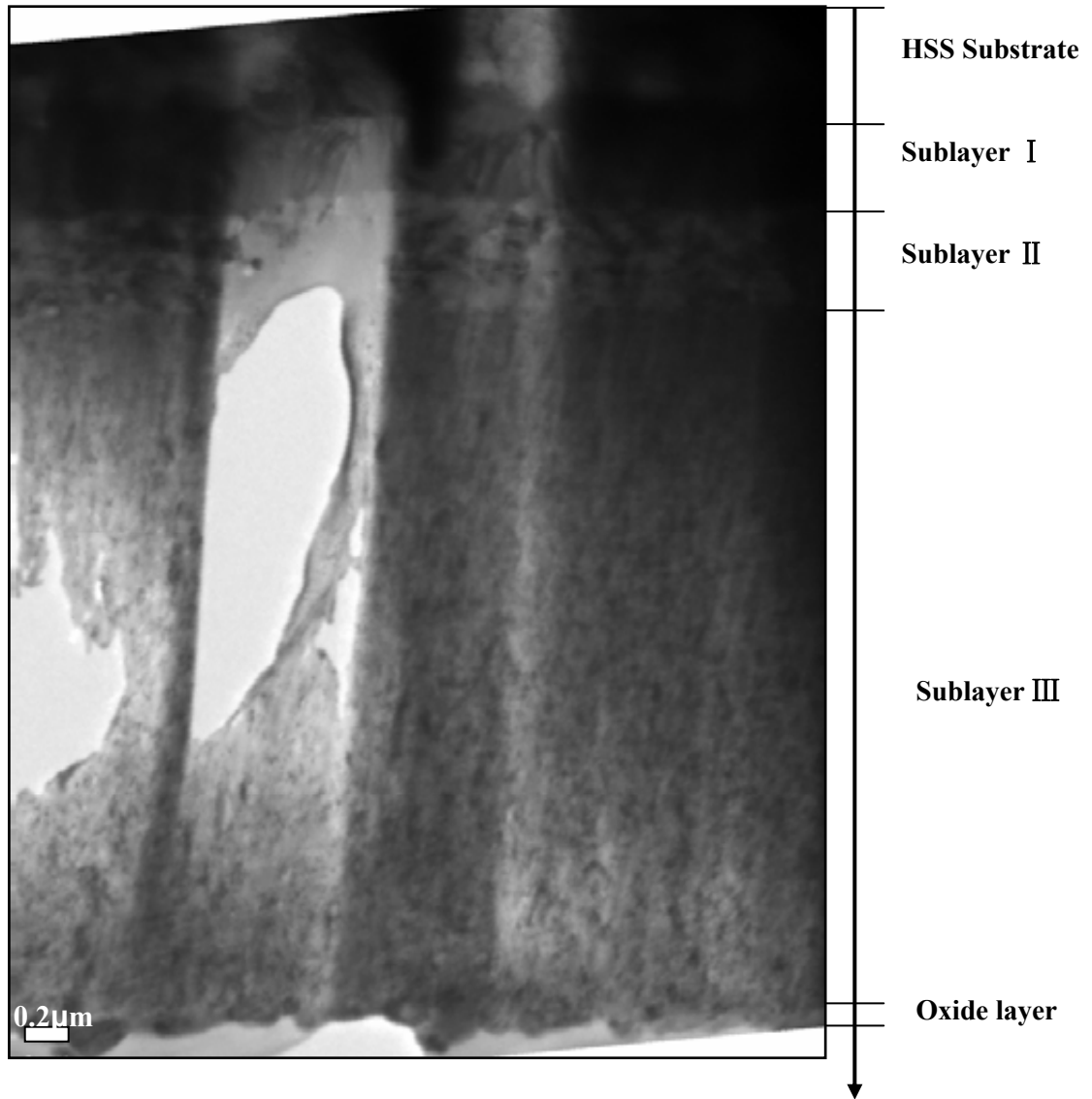
Figure 4.5-10: Cross-sectional TEM micrograph of oxidised CrAlTiN-0# sample
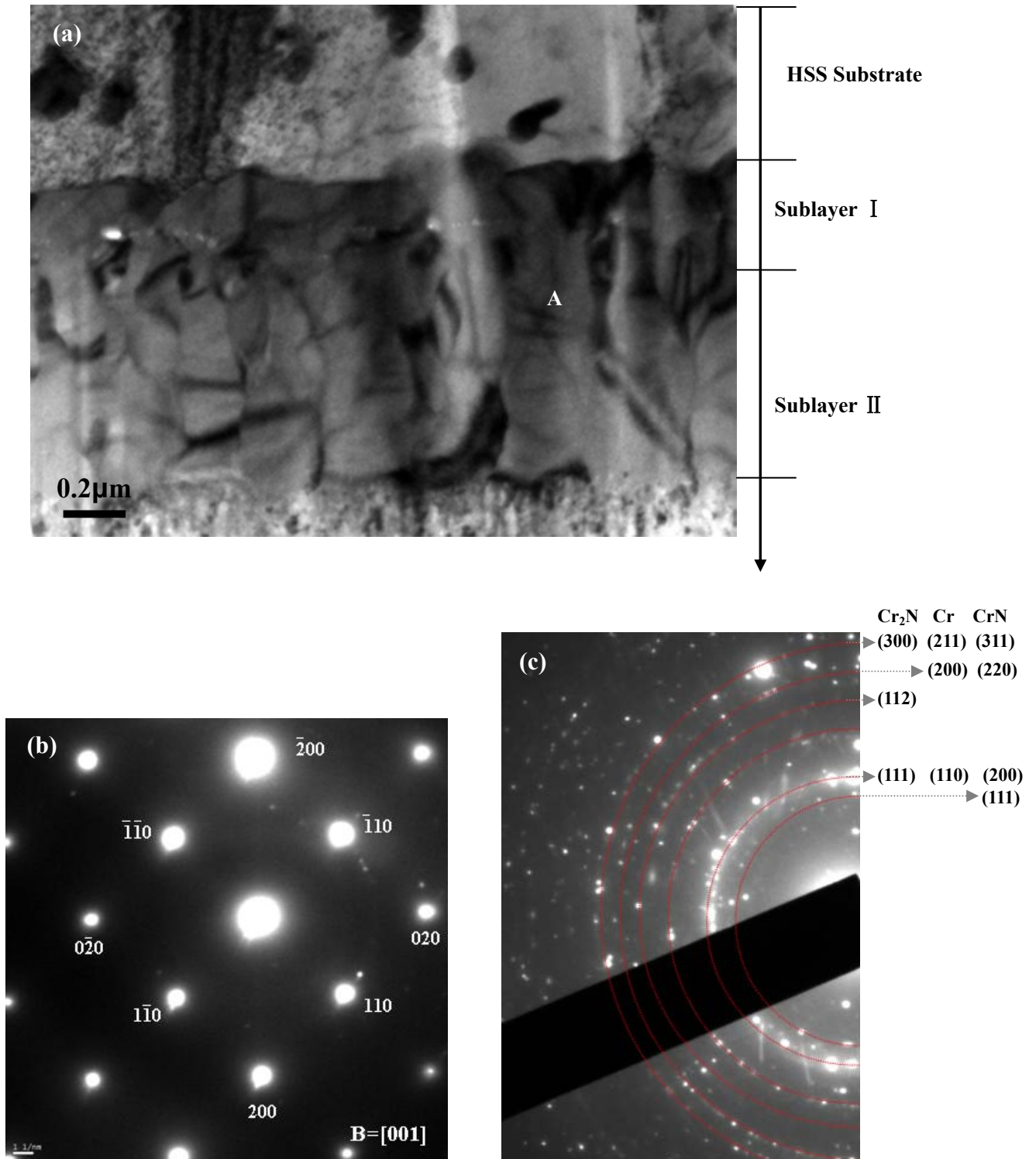
Figure 4.5-11: TEM micrograph (a) and diffraction patterns on substrate (b) and sublayers Ⅰ and Ⅱ (c) from 800 ℃/2 hrs oxidised CrAlTiN-0# sample
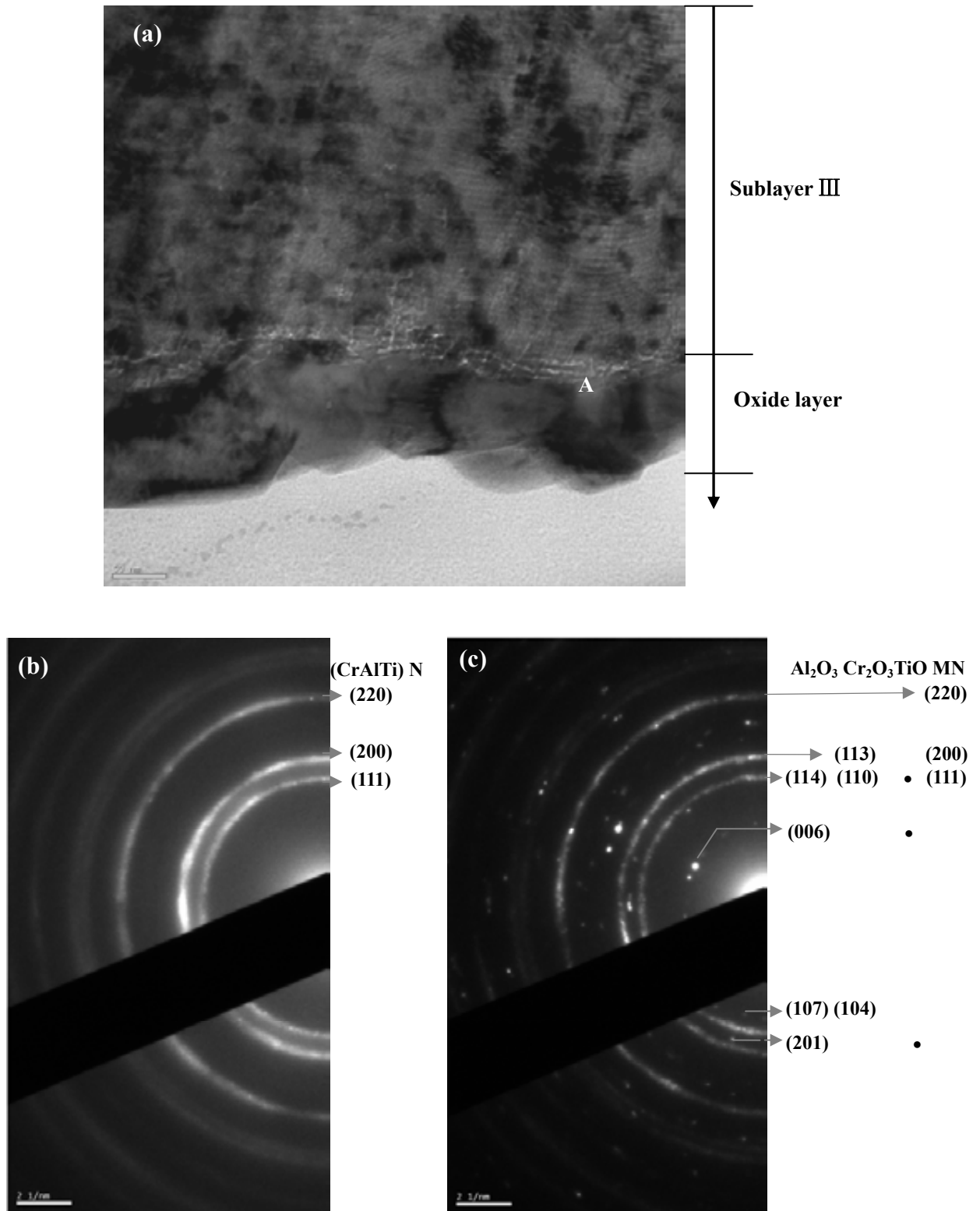
Figure 4.5-12: TEM micrograph (a) and diffraction patterns on
Sublayer Ⅲ (b) and Sublayer Ⅲ with oxide layer (c) from 800 ℃/2 hrs oxidised CrAlTiN-0# sample

HSS Substrate

Sublayer Ⅰ

Sublayer Ⅱ

Sublayer Ⅲ

Sublayer Ⅳ

Oxide layer

W layer

0.2μm
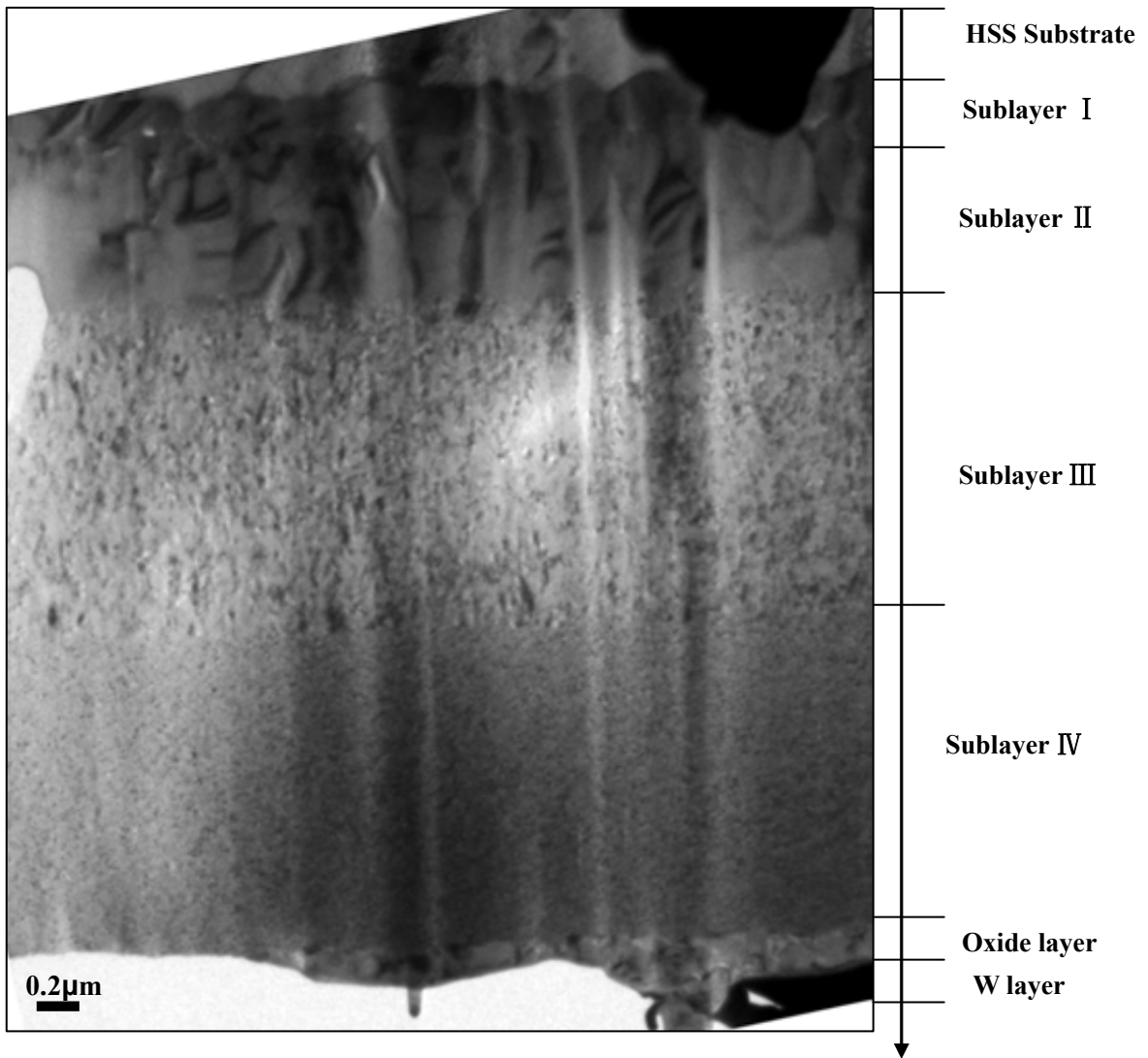
Figure 4.5-13: Cross-sectional TEM micrograph of oxidised CrAlTiCN-3# sample
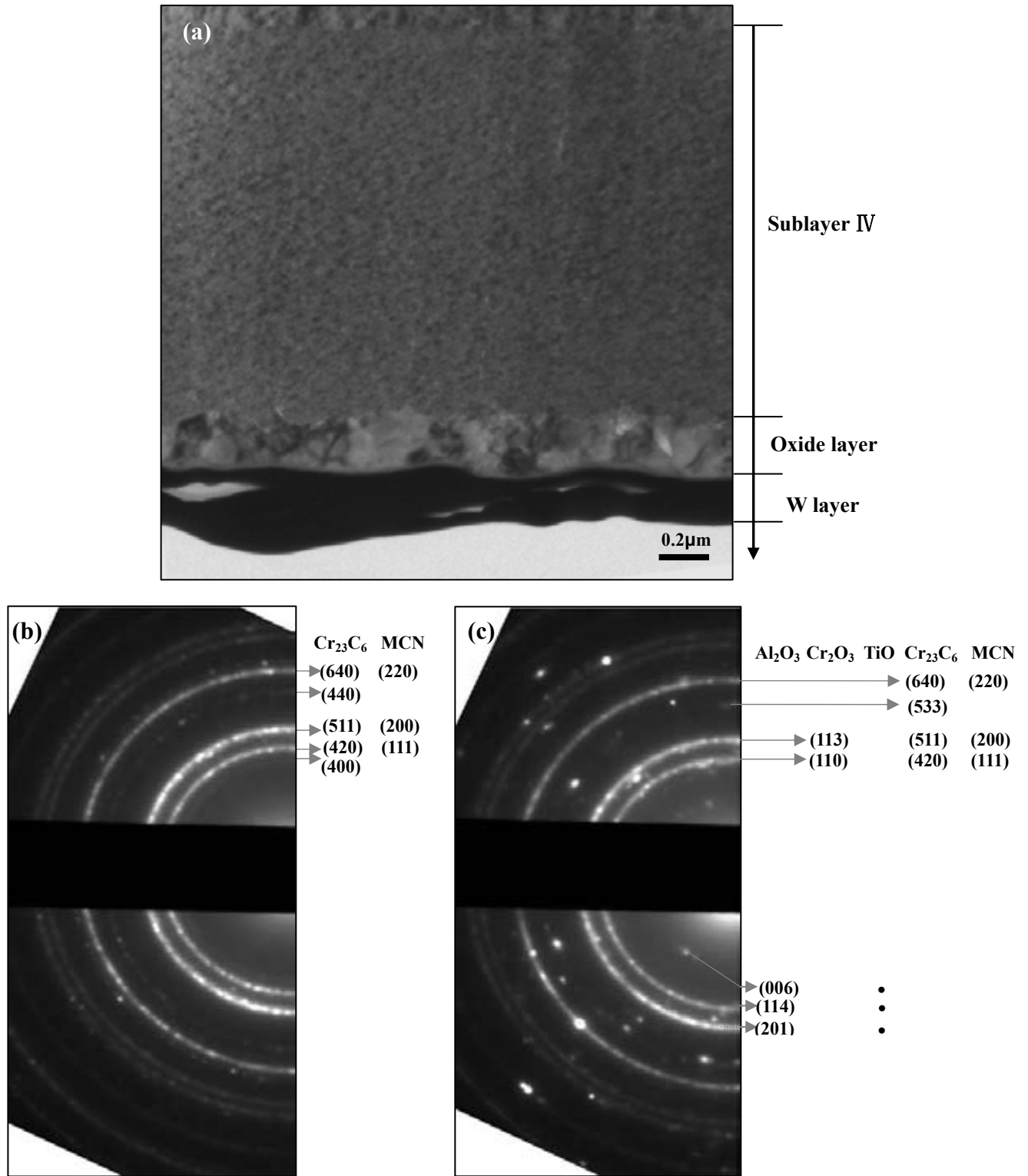
Figure 4.5-14: TEM micrograph (a) and diffraction patterns on Sublayer Ⅳ (b) and Sublayer Ⅳ with oxide layer (c) from 800 ℃/2 hrs oxidised CrAlTiCN-3# sample
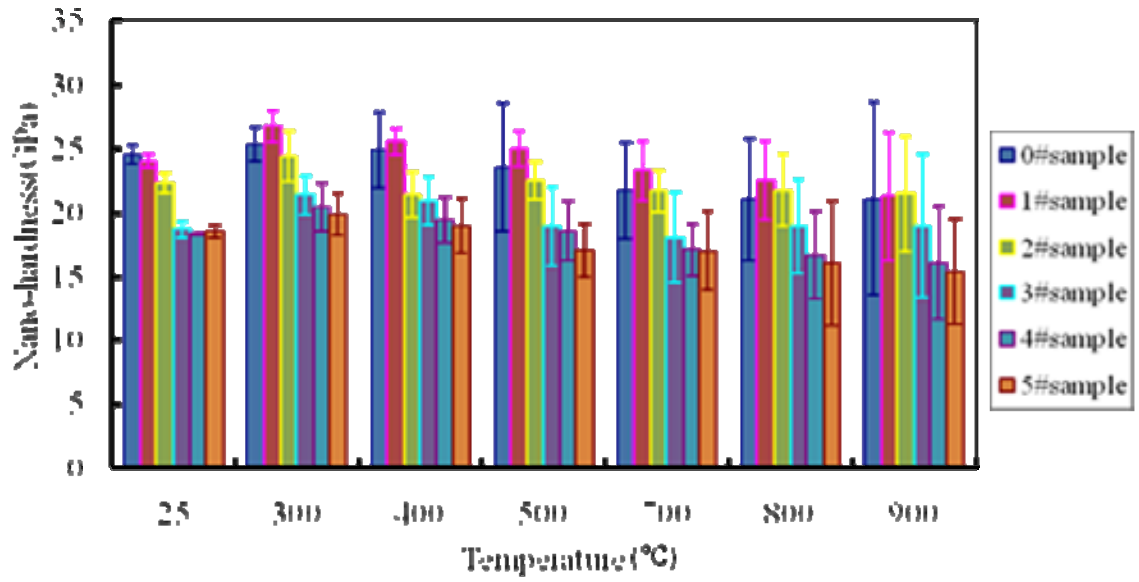
(a)
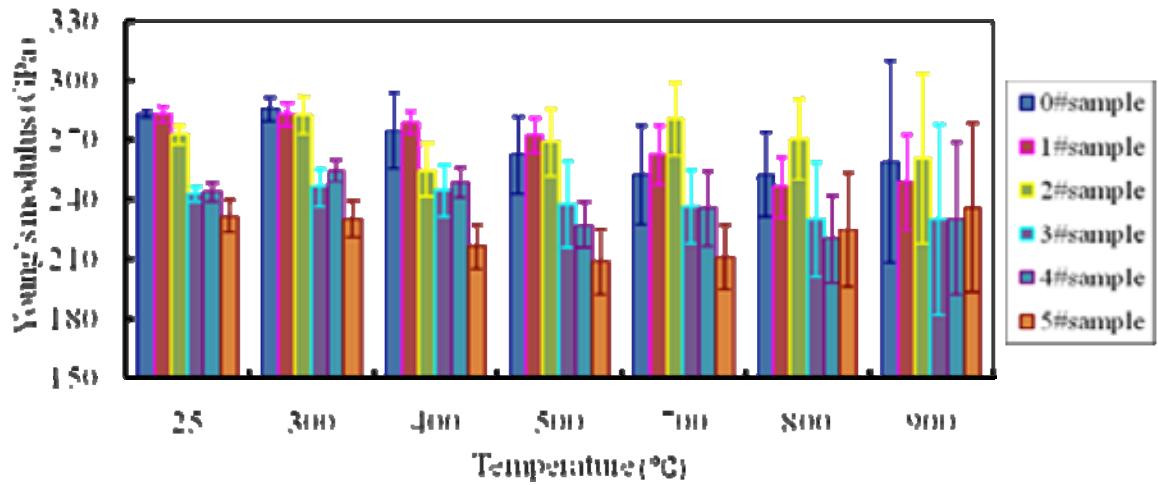
(b)

Figure 4.5-15: Nano-hardness (a) and Young's modulus (b) of oxidised coatings
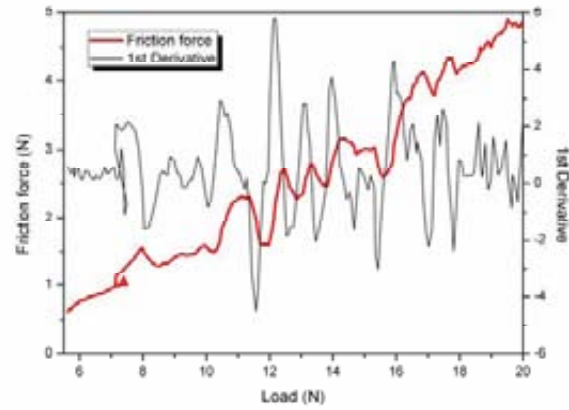
(a) CrAlTiN-0#
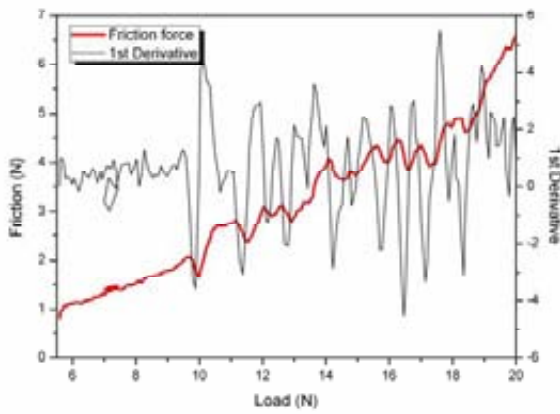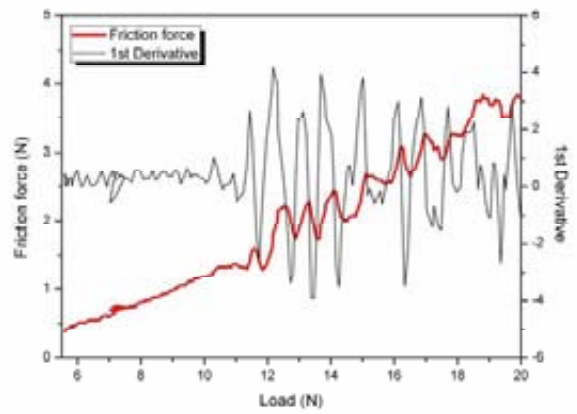
(b) CrAlTiCN-3#

(c) CrAlTiCN-5#

Figure 4.5-16: Friction force and its first derivation against scratch load
from oxidised (a) CrAlTiN-0#, (b) CrAlTiCN-3# and (c) CrAlTiCN-5# samples
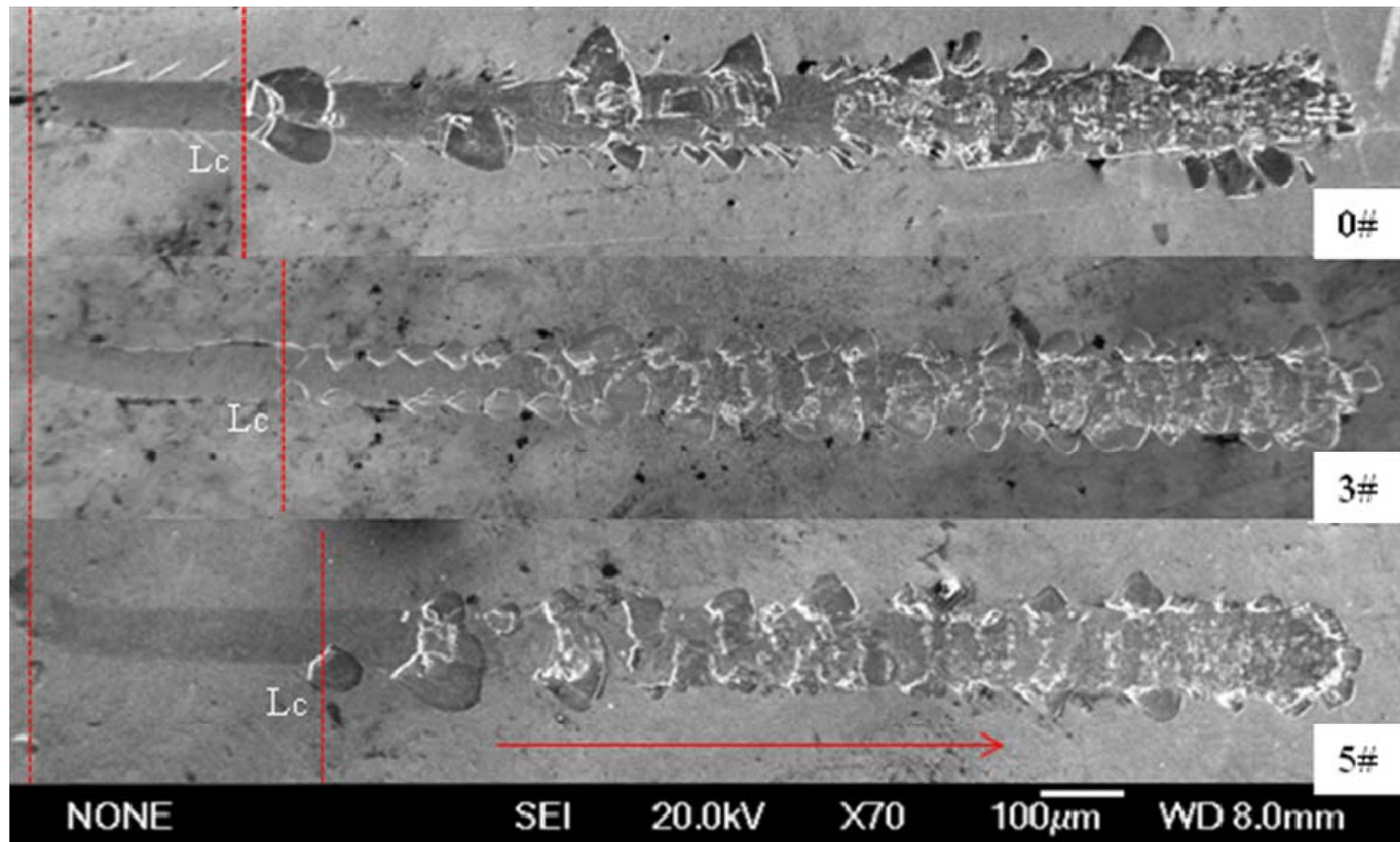
Figure 4.5-17: Overview scratch tracks of 0#, 3#, and 5# samples after oxidation at 700℃
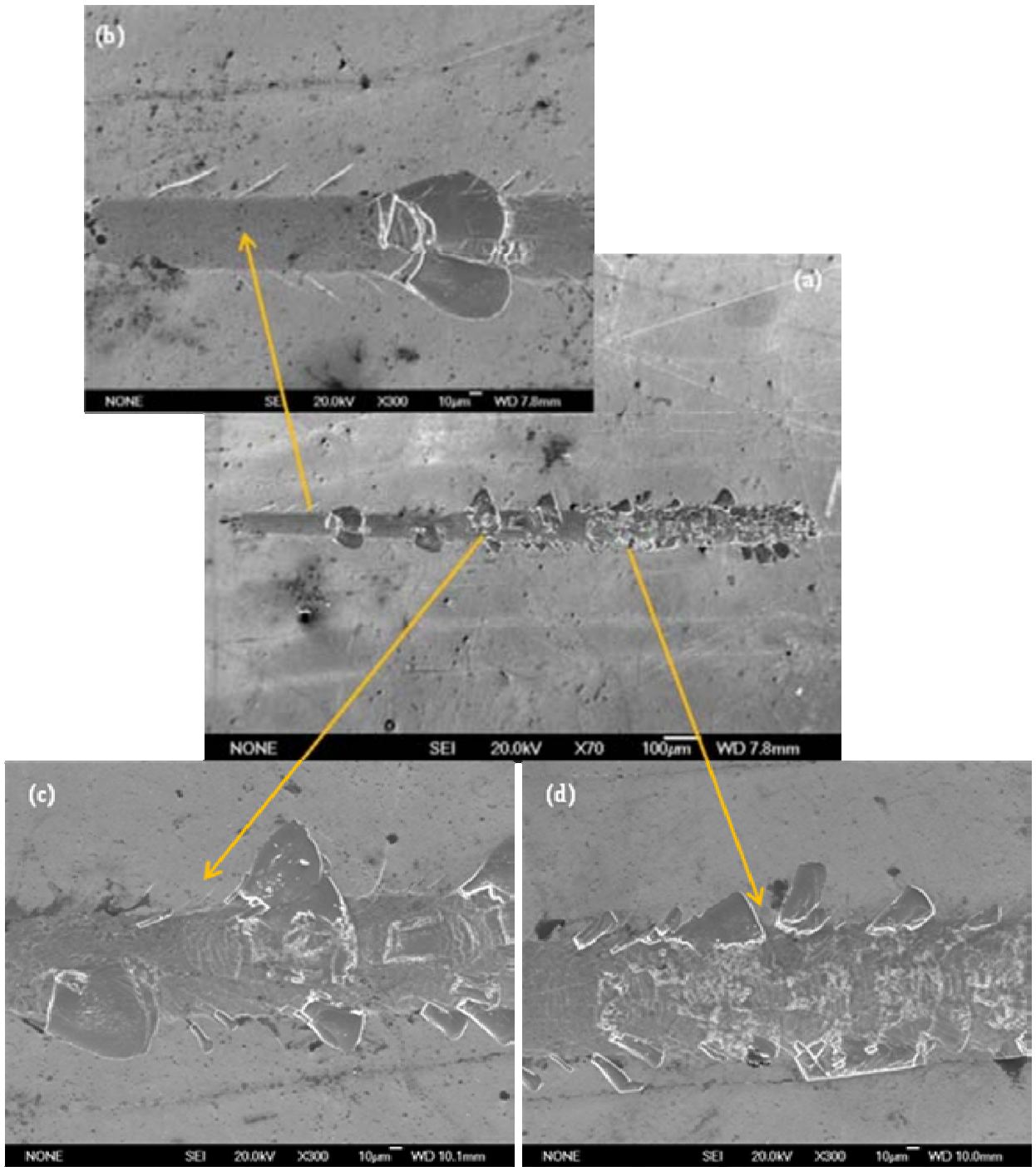
Figure 4.5-18: SEM images of the scratched track from 700℃/ 2 hrs oxidised CrAlTiN-0# sample
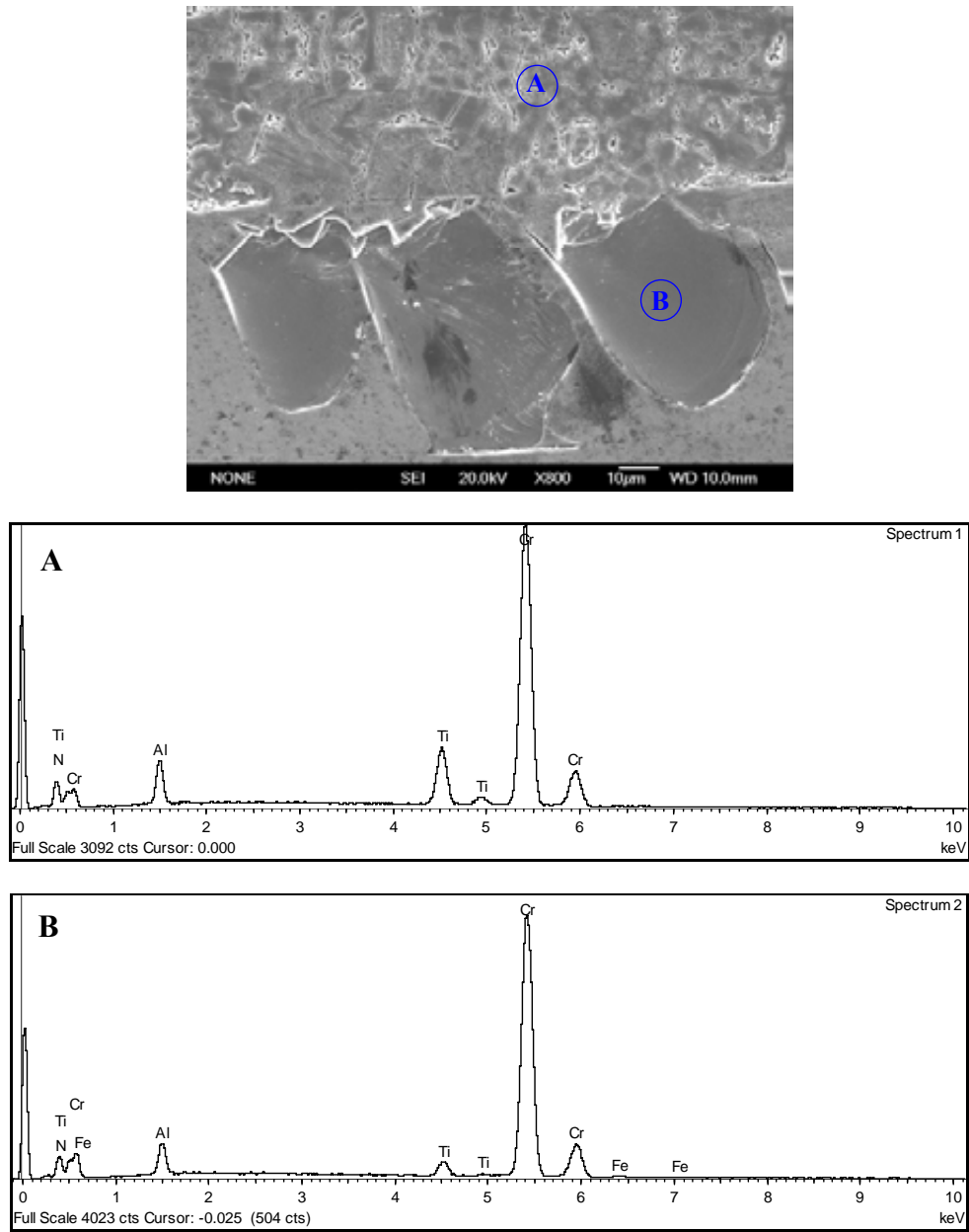
Figure 4.5-19: SEM images of the side region of the scratched track and EDX spectrums from 700℃/ 2 hrs oxidised CrAlTiN-0# sample
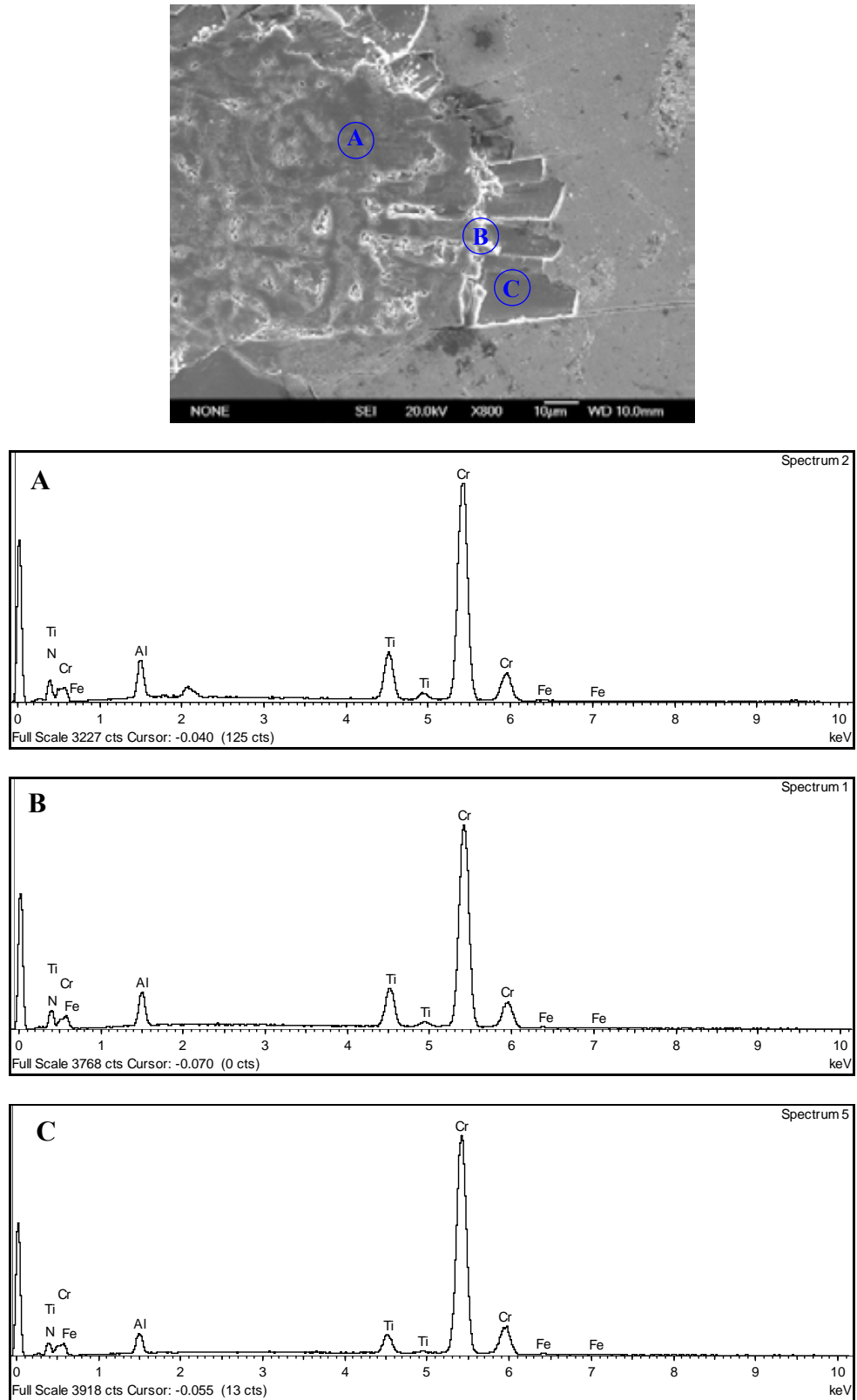
Figure 4.5-20: SEM images of the end region of the scratched track and EDX spectrums from 700℃/ 2 hrs oxidised CrAlTiN-0# sample
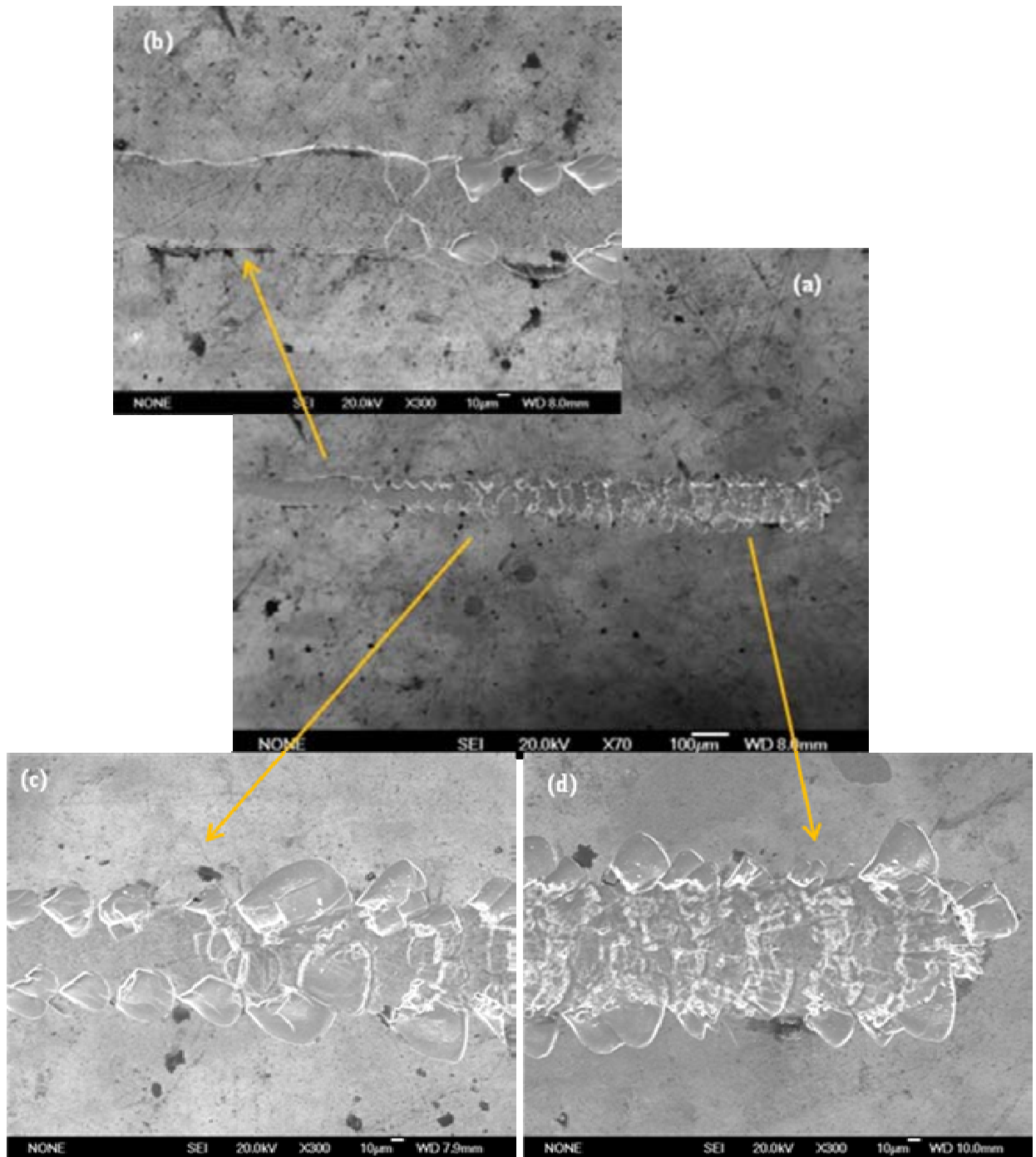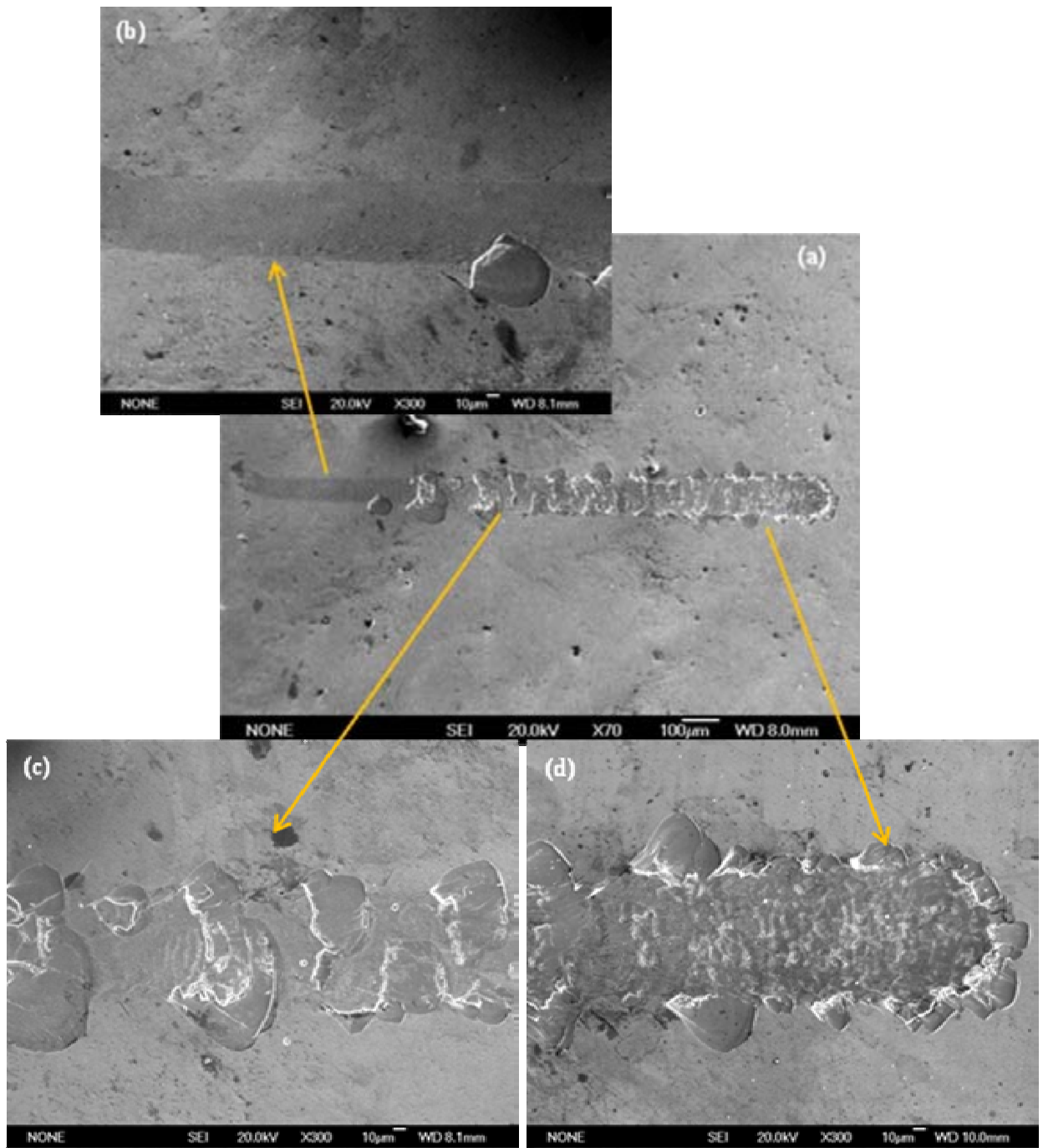
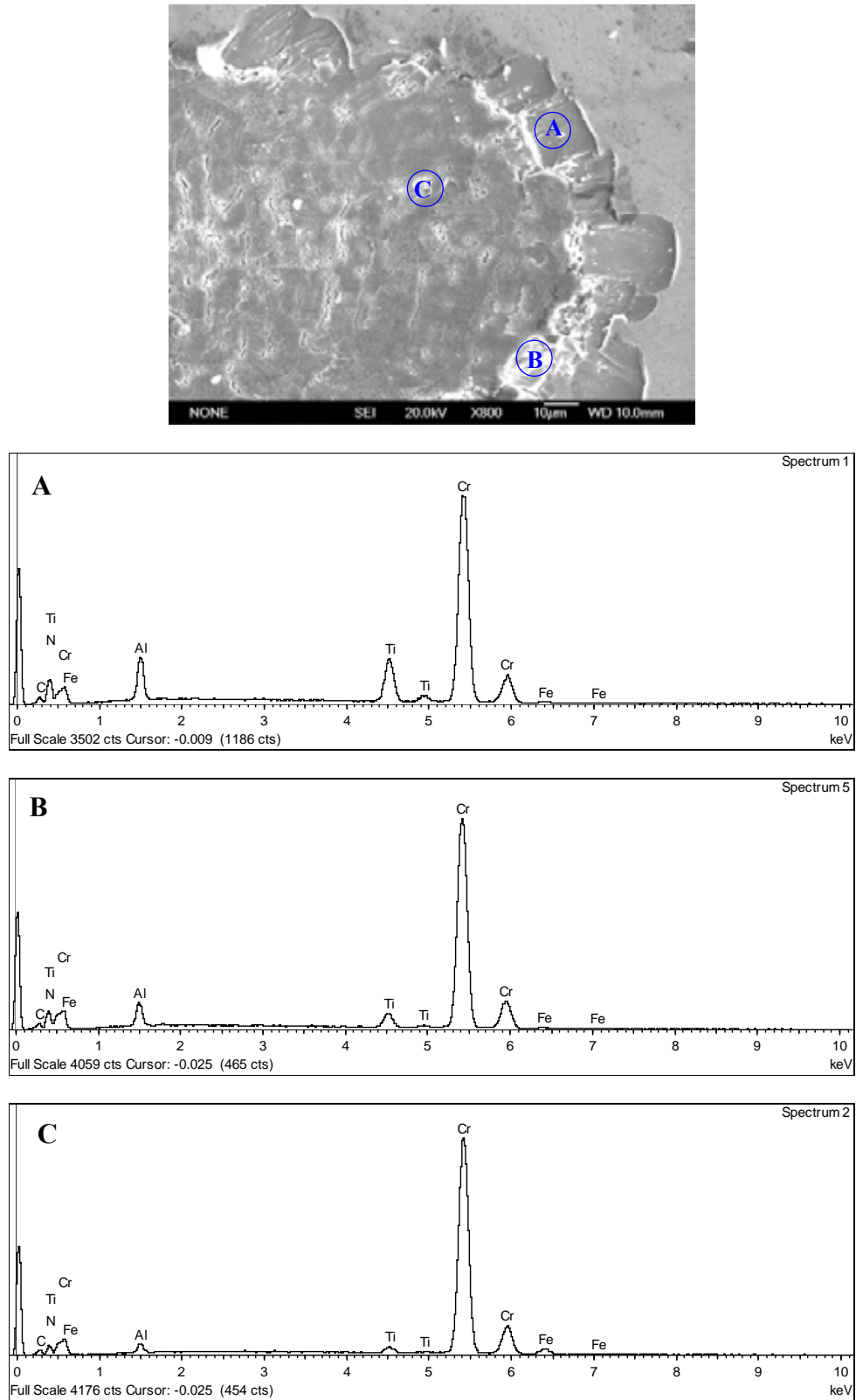Figure 4.5-21: SEM images of the scratched track from 700℃/ 2 hrs oxidised
CrAlTiCN-3# sample
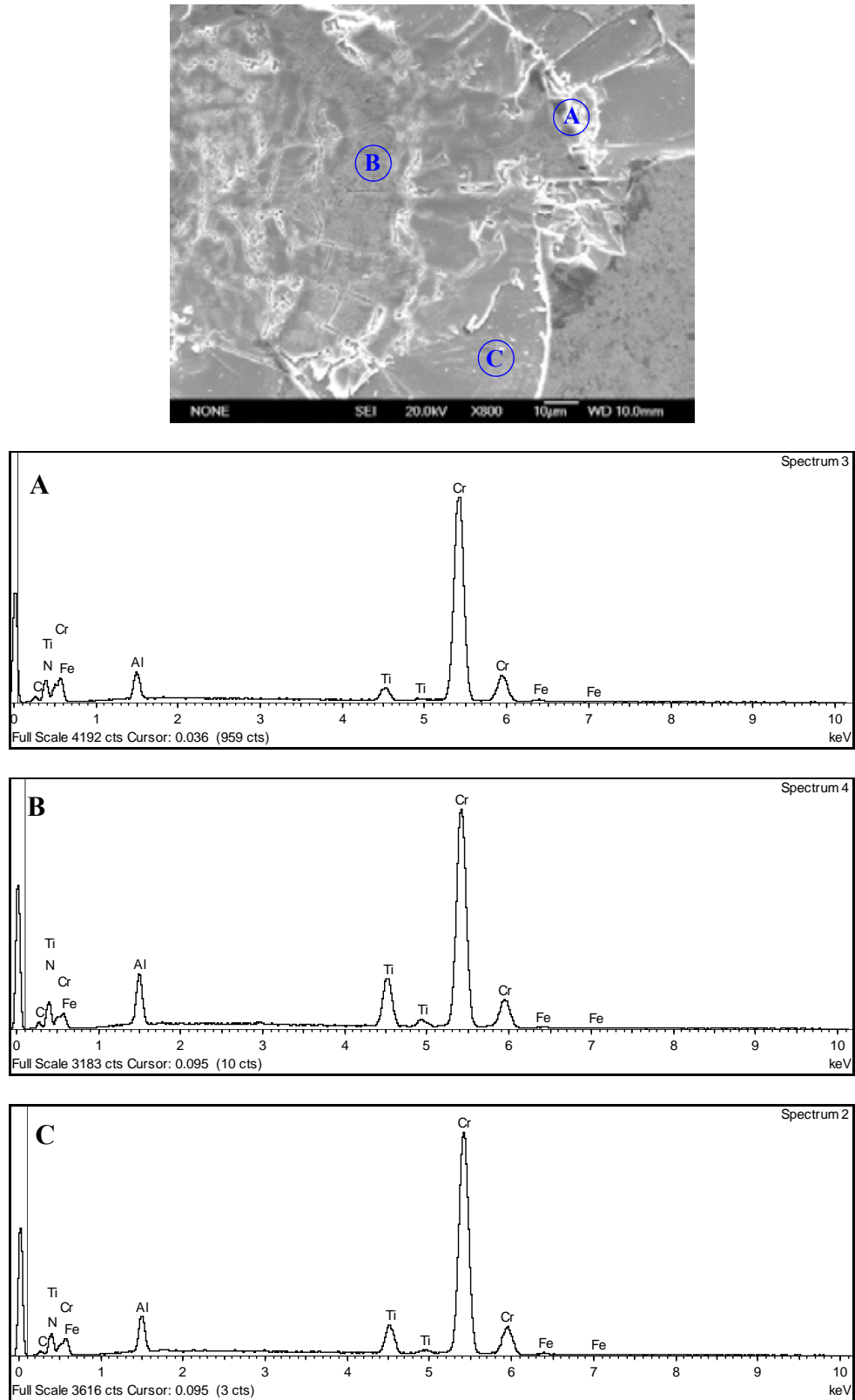
Figure 4.5-22: SEM images of the end region of the scratched track and EDX spectrums from 700℃/ 2 hrs oxidised CrAlTiCN-3# sample

Figure 4.5-23: SEM images of the scratched track from 700℃/ 2 hrs oxidised
CrAlTiCN-5# sample

Figure 4.5-24: SEM images of the end region of the scratched track and EDX spectrums from 700℃/ 2 hrs oxidised CrAlTiCN-5# sample
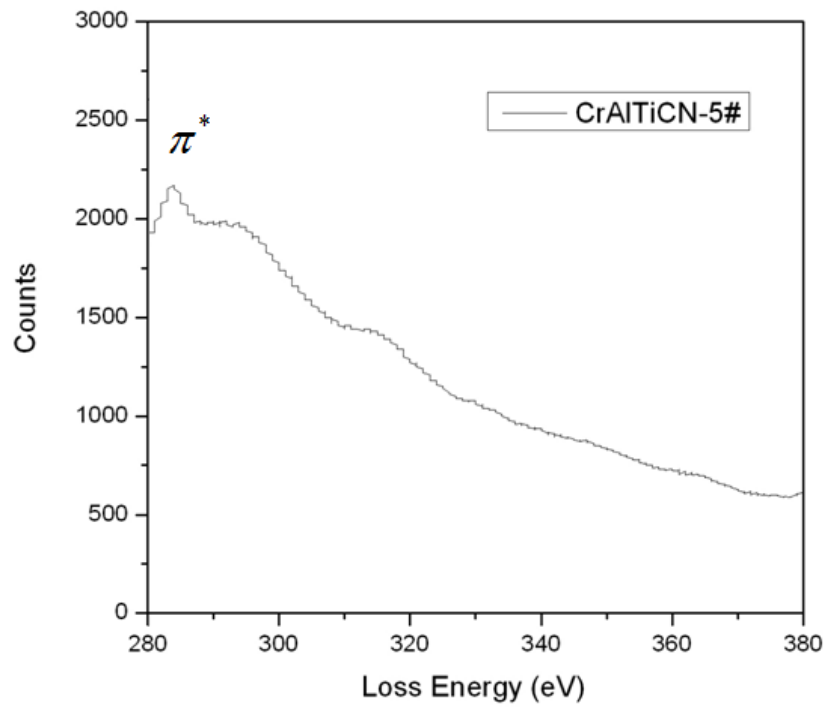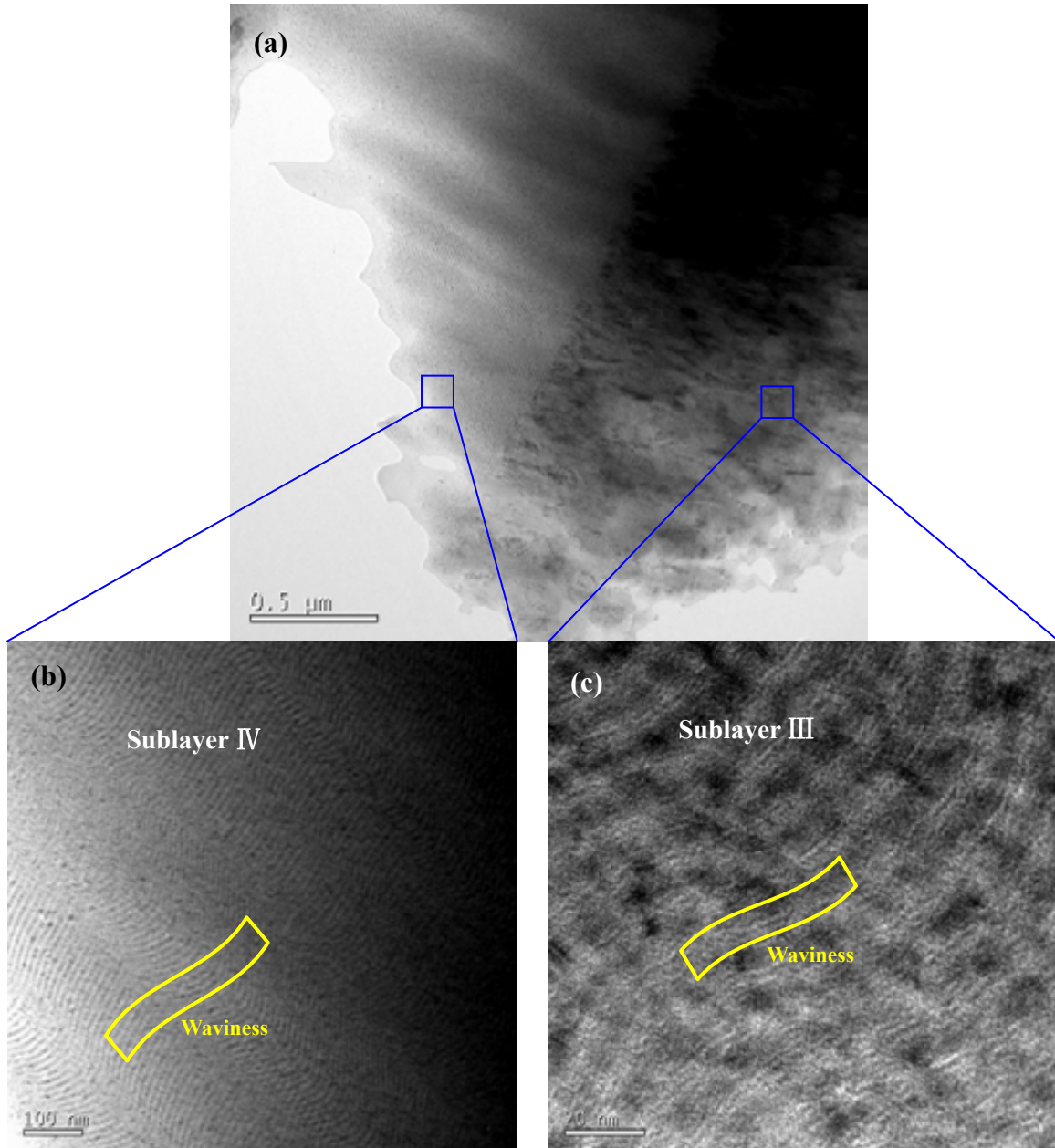
Figure 5.1-1: EELS spectrum for CrAlTiCN-5# coating

Figure 5.1-2: TEM morphologies showing waviness features on sublayers Ⅲ and Ⅳ
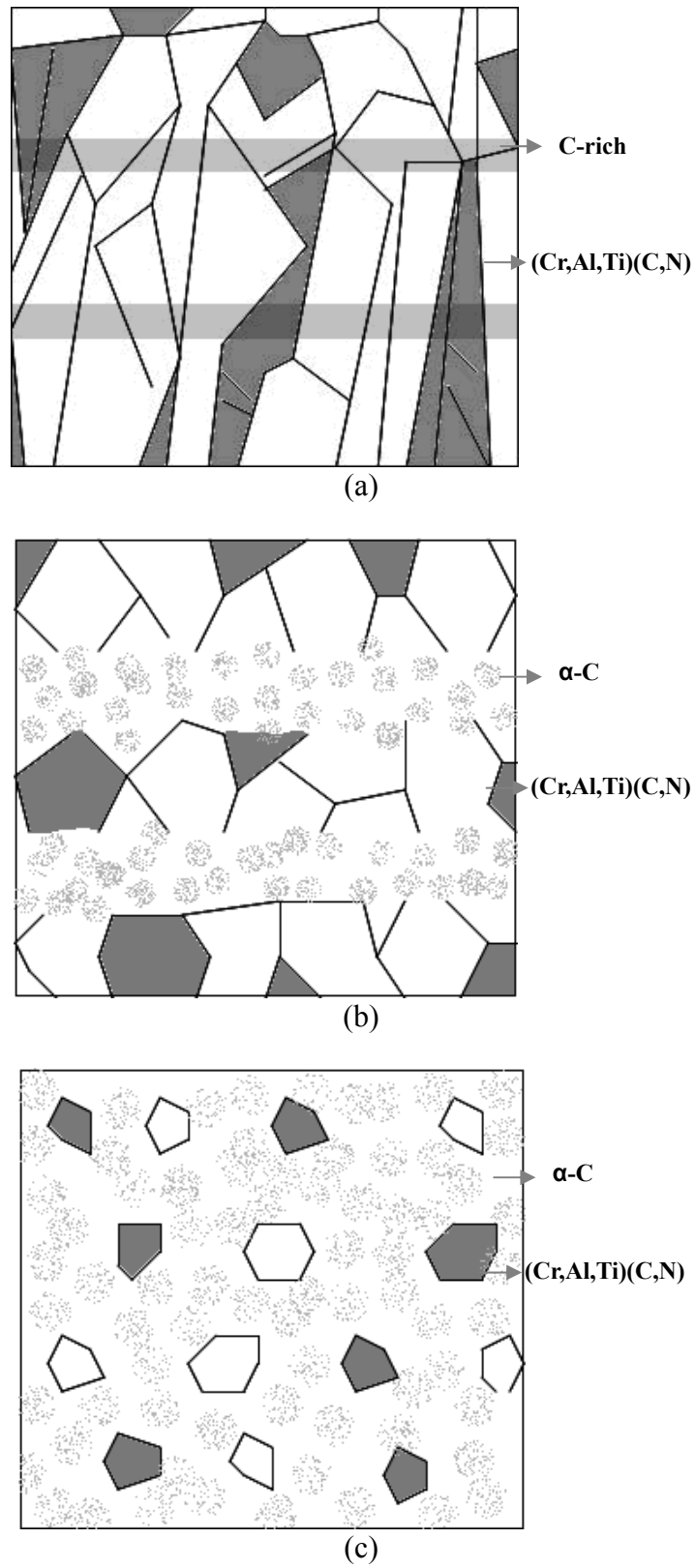from CrAlTiCN-5# coating

(a)

(b)

(c)

Figure 5.1-3: Schematic drawing showing evolution of the microstructure of carbon-doped CrAlTiCN coatings with (a) low-carbon; (b) medium-carbon; (c) high-carbon content
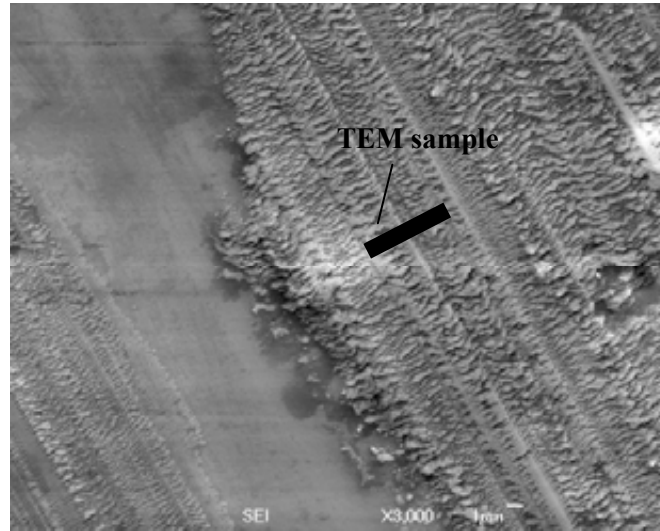
Figure 5.3-1: SEM image showing tribolayer formed in CrAlTiCN-5# sample
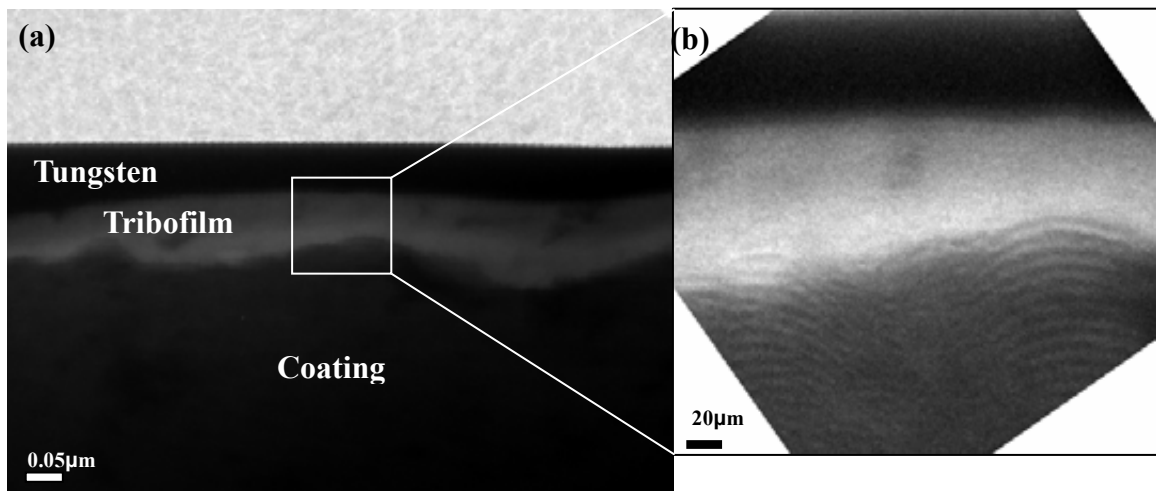

Figure 5.3-2: Cross-sectional TEM observation of the tribofilm slid
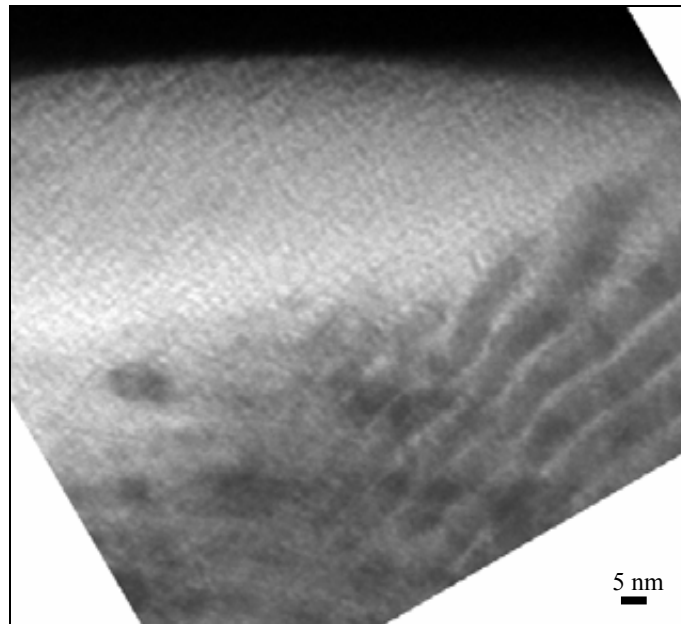from CrAlTiCN-5# coating

Figure 5.3-3: High resolution image of tribofilm from CrAlTiCN-5# coating

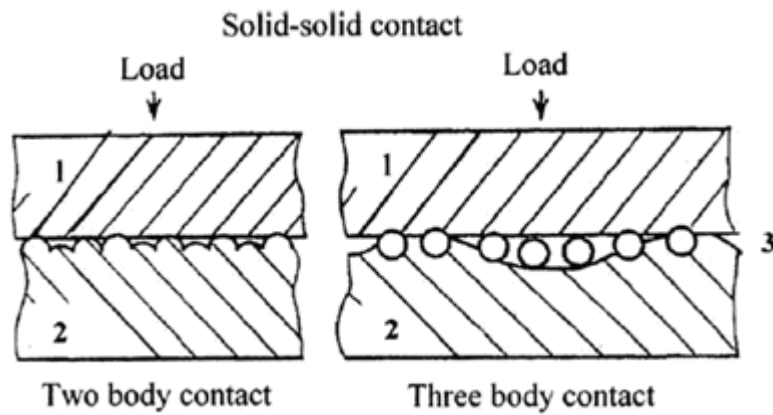Figure 5.3-4: Schematics of two-body and three-body contact of rough surfaces [350]
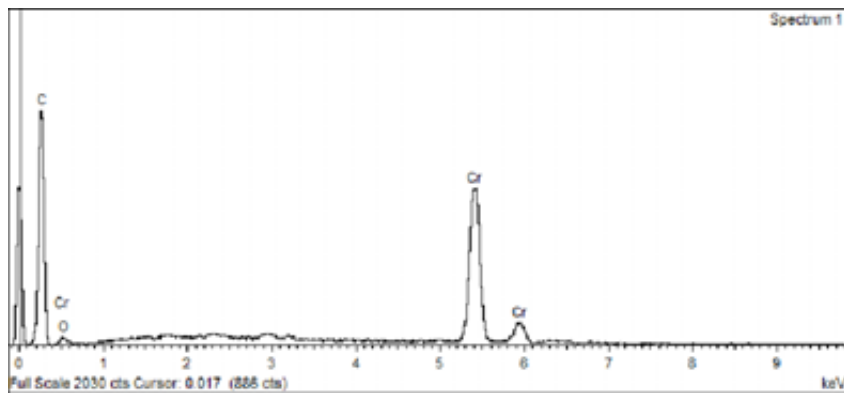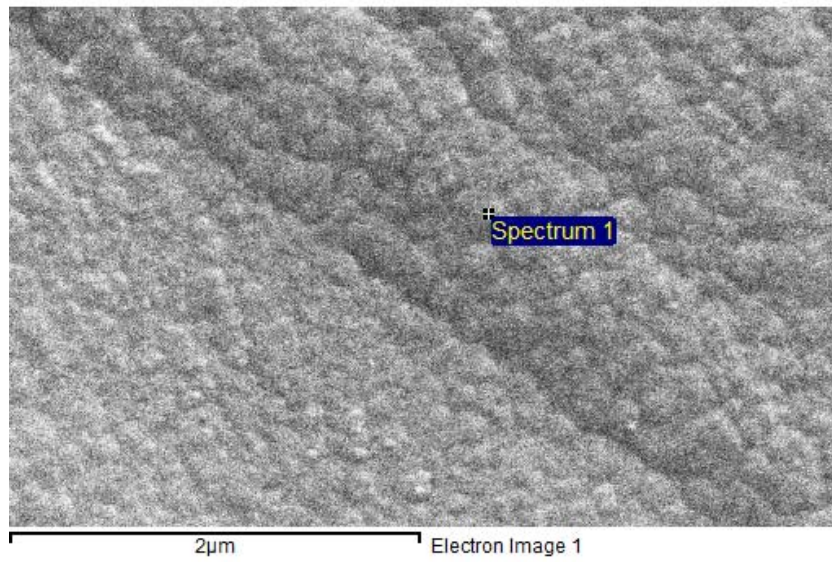
Element	Cr	C	O
at%	19.27±0.43	79.67±0.43	1.06±0.16

Figure 5.3-5: SEM images and EDX compositional analysis of as-deposited GLC coating
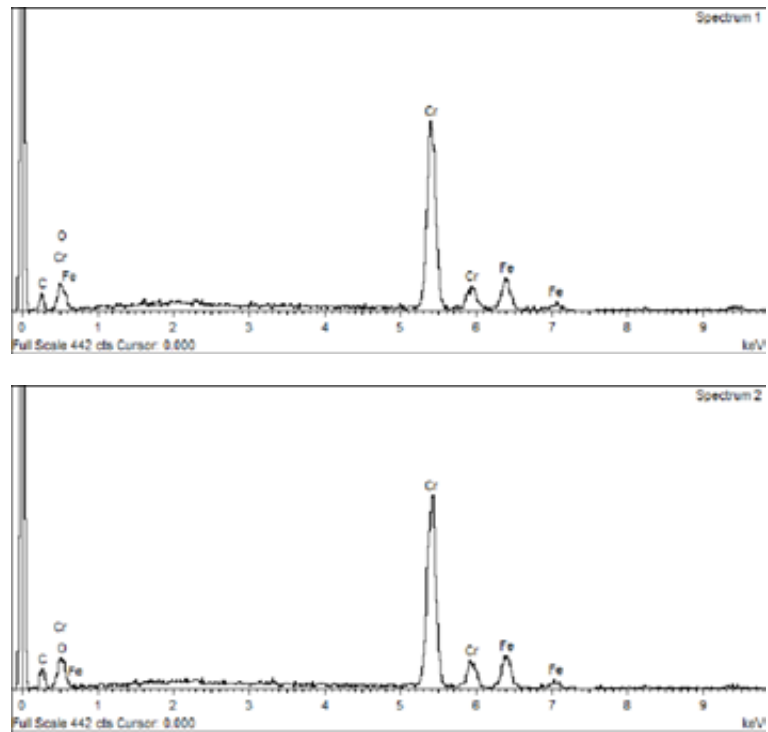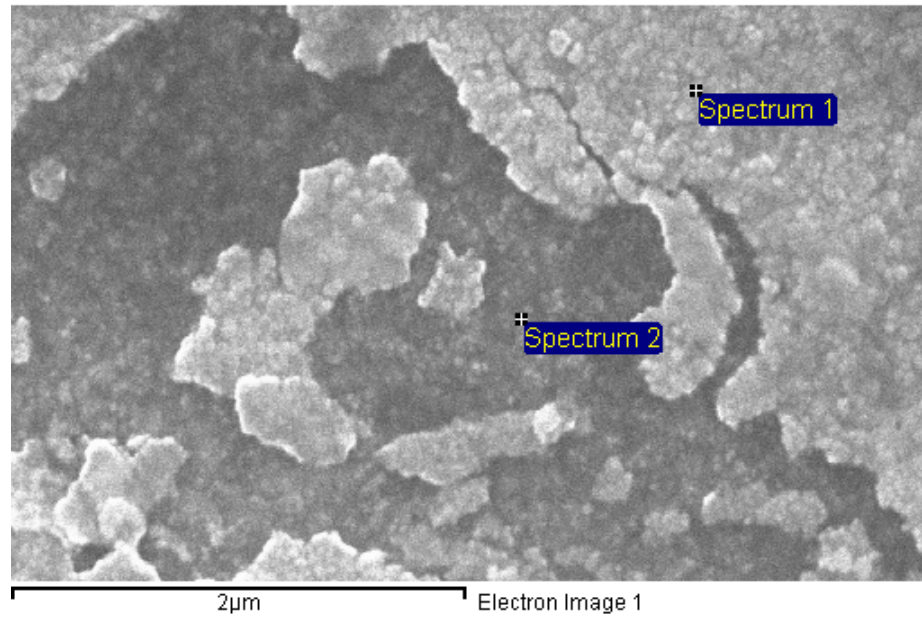
Element	Cr	C	O	Fe
Spectrum 1	61.39±1.00	20.09±0.69	6.38±0.54	12.14±0.75
Spectrum 2	58.61±0.99	21.72±0.72	7.37±0.56	12.30±0.73

Figure 5.3-6: SEM images and EDX compositional analysis of oxidised GLC coating
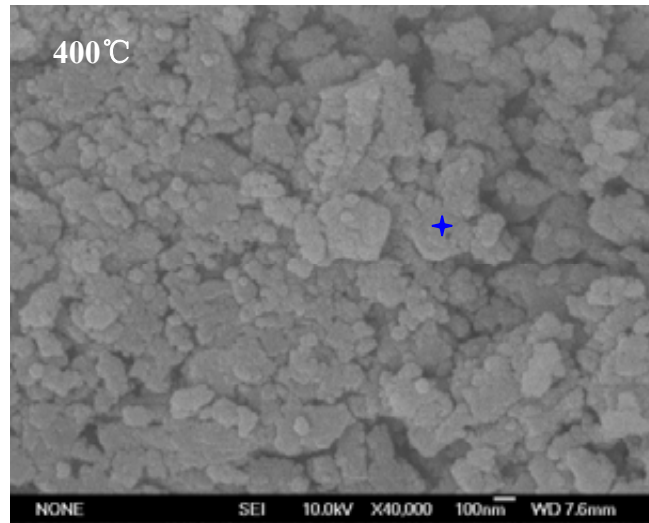
Element	C	O	Cr	Fe
Content (at%)	29.26±0.98	10.37±0.05	44.37±0.76	16.00±0.55

(a)
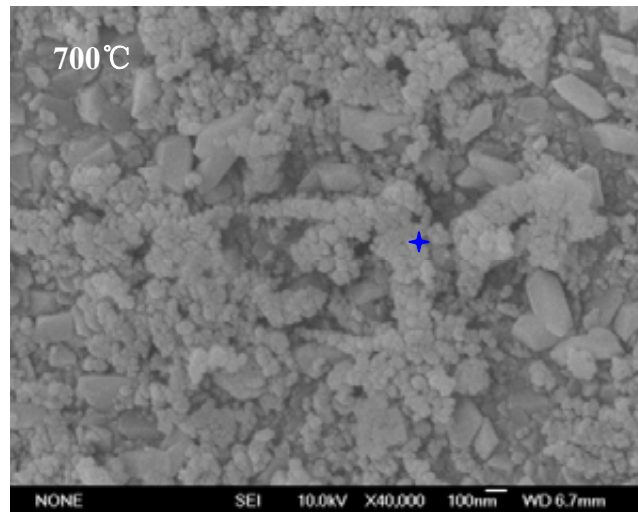
Element	C	O	Cr	Fe
Content (at%)	15.57±0.32	51.70±0.54	2.42±0.18	30.31±0.43

(b)

Figure 5.4-1: SEM images and EDX compositional analysis of GLC coating oxidised at
(a) 400℃; (b) 700℃
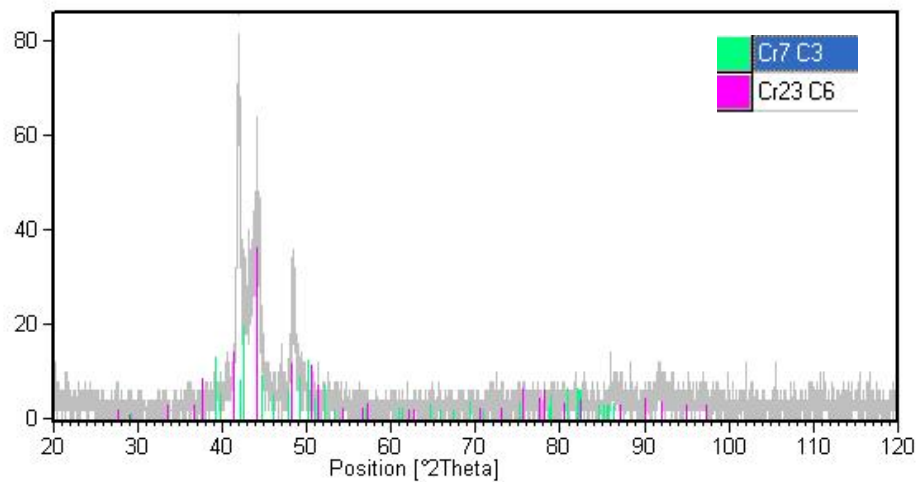
(a)
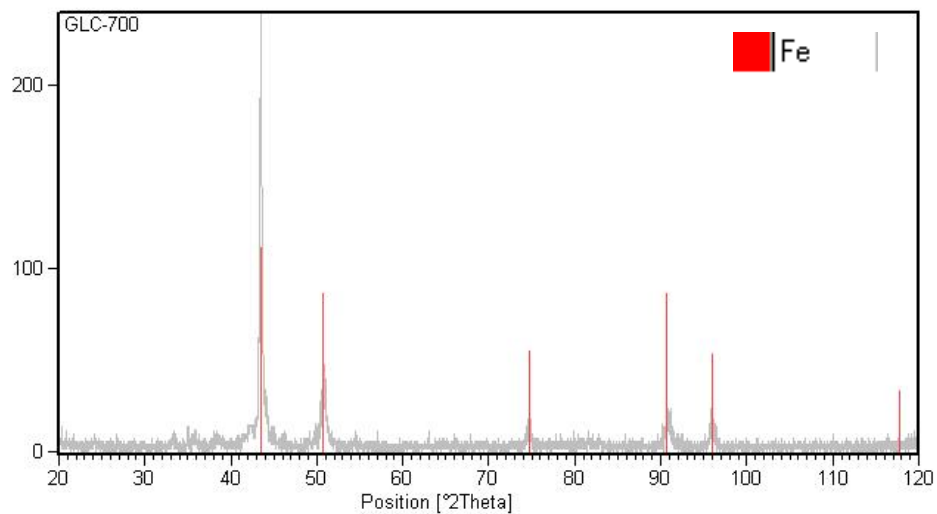
(b)

Figure 5.4-2: XRD patterns obtained on GLC coating oxidised at:
(a) 400℃; (b) 700℃

Appendices

A-1 Calculation of d-spacing from TEM

For Figure 4.2-9, the camera constant used (Lλ) is 1.25 nm². The shortest radius for Fig.

4.2-9b is 5.2 mm. According to equation

$$d = \frac{L\lambda}{R}$$

Therefore the d-spacing (d) =0 .2404nm

This is then repeated for the other SAD

A-2 Calculation of the Contact Pressure and Area Radius

Example calculation: of the contact pressure and the contact area that occur throughout the

pin-on-disc test. The calculations for the reciprocating wear test follow using the according

variables.

Data can be obtained from Table A-8

Radius of sphere counterface (R): 2.5 mm

Young's modulus of CrAlTiCN-5# (E): 230 GPa

Young's modulus of WC-Co sphere (Ei): 600 GPa

Poisson ratio of CrAlTiCN coating (v): 0.23

Poisson ratio of WC-Co sphere (vi): 0.22

Substituting the values in Equations A-1

$$E^* = \frac{1}{\dfrac{1-\upsilon^2}{E} + \dfrac{1-\upsilon_i^2}{E_i}} \qquad \text{(A-1)}$$

E*=186 GPa

Substituting the values in Equations A-2

$$P_0 = \frac{1}{\pi}\left(\frac{6PE^{*2}}{R^2}\right)^{1/3} \qquad \text{(A-2)}$$

Contact pressure (P_0) =2.668 GPa

Substituting the values in Equations A-3

$$a = \left(\frac{3RP}{4E^*}\right)^{1/3} \qquad \text{(A-3)}$$

Contact area radius (a) =0.05984 mm

A-3 Tables

Table A-1 Cr (No. 00-006-0694)

h	k	l	d (nm)	2θ	I (%)
1	1	0	0.20390	44.393	100.0
2	0	0	0.14419	64.583	16.0
2	1	1	0.11774	81.724	30.0
2	2	0	0.10195	98.150	18.0
3	1	0	0.09120	115.264	20.0

Table A-2 CrN (No. 00-003-1157)

h	k	l	d (nm)	2θ	I (%)
1	1	1	0.240	37.442	80.0
2	0	0	0.207	43.694	80.0
2	2	0	0.147	63.204	100.0
3	1	1	0.125	76.084	88.0

Table A-3 Cr$_2$N (No. 00-001-1232)

h	k	l	d (nm)	2θ	I (%)
1	1	0	0.238	37.768	25.0
0	0	2	0.222	40.606	25.0
1	1	1	0.210	43.038	100.0
1	1	2	0.163	56.403	25.0
3	0	0	0.138	67.861	25.0
2	1	2	0.127	74.679	20.0

Table A-4 Cr$_2$O$_3$ (No.00-038-1479)

h	k	l	d (nm)	2θ	I (%)
0	1	2	0.363132	24.494	73.0
1	0	4	0.266533	33.597	100.0
1	1	0	0.247969	36.196	93.0
0	0	6	0.226585	39.749	7.0
1	1	3	0.217520	41.480	35.0
2	0	2	0.204771	44.194	6.0
0	2	4	0.181521	50.220	38.0
1	1	6	0.167237	54.853	87.0

Table A-5 Al₂O₃ (No. 00-010-0414)

h	k	l	d (nm)	2θ	I (%)
0	0	6	0.378	23.517	10.0
1	1	0	0.280	31.937	50.0
1	0	7	0.268	33.408	70.0
1	1	4	0.251	35.744	30.0
2	0	1	0.241	37.281	30.0
2	0	4	0.224	40.227	30.0
2	0	5	0.214	42.195	30.0

Table A-6 TiO (No. 00-088-0117)

h	k	l	d (nm)	2θ	I (%)
			0.3750	23.707	60.0
			0.3320	26.823	80.0
			0.2950	30.273	60.0
			0.2790	32.292	60.0
			0.2770	32.292	60.0
			0.2441	36.790	30.0
			0.2414	37.217	60.0
			0.2390	37.604	80.0
			0.2098	43.081	80.0
			0.2069	43.716	100.0
			0.1942	46.738	10.0

Table A-7 Cr$_{23}$C$_6$ (No 00-035-0783)

h	k	l	d (nm)	2θ	I (%)
4	0	0	0.266579	33.591	4.0
4	2	0	0.238305	37.718	23.0
4	2	2	0.217615	41.461	24.0
5	1	1	0.205199	44.097	100.0
4	4	0	0.188403	48.266	20.0
5	3	3	0.162607	56.552	2.0
6	4	0	0.147877	62.786	1.0

Table A-8 Fe (No. 00-006-0696)

h	k	l	d (nm)	2θ	I (%)
1	1	0	0.20268	44.674	100.0
2	0	0	0.14332	65.023	20.0
2	1	1	0.11702	82.335	30.0
2	2	0	0.10134	98.949	10.0
3	1	0	0.09064	116.390	12.0

Table A-9 Modulus and Poisson ratio of materials used for tribological tests

Material	Modulus, E (GPa)	Poisson ratio, v
Cobalt-Chromium	230	0.3
Tungsten Carbide	600	0.22
Diamond	1220	0.1-0.29
CrAlTiCN coating	283-231	0.23 [1]

Values obtained from data sheets of supplier

[1] Q. Luo, A. H. Jones, High-precision determination of residual stress of polycrystalline coatings using optimized XRD-sin$^2\Psi$ technique, Surface & Coatings Technology, Processing